Thermochimica Acta, 22 (1977) 1–156

A review

Emanation thermal analysis

VLADÍMIR BALEK
Nuclear Research Institute, 250 68 Řež (Czechoslovakia)

CONTENTS

INTRODUCTION

During the past two decades the family of thermoanalytical methods has been complemented by the technique of emanation thermal analysis, a method which is based on the inert gas release from solids. The emanation method, known in radiochemistry for more than half a century, has undergone in recent years a particularly important development in theory, instrumentation and application. Requirements of nuclear technology, i.e., to understand inert gas behaviour in irradiated nuclear fuels, as well as the rapidly increasing knowledge of the solid state, contributed to the development of the theory of the method. The requirements of more and more sensitive experimental techniques in the investigation of solid-state processes, together with modern nuclear instrumentation developed in recent decades, facilitated the expansion of the emanation method to various branches of science and technology. The method has found diverse application in solid-state chemistry, physical chemistry, mineralogy, metallurgy, silicate chemistry and ceramics, polymer chemistry, etc. Inert gases have become the trace indicators of the solid state and its changes. They have also been widely used as universal indicators in analytical chemistry for the analysis of gases, liquids and solids.

The number of publications dealing with the matter has steadily increased since the beginning of this century. Review articles by Zimens[1] (1942, 1943) and Hahn[2] (1949) were followed by surveys of inert gas applications in various branches by Chleck et al.[3] (1963), Zhabrova and Shibanova[4] (1967), Ichiba[5] (1968), Balek and Zaborenko[6] (1968), Tölgyessy and Varga[7] (1970), Balek[8-10] (1964, 1969, 1970), Matzke[11, 12] (1969, 1970), Bussière[13] (1972), Felix[14, 15] (1973) and others. An important place was allocated to the emanation method and the inert gas diffusion solids in monographs by Hahn[16] (1936), Wahl and Bonner[17] (1951) and Adda and Philibert[18] (1966). Zimen, Freyer[19] (1966, 1968) and Zimen and Mickeley[20] (1973) issued a bibliography on the inert gas release from solids.

However, a summarizing and classifying survey of the practical viability and limitations of emanation thermal analysis for the solution of specific problems in various branches together with an outline of the state of present-day theories and their feasibility does not exist in recent literature. The present work aims at improving this situation and the facilitation of further application of emanation thermal analysis.

The subject matter is divided into six Chapters. Chapter 1 gives the definition and historical development of the method. Chapter 2 deals with techniques used for the labeling solids by inert gases. Chapter 3 and 4 outline the theories of inert gas release from solids in cases of introducing into the solid inert gas as such and its parent, respectively. Chapter 5 deals with the measurement of inert gases used in ETA. The possibilities and limitations of the method itself as well as some important applications are dealt with in Chapter 6.

The present work does not pretend to give an exhaustive bibliography on emanation thermal analysis; it is intended rather to give instructive guidelines. Certain

principles of radiochemistry and nuclear physics related to the method are given here, since many readers may be unfamiliar with these concepts.

During the years of collecting material for this review a number of institutions and persons from all over the world have been helpful to the author who is especially indebted to M..cow State University and Profs. A. N. Nesmejanov and K. B. Zaborenko (USSR); Prof. W. Seelman-Eggebert; Dr. Hj. Matzke; Messrs. Netzsch—Gerätebau and Dr. W. D. Emmerich (Federal Republic of Germany); The Institute for Catalysis Research; Dr. P. Bussière and Prof. G. Claudel (France); Prof. R. Kelly (Canada); Prof. F. W. Felix (Berlin-West); Prof. J. Arvid Hedwall (Sweden); Prof. J. Tölgyessy and Dr. Č Jech (Czechoslovakia). The work could not have appeared in its present form without fruitful discussions and criticism of Drs. P. Holba, K. Habersberger and other colleagues of Prague and Řež. Numerous foreign colleagues are also acknowledged for permission to reproduce their graphical documentation. Many thanks are due to Professor W. W. Wendlandt, Editor-in-Chief of *Thermochimica Acta*, Texas, U.S.A., for his encouragement and critical remarks, and to Dipl. ing. K. Čáslavský, Prague, for the careful reading of the manuscript. Finally, the author thanks Mr. M. Prachař for preparation of the line-drawings.

Chapter 1

BASIC PRINCIPLES AND HISTORICAL DEVELOPMENT

1.1 Definition of the method

Emanation thermal analysis (ETA) is the method by means of which information about the solid state and its changes is obtained on the basis of inert gas release from solids measured at various temperatures. Strictly speaking, emanation thermal analysis is not a method of analysis. The parameter measured, i.e., the total amount of inert gas* released or the velocity of inert gas release are used for the characterization of the solid state.

Inert gas atoms are used as trace indicators of the solid state and its changes. With ETA, both radioactive and non-radioactive (stable) inert gas isotopes can be used, nevertheless the radioactive inert gases are more advantageous for their easy and sensitive detection. The inert gases do not react with the solid, in which they were incorporated in trace amounts before the measurement. The inert gas release measured is controlled by physico-chemical processes of the solid studied. Structural changes, interaction of the solid sample with surrounding medium, or the establishing of chemical equilibrium which take place in solids bring about microscopical processes followed by the inert gas release.

1.2. Terminology

The radiochemical method proposed by Hahn[16] for the investigation of solids by natural radon isotopes (emanation) has usually been called the Hahn emanation method. Later, when other labeling techniques and inert gases were used, various names for the method concerned were invented, such as the method of emanating power (la méthode du pouvoir d'émanation[21]), the evolution of radioactive inert gases (l'émission des gaz rares radioactifs, EGGR[22]), the method of surface gas labeling[23–26], etc. A more general term, the radio-release method[27], has sometimes been used in this connection. The radio-release method using the radioactive isotope of krypton for the labeling solids has been called dekryptonation thermal analysis[28]. In spite of the fact that various gases and various techniques of sample labeling can be used with the method in question we have proposed[10, 29, 30] the term emanation thermal analysis, taking into account its historical development. The abbreviation of the term is ETA. The name, "emanation method", should be reserved for the radioanalytical method of radium determination in mineral waters based on the measurement of radon, the daughter decay product of radium.

---

* The inert gas is generally any gas which does not undergo any chemical interaction with the solid investigated under the given conditions. Noble gases of Group zero of the Periodi Table are most commonly used.

1.3. Historical development

The existence of radioactive emanation was first described by M. Curie[31] in 1900, i.e., only a few years after the discovery of radioactivity. Rutherford[32] (1901) in Great Britain and Kolovrat-Chervinskii[33] (1907) working in the laboratory of M. Curie in Paris first showed that the release of radioactive emanation from radium salts is dependent on temperature.

In the 1920's and 1930's Hahn and his co-workers developed in the Kaiser Wilhelm Institute for Chemistry in Berlin, Germany, the emanation method which enabled the investigation of surface changes of precipitates[34] and modification changes of solids[35].

Baranow and his co-workers[36] (1936) in the U.S.S.R. were engaged in emanation measurements of soils. Many publications of that time came also from other laboratories, such as the Institute for Metallurgy in Stuttgart (Werner et al.), the Chemistry Institute of the Technical University in Stuttgart, Germany (Fricke and his co-workers), and the Radiological Institute in Prague, Czechoslovakia (Běhounek).

In spite of the fact that, after the discovery of uranium fission by Hahn and Strassman[37] (1938, 1939), the interest in naturally radioactive nuclides declined, the emanation method has been further developed in Germany under Professor O. Hahn. There, Flügge and Zimens[38] (1939) devised the first theory of the emanation method, Zimens published papers[1] summarizing all the work concerning this subject matter. Research work on the emanation method was carried out even during World War II, particularly in the Institute for Silicate Research in Gothenborg, Sweden, under Professor J. Arvid Hedvall (Jagitsch and others).

After 1945, several research groups in Europe and elsewhere were engaged in the application of inert gas release from solids, such as those at the Technical University Stuttgart under Professor R. Fricke; at the University of Mainz, F.R.G. under Professor F. Strassman; at the University of Graz, Austria under Professor G. Hüttig; at the Chalmers University of Technology, Göteborg, Sweden (Zimen and his co-workers, Lindner and his co-workers): at the University of Braunschweig, F.R.G.; (Lindner, Matzke et al.); at U.K. Atomic Energy Research Establishment, Harwell, Great Britain (Gregory, Moorbath and others); at the University of Melbourne, Australia (Anderson, Baulch and others); at the Nuclear Research Center Ispra, Italy (Kelly, Matzke et al.); and at the Hahn-Meitner Institute for Nuclear Research, Berlin-West (Zimen, Felix, Gaus and others).

Numerous studies on the emanation power of minerals were published at the Khlopin Institute of Radium in Leningrad, U.S.S.R., by Starik and his co-workers. The release of inert gases of radiogenic origin concerning the determination of the absolute age of geological materials was studied at the Academy of Sciences, Moscow, U.S.S.R. (Gerling et al.); at the Leningrad State University, U.S.S.R. (Murin et al.); and at Dagestan State University, Makhatschkala, U.S.S.R. (Amirkhanov et al.).

A number of experimental and theoretical papers were published by two

research groups in Moscow; at Moscow State University (Zaborenko and her co-workers) and at the Academy of Sciences (Zhabrova and her co-workers).

In France, the emanation method has been experimentally and theoretically developed at the Institute for Catalysis Research, Villeurbanne—Lyon (Bussière, Claudel and others).

In a number of laboratories all over the world various techniques for the labeling of solids have been developed. For example the labeling techniques based on the recoil effect of fission inert gases were developed at the Japan Atomic Energy Research Institute, in Tokai-Mura (Yajima and his co-workers); Nuclear Reactor Center Seibersdorf, Austria (Koss); North Caroline State University; and Battelle Memorial Institute, Columbus, OH, U.S.A. (Morrisson, Elleman).

The diffusion technique for labeling solids by krypton was established by Chleck and his co-workers at Parametrics Inc., MA, U.S.A. Other techniques of the inert gas incorporation into solids were developed at the Chalk River Nuclear Laboratories, Canada (Kelly and others); at the Czechoslovak Academy of Sciences, Prague, Czechoslovakia (Jech); and at the University of Technology, Bratislava, Czechoslovakia (Tölgyessy and his co-workers).

Ion bombardment techniques, largely developed in the 1950's and 1960's for the purpose of electronics, have been succesfully used also for the labeling of solids by inert gases. The studies concerning this subject were carried out, e.g., at the Chalk River Nuclear Laboratories, Canada (Davies et al.); at the National Research Council, Canada (Kornelsen et al.); at the University of Aarhus, Denemark (Almén and Bruce, Lindhard and others); and at the University of Liverpool, Great Britain. (Carter et al.).

In this way, various problems of solid-state chemistry, metallurgy, physical chemistry, catalysis and other branches have been investigated by means of inert gases. On the other hand, the inert gases brought about some problems in nuclear technology, such as the swelling of nuclear fuel material. Numerous inert gas diffusion studies have been conducted in various laboratories (like the Argonne National Laboratory, Brookhaven National Laboratory, U.S.A. The Nuclear Research Center, Saclay in France; Chalk River Nuclear Laboratori , Canada; and the Japanese Atomic Energy Research Institute) to improve the understanding and control of the process of swelling of nuclear fuel and the fission product release in nuclear reactor fuels. In place of reactor fuels, non-fissionable solids such as alkali and alkaline-earth halides have been frequently investigated with the expectation of getting a better insight into more complicated fissionable material. For this purpose labeling techniques based on the neutron activated nuclear reactions have been suggested and developed in the Hahn-Meitner Institute for Nuclear Research, Berlin-West (Zimen, Felix and their co-workers): at the Nuclear Research Center Karlsruhe, F.R.G. (Schmeling et al.); and at the Nuclear Research Center Studsvik, Sweden (Lagervall).

In the U.K. Atomic Energy Research Establishment, Harwell, and Oxford University, England, theoretical studies were carried out by Lidiard and Norgett (1968), which signified the beginning of a new insight on the inert gas release processes

from irradiated solids. Theoretical studies done by Kelly, Matzke and Jech at Nuclear Research Center, Ispra, Italy, McMaster University, Hamilton, Canada and the European Institute for Transuranium Elements, Karlsruhe, F.R.G., between 1964 and 1970 established the bases for the evaluation of inert gas release measurements from solids labeled by ion bombardment.

Thermoanalytical methods (such as DTA, TG/DTG, dilatometry), X-ray patterns etc., have often been used as supplementary methods of ETA. However, questions were raised concerning the comparison and interpretation of the results of the above-mentioned methods. To answer these questions and to find new applications of ETA, systematic work has been undertaken by Balek and his co-workers at the Charles University, Prague, and the Nuclear Research Institute Řež near Prague, Czechoslovakia.

Instruments permitting simultaneous ETA measurements with such methods as DTA, TG/DTG, EGA and dilatometry, have been designed in various European laboratories and have been commercially available from Messrs. Netzsch-Gerätebau Inc., Selb. F.R.G. These instruments differ greatly from the laboratory apparatus used by Hahn in the 1920's and 1930's. Instead of an ionisation chamber connected to an electroscope, the scintillation or semiconductor detectors are used to measure the amount of radioactive inert gas released. Mass spectrometric detection or thermal conductivity detection is used for non-radioactive gases. New equipments are equipped with automated temperature control and automatic recording of all of the parameters measured.

The switch over from the emanation methods to emanation thermal analysis described above can also be documented by a number of publications dealing with the inert gas release. Fig. 1 shows the diagram of the number of papers published in each decade from 1900 to 1970.

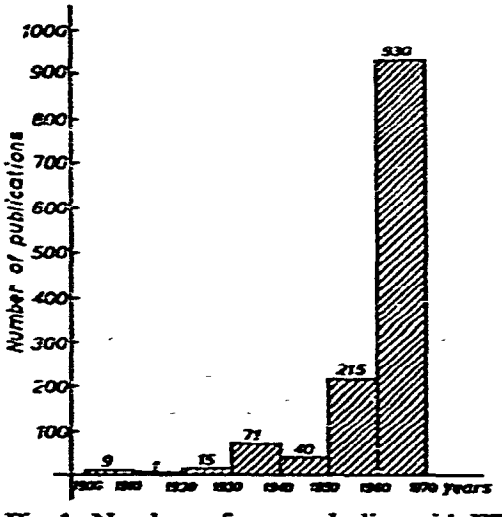

Fig. 1. Numbers of papers dealing with ETA published in the decades between 1900 to 1970.

Chapter 2

LABELING OF SAMPLES

In most cases materials to be examined by ETA do not contain the inert gas, and it is therefore necessary to label the solid with the inert gas in order to make possible the subsequent measurement of gas release from the sample. The techniques of labeling consist, in general, either in the introduction of the inert gas itself, or in the incorporation of its parent nuclide (as the inert gas source) into the solid. The most common techniques of the incorporation of inert gas itself are based on:

(i) the diffusion of inert gas into solid under high pressure and temperature;

(ii) the inclusion of inert gas by sample during its preparation or phase transitions in the gas atmosphere;

(iii) the bombardment of the sample surface by accelerated ions of inert gases.

For the introduction of parent nuclides the so-called (i) incorporation technique, (ii) impregnation technique, or (iii) recoil technique are mainly used.

2.1. Inert gas sources

Natural radioactive inert gases such as radon isotopes or common non-radioactive inert gases (e.g., argon, krypton, xenon) and their radioactive isotopes can generally be used for ETA-measurements. The radioactive inert gases are preferred because of their easy detection. Radioactive isotopes of inert gases which can be used in ETA and their characteristics[39] are listed in Table 1.

Nuclear reactions yielding inert gas nuclides can be used for the production of inert gases. Examples of nuclear reactions producing inert gas of not too short half-life in amounts sufficient for the emanation measurement are given in the following sections.

2.1.1. Nuclear reactions producing inert gases

(*a*) *Alpha decay.* The list of inert gas nuclides formed by alpha decay of their ancestors is given in Table 2. By subsequent decay of inert gas atoms non-gaseous products, called "active deposit", are formed. The naturally radioactive parent atoms, the proper inert gas atoms and the active deposit atoms belong to chains of successive decays which constitute radioactive families or series[40].

(*b*) *Beta decay.* Artificially produced radioelements undergoing beta decay can also be used for the production of inert gas atoms. Some of the gases and parent nuclides are listed in Table 3.

(*c*) *Neutron activated reactions.* The inert gas atoms can be formed in a number of solids by neutron irradiation in nuclear reactors. Neutron activated nuclear reactions (n, p) (n, α) and (n, γ) and fission (n, f) occur in these cases. Table 4 lists the inert gases which can be produced by fast neutron irradiation in compounds containing alkali and alkaline earth elements.

TABLE 1

RADIOISOTOPES OF INERT GASES

Inert gas nuclide	*Half-life*	*Decay mode and energy*	*Way of production*
^{6}He	~0.8 s	$-\beta$ 3.5 MeV	^{9}Be (n, α)
^{23}Ne	38 s	$-\beta$ 4.4 MeV $-\gamma$ 439 keV	^{22}Ne(n, γ); ^{23}Na(n, p), ^{26}Mg(n, α)
^{24}Ne	3.38 min	$-\beta$ 2.0 MeV $-\gamma$ 874 keV	^{22}Ne(t, p)
^{37}Ar	35.1 day	El. capture	^{34}S(α, n); ^{37}Cl(d, 2 n); ^{37}Cl(p, n) ^{39}K(d, α) ^{35}Ca(n, α)
^{39}Ar	269 yr	$-\beta$ 0.6 MeV	^{38}Ar(n, γ) ^{39}K(n, p)
^{41}Ar	1.83 h	$-\beta$ 1.2 MeV γ 1.3 MeV	^{40}Ar(d, p), ^{40}Ar(n, γ); ^{41}K(n, p)
^{42}Ar	33 yr	$-\beta \sim$ 0.6 MeV	^{41}Ar(n, γ), parent ^{42}K
^{76}Kr	14.6 h	El. capture	^{89}Y(p, spallation)
^{77}Kr	1.24 h	$+\beta$ 1.9 MeV γ 130 keV	^{74}Se(α, n)
^{79}Kr	34.9 h 50 s	El. capture γ 130 keV	^{76}Se(α, n), ^{79}Br(d, 2n); ^{79}Br(p, n) ^{78}Kr(n, γ)
^{81}Kr	2.1×10^{5} yr 13.3 s	El. capture γ 191 keV	^{81}Br(p, n); ^{80}Kr(n, γ) daughter ^{81}Rb
^{83m}Kr	1.83 h	γ 9 keV	^{80}Se(α, n), ^{82}Kr(d, p), ^{82}Kr(n, γ) X-rays on ^{83}Kr, fission U, daughter ^{83}Br, daughter ^{83}Rb
^{85m}Kr	4.48 h	$-\beta$ 0.8 MeV γ 151 keV	^{85}Se(α, n); ^{84}Kr(n, γ) ^{85}Rb(n, p); ^{88}Sr(n, α), fission U, daughter ^{85}Br
^{85}Kr	10.76 yr	$-\beta$ 0.7 MeV	^{84}Kr(n, γ), fission U
^{87}Kr	76.3 m	$-\beta$ 3.5 MeV γ 403 keV	^{86}Kr(n, γ), ^{87}Rb(n, p), fission U
^{88}Kr	2.80 h	$-\beta$ 0.5 MeV γ 2.39 MeV	fission U, Th
^{89}Kr	3.18 m	$-\beta$ 3.5 MeV γ 221 keV	fission U, Pu
^{90}Kr	32.3 s	$-\beta$ 26 MeV γ 1.19 MeV	fission U, Pu
^{91}Kr	8.6 s	$-\beta$ 4.6 MeV γ 109 keV	fission U, Pu
^{92}Kr	1.84 s	$-\beta$ 4.6 MeV γ 142 keV	fission U, Pu, Th
^{93}Kr	1.29 s	$-\beta$ 6.2 MeV γ 1.12 MeV	fission U, Pu
^{94}Kr	0.2 s	$-\beta$	fission U
^{121}Xe	38.8 m	$+\beta$ 2.8 MeV γ 253 keV	^{127}I(p, 7n)
^{123}Xe	20.1 h	El. capture γ 350 keV	^{127}I(p, 6n)
^{125}Xe	2.08 h	El. capture $+\beta$ 1.5 MeV	^{127}I(p, 5n)
^{125m}Xe	5.7 s	γ 112 keV	^{127}I(α, 6n), ^{125}Cs; daughter ^{125}Cs
^{125}Xe	16.8 h	El. capture $+\beta$ γ 188 keV	^{122}Te(α, n); ^{124}Xe(r, γ)

TABLE 1 *(continued)*

RADIOISOTOPES OF INERT GASES

Inert gas nuclide	*Half-life*	*Decay mode and energy*	*Way of production*
^{127m}Xe	70 s	γ 125 keV	^{127}I(α, 4n) ^{127}Cs; daughter ^{127}Cs
^{127}Xe	36.4 d	El. capture γ 188 keV	^{126}Te(α, n); ^{127}I(d, 2n) ^{127}I(p, n); ^{126}Xe(n, γ)
^{129m}Xe	8.89 d	γ 40 keV	^{128}Xe(n, γ)
^{131m}Xe	12.0 d	γ 164 keV	^{131}Xe(n, n'); fission U
^{133m}Xe	2.2 d	γ 233 keV	^{132}Xe(n, γ); fission U
^{133}Xe	5.29 d	$-\beta$ 0.3 MeV γ 81 keV	^{132}Xe(n, γ); ^{132}Xe(d, p); ^{134}Xe(n, 2n) ^{130}Te(α, n); ^{133}Cs(n, p); ^{136}Ba(n, α) fission U
^{135m}Xe	15.3 m	γ 527 keV	^{136}Xe(n, 2n); ^{134}Xe(n, γ) ^{138}Ba(n, α) fission U
^{135}Xe	9.17 h	$-\beta$ 0.9 MeV γ 250 keV	^{134}Xe(n, γ); ^{134}Xe(d, p); ^{136}Xe(n, 2n) ^{138}Ba(n, α); fission U
^{137}Xe	3.83 m	$-\beta$ 4.1 MeV γ 455 keV	^{136}Xe(n, γ); fission U
^{138}Xe	14.1 m	$-\beta$ 0.8 MeV γ 258 keV	fission U
^{139}Xe	39.7 s	$-\beta$ 4.6 MeV γ 219 keV	fission U, Th
^{140}Xe	13.5 s	$-\beta$ 2.6 MeV γ 806 keV	fission U, Th
^{141}Xe	1.79 s	$-\beta$ 4.9 MeV γ 119 keV	fission U
^{143}Xe	0.83 s	$-\beta$ γ 572 keV	fission U
^{206}Rn	5.67 m	α 6.26 MeV El. capture	^{197}Au(^{14}N, 5n)
^{207}Rn	9.3 m	El. capture α 6.126 MeV γ 345 keV	^{197}Au(^{14}N, 4n)
^{208}Rn	24.4 m	α 6.14 MeV El. capture	Spallation Th; Pb(^{12}C, spall)
^{209}Rn	30 m	El. capture + β α 6.039 MeV	Spallation Th; Pb(^{12}C, spall)
^{210}Rn	2.4 h	α 6.04 MeV El. capture γ 458 keV	Spallation Th; Pb(^{12}C, spall)
^{211}Rn	14.6 h	El. capture α 5.783 MeV γ 684 keV	Spallation Th; Pb(^{12}C, spall)
^{212}Rn	24 m	α 6.264 MeV	Spallation Th; Pb(^{12}C, spall)
^{219}Rn	3.96 s	α 6.819 MeV γ 271 keV	Member of ^{235}U decay chain
^{220}Rn	55.6 s	α 6.288 MeV γ	Member of ^{232}Th decay chain
^{221}Rn	25 m	$-\beta$ $\alpha \sim 6.0$ MeV	^{232}Th(p, spall)
^{222}Rn	3.824 d	α 5.48966 MeV γ	Member of ^{238}U decay chain

TABLE 2

INERT GAS NUCLIDES PRODUCED BY α-DECAY

Ancestors		*Inert gas*		*Active deposit*	
Half-life $t_{1/2}$	*Nuclides*	*Nuclides*	*Half-life* $t_{1/2}$	*Nuclides*	*Half-life of the longest-lived nuclide*
1.600 a	$^{226}Ra \xrightarrow[4.78\ MeV]{\alpha}$	$^{222}Rn \xrightarrow[5.5\ MeV]{\alpha}$	3.82 d	^{218}Po, ^{214}Pb, ^{214}Bi, ^{214}Po, ^{210}Tl, ^{210}Pb, ^{210}Bi, ^{210}Po	^{210}Pb 22 a
1.91 a	^{228}Th $\alpha \downarrow$ 5.42 MeV			^{216}Po, ^{212}Pb, ^{212}Bi, ^{212}Po, ^{208}Tl	^{212}Pb 10.6 h
3.64 d	$^{224}Ra \xrightarrow[5.68\ MeV]{\alpha}$	$^{220}Rn \xrightarrow[6.29\ MeV]{\alpha}$	55.6 s		
21.8 a $\beta \downarrow$ 0.045 MeV	^{227}Ac			^{215}Po, ^{215}Bi, ^{211}Pb, ^{211}Bi, ^{211}Po, ^{207}Tl	^{215}Bi 7.4 m
18.7 d $\alpha \downarrow$ 6.04 MeV	^{227}Th				
	$^{223}Ra \xrightarrow{\alpha}$	$^{219}Rn \xrightarrow[6.82\ MeV]{\alpha}$	3.96 s		

TABLE 3

INERT GAS NUCLIDES PRODUCED BY β-DECAY

Half-life	*Ancestor nuclides*	*Inert gas nuclides*	*Half-life*
69 s	^{83}Se		
25 m	$\beta\downarrow\downarrow\beta$		
2.4 h	$^{83}Br \xrightarrow{\beta}$	$^{83}Kr \xrightarrow{\gamma}$	1.9 h
54 m	^{133}Te		
12.5 m	$\beta\downarrow\downarrow\beta$		
20.8 h	$^{133}I \xrightarrow{\beta}$	$^{133}Xe \xrightarrow{\beta}$	5.6 d
6.7 h	$^{135}I \xrightarrow{\beta}$	$^{135}Xe \xrightarrow{\gamma}$	15.6 m
		$\xrightarrow{\beta}$	9.1 h

TABLE 4

INERT GAS NUCLIDES PRODUCED BY (n, p) AND (n, α) NUCLEAR REACTIONS

*M (n, p) G**		*M (n, α) G**	
Li	^{6}He	Be	^{8}Be
Na	^{23}Ne	Mg	^{23}Ne
K	^{39}Ar, ^{41}Ar	Ca	^{37}Ar, ^{41}Ar
Rb	^{85m}Kr, ^{87}Kr	Sr	^{85m}Kr
Cs	^{133m}Xe, ^{133}Xe	Ba	^{135}Xe, ^{133}Xe

TABLE 5

INERT GAS NUCLIDES PRODUCED BY (n, γ) NUCLEAR REACTIONS

*X (n, γ) X** $\xrightarrow{-\beta}$ *G (stable)*				*G (n, γ) G**
F	$\xrightarrow{11\text{ s}}$	^{20}Ne		
Cl	$\xrightarrow{37\text{ m}}$	^{38}Ar	→	^{39}Ar 269 a
Br	→	^{80}Kr		
	$\xrightarrow{36\text{ h}}$	^{82}Kr	→	^{83m}Kr 1.9 h
I	$\xrightarrow{25\text{ m}}$	^{128}Xe	→	^{129m}Xe 8.0 d

The possibilities of (n, γ) nuclear reactions by thermal neutrons are shown in Table 5—on the left. By (n, γ) reactions radioactive halogen atoms are produced which are transformed by beta decay into stable inert gas atoms. During the reactor irradiation of the stable inert gas, a second neutron activation process produces detectable amounts of radioactive inert gas nuclides (see Table 5—on the right). By fission reactions (n, f) of uranium or thorium several Kr and Xe isotopes (e.g., ^{88}Kr, ^{133}Xe, ^{135}Xe) are formed amongst a large variety of other nuclides.

2.1.2. Labeling sources

Parent nuclides producing inert gas by nuclear reactions are designated as labeling sources of inert gas atoms, and used either as external or internal labeling sources.

Two cases of external labeling sources are:

(1) Radium nuclide, ^{226}Ra, is adsorbed on the sample surface and radon nuclide, ^{222}Rn, is formed by its alpha-decay and introduced into the sample by recoil energy,

(2) Uranium foil enriched by ^{235}U surrounding the sample in the flux of thermal

neutrons is an external source of fission inert gases. Inert gases are then introduced into the sample surface by the action of their recoil energy.

The concept of an internal labeling source assumes the incorporation of inert gas parent nuclides into the lattice. In some cases ions of parent nuclides are constituting the lattice.

In this chapter various techniques of labeling solids with inert gases will be described. The techniques are divided into two groups:

(i) techniques introducing the parent nuclide of inert gas;

(ii) techniques introducing the inert gas without the parents.

2.2. Techniques introducing the parent nuclide of inert gas

2.2.1. Incorporation technique

This technique proposed and developed by Hahn[16] and his co-workers in the 1920's and 1930's should be named first of all. The technique consists in incorporation of a parent nuclide producing the inert gas into the solid. The introduction of the parent atoms into the labeled solid is usually accomplished by common crystallization or co-precipitation from the solution containing the radioactive parent nuclide in trace concentrations[10], e.g., 10^{-11} n-solution of ^{228}Th representing about 4×10^3 $s^{-1}ml^{-1}$.

For metal oxide hydrates of gel structure, the adsorption of the parent nuclide atoms into the precipitate can be used. In the case that the specimen is a compound where crystallization or adsorption of the parent nuclide cannot be carried out, it is possible to label another compound from which the desired compound can be prepared. In this way inorganic oxides were prepared by the thermal decomposition of hydroxides, carbonates, oxalates etc.[41]. Mixed oxides of the spinel type are prepared[42] by heating the mixture of simple oxides, hydroxides or carbonates. Metal nickel containing the parent nuclide, ^{226}Ra, was prepared by the reduction of labeled NiO in hydrogen[43].

Zeolites (chabazite and heulandite) were labeled by exchanging calcium ions for barium ions charged with ^{226}Ra[44]. It was shown that the ion exchange for radium actually takes place in the bulk of the mineral and that radium is not merely adsorbed upon the surface of the crystallites whose granular diameter was 0.13 mm. Radium was successfully incorporated into metals by electrolysis or melting[45]. Incorporation of the parent nuclide, ^{133}I, into AgI can be achieved by its precipitation from a solution containing ^{133}I. Labeling of alkali iodides with ^{133}Xe was successfully accomplished[46] by growing the crystals from the melt containing ^{133}I. The resulting specific activity of the labeled samples[10] was usually 3.7×10^4 s^{-1} (i.e. 1 microcurie) of ^{228}Th per gram of sample.

The distribution of the incorporated parent should obviously be uniform if it can be grown isomorphously into the crystal lattice, e.g., as radium in barium salts. With regard to the spatial distribution of the inert gas atoms formed as daughter products of ^{228}Th in a solid, the following considerations seem to be justified. When

an atom of ^{228}Th disintegrates, the resulting atom of ^{224}Ra is ejected along a recoil path some 20–30 nm in length; the same occurs when atoms of ^{224}Ra disintegrate into ^{220}Rn. Irrespective of whether the parent, ^{228}Th, was grown isomorphously on a proper cation site, or located on a surface or an interstitial position, there is a very high probability that both the daughters, ^{224}Ra and ^{220}Rn, end up in some interstitial position remote from vacant cation sites. This can lead to a random distribution of ^{224}Ra and ^{220}Rn atoms within the lattice which in a statistical way can (but need not) result in a uniform spatial distribution. The final distribution is dependent on the structure of the labeled solid and can be changed as a result of diffusion by heating of the sample[13]. When the density of trapping sites for ^{224}Ra and ^{220}Rn in the structure of a labeled solid is high enough, the uniform distribution of the parent should remain during heat treatment.

2.2.2. Impregnation technique

In cases where no possibility of introducing the parent nuclide during the preparation of the sample exists, it is possible to use the so-called impregnation technique. This technique consists of treating a substance to be labeled with a solution containing the radioactive parent nuclides. The specific radioactivity of the commonly used labeling solutions containing ^{228}Th and ^{224}Ra is in the order of 10^4 $s^{-1}ml^{-1}$ (i.e., several microcuries ml^{-1}). The impregnation technique was successfully used for labeling minerals, various chemical products delivered commercially, etc. The resulting specific activity of the labeled samples is in the order of 10^4 $s^{-1}g^{-1}$ (i.e., of several microcuries g^{-1}).

As to the distribution of the labeling atoms in the solid the following considerations can be made. We can suppose that the ^{228}Th parent atoms are present, after labeling by the impregnation technique, only on the surface of the solid (see Fig. 2). The daughter products, ^{224}Ra and ^{220}Rn, are immediately injected as a result of their recoil into the depth of the grains. The maximum depth of penetration of ^{220}Rn is two path lengths of the recoil in the given substance. This is about[47] 60 nm in the substance of a mean density of 3 g cm^{-3}. If no special homogenization measures are taken, the impregnation technique usually yields a non-uniform distribu-

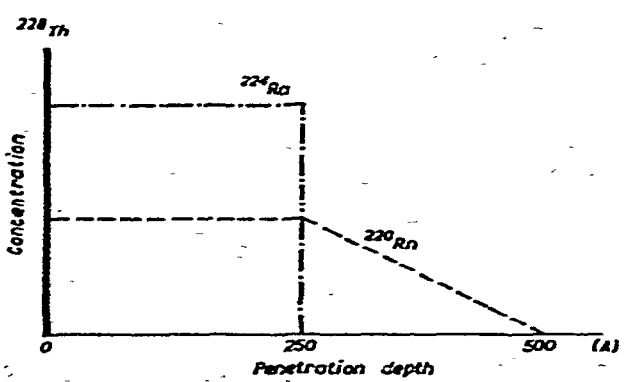

Fig. 2. Distribution of ^{228}Th, ^{224}Ra and ^{220}Rn in a grain of solid labeled by impregnation technique.

tion both of the parent nuclides and the inert gas atoms in the solid. In cases where the dimensions of grains of the solid to be labeled are of the order of hundredths of a micrometer, the uniform distribution of the inert gas can be assumed. By heating solids to their melting temperatures, the initially non-uniform distribution of the parent nuclides obtained by the impregnation technique can be changed in some cases to a uniform one.

2.2.3. Recoil technique

An interesting way to incorporate the ^{224}Ra parent nuclide was proposed by Jech[48]. This technique is based on the effect of recoil of radium (^{224}Ra) atoms at the moment of their formation by alpha decay from thorium (^{228}Th). Atoms of ^{224}Ra from the ^{228}Th recoil source possess energies between 500 and 100 keV which are sufficient for their implantation into the surface layers of solids. The concentrations of 5×10^6 to 1×10^7 ^{224}Ra atoms per cm^2 of surface were obtained which give radon concentrations of 8×10^3 to 4×10^4 of ^{220}Rn atoms per cm^2 of surface.

2.2.4. Use of inert gas radiogenic formation in minerals

It is obvious that uranium, radium and thorium isotopes present in natural minerals can be considered as the parent nuclides of inert gases. Inert gases of radiogenic origin are in some cases present in an amount sufficient to allow emanation measurements. Analogically, ^{40}Ar is formed in minerals by the decay of the natural radioactive isotope, ^{40}K. Over a long period there accumulates a measurable amount of radiogenic argon which is often used for the determination of the absolute age of minerals and rocks[49, 50].

2.2.5. Production of inert gas atoms from corresponding parent nuclides

(*a*) *Spontaneous radioactive decay.* The amount of inert gas atoms N_2 formed as a daughter product from the parent atoms in time t can be expressed by the following equation[40]

$$N_2 = [\lambda_1/(\lambda_2 - \lambda_1)]\, N_1^0\, (e^{-\lambda_1 t} - e^{-\lambda_2 t}) \qquad (1)$$

where N_1^0 denotes the amount of the parent atoms present in the sample at time $t = 0$ after labeling, λ_1 and λ_2 denote the characteristic decay constants of the parent and daughter atoms, respectively*. As the parents, ^{228}Th, ^{226}Ra and ^{227}Ac are of a longer half-life ($\lambda_1 \ll \lambda_2$ and $(t_{1/2})_1 \gg (t_{1/2})_2$), than the daughter inert gas atoms (^{220}Rn, ^{222}Rn and ^{219}Rn, respectively) and the activity does not decrease measurably during many daughter half-lives, a state called radioactive equilibrium is reached in the sample after a certain time[40] (10 daughter half-lives are usually taken). It can be readily seen from relation (1) that after this certain time, $e^{-\lambda_2 t}$ is negligible compared with $e^{-\lambda_1 t}$. Since the amount of the parent atoms present at time t equals $N_1 = N_1^0 \times$

* The half-life $t_{1/2}$ is the time interval required for N to fall from any particular value to one-half of that value, being related to the decay constant as $t_{1/2} = \ln 2/\lambda = 0.69315/\lambda$.

$e^{-\lambda_1 t}$ and $\lambda_1 \ll \lambda_2$ we can write, $N_2/N_1 = \lambda_1/\lambda_2$. This means that the amounts of parent and daughter atoms present in the labeled solid in the equilibrium state is constant. In the case of relatively long parent's half-life we can speak of the stable (continuous) inert gas source. If the parent is shorter lived than the radioactive inert gas, which is true in the case of iodine, ^{133}I ($t_{1/2}$ = 20.8 h), used as the parent nuclide of xenon, ^{133}Xe ($t_{1/2}$ = 5.6 d), after a certain time (10 parent half-lives) the first term in the equation (1) $e^{-\lambda_1 t}$ is negligible compared with $e^{-\lambda_2 t}$. This means that the parent atoms of ^{133}I after this time are practically fully decayed and the amount of the daughter inert gas, ^{133}Xe, present in the sample diminishes according to its half-life. In this case we can speak of a temporary inert gas source.

As to the amount of the radioactive parent nuclide used for the incorporation into the labeled solids, a trace amount is usually taken. For example in the case of ^{228}Th, we customarily label a solid to achieve the specific activity of 1.0 microcurie (3.7×10^4 s^{-1}) of parent isotope ^{228}Th per 1 gram of the sample. When radiochemical equilibrium between the parent and daughters nuclides is established, this corresponds to the presence of about 3×10^{12} atoms of ^{228}Th, 10^{10} atom of ^{224}Ra and 5×10^5 atoms of ^{220}Rn per gram of material of any instant[47]. This corresponds to a ^{220}Rn concentration of about 10^{-14} to 10^{-13} atom %.

Using ^{133}I as the parent nuclide for ^{133}Xe, concentrations of 5×10^{10} to 4×10^{12} atoms of ^{133}Xe per cm^3 of KI, RbI and CsI are obtained[46]. The gas concentration of 4×10^{12} Xe-atoms per cm^3 corresponds to 4×10^{-10} mole fraction in KI.

(*b*) *Neutron activated reactions.* The amount N_2 of the inert gas present in the labeled substance as formed by neutron irradiation can be expressed by the following equation[40]:

$$N_2 = \phi \sigma N_1 (1 - e^{-\lambda_2 t}) \qquad (2)$$

where N_2 denotes the amount of the inert gas, N_1 is the amount of parent (target) nuclide, λ_2 is the decay constant of the inert gas, ϕ is total flux of neutrons, σ is cross section of the target, t is time. The target used in the nuclear reaction can be considered as a temporary labeling source of inert gas, the duration of which is given by the time of neutron irradiation.

Figure 3 shows the nuclides of the periodic system which can be utilized for the inert gas formation by neutron irradiation.

The (n, p) and (n, α) reactions listed in Table 4 were advantageously used for inert gas formation by Kalbitzer[51] and others[52–54], Schmeling[55] and Felix and co-workers[14, 15, 56].

Different combinations of gas producing reactions activated by neutrons are possible and offer an opportunity to label a solid with two various gases: *e.g.*, by neutron irradiation of KI and RbI, the gas mixture of Ar/Xe and Kr/Xe can be produced. U-doped alkaline earth fluorides take sufficient U^{4+} into the lattice so that Kr and Xe can be introduced besides the gases produced by the (n, α) reaction[56]. Table 6 summarizes inert gas concentrations produced by reactor irradiation in RbI

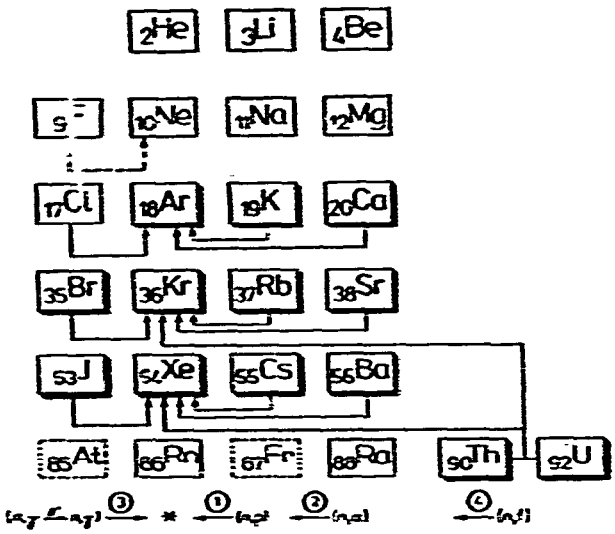

Fig. 3. Nuclides and neutron nuclear reactions utilizable for production of radioactive inert gases with half-life greater than 1 hour.

TABLE 6

INERT GAS CONCENTRATIONS IN SOLIDS PRODUCED BY NEUTRON IRRADIATION

System sample/gas	*Producing reaction*	*Gas concentration (atoms cm^{-3})*	*Dose neutrons per cm^2*	*Ref.*
RbI/Kr	^{85}Rb (n, p) ^{85}Kr	1×10^{11} to 1×10^{15}	10^{14} to 6×10^{14}	56
		3×10^{17}	1×10^{19}	51
RbI/Xe	^{127}I (n, p)$^{127}I \rightarrow {}^{128}Xe$	3×10^{14}	4×10^{15}	56
CaF_2/Ar	^{44}Ca (n, α) ^{41}Ar	10^{12} (10^{7})	10^{15}	52
	CaF_2 dopped	5×10^{14}	3×10^{12} fission	
CaF_2/Xe	with 0.055 mol % U		fragment/cm^2	62
	^{235}U (n, f) ^{133}Xe ...			
	^{135}Xe			
	^{88}Kr			

and CaF_2 pure and doped with U. The distribution of inert gas produced by nuclear reactions depends on the distribution of the target element in the solid. If it is uniform, the gas distribution can also be assumed to be uniform.

2.3. Techniques for introducing the inert gas without parent

After experimental investigations, it seems that under ordinary conditions the inert gas atoms do not dissolve in metals and ionic crystals and do not permeate through them. The conditions of high energy gas ions, high temperature and high gas pressure are required for impelling the inert gas into the solid. There exists a number of techniques which can be used for direct incorporation of inert gas atoms

into solids. All of them are, in general, characterized by a definite quantity of the introduced gas which decreases at the time of storage or during the measurement. The most common techniques are based on:

(i) the recoil effect of nuclear reactions;
(ii) ion bombardment;
(iii) diffusion technique;
(iv) direct gas introduction during sample preparation or phase transitions.

2.3.1. Techniques utilizing the recoil energy of nuclear reactions

These techniques need intimate contact of the labeled solid with the external inert gas source. This contact is achieved by the adsorption of alpha-decaying parent nuclide on the surface, by irradiation of specimen wrapped in uranium foil, or surrounded by an atmosphere of the inert gas. Recoil energies of alpha-decay and neutron-activated reactions have been utilized for the inert gas introduction.

2.3.1.1. Alpha-decay. For introducing radon into a solid, it is possible to use the recoil energy (85 keV per atom) of its atoms freshly formed by the decay of radium. Lindner and Matzke[57] have used this technique for labeling a large number of ionic compounds in a powder state. ^{222}Rn ions are adsorbed from a solution on the surface of the labeled sample. After a certain time (optimally 5 weeks, i.e., 10 half-lives of ^{222}Rn, when the equilibrium concentration of the radon formed is achieved) about 50 per cent of the radon formed penetrates into the sample surface. The radium is then washed from the surface of the powder. The labeling performed is superficial with nearly linear distribution of the inert gas. With a sufficiently fine powder (particle size 0.1 μm) a uniform distribution of the inert gas can be obtained.

2.3.1.2. Neutron-activated reactions. Using parent nuclides as external labeling sources of inert gases, recoil energy of following neutron-activated reactions can be used for the inert gas incorporation (see Table 7).

The use of fission reaction for introduction of inert gases into non-fissionable solids was chosen as an example. By fission reaction (n, f) several Kr and Xe isotopes (^{88}Kr, ^{133}Xe, ^{135}Xe) are formed amongst a large variety of other nuclides. However, after a decay period of about five days after the neutron irradiation, no fissionable material contains any radioactive gas but ^{133}Xe ($t_{1/2}$ = 5.6 d).

TABLE 7

NEUTRON ACTIVATED REACTIONS PRODUCING INERT GASES

Target atoms	*Reaction type*	*Activating particle*
Alcalic metal	n, p	fast neutrons
Earth alcaline	n, α	fast neutrons
Halogen	n, γ	thermal neutrons
Uranium	n, f	thermal neutrons
Thorium	n, f	fast neutrons

The labeling of non-fissionable solids can be done by irradiating the sample to be labeled in contact with a fissionable solid. The labeled solid was mixed with fine uranium oxide powder. With the weight ratio of UO_2 to the labeled substance of 30 : 1, about 90 per cent of the gaseous fission products are found in the solid[58]. This technique was applied by Yajima et al.[58] for labeling oxides, by Kawasaki[59], by Koss[60] for labeling various metal wires and foils, by Morrison et al.[61] for labeling single crystals alpha-Al_2O_3, BeO, MgO, and ZrO_2. In the last group of cases, the exposure level was such that the normal fission product content was 10^{13} fission atoms per cm^2 at the surface of the samples. Following the irradiation, the UO_2 was separated from the specimen and the samples were cleaned with distilled water in an ultrasonic bath. Similarly, Elleman and co-workers[62] used the recoil energy of the fission reaction to prepare CsI labeled by ^{133}Xe. The crystals were surrounded with enriched ^{235}U uranium foil and irradiated with thermal neutrons. This technique has the advantage of being applicable to any non-fissionable solid. The fission recoil labeling was carried out at 3×10^{12} fission fragments/cm^2, i.e. 5×10^{14} Xe-atoms/cm^3 yielding a 5×10^{-3} mole fraction in KI[62]. As to the distribution of the inert gases, it should be born in mind that the fission recoil ranges are low in most solids (about 10 μm) so that this technique is suitable for the labeling of the surface layers.

Another example of inert gas incorporation into a solid based on the recoil effect is the (n, γ) reaction in the atmosphere of an inert gas. This technique was used by Kelly[63] for the labeling of aluminum, TiO_2 and numerous other powders with argon, krypton and xenon. The sample is placed in an atmosphere of an inert gas in a sealed ampoule and irradiated with a flux of fast neutrons. The neutron bombardment results in a (n, γ) reaction and gives rise to radioactive inert gas atoms which are implanted into the surface of the solid. About 10–20 per cent of radioactive xenon-isotopes formed by nuclear reaction are fixed as a result of the 100 eV-recoil energy in the surface layers of the solid.

2.3.2. Ion bombardment

The great possibility of the ion bombardment technique for implanting inert gas atoms into solids has been described in numerous papers published since 1950 and in two monographs by Carter and Colligon[64] and by Dearnaley and co-workers[65]. There exists a great methodical variability of the ion bombardment technique which, obviously, can be applied to any solid material.

2.3.2.1. Apparatus. At present there exists a whole range of techniques for ion bombardment. In one technique, ionized atoms are accelerated with a high voltage[66–68] and in others, ionization and accelerations of gas atoms occur in a discharge[69, 70, 26] or a microwave plasma[71]. The process of introducing gases into solids used in these pumps has been studied[72]. Ion-bombardment equipment most frequently used for the implantation of inert gases into solids can be characterized by the following principles:

(a) In a vacuum discharge tube, atoms of the inert gas are ionized by electrons emitted from the cathode or a high-frequency discharge. The ions formed are

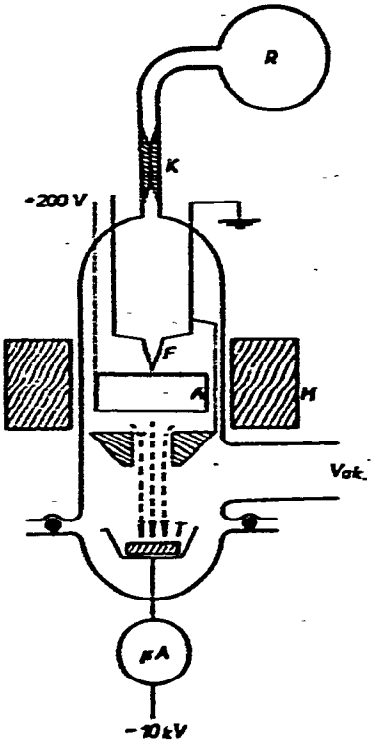

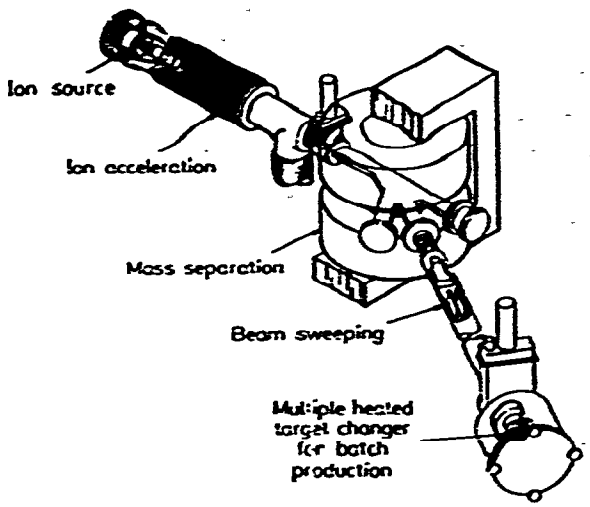

Fig. 4. Diagram of apparatus for ion bombardment by ion source with a c.c. voltage. R = reservoir of the radioactive inert gas; K = capillary valve; F = filament; A = ion accelerator; M = permanent magnet; T = target (sample to be labeled); Vak = vacuum pump; and μA = a microamperometer.

Fig. 5. Schematic drawing of an electromagnetic separator.

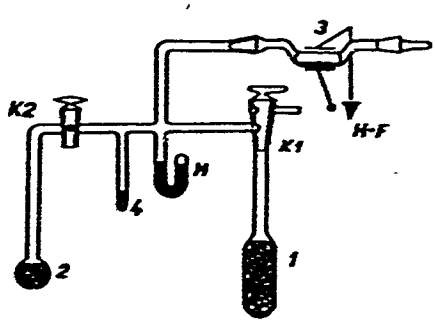

Fig. 6. Diagram of apparatus for introducing a gas by ion bombardment in a high-frequency discharge. 1 = adsorption pump; 2 = inert radioactive gas reservoir; 3 = sample cell; 4 = metallic calcium for inert gas purification; H-F = high-frequency field generator; M = vacuometer; K_1, K_2 = valves in glass apparatus.

accelerated by the potential drop and strike the target connected to a cathode with an energy which depends on the voltage. Some of the impinging ions are trapped in the material of the target. A diagram of this kind of apparatus is shown in Fig. 4. The ion source by Carter[73] operates in a rather high vacuum (10^{-4}–10^{-3} Pa). Equipment of this type makes it possible to produce a highly concentrated beam of highly energetic ions (up to 100 keV) and is best suited for labeling metal targets or bulk material.

(b) Some authors, such as Almen and Bruce[74] and Davies and co-workers[75, 76],

have used ion sources with an electromagnetic isotope separator and obtained very well-defined beams of ions with definite energy, mass, charge and entrance angles. The schematic drawing of an electromagnetic separator is shown in Fig. 5. It consists of an ion source, mass separator and a target chamber. The gas atoms to be implanted are ionized to obtain the required type of ions. These ions are extracted from the source and accelerated in a strong electric field. The beam is then deflected by a magnet and slit configuration, so that the desired ions can be separated from the unwanted ones having different masses. A second acceleration step which is not shown in Fig. 5 is often applied after the mass separation before the ions impinge on the target. The beam is scanned across the target to obtain homogeneous labeling.

(c) An apparatus for introducing gas traces into solids in a high-frequency discharge was proposed by Jech[25]. The schematic drawing of the apparatus as described in ref. 77 is shown in Fig. 6. The sample to be labeled is placed in a small thick-walled glass cell connected to a vacuum apparatus. After a vacuum of about 1.3 Pa has been produced in the cell, a small amount of the radioactive gas is introduced, so that the final pressure does not normally exceed 7–70 Pa. Ions of the inert gas are formed and accelerated with a pulsed high-frequency field with a maximum voltage of 15 kV, produced with a Tesla transformer. The accelerated ions penetrate the surface layers of the solid to a depth of 1 to 10 nm. The apparatus of this type is capable of operating with a higher pressure of the inert gas than the above described apparatus using the beam technique.

It should be noted that under conditions of 1.3 Pa pressure in the latter type of apparatus, it is difficult to determine the exact parameters of the bombardment process. Doubly and triply charged ions of the gas are produced in the discharge in addition to singly charged ions of the gas and bombard the surface with energies that are two or three times as high as those of singly charged ions. It is impossible to focus the beam ions, the ions obtained are not mono-energetic and finally, ions of residual gases of the working space also participate in bombardment at low vacuum. However, apparatus in which the acceleration of ions is based on the discharge, are more simple and the labeling of samples can be carried out more rapidly since it does not require prolonged pumping of the apparatus. This method of introducing the inert gas is convenient for the use of labeling surface layers of solids causing low radiation damage. It is also more suitable for powders since the unconcentrated beam of ions labels the whole surface of the powder. With the ion bombardment, samples can usually be labeled using doses of the order from 10^{10} ions cm^{-2} (corresponding to gas concentration of about 10^{-5} at %) to 10^{16} ions cm^{-2} (3 at. %).

In general, the ion bombardment technique has a number of advantages. The specimen can easily be handled and used immediately after labeling. In the case of reactor irradiated samples, which are frequently highly radioactive, long waiting times are necessary. On the other hand, some difficulties are connected with the application of the ion bombardment technique, such as damage in the surface layers of the crystal lattice.

2.3.2.2. Trapping efficiency. In using the method of ion bombardment for

introducing inert gases into a solid we must remember that not all ions reaching the surface are introduced into the substance. The degree of introduction is characterized by the efficiency of trapping η, sometimes called the trapping probability which is defined as the ratio of the number of atoms which remain trapped in the solid to the total flux of ions reaching the sample surface during the bombardment[64]. We can assume that entrapment of inert gas atoms by a solid consists of the following processes:

(a) Penetration of the incident ion through the surface layer of atoms.

(b) Migration within the lattice where a certain possibility exists that the inert gas atom escapes through the surface.

(c) Eventual trapping within the lattice, in interstitial or in regular sites or in other lattice defects produced by radiation.

Considering the first requirement for trapping, penetration through the surface layer necessitates the bombardment ion passing within a distance of 0.5 lattice spacings from a surface atom at the most.

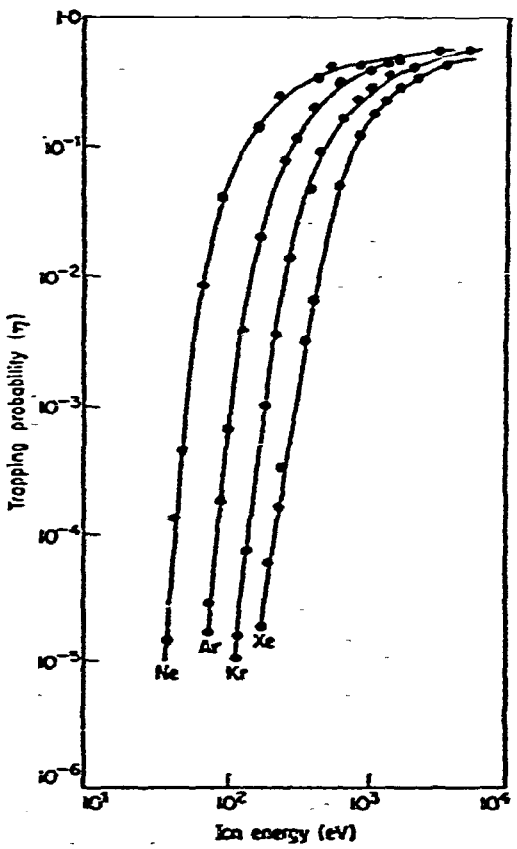

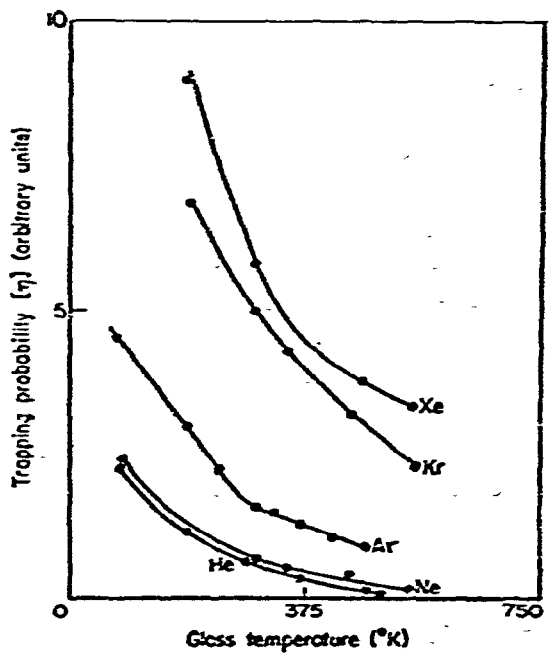

Fig. 7. The trapping probability η as a function of ion energy for Ne^+, Ar^+, Kr^+, Xe^+ ions incident on W.

Fig. 8. The form of the variation of the ion trapping probabilities for 250 eV inert gas ions on a Pyrex glass surface as a function of the temperature of the glass.

The trapping efficiency η of ions in a substance, at constant temperature, depends on the character of ion, its energy and the material of the target. The trapping efficiency, η, in tungsten for various inert gases in relation to the energy of ions, obtained by Kornelsen[67] is given in Fig. 7. This diagram reveals that at ion energies $\leq$ 100 eV the trapping efficiency is very low, $< 10^{-1}$ for all ions but rapidly increases at 3 keV to about 0.6. The effect of the mass of the ions appears only at energies lower than 1 keV. The trapping efficiency normally increases with a decreasing mass of the bombarding ion. Other works at higher energies conducted by Brown and Davies[78] and Almen and Bruce[74] indicate that, at energies below 5 keV, η is always lower than 1 for many metals but tends rapidly to unity above this value of energy. The decrease of the trapping efficiency with increasing target temperature for glass[79] is shown in Fig. 8. The release of trapped atoms occurs at the target temperature and can be expected to increase as the temperature is increased, resulting in a reduction in the effective value of the trapping efficiency. On the other hand, the increase of η was observed as the target was cooled below room temperature.

The material of the target also affects the efficiency of trapping. A gas enters metal targets at ion energies of about 100 eV with a trapping efficiency in the order of 10^{-6} to 10^{-2}. The trapping efficiency of inert gas ions in aluminum is higher than in tungsten. Considerably higher values of trapping efficiency were found for glass ($\eta = 0.6$) with the same energy of bombarding ions[80]. The larger value of η for glass can be explained on the basis of larger average interatomic spacing and weaker interatomic potentials resulting in easier penetration of the impinging ion. Almen and Bruce[74] have measured η for inert gas atoms incident upon a number of materials. The η values for Kr-ions of 45 keV energy were always close to unity for target atom masses < 25. The trapping efficiency of inert gas ions in a substance is also affected by the physical state of the material. The nature of the sites occupied by the gas atom introduced into the lattice depends on the structure and the state of the crystal lattice.

2.3.2.3. Penetration of inert gas ions. The energetic ions which have passed a solid surface are slowed down by elastic collisions with electrons and target atoms and by displacement cascades around the path of the ions penetrating the solid. The slowing down of energetic heavy ions, such as the inert gas ions, is strongly dependent on the energy, mass and charge of ions, on the mass of the target atoms and on temperature. For single crystal targets it depends, moreover, on the crystallographic orientation of the lattice with respect to the direction of incident ion beam. All of these factors affect the resulting distribution of the inert gas atoms within the solid.

As the penetration of energetic inert gas ions is of general importance with the labeling of solids, basic theoretical relations and experimental techniques concerning the problem are summarized here. The stopping power or the specific energy loss dE/dx is taken to be due to both electronic and nuclear stopping. At lowest ion energies nuclear stopping dominates, at higher ion energies electronic collisions are more important. The following expression for electronic stopping power can be given[81]

$$-dE/dx = 4\pi Z_1^2 e^4 N B/mv^2 \qquad (3)$$

where Z_1 is the atomic number of the ion, e is the change on the electron, N is the number of target atoms per unit volume, m and v are the electronic mass and velocity, respectively, and B is a dimensionless "stopping number". Bethe[82] gave a quantum mechanical derivation of $B = Z_2 \ln (2mv^2/I)$, where Z_2 is the atomic number of the target atom, I is the average excitation energy of the electron in the target, which is after Bloch[83] proportional to Z_2.

The nuclear stopping power has been evaluated in theoretical works by Bohr[84], Nielsen[85], Lindhard et al.[86, 87], and Holmes and Leibfried[88]. Bohr[84] originally proposed that the elastic nuclear collision process responsible for the slowing down of heavy ions of low velocity occurs in an exponentially screened Coulomb field. Recently, Lindhard et al.[87], by substituting a Thomas-Fermi potential in place of the exponentially screened potential, obtained a range-energy expression that is reasonable with experiments[89]. They suggested a universal range–energy curve in terms of suitable dimensionless range and energy parameters ρ and ε, respectively, given by

$$\rho = R N M_2 4\pi a^2 M_1/(M_1 + M_2)^2 \tag{5}$$

$$\varepsilon = E a M_2/Z_1 Z_2 e^2 (M_1 + M_2) \tag{6}$$

where R is the range, E is the energy, N is the number of target atoms per unit volume, Z_1 and Z_2 are the nuclear charges of the incoming particle and the target atom, respectively, M_1 and M_2 are the corresponding masses, e is the electronic charge and a is the screening radius used by Lindhard et al.[87] which equals $a = a_B \times 0.8853$, where a_B is the Bohr screening radius[84]. The calculations result in a set of curves of ρ versus ε. The LSS theory has been found to predict satisfactoriiy the penetration ranges of heavy ions in amorphous and polycrystalline solids.

The increased penetration occurring along the more open directions between the closed packed rows of atoms due to a channeling in single crystals has been identified on the basis of computer calculations by Robinson and Oen[90]. The experimental techniques for determining the penetration ranges of ions can be summarized into three groups:

(i) "Stripping" techniques based on the stripping away of a given thickness of material from bombarded specimen and on the subsequent measuring of the amount of the remaining inert gas or the amount of the inert gas removed. Anodic stripping was developed by Davies et al.[91, 92]; chemical and electrochemical stripping techniques by Bredov and Okuneva[93]; and mechanical vibratory polishing owes its development to Whitton[94]. Lutz and Sizmann[95] also employed sputtering to remove known thickness layers from metals.

(ii) Techniques based on the determination of the changes in the properties of the specimens caused by labeling bombardment, such as refractive index in transparent materials[96], and electrical resistivity of semiconductors[97], etc.

(iii) Techniques making use of α or β radioactivity of labeling atoms. These techniques are based on the fact that the energy spectra of α-particles and low energy β particles are degraded according to the depth of the radioactive atoms below the surface. Domelij et al.[98] established the penetration ranges of ^{222}Rn-ions of energies

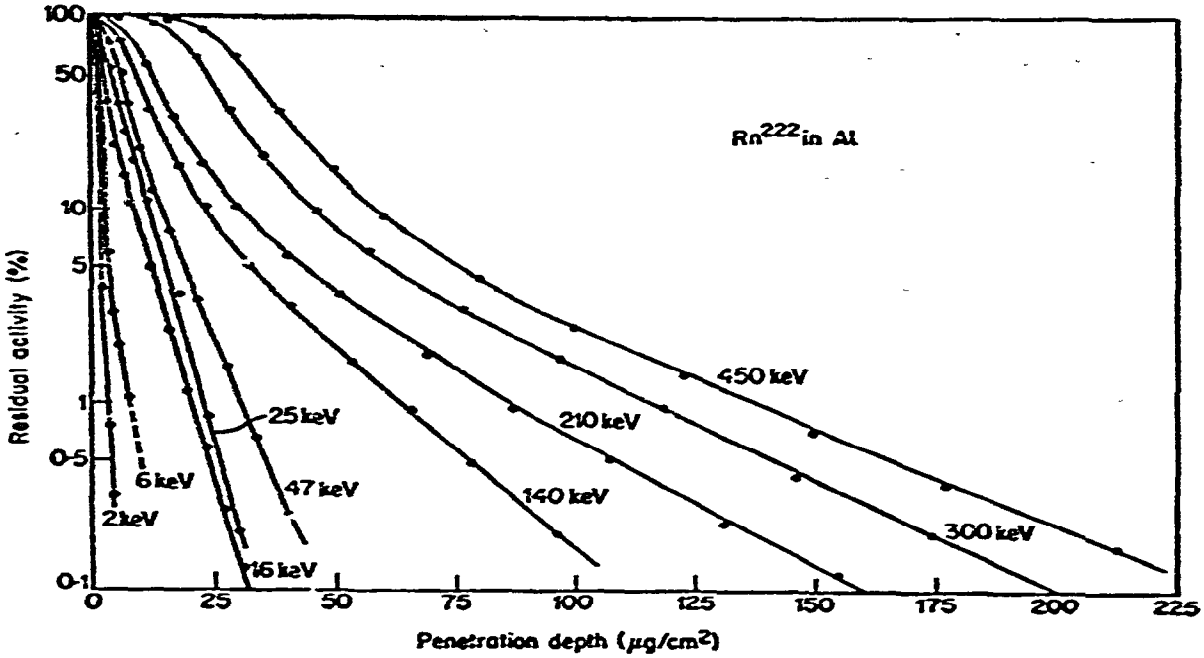

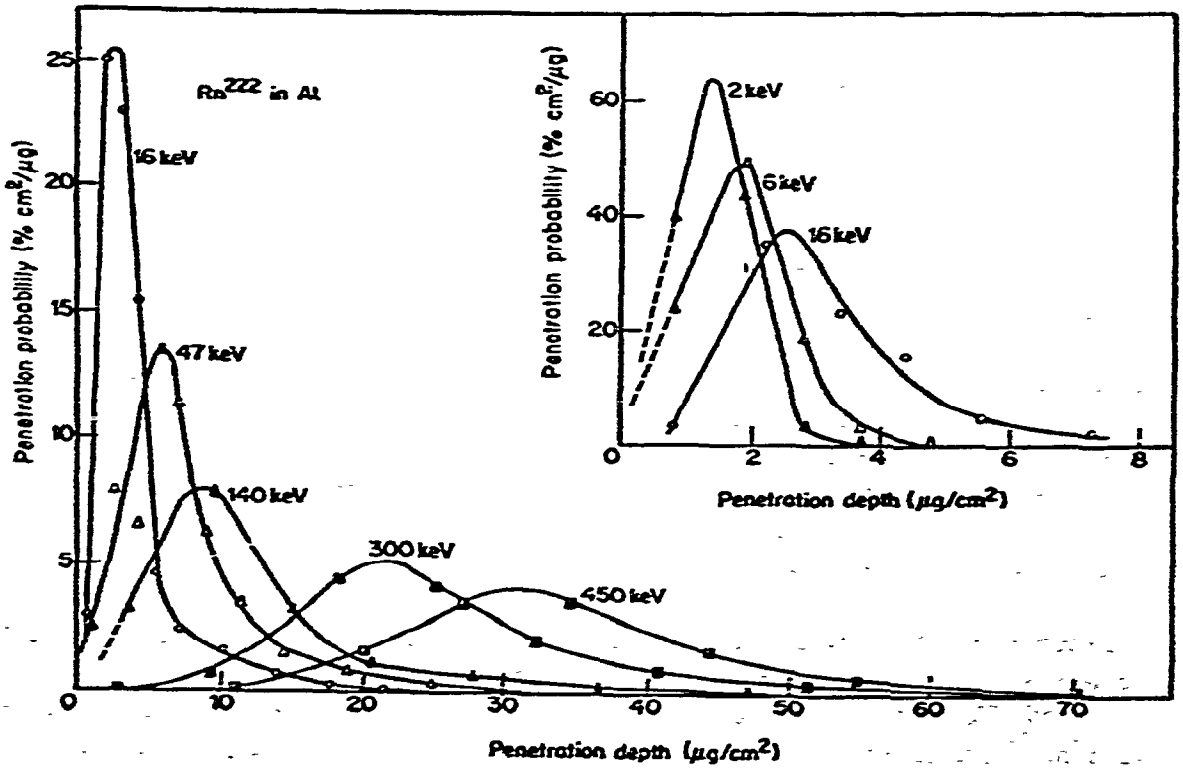

Fig. 9. (a) Integral range distributions for ^{222}Rn in Al. (b) Differential range distributions for ^{222}Rn in Al (cf. ref. 102).

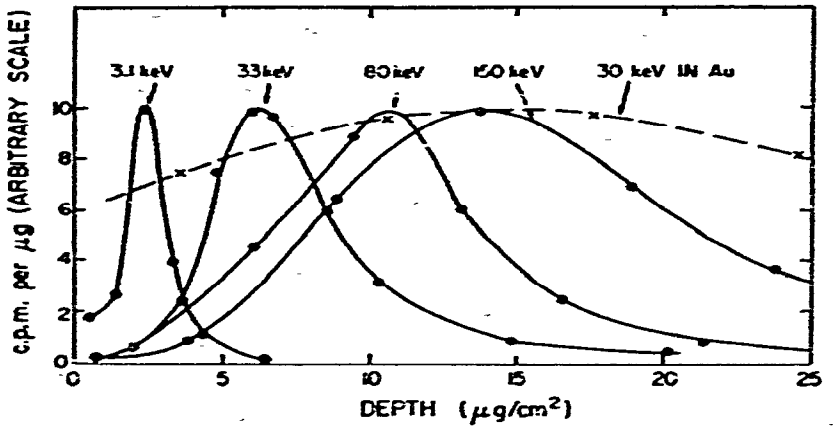

Fig. 10. Differential range distribution curves normalized to same peak height for ^{133}Xe in Al and Au targets. The bombarded energy is indicated beside each curve (● Al; × Au) (cf., ref. 76).

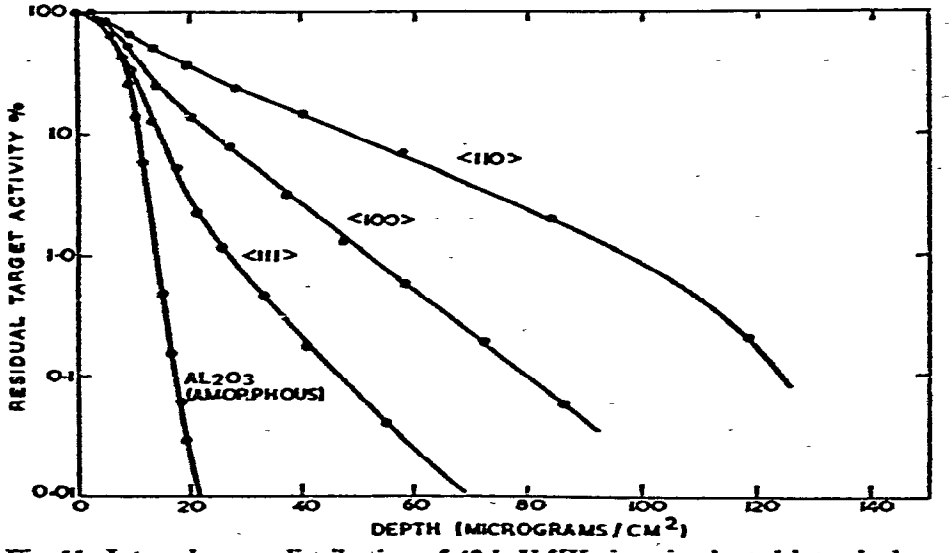

Fig. 11. Integral range distribution of 40 keV ^{85}Kr ions implanted into single crystal of aluminum along different crystal directions (cf. ref. 105).

70–210 keV in aluminum, silver, gold and tungsten. Ranges of ^{125}Xe-ions in Al, Be, Ni, Zr, Ta and Au were successfully determined by Bergstrom[99] and Graham[100, 101]. Some examples of ion ranges in amorphous and crystalline materials are given below.

The differential and integral range curves for ^{222}Rn in aluminum obtained by Davies et al.[98, 102] are shown in Fig. 9a, b. Energies from 2 to 450 keV and total fluxes 10^{20} atoms cm^{-2} were used.

The penetration depth is usually expressed as the total weight of target per unit area (in $\mu g\ cm^{-2}$) as the number of atom layers or as distance from the surface (in nanometers). The depth of 1 $\mu m\ cm^{-2}$ corresponds approximately to 16 atom layers of aluminum, i.e., 4 nm.

Figure 10 gives curves of the differential distribution of xenon atoms in alumi-

nium and gold. Energies from 3.1 to 150 keV were employed. These are indicated beside each curve[76].

The results of Figs. 9 and 10 illustrated well the general behavior of range distribution in relation to the ion energy for unsaturated targets. The distribution profiles distinctly indicate non-uniform distributions. The distribution of the embedded atoms is seen to consist of an asymmetric peak with an exponential tail. With an increase in the energy of the ions the maximum is shifted towards greater distances from the surface. In addition, the range distribution curves are much narrower for materials consisting of the light elements (with lower Z) such as aluminum than for heavier elements, such as gold (see Fig. 10). The distribution curves are considerably broadened using large integral flux ($> 10^{10}$ ions cm^{-2}) during a long bombardment, peaking at lower penetration depth. The peak occurs at only half the depth observed in the trace bombardment. Similar results were obtained by Davies and co-workers[102–105] for the distribution of various inert gases in a series of metals and oxides (Al, W, Ag, Si, Ge, Al_2O_3, WO_3 etc.). Figure 11 shows a comparison of the range distribution of 40 keV ^{85}Kr in specific directions of aluminum single crystal and in amorphous aluminum oxide measured by Piercy et al.[105]. The deep penetrations are typical channeling events and are markedly different from the results of the isotropic (amorphous) solid. Direction ⟨110⟩ exhibits the deepest penetration. It is to be noted that by heating the crystal to 1200 K during bombardment, the channeled ion ranges were considerably reduced below the values obtained at room temperature. This indicates an increased stopping due to thermal vibrations of the lattice atoms.

It can be concluded that the exact estimation of the penetration depth and the distribution profile of inert gas atoms introduced into the solids by ion bombardment is rather complex.

2.3.2.4. Saturation value. Experiments have shown that the curves of the dependence of the inert gas concentration trapped within the solid on the flux of bombarding particles reaches a saturation value. The saturation value q for a given inert gas and a given target material is usually expressed as the total weight of the sample per unit area in $\mu g\ cm^{-2}$ or in the number of atom layers. Target saturation occurs when the integrated flux of incident particles is sufficient to damage and to sputter away a significant amount of the target material and some of the collected gas atoms escape as well. The variation of q with ion energy has been measured by Colligon and Leck[106] and Kornelsen[107] using ion beam apparaturses. The former found that the saturation value q increased almost linearly with ion energy from 0.7 keV to 3.75 keV for inert gases in Ni, Mo and Pt. At the highest energies, the saturation levels were in the order of three to thirty atomic distances. The saturation value q for inert gas atoms differs for various materials. The q values for krypton ions measured by Almen and Bruce[74] are collected in Fig. 12. All of these values were obtained at the same energy and current density of krypton bombardment (45 keV and 10 $\mu A\ cm^{-2}$). The variation of q with target atom mass is periodic showing maxima and minima. The minima correspond to the minima of trapping efficiency η and to maxima in the sputtering.

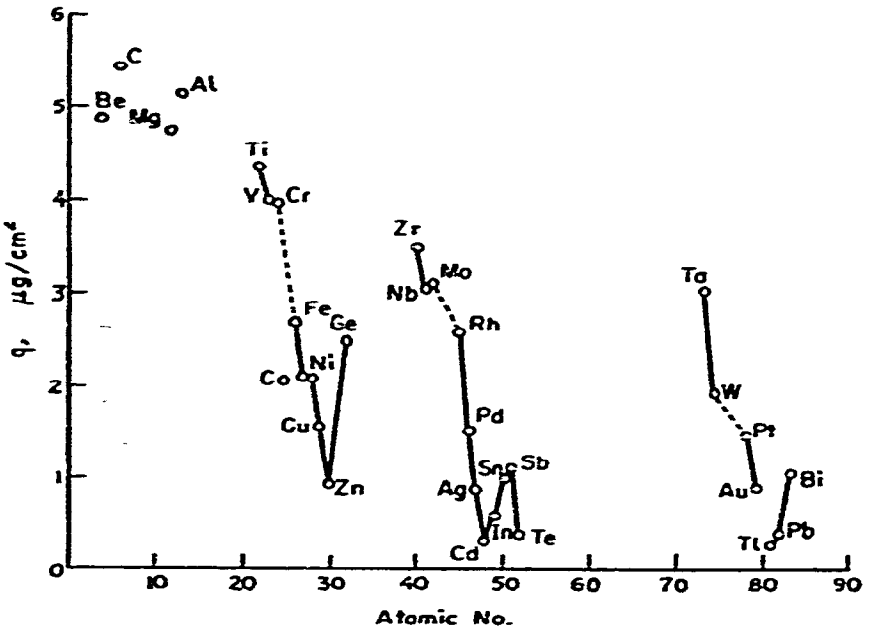

Fig. 12. Saturation values (q) of Kr in different targets. Ion current density = 0.1 μA · mm^{-2}; ion energy = 45 keV. (cf. ref. 74).

It is interesting to state that the saturation value q reaches a maximum for elements belonging to the same group of the periodic table, i.e., for Group IVa (Ti, Zr, Hf). A minimum in the saturation value q is found for elements Zn and Cd (Group 2b). An approximate relationship between binding energies of the elements and the trapping efficiency can be noted. A study of sputtering carried out by the same authors[74] explained this correlation. The sputtering ratio was found to be inversely related to the binding energy. As it might be expected, the less strongly held atoms were more easily sputtered off.

Some interesting conclusions on the dependence of saturation value q upon the surface orientation of single crystal targets were made by Almen and Bruce[74]. Their observation can be explained by ion channeling along preferred open crystal directions. In single crystal targets, as observed experimentally[65], an appreciable fraction of incident atoms can travel very large distances into the target. It has been established that this is a result of ion penetration along axes denoted as channels in the crystal where the energy loss of penetrating atoms to target atoms is small because of crystal symmetry.

2.3.3. Diffusion technique

The original method was used for the preparation of ^{85}Kr labeled solids by Chleck et al.[3]. They introduced krypton into various substances at an elevated temperature and gas pressure. The essential element of the labeling apparatus by this technique is a pressure vessel in which the material to be labeled is placed[3]. Detailed views of the pressure vessel modified by Tölgyessy[108] are shown in Fig. 13a, b. The

Fig. 13. (a) Steel vessel for kryptonation at high temperature and increased pressure (cf. ref. 108). 1 = Steel vessel body; 2 = sample to be labeled; 3 = metal (Pt) springs; 4 = perforated steel plate; 5 = ampoule containing ^{85}Kr; 6 = rubber sealing; 7 = plug screw. (b) Pressure vessel for diffusion kryptonation of melts (cf. ref. 108). 1 = steel jacket; 2 = metal plug; 3 = needle valve.

inert gas (krypton) is introduced at normal temperature and pressure, the vessel is closed off from the remainder of the system and the temperature is raised by oil bath, heating tape or furnace to 300°C. The pressure was controlled and reached 7.100 kp cm^{-2} and kept under these conditions for several hours. At the completion of a run the material is quenched by immersing the pressure vessel in liquid nitrogen. The relation of the amount of gas collected in a solid to the time under given temperature and pressure is expressed by the following equation[3]

$$M \propto p\,(D_0 t)^{1/2} \exp(-\Delta H/2RT) \qquad (7)$$

This means that the amount M of the inert gas collected per square centimeter is directly proportional to the pressure p, proportional to the square root of the time t and exponentially proportional to the temperature T; ΔH signifies the activation enthalpy of inert gas diffusion and R is the molar gas constant. The experimentally found penetration depth was in the order of magnitude 10 to 1000 $\mu g\ cm^{-2}$, i.e., 10^2 to 10^4 nm. It depended exponentially on the temperature and is a function of the square root of the time.

The radioactive nuclide, ^{85}Kr, is mostly used for the diffusion labeling technique. The nuclear characteristics—half-life 10.25 years, 0.672 MeV-β emission (see Table 1)—are very suitable for the labeling of solids. The diffusion technique was used to introduce ^{85}Kr into more than 250 different solids including metals, inorganic, and organic compounds, in the form of foils, powders and single crystals. The krypton atoms diffuse into the solids and remain in general on substitutional positions in the metal lattice (the diameter of Kr-atom is too large for ordinary interstitial position). In some solids, such as those with a graphite structure, there are regular interstitial

voids of sufficient dimensions to accumulate inert gas atoms. Materials of this type (boron nitride and molecular sieves) give the highest specific activities (6×10^5 and 7×10^6 s^{-1} mg^{-1}, i.e., 16 and 200 μCi mg^{-1}, respectively) of all materials prepared by Chleck[3]. The inert gas atoms can be fixed on various lattice imperfections including the grain boundaries.

The diffusion technique is especially suitable for the labeling of organic compounds. It has been pointed out in the literature that the presence of hydroxyl groups, which are able to be mutually bounded by a hydrogen bound, is necessary for the formation of the crystal lattice permitting incorporation of the gas molecule. Krypton was found bonded considerably weaker in organic compounds than with metals labeled by diffusion technique[109]. It was shown that the presence of inert gas atoms in the crystal lattice has little or no effect on the chemical properties of the host solid[3].

Additional experimental arrangements for the diffusion technique were proposed. Trofimov[109] prepared xenon labeled *p*-cresole in a thick-wall glass vessel, containing the sample in the xenon atmosphere, by cooling it to the temperature of liquid nitrogen and by subsequently keeping at room temperature for a week. By heating to room temperature the gas pressure in the vessel increased to about 3×10^6 Pa (~ 30 atm.) The clathrate compound of composition $[Xe][C_7H_8O]_6$ was reported[109] to be prepared.

Tölgyessy et al.[110] proposed a microdiffusion technique for labeling powders which reduced the losses of residual inert gas after labeling. The labeling was provided in a thick-walled capillary which is schematically shown in Fig. 14a. After injecting krypton in the capillary containing the sample the capillary was attached by a holder (see Fig. 14b) to a nitrogen bomb, the pressure of 3×10^6–10^7 Pa (i.e. 30–100 atm.) being subsequently set for the necessary time. Should a higher quantity of the inert

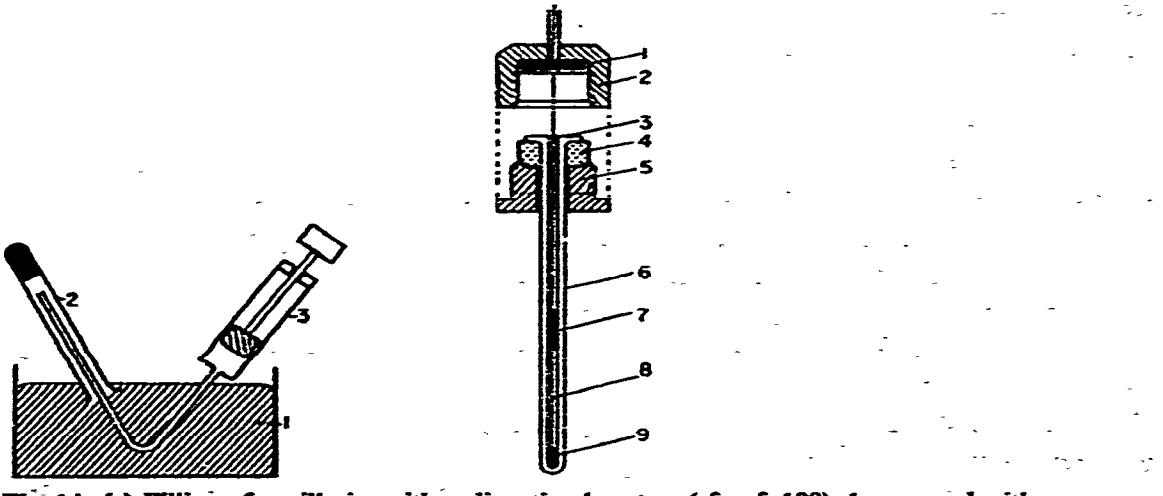

Fig. 14. (a) Filling of capillaries with radioactive krypton (cf. ref. 108). 1 = vessel with mercury; 2 = sample to be labeled in a glass capillary; 3 = syringe. (b) Diffusion kryptonation (cf. ref. 110). 1 = matrix sealing; 2 = matrix; 3 = ground part of capillary; 4 = rubber sealing; 5 = screw with an opening; 6 = glass capillary; 7 = movable mercury plug; 8 = gaseous ^{85}Kr; 9 = sample to be labeled.

TABLE 8

KRYPTONATION OF POWDERS

Substance	*Krypton pressure Pa*	*Temperature (°C)*	*Time of diffusion (h)*	*Specific activity ($s^{-1}g^{-1}$)*
$AgIO_3$	6.7×10^6	25	50	28 170
KCl	7.9×10^5	200	10	1.080
NH_4NO_3	8.8×10^5	20	5	1·630

TABLE 9

ACTIVITY OF KRYPTONATED PELLETS

Substance	*Pellets pressing (Mp cm^{-2})*	*Surface specific activity ($s^{-1}cm^{-2}$)*
$AgIO_3$	0.9	39 170
KCl	3.0	690
NH_4NO_3	2.0	350

gas be incorporated into a solid, a technique proposed by Jesenák et al.[111] can be used. This technique is based on labeling of powdered material by diffusion or ion bombardment followed by pressing the labeled powder into a solid of desired size and shape. The solid will be locally inhomogeneous. This technique was advantageously used for preparation of labeled solids, as $AgIO_3$, KCl, $AgNO_3$ used for analytical purposes. The specific activities of $AgIO_3$, KCl, NH_4NO_3 (grain size 0.1 mm) achieved by diffusion technique at elevated temperature and Kr-pressure, as well as of pellets (diameter 10 mm and 1 mm thick) obtained by pressing the labeled samples are given in Tables 8 and 9.

2.3.4. Direct gas introduction during sample preparation or phase transition

In some types of solids the inert gas can be advantageously incorporated during the formation of the solid. In the following, examples of processes are given which can be used for the direct sample labeling if they are carried out in atmosphere of inert gas:

(a) crystallization from a melt or solution;

(b) sublimation of the solid;

(c) evaporation and condensation of a thin film of metals onto a cold surface;

(d) polymerization of monomers;

(e) tempering of solid in the temperature range where phase transition or another process takes place.

The choice of the technique for inert gas introduction depends mainly upon the character of the solid to be labeled and the aim for which the labeled solid should be prepared. Incorporation of inert gas atoms during the formation of the solid phase was first used for the preparation of the so-called radioactive kryptonates of clathrate

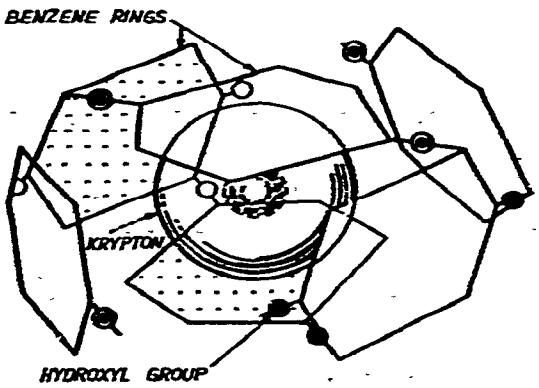

Fig. 15. Diagram of hydroxyquinoline clathrate.

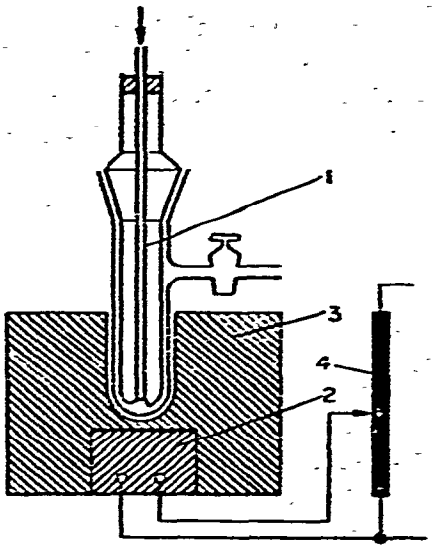

Fig. 16. Diagram of apparatus for sublimation kryptonation (cf. ref. 7). 1 = Glass apparatus; 2 = electrical heating; 3 = aluminium block; 4 = transformer.

type. Chleck et al.[112] prepared ^{85}Kr-labeled hydroxyquinoline by slow crystallization of hydroxyquinoline from a melt under a positive pressure of krypton gas containing ^{85}Kr. A scheme for the hydroxyquinoline molecule labeled with krypton is demonstrated in Fig. 15. It is a typical clathrate compound. The atom of ^{85}Kr is trapped in a trimer of β-hydroxyquinoline $[C_6H_4(OH)_2]_3$ [^{85}Kr].

By crystallization from both a melt and a solution the homogeneous labeling of samples can be accomplished. The condensation of the solid during sublimation offers very favorable conditions for incorporation of inert gases (mainly used for ^{85}Kr) into the crystalline lattice of the solid when it forms a clathrate type lattice. The simple apparatus used for this labeling is schematically shown in Fig. 16.

Tölgyessy and co-workers[113] showed the possibility of preparing krypton labeled polymers by arranging polymerization in an atmosphere of the noble gas. Monomers such as methylmethacrylate, vinylbenzene, styrene and acrylonitril were polymerized in this way. During polymerization under static or dynamic conditions ^{85}Kr was captured by the polymer and was found to be uniformly distributed in the resulting plastic.

Sizmann and Rup[114] succeeded in incorporating ^{85}Kr into quartz during the polymorphic transformation. If quartz is heated in an atmosphere of krypton, during the phase conversion of β quartz into β cristoballite noble gas atoms enter the crystal lattice. It is interesting that there is no capture of krypton by the lattice during the phase transitions $\alpha \rightarrow \beta$ quartz and $\alpha \rightarrow \beta$ cristoballite. The authors ascribe this fact to the different character of the phase transitions. In the last two cases, only the valence angles change and the bonds are not actually broken. In the case of the β quartz to β cristoballite conversion, a completely new lattice is formed.

Hidalgo and Sizmann[115] accomplished labeling of alumina powder, Al_2O_3, by the heating at temperatures higher than 1323 K in a gas atmosphere containing ^{85}Kr. The gas inclusion in this temperature range is explained by recrystallization, closure of pores and sintering.

2.4. The choice of labeling technique

The techniques used by various authors for labeling of solids with inert gases were summarized in this chapter. The technique chosen for labeling the studied substance depends upon the character of the substance and on the end to be reached by the inert gas release measurement. Techniques based on the introduction of parent nuclides of inert gases are usually applied to substances when information on changes of surface or structure in relation to temperature or time is required. Heating, cooling, re-heating etc., can be applied without any danger that the inert gas will be exhausted. The sample labeled with the parent of inert gas can be used for ETA measurement many times, even after long storage, as long as the parent of inert gas does not disintegrate.

In contrast to these techniques, the amount of a gas introduced into the sample without a parent decreases with time. It decreases continuously during sample heating and can be exhausted even before high temperature changes occur in a substance. In this case, repeated labeling should be made after cooling the sample to room temperature.

The labeling of samples by the inert gas without parent is usually applied when the gas release is to be followed in one heating run only without the necessity to follow the release behavior during sample cooling. On the other hand, labeling based on the direct introduction of the inert gas makes it possible to use a greater variety of inert gases. The homogeneous labeling by nuclear reactions and the ion bombardment found an advantageous use in studying the properties of crystal lattice, namely its defects.

By varying the conditions for labeling (neutron flux, type of nuclear reaction, or dose and energy in ion bombardment), it is possible to separate different release processes which otherwise could occur simultaneously leading to a release behavior which would be difficult to interpret. By varying the ion dose in the ion bombardment, the gas concentration can easily be varied without changing the purity of the specimen, thus avoiding the disturbing impurities that are produced during reactor irradiation. By varying the energy of gas ions, the position of the gas (or median range of the gas ions) with respect to the surface can be chosen, thus enabling a separation of surface and bulk release processes. Moreover, the effect of radiation damage or specific impurities on release can easily be studied in double bombardments.

The ion bombardment together with the diffusion technique are used for producing krypton-labeled compounds called kryptonates. The latter have found wide application in analytical chemistry as very sensitive analyzers of gases and liquids.

Chapter 3

INERT GAS RELEASE FROM SOLIDS CONTAINING CORRESPONDING PARENT NUCLIDES

Inert gas release from a solid depends not only on the properties of the solid but also on the labeling, i.e., whether the inert gas itself or its parent nuclide was introduced into the solid, and on their distribution. Therefore, the inert gas release behavior will be described separately:

(i) for solids containing a parent nuclide of the inert gas;

(ii) for solids containing the inert gas without parent nuclide.

In this chapter, these cases of inert gas release are treated where they are parent nuclides of inert gas atoms introduced in the solid. The cases discussed below deal with the samples of various grain shapes labeled by incorporation, impregnation and recoil techniques (for the description of labeling techniques see Chapter 2). In all cases, parent nuclides which are in the solid give rise to inert gas atoms.

3.1. Processes of inert gas release

Generally, there are two processes which contribute to the release of inert gas from the solid containing corresponding parent nuclide:

1. The recoil of freshly generated inert gas atoms. If the parent atom lies close to the surface of the grain the recoil energy of the order 100 keV which the inert gas atom gains during the decay of the parent may be sufficient to eject it from the solid.

2. The diffusion of inert gas in the solid.

The schematic drawing of the processes of inert gas release from a spherical grain of solid is shown in Fig. 17. Both processes are affected by the physical properties of the solid and by the structural and chemical changes taking place in the solid. For the sake of simplicity, we shall first deal with the case when, above the given temperature range, there are no changes in the state of the solid studied.

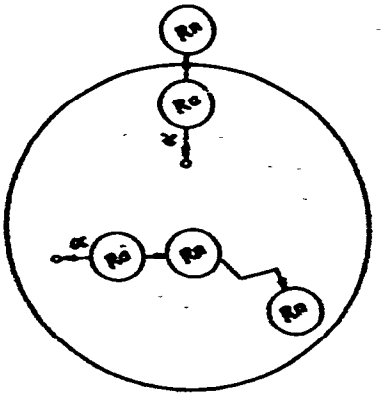

Fig. 17. The recoil and diffusion processes of inert gas release from a spherical grain.

The theories of both recoil and diffusion processes were first developed by Flügge and Zimens[38]. The authors assumed an assembly of uniform (spherical) particles within which the distribution of the inert gas parent (Ra-atoms) is uniform and constant. The recoil release of the inert gas from solids of various grain shapes with a non-uniform distribution of the parent nuclide was recently treated by Bussière et al.[116]. Kapustin and Zaborenko[117] proposed solutions for inert gas release from solids with uniform, linear or exponential distributions of the inert gas. Cases are treated for both time-independent (stationary) and time-dependent concentration profiles.

The formal treatment assumes that there is a continuous source of inert gas atoms provided that radioactive equilibrium is maintained; this means that the rate of inert gas formation by decay of parent is equal to the sum of the rate of its decay and the rate of its escape from the grain.

Experimental measurements give the total emanating power E defined by Hahn[16] as

$$E = \dot{N}_{rel}/\dot{N}_{form} \tag{8}$$

where $\dot{N}_{rel}$ denotes the number of emanation atoms released from the solid in unit time, $\dot{N}_{form}$ denotes the number of emanation atoms formed within the solid in unit time. The total emanating power may be represented as the sum of two terms

$$E = E_R + E_D \tag{9}$$

where E_R, the recoil fraction, represents the fraction $(\dot{N}_{rel})_R/\dot{N}_{form}$ of all emanation atoms for which the recoil tracks end outside the solid, and E_D, the diffusion fraction, represents the fraction $(\dot{N}_{rel})_D/\dot{N}_{form}$ escaping by diffusion during the lifetime of the emanation atom.

3.2. Recoil emanating power E_R

3.2.1. The spherical grain

(*a*) *Uniform distribution of the inert gas parent.* Flügge and Zimens[38] evaluated E_R for a single spherical grain on the basis of the following model (see Fig. 18a). The parent nuclides of emanation (Ra-atoms) are uniformly distributed within the grain. A recoil atom (Rn) can escape from the surface of a grain only if its parent lies within the recoil range R of the surface. Of these, only a fraction escapes by recoil. Only half of those found at the surface escape and none formed at the distance R from the surface. The probability of inert gas escape by recoil from the position in depth r from the surface $q(r)$ is given by the ratio of the surface of the spherical segment with a radius R which protrudes outside the original spherical grain to the total surface of the sphere with the radius R (see Fig. 18a).

$$q(r) = 2\pi R(R - \xi)/2\pi R^2 = (R - \xi)/R \qquad \text{for } \xi \leq R \tag{10}$$

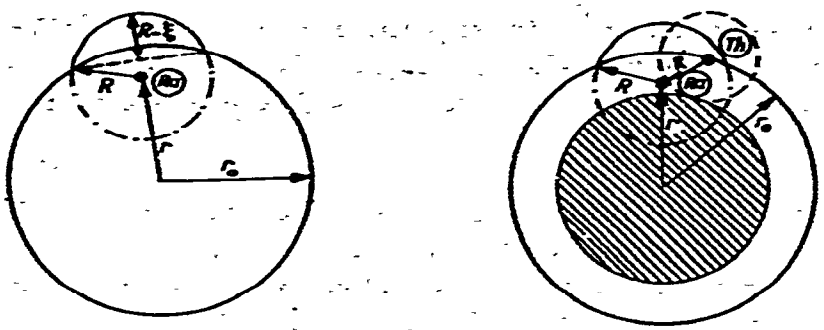

Fig. 18. Model of emanation release by recoil from a spherical grain. (a) Case of uniform distribution of inert gas parent (^{224}Ra). (b) Case of non-uniform distribution of inert gas parent (^{228}Th being situated on the grain surface).

The total quantity of the emanation escaping by recoil through the surface of the grain with radius r_0 in unit time is given by the following relationship

$$(N_{rel})_R = C\Lambda\, 4\pi \int_{r_0-R}^{R} q(r)\, r\, dr \tag{11}$$

where C is the concentration of the parent, supposed to be constant in time and volume, Λ is the decay constant of the parent (Ra atoms), and product $C\Lambda$ is the number of emanation atoms formed in unit volume per time unit.

By solution of the integral, the following expression is obtained:

$$(N_{rel})_R = C\Lambda\pi\,(Rr_0^2 - R^3/12) \tag{12}$$

The quantity of the emanation atoms formed in the particle in unit time equals to

$$N_{form} = 4\pi\, r_0^3\, C\Lambda/3 \tag{13}$$

For the emanating power due to recoil E_R of single particles the following expression was obtained:

$$E_R = (N_{rel})_R/N_{form} = 3R/4r_0 - R^3/16r_0^3 \tag{14}$$

Expression (14) is valid for $r_0 > R/2$. For $r_0 \leq R/2$, $E_R = (N_{rel})_R/N_{form} \to 1$, i.e., every just formed emanation atom escapes by recoil. Since for most usual solids r_0 is of the order ~ 0.01 μm, this relationship can be used for particles of diameters equal or greater than this value of 0.01 μm. For larger particles ($r_0 \sim 1$ μm) the second term becomes negligible and we can write

$$E_R = 3R/4r_0 \tag{15}$$

(*b*) *Non-uniform distribution of the inert gas parent.* Quet et al.[118] considered a simple spherical grain of solid labeled by ^{228}Th using the impregnation technique. This means that ^{228}Th atoms are situated on the surface of grain with radius r_0

(see Fig. 18b). Recoiled atoms of radium ^{224}Ra are generated by the decay of ^{228}Th and stopped at the distance R' from the surface of the grain. The probability dP to find the recoiled Ra-atom within $r + dr$ from the surface ($r < R'$) can be expressed by

$$dP = (r/2R'r_0)dr \tag{16}$$

From eqn (16), it follows that $dP = 0$ for $R' < r \leq r_0$. This means that the core with radius ($r_0 - R'$) in the middle of the grain contains no radon atoms.

Having estimated the probable density of radium atoms within the grain, it is possible to evaluate the recoil emanating power, E_R. This model is described in Fig. 18b. Using eqns (14)–(18) we can write:

$$E_R = \int_0^{R'} q(r)(dP/dr)dr \tag{17}$$

where q is the probability of inert gas escape owing to Rn-recoil (See eqn (10)). For the case when the radius of grain is much larger than the recoil ranges R' and R of radium and radon atoms, respectively (recoil ranges R and R' are in the order of tens μm) the expression for E_R was evaluated and is given in a simplified form as eqn (18):

$$E_R = 1/2 - R'/4R + (5R' + 3R^2)/12\, r_0\, R \tag{18}$$

for $r_0 \gg R, R'$.

The expression for E_R corresponding to the case of $r_0 < R \leq 2\, r_0$ is given in ref. 118.

3.2.2. The cubic grain, slab and cylindrical sample

(*a*) *Uniform distribution of the inert gas parent.* For a small cube having the side of a $\geq 2R$, Kurbatov[119] derived the relationship

$$E_R = 1.5(a - 2R)^2R/a^3 + 5.364(a - 2R)R^2/a^3 + 4.776\, R^3/a^3 \tag{19}$$

For large cubes ($a \gg R$), eqn (19) is reduced to

$$E_R = 3R/2a \tag{20}$$

For slabs of thickness e, the following values of E_R were estimated[116]

$E_R = 0.5$ for $e = R$

$E_R \to 1$ for $e \ll R$

For a cylinder of radius r_0 and of height h, Kapustin and Zaborenko[117] derived:

$$E_R = (1/2)(R/r_0 + R/h - 2R^2/hr_0 + R^3/hr_0^2) \tag{21}$$

For a cylindrical sample of comparable dimensions, $h = 2r_0$, the emanation release is fully due to recoil (i.e., $E_R = 1$ becomes when $R/r_0 \geq 1.56$).

(*b*) *Non-uniform distribution of the inert gas parent.* For slabs of a thickness smaller than other dimensions and larger than $R' + R$, the following formulae were

derived. The probable density of radium atoms equals $dP = 1/2R'$ which has the same value as that obtained from eqn (16) for a spherical grain with $r_0 \gg R'$.

The expression for E_R

$$E_R = (1/2) - R'/4R \tag{22}$$

is the limit form of expression (18) and is valid for spherical grains of the radius very large in comparison to R' and R.

3.2.3. Recoil emanating power and surface area

(*a*) *Uniform distribution of the inert gas parent.* For the relatively large single grains of any shape (of dimensions comparable to 1 μm) the recoil emanating power can be expressed using specific surface area $S_{sp} = S/M$ and density ρ. The following expression results from eqn (15):

$$E_R = (R\rho\, S_{sp})/4 \tag{23}$$

Thus, there exists a direct proportionality between E_R and surface area S_{sp}.

(*b*) *Non-uniform distribution of the inert gas parent.* For single crystal grains large enough in comparison to the recoil ranges of the inert gas and its parent atoms, a single relationship was found between E_R and S_{sp}. For example, for spherical grains, the following expression results from eqn. (18):

$$E_R = (1/2) - (R'/4R) + (5R'^2 + 3R^2)\rho\, S_{sp}/36R \tag{24}$$

In this case, a linear dependence between E_R and S_{sp} was found instead of the direct proportionality, valid for the case of uniform distribution of the parent nuclide in the grains.

3.2.4. Estimation of recoil range R

For the practical use of emanating power expressions, it is necessary to estimate the penetration range of recoil atoms, called recoil range R. Various ways were described to calculate the recoil range.

A rather approximative way proposed by Flügge and Zimens[38] (1939) consists in applying the semi-empirical expression:

$$R = (C/\rho)(\overline{A/s}) \tag{25}$$

where C is a proportionality constant that increases with the energy of recoiled atoms, ρ is the density of the solid, A is the atomic weight, and s is the atomic stopping power of the solid related to the atomic stopping power of air. The constant C was evaluated from the emanation power due to recoil measured glass rods[38]. The recoil ranges obtained by means of eqn (25) led to values of $C = 57 \times 10^{-8}$ and 74×10^{-8} for ^{222}Rn and ^{220}Rn, respectively. The Flügge-Zimens recoil range eqn (25) has been subjected to various objections on both experimental and theoretical grounds[121].

More recently, Bohr[84] (1948) proposed the range–energy relation in terms of modern theories of stopping of atomic particles:

$$R = m_e \varepsilon_R / (\pi N \cdot \hbar^2 Z_1^{2/3} Z_2) \tag{26}$$

where R is the recoil range, ε_R the recoil energy, m_e is the electron mass, N is the number of atoms of stopping material/cm^3, $\hbar$ is Planck constant equalling 1.0545×10^{-23} J s^{-1}, Z_1 and Z_2 are the charges of the nuclei of the recoil atom and the struck atom, respectively. The recoil energy, ε_R, is calculated from alpha-particle decay energy ε_α using the relation, $\varepsilon_R = 4. \varepsilon_\alpha / M$, where M is the mass of the recoil atom. The calculation of straggling or mean square deviation from the mean range R is given in ref. 84.

Recoil ranges in solids labeled by impregnation or recoil techniques can be estimated by the expressions and experimental methods developed for determining the penetration range of atoms in ion-bombardment labeling (see paragraph 2.3.2.3.). To assist the reader in visualizing the recoil ranges of radium and radon atoms, some values obtained by different authors[47, 118] are quoted below:

Recoil ranges of ^{220}Rn	in MgO:	$R = 41.7$ nm
	in SiO_2:	$R = 65.4$ nm
	in Ba-stearate:	$R = 94$ nm
	in air:	$R = 8.3 \times 10^4$ nm
Recoil ranges of ^{224}Ra	in MgO:	$R = 39.5$ nm
	in SiO_2:	$R = 61.0$ nm

3.3. Diffusion emanating power E_D

Two shapes of grains considered in the literature are: (i) sphere, and (ii) cylinder.

3.3.1. The spherical grain

The quantity of emanating atoms released by diffusion from a spherical grain is given by:

$$(N_{rel})_D = -D\, 4\pi r_0\, (\partial c/\partial r)_{r=r_0} \tag{27}$$

where D is the diffusion coefficient of inert gas in the sample, c is the concentration of the inert gas atoms in the volume unit, and $(\partial c/\partial r)_{r=r_0}$ is the concentration gradient of the inert gas at the surface of the grain. The diffusion fraction of emanating power, E_D, can be evaluated using Fick's 1st law as the ratio

$$E_D = (N_D)_{dif}/N_{form} = -(3D/CAr_0)\, (\partial c/\partial r)_{r=r_0} \tag{28}$$

For the evaluation of the concentration function $c(r, t)$ the following differential equation based on Fick's 2nd law, considering the recoil effect, the formation and decay of emanation was used:

$$\partial c/\partial t = D\nabla^2 C + AC - \lambda c - ACq(r) \tag{29}$$

where ∇^2 is the Laplace operator, D is the diffusion coefficient of emanation, $D\nabla^2 C$ denotes the amount of emanation atoms which diffuse through unit volume, AC

denotes the amount of emanation atoms formed in unit time, λc denotes the amount of emanation atoms decaying in unit time, and $AC\ q(r)$ denotes the amount of emanation lost by the recoil. If the grain is homogeneous and isotropic, $q(r)$ depends only on r and can be obtained from geometrical considerations as follows:

$$q(r) = \begin{cases} 0 & \text{for } r \leq r_0 - R \\ [2Rr - (r_0^2 - R^2) + r^2]/2Rr & \text{for } r_0 - R \leq r \leq r_0 \end{cases} \tag{30}$$

For the solution of the concentration function $c(r, t)$, Flügge and Zimens[38] assumed the limit conditions of the radioactive equilibrium: c, $\partial c/\partial t$ are constant and time-independent, $c_0(r) = c_0 = \text{const}$ (a uniform distribution of inert gas within the whole grain), concentration of the gas on the surface being zero $c(r_0) = 0$.

Finally, the emanating power due to diffusion was evaluated in terms of two dimensionless parameters x and y:

$$E_D = (3/2y^2)\{1/x - ([\sinh y(1 - x)]/x \sinh y) - 1\} +$$

$$+ (3/y)\{(1 - x/2 - 1/xy^2) \operatorname{cth} y + [\cosh y(1 - x)]/xy^2 \sinh y\} \tag{31}$$

where $x = R/r_0$, $y = r_0(\lambda/D)^{1/2}$. Parameter x (the ratio of recoil depth R to particle radius r_0) denotes the thickness of the surface layer relevant to the recoil fraction of the emanating power. Parameter y is the ratio of particle radius r_0 to the characteristic "diffusion path", $(D/\lambda)^{1/2}$, which passes in average an inert gas atom by diffusion during its lifetime. Equation (31) can be simplified for large particles, where $r_0 \gg R$, $x \ll 1$ as $E_D = (3/y)(\operatorname{cth} y - 1/y)$, and for samples with a relatively small D, $y \gg 1$, we can finally make the simplification:

$$E_D = 3/y = (3/r_0)(D/\lambda)^{1/2} = (D/\lambda)^{1/2} \rho S_{sp} \tag{32}$$

Equation (32) gives a good approximation for large single particles in which the inert gas diffusion coefficient D is small ($E_D < 0.3$). For higher emanating powers the expression becomes more involved. However, Flügge and Zimens[38] have conveniently tabulated the relationship between y and E_D for the full range of values.

Kapustin and Zaborenko[117] evaluated the E_D-function assuming various limit conditions: various concentration profiles (i) homogeneous, (ii) linear, (iii) exponential, the gas concentration on the surface of the grain being different form zero (i.e., $c(r_0) = c_s \neq 0$), and considering the cases of (a) time-independent (stationary) and (b) time-dependent concentration profiles.

We will summarize here the formulas proposed.

(a) Time-independent concentration profiles and limit conditions $c(0) < \infty$, $c(r_0) = c_s \neq 0$.

$$E_D = (3/2y^2)\{1/x - 1 + a + \operatorname{cth} y\,[y(1 - a) - (1/xy) - (xy/2)] -$$

$$- ([\operatorname{sh} y(1 - x)]/x \operatorname{sh} y) + [\operatorname{ch} y(1 - x)]/xy \operatorname{sh} y\} \tag{33}$$

where $x = R/r_0$, $y = r_0(\lambda/D)^{1/2}$, $a = 2\lambda c_s/AC$ (34)

Using the work and method of Flügge and Zimens[38], the following approximative solutions were obtained,

(1) for small grains, with $R = 2r_0$ $(x = 2)$

$$E_D = 3a\,(1 - y \operatorname{cth} y)/2y^2 \tag{35}$$

(2) for large grains, where recoil path $R \ll r_0$ $(x \ll 1)$

$$E_D = 3\,(2 - a)\,[\operatorname{cth} y - (1/y)]/2y \tag{36}$$

and for $y \gg 1$, $\operatorname{cth} y \simeq 1$ we obtain for E_D

$$E_D = 3\,(2 - a)/2y \tag{37}$$

(b) Time-dependent concentration profiles and limit conditions $c(0, t) < 0$, $c(r_0, t) = c_1$, $c(r, 0) = c_0(r)$. The initial gas concentration in grains of various concentration profiles depends on the radius r_0 only. The formulas for E_D given below were evaluated with the assumption of $R \ll r_0$, $x \ll 1$, using dimensionless parameters x, y, a (the same as in eqn (34)), and $b = c_0\lambda/AC$. The following cases of concentration profiles are treated:

(i) homogeneous distribution $c_0(r) = c_0 = \text{const}$

$$E_{D_1} = [3(2 - a)/2y] + (6/y^2) \sum_{n=1}^{\infty} \exp - [\pi^2 n^2/y^2) + 1]\,\lambda t \times$$

$$\{b - 1 + [(1 - a)\,\pi^2 n^2/2(y^2 + \pi^2 n^2)]\} \tag{38}$$

(ii) linear distribution $c_0(r) = (c_0/r_0)r$

$$E_{D_2} = [3(2 - a)/2y] + (6/y^2) \sum_{n=1}^{\infty} \exp - [(\pi^2 n^2/y^2) + 1]\,\lambda t \times$$

$$\{b - 1 + [(1 - a)\,\pi^2 n^2/2(y^2 + \pi^2 n^2)] + 2b(1 - \cos \pi n)/\pi^2 n^2\} \tag{39}$$

(iii) exponential distribution $c_0(r) = c_0 \exp r/r_0$

$$E_{D_3} = [3(2 - a)/2y] + (6/y^2) \sum_{n=1}^{\infty} \exp - [(\pi^2 n^2/y^2) + 1]\,\lambda t \times$$

$$\{b - 1 + [(1 - a)\,\pi^2 n^2/2(y^2 + \pi^2 n^2)] - (b\pi n/(1 + \pi^2 n^2) \times$$

$$\exp - [[(1 - \pi^2 n^2)/(1 + \pi^2 n^2)] - [2(-1)^n/(1 + \pi^2 n^2)] + (1 + \pi^2 n^2)/\pi n]\} \tag{40}$$

The first three terms of eqn (40) are sufficient for practical applications.

3.3.2. The cylindrical sample

The formulas for the emanating power due to diffusion E_D for the case of a cylindrical sample (a pellet) of comparable radius r_0 to the height h were derived under

similar considerations as in the case of a spherical grain by Kapustin and Zaborenko[122]. For E_D of a cylindrical sample, we can write

$$E_D = -[2D(r_0 + h)/r_0 h\Lambda C](\partial c/\partial r)_{r=r_0} \quad (41)$$

(a) For the time-independent concentration profile assuming limit conditions $c(0) < \infty$, $c(r_0) = 0$, rather involved formulas for E_D are arrived at[122]. However, after simplification for large grains (i.e., $y(1 - x) \gg 1$ and $y \gg 1$) the following relationship is obtained

$$E_D = (1 + z)/yz \quad (42)$$

where $y = r_0(\lambda/D)^{1/2}$, $z = h/r_0$.

(b) For the time-dependent concentration profiles (homogeneous, linear and exponential), the resulting expressions of E_D are rather complex as can be seen from ref. 122. As with the spherical grains, the authors analyzed the cases of $R \ll r_0$, $y(1 - x) \gg 1$ and $y \gg 1$.

3.4. Total emanating power

The expression for the total emanating power, E, is obtained by the addition of the two terms for E_R and E_D, which are given above for various sample shapes, size and gas concentration profiles. The appropriate expression describing the experimental data (the total emanating power is usually obtained) is obtained by taking into account the size, shape and mode of preparation (labeling) of the sample. Expressions for the total emanating power for two cases of sample shape, supposing a homogeneous distribution, under limit conditions $c(r_0) = 0$ are given below (using the dimensionless parameters $x = R/r_0$, $y = r_0(\lambda/D)^{1/2}$, $z = h/r_0$).

(i) The case of spherical particles[38] with a diameter of 1 μm for $E_R < 0.3$ ($x \ll 1$) and $E_D < 0.3$ ($y \gg 1$)

$$E = E_R + E_D = 3x/4 + 3/y = [R/4 + (D/\lambda)^{1/2}] \cdot \rho S_{sp} \quad (43)$$

(for the description of D, ρ, S_{sp} see eqn (32)).

(ii) The case of cylindrical sample[122] of comparable dimensions

$$E = E_R + E_D = [(z + 1)/z](x/2 + 1/y) \quad (44)$$

3.5. Apparent emanating power and its time-dependence

The above expressions for emanating power, E, were derived assuming a radioactive equilibrium between the parent nuclide and the inert gas, i.e., a constant concentration of the inert gas atoms in the solid. However, in the time interval before the radioactive equilibrium is established, the value E of emanation power is time-dependent and the term of "apparent emanating power" should be used. The following considerations can be made in this respect: All the gas atoms that escape

from grains by recoil do so immediately after being generated. Therefore, the rate of escape by recoil does not depend on the concentration of inert gas atoms in the grain or on the time interval between the sample labeling and the ETA measurement. On the other hand, the rate of escape by diffusion does depend on the concentration of inert gas atoms in the grain and, therefore, on the age of the labeled sample, until the radioactive equilibrium is reached. The apparent emanating power "E_0" of a freshly labeled sample from which inert gas atoms escape only by recoil should therefore be equal to E_R. The value of "E" increases in time, until it reaches its saturation value, when the equilibrium is established. The following expression for apparent emanating power "E_t" was proposed[38]:

$$\text{“}E_t\text{”} = E_R + E_D[1 - \lambda t/(\exp(-\lambda t) - 1)] \tag{45}$$

where "E_t" is the apparent emanating power at time t elapsed since the sample labeling, λ is the decay constant of the inert gas. As follows from eqn (45), the equilibrium is supposed to be established in the time comparable to $1/\lambda$, i.e., to the half-life of the inert gas atoms.

The term for apparent emanating power should also be used when destruction of radioactive equilibrium takes place, such as by an abrupt increase of inert gas release rate on heating of the sample. Assuming that the release rate of inert gas from the solid is directly proportional to the amount of inert gas in the solid, the following expression for the time-dependence of the apparent emanating power "E_t" was derived[1]:

$$\text{“}E_t\text{”} = E_1\{1 + [(E_2 - E_1)/(1 - E_2)][\exp[-\lambda t/(1 - E_2)]]\} \tag{46}$$

where "E_t" is the apparent emanating power at time t passed after the change, E_1 is the emanating power before the change, E_2 is the emanating power after the change and λ is the decay constant of the inert gas. From eqn (46), it follows that a new radioactive equilibrium is established after a sudden change of inert gas is released in the time $1/\lambda$, i.e., with the inert gas half-life.

3.6. Emanating power of a finely dispersed solid

The above expressions for emanating power were evaluated under consideration of large single particles $\sim$ 1 μm in which the diffusion coefficient is small. The expressions remain unchanged also for the case of a powder when spacing of grains is larger than the recoil range. To consider the grains of a powder in air as isolated, the grain size of some tens of micrometers is required. For a powder with smaller grains than the size mentioned, the recoil path can affect several grains and the expressions developed above for single grains are no longer applicable. For the case when the distance between individual grains or pore volume is smaller, Zimens[1] considered the following model: When a recoiling inert gas atom passes across a pore and strikes a second grain before being slowed down to thermal energies ($\sim$ 0.1 eV), it will penetrate the second grain. If it is to contribute to the emanating power of the

sample, it must diffuse out of the second grain into the pore and into the free gas space above the sample. Zimens[1] calls these inert gas atoms, that penetrate a second grain, indirect recoil atoms, and those that are stopped in the pores, direct recoil atoms. The symbol, E_{Ri}, is used to represent the fraction of inert gas atoms that escape from a solid sample by indirect recoil, and E_{Rd} is used to represent the fraction of those that escape by the direct recoil. For an aggregate of grains, E_R in eqns (14), (18), (21) and (22) is given by the sum of both terms E_{Ri} and E_{Rd}

$$E_R = E_{Rd} + E_{Ri} \tag{47}$$

Flügge and Zimens[38] calculated that for a dry powder E_{Rd} cannot be greater than 0.1. Qualitatively, their arguments are that for small grains ($\sim$ 1 μm) from which a large fraction of the inert gas atoms may recoil, the air gap between the grains is much less than the recoil range in air ($\sim$ 100 μm). Consequently, only a small fraction of the recoil atoms are slowed to thermal energies in the air-filled pores. For large grains ($\sim$ 1 μm), even though the air gap is sufficiently large to stop a large fraction of the recoiled atoms, the specific surface is so small that E_{Rd} is also less than 0.1. In the finely dispersed solid consisting of grain aggregates, E_R is usually found larger than 0.1. The larger part of E_R is then composed of indirect recoil atoms, E_{Ri}.

To understand the relatively higher value of E_{Ri} in comparison to E_{Rd}, it is necessary to note that the recoil atom causes along its path a damage to the lattice. The diameter of the damaged area depends on the recoil range and was estimated to be 0.1 μm, and the path of the atom recoiling from the surface of one grain into a second grain was estimated to be 0.1 μm. Moreover, in the surface layers of the fine grains where the indirect recoil atoms of emanation are trapped, a relatively high degree of lattice disorder exists, depending on the conditions of the preparation of the sample.

It is obvious that inert gas atoms may diffuse through the region of the damaged lattice more rapidly (D value is higher) than through the undamaged regions of lattice.

This model was successfully proven in practice and can be used for the explanation of the relatively high value of emanating power at room temperature of finely dispersed oxides, as MnO_2, NiO, Al_2O_3, metal hydroxides etc.[116].

For the fraction of indirect recoil atoms that escape by diffusion through the described lattice, the damage apparently differs from one solid to another and depends on the structural properties of the solid concerned. Götte[123] obtained evidence for the indirect recoil effect and the evidence indicating that the release rate of inert gas atoms from damaged grains is largely dependent on the composition (mainly structure) of the solid. When a zinc hydroxide preparation, with an emanating power for ^{220}Rn of 0.22, was mixed with inactive iron(III) hydroxide, the emanating power increased to 0.60; when mixed with iron(III) oxide, the emanating power decreased to 0.11. Therefore, it is possible to conclude that the release of indirect recoil atoms from iron(III) hydroxide is easier than from iron(III) oxide.

3.7. Temperature-dependence of emanating power

3.7.1. Direct recoil emanating power E_{Rd}

The emanating power due to direct recoil, E_{Rd}, is temperature-independent since the thermal energy (~ 0.1 eV) is insignificant compared with recoil energies (~ 100,000 eV for recoil atoms resulting from alpha decay). However, diffusion processes are dependent on temperature. We can say that, if the emanating power is experimentally found to be temperature-independent over a reasonable temperature range, the diffusion process must be absent ($E_D = 0$) or its contribution to the release is 100% ($E_D = 1$). For low temperature-independent emanating powers, E_D must be close to zero.

3.7.2. Indirect recoil emanating power E_{Ri}

From the preceding paragraph 3.6., it follows that the emanating power due to indirect recoil E_{Ri} is temperature-dependent. The release of the indirect recoil inert gas atoms can be controlled either by diffusion in pores of about 0.1 μm diameter (in larger pores the diffusion coefficient D and the diffusion path at room temperature are great enough) or by diffusion in the regions of the damaged lattice.

For the first case we can suppose that

$$D \propto T^{1/2} \text{ or } \log D = 1/2 \log T + k \tag{48}$$

For the second case D varies with temperature as

$$D \propto \exp(-\Delta H'/RT) \text{ or } \log D = -\delta H'/RT + \text{const} \tag{49}$$

$\Delta H'$ being the activation enthalpy of damage diffusion and T the absolute temperature. The amount of emanation atoms which escape from the damaged regions of the solid during their lifetime is proportional to the diffusion path, $(D/\lambda)^{1/2}$.

3.7.3. Diffusion emanating power E_D

The emanating power due to diffusion, E_D, depends on temperature since D varies with temperature as

$$D = D_0 \cdot \exp(-\Delta H/RT) \tag{50}$$

Then we can write for spherical grains of the solid in temperature equilibrium:

$$E_D = 3/y = 3/r_0 (D_0/\lambda)^{1/2} \exp(-\Delta H/2RT) =$$

$$= (D_0/\lambda)^{1/2}(S/M)\rho \exp(-\Delta H/2RT) \tag{51}$$

where ΔH denotes the activation enthalpy for diffusion of inert gas atoms in the solid, R the gas constant, and T the absolute temperature. Experimental data complying with eqn (51) are usually obtained only with samples annealed at a temperature somewhat above the temperature range within which the emanating power is measured. This annealing prevents the occurrence of water desorption, chemical reaction,

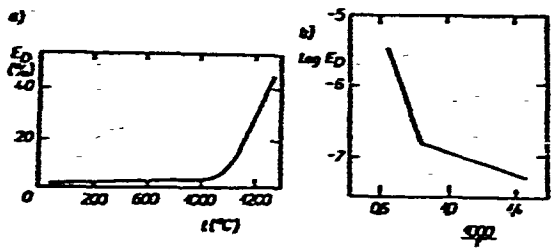

Fig. 19. Temperature-dependence of emanating power. (a) relationship E versus T. (b) relationship log E_D versus $1/T$.

recrystallization, sintering or other structural changes which might occur in the solid within the temperature range considered.

Aluminum oxide, Al_2O_3, homogeneously labeled by ^{228}Th and annealed at 1350°C (1623 K), which is usually taken as the reference material for DTA, is used as an example[8] for diffusion emanating power, E_D, related to temperature within the range, 20–1250°C (293–1523 K) (see Fig. 19). In the absence of any chemical or structural changes the E_D–T curve has an exponential form as shown in Fig. 19a. Figure 19b shows the relationship, log E_D versus $1/T$. Values of E_D were obtained from the total measured emanating power reduced by E_R, the latter being the value of E at room temperature. The emanation release due to diffusion in the annealed Al_2O_3 sample is determined by transport processes taking place in the imperfect crystal lattice during heating. On the curve plotted with a semilogarithmic scale (Fig. 19b), usually two or more linear sections may be distinguished corresponding to various transport mechanisms. In the low temperature section, the diffusion mechanism controlled by the presence of frozen-in defects is supposed. The high temperature section is believed to correspond to the equilibrium state of the lattice defects. The mechanism of volume diffusion is considered in this temperature region[8].

From the slopes $\partial \log E_D/\partial T$ of the linear sections, values for the activation enthalpy, ΔH of diffusion of emanation in the respective temperature region, can be evaluated using the following formula:

$$\Delta H = 38.38\,[\log E_2 - \log E_1]/[(1/T_2) - (1/T_1)] \text{ in kJ mol}^{-1} \quad (52)$$

The intersection temperature τ of the two temperature regions is termed the Tammann temperature[124], which can be interpreted in the following way: By annealing of the Al_2O_3 sample to 1350°C (1623 K), a thermal equilibrium of lattice defects has been established. During sample cooling, the established equilibrium is frozen at a definite temperature, τ. As shown by Tammann[124], this temperature is related to the absolute melting point of the solid and has been reported for ionic salts and oxides to be about one half and for metals as about one third of the absolute melting point. The frozen high-temperature equilibrium can be considered to be the controlling factor of the diffusion emanation release during the re-heating of the annealed sample to temperatures, $T < \tau$. At temperatures $T \geq \tau$, the emanation release is controlled by the high-temperature equilibrium of the lattice defects.

The evaluation of the diffusion coefficient, D, in relation to T within the respective temperature ranges can be accomplished from the experimentally obtained E_D values using eqn (32). It should be remembered that the diffusion of emanation in solids is an impurity-diffusion process. The diffusion parameters evaluated from the emanating power measurements describe the mobility of the inert gas within the solid.

3.8. Factors influencing the emanating power of solids

3.8.1. Porosity

In common powdered samples, the inert gas atoms, that reach gas-filled pores with thermal energy, rapidly diffuse into the free gas space above the samples unless they are adsorbed on the surfaces of the grains. This conclusion can be reached from a consideration of pore lengths and diameter and inert gas diffusion velocity and it is essential to the explanation of the high emanating power of many preparations. For example, a powdered barium palmitate sample emanates ^{220}Rn with an efficiency of 99%[1]. Therefore, only 1% of the ^{220}Rn atoms (half-life 55.6 s) decay during the time required for their diffusion from the solid grains and from the gas-filled pores.

From studies with barium carbonate[1, 38] and iron(III) oxide[125], it appears that compression of a powder has little effect on its emanating power until the volume of the pores becomes less than the volume of the grains ($r \sim 10^{-1}$ μm). The

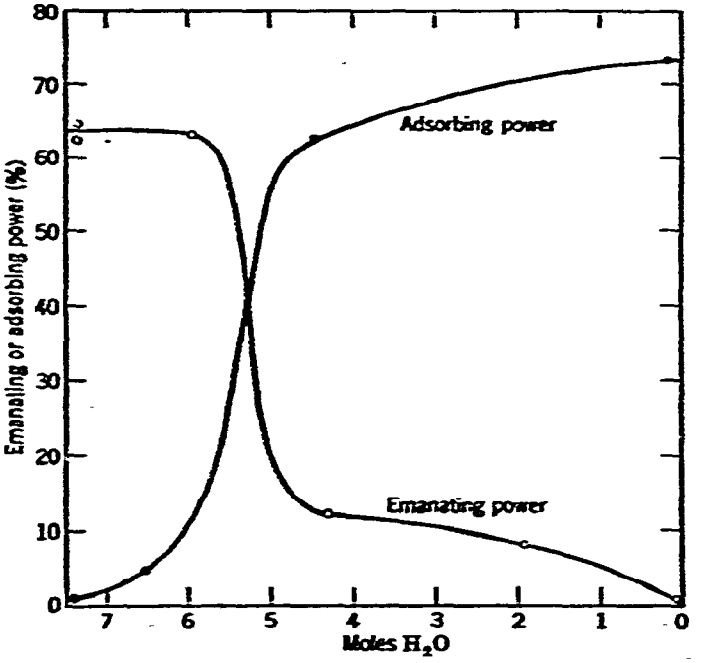

Fig. 20. Effect of dehydration on the emanating and adsorbing powers of chabazite for radon at 20°C. Adsorbing power is expressed as percentage of radon adsorbed on 1 gram of substance (cf. ref. 44).

decrease in emanating power, when the volume of the pores becomes less than the volume of the grains, may be due to the closing of some of the pores.

3.8.2. Adsorption of inert gas

If the inert gas is adsorbed on the surface of the grains, diffusion from the pores will be hindered and the emanating power reduced. The amount of adsorption was studied by Müller[44] with an external source of radioactive inert gas. He found that when labeled chabazite, a zeolite containing 7.4 moles of water per gram formula weight, was dehydrated, its emanating power for ^{222}Rn decreased (see Fig. 20). When he exposed a similar but not labeled sample of chabazite at 293 K (20°C) to an external source of radon, he found that the fraction of radon adsorbed increased with dehydration. This indicated that the decrease in emanating power with dehydration is largely due to adsorption. The problem of the adsorption of radioactive inert gases is also treated in numerous papers: e.g., on SiO_2[126, 127], charcoal[128, 129], Fe_2O_3[130–132], $Fe(OH)_3$[132, 133], ZnS[134], $Cr(OH)_3$[133] and ZrO_2[132]. It can be summarized that the adsorption of inert gases is particularly remarkable with samples of large surface area and from about 208 K (— 65°C), the boiling point of radon, up to temperatures somewhat above laboratory temperature.

3.8.3. Adsorption of liquids

The presence of a liquid, such as water, in the pores of a powder will hinder the escape of the inert gas. The short-lived inert gases (^{219}Rn and ^{220}Rn) do not escape quantitatively from liquid-filled pores. The effects of adsorption of inert gases and liquids on the surface of studied samples are to be taken into account by the quantitative interpretation of the emanating power data.

3.8.4. Grain size (surface area)

It follows from eqn (43) that E_R and E_D both depend on the grain size, $1/r_0$ (surface area $S/M = S_{sp}$). The diffusion fraction E_D is moreover directly proportional to $D^{1/2}$. It holds therefore that

$$E \propto (1/r_0)\, D^{1/2} = (1/r_0) \exp(-\Delta H/2RT) \tag{53}$$

Using this equation the importance of grain size (surface area) in relation to the emanation power E will be estimated below. By plotting E against T for a given grain radius r_0, a given activation enthalpy ΔH of diffusion, four theoretical curves are obtained (Fig. 21). It can be seen from Fig. 21 that the change of the grain radius causes an considerable change in the E–T curve. If, for example, a recrystallization takes place at 1200 K in the sample, curve 1 changes to curve 2.

3.8.5. Texture and structure

The emanating power is largely dependent on the texture and structure of the solid. At room temperature the majority of inorganic salts, glasses and ignited metal oxides are poor emanators ($E = 0.01$), whereas metal hydroxides, some organic and

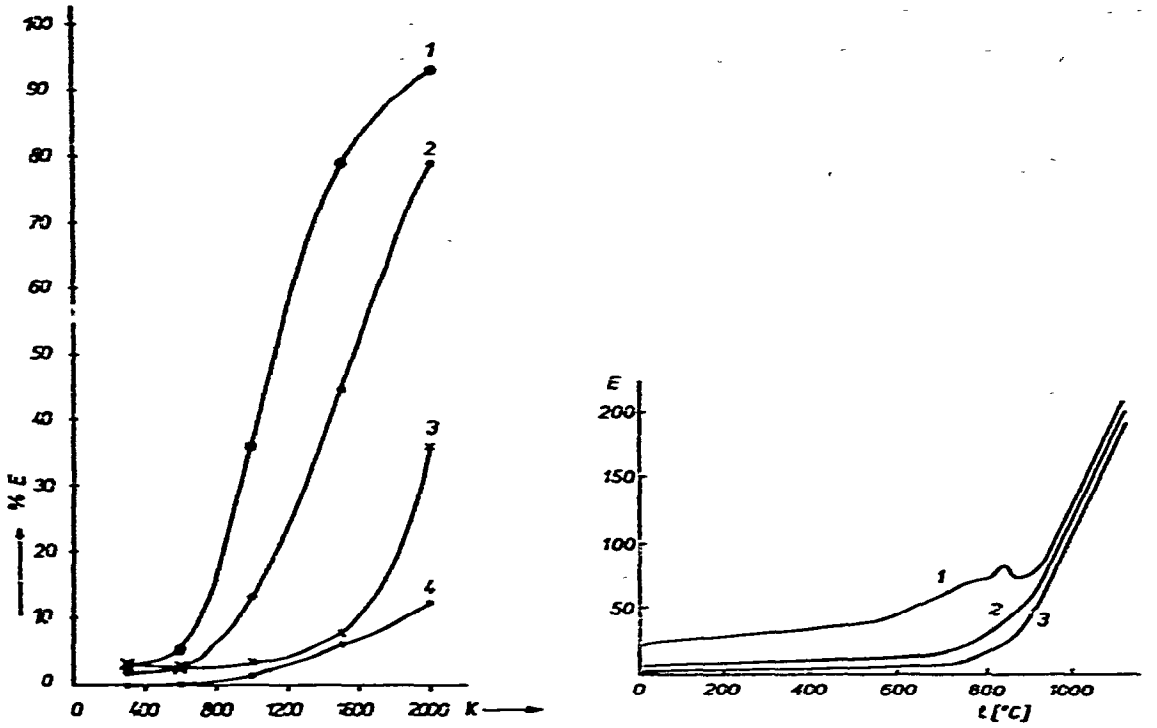

Fig. 21. Emanating power as dependent on grain radius and activation enthalpy of ^{222}Rn diffusion. (1) $r_0 = 1$ μm, $\Delta H = 62.8$ kJ mol^{-1}; (2) $r_0 = 2$ μm, $\Delta H = 62.8$ kJ mol^{-1}; (3) $r_0 = 20$ μm, $\Delta H = 62.8$ kJ mol^{-1}; (4) $r_0 = 1$ μm, $\Delta H = 125.6$ kJ mol^{-1}.

Fig. 22. ETA heating curves of iron (III) oxide samples differing in texture: samples were prepared by heating of iron(-II,III) carbonate in air to 700 (1), 900 (2) and 1100°C (3). Heating rate 5°C min^{-1}.

high-molecular substances were found good emanators. In a homologous series of organic salts the emanating power appears to increase with increasing chain length[135]. The differences in emanating power of finely dispersed samples at room temperature seem to be due to the indirect recoil escape, E_{Ri}, of the inert gas and to its diffusion in pores. Due to its texture, the emanating power of any material strongly depends on the way of preparation.

For illustration, three specimens of iron(III) oxide[136] will be described, which were prepared by the heating of iron(II, III) carbonate in air to 973 K (700°C) — sample 1, 1173 K (900°C) — sample 2, and 1373 K (1100°C) — sample 3, and subsequently quenched. The ETA heating curves of iron(III) oxide samples differing in texture are demonstrated in Fig. 22. Differences in emanating power measured at room temperature are caused[136] by different surface areas (53, 1.8 and 1.0 m^{2}g^{-1} for samples 1, 2 and 3, respectively), and by porosity. The ETA heating curves of the three samples show the differences in their textures: emanating power measured in the temperature range between 293 and 1073 K (20 and 800°C) were caused mainly by diffusion in pores and in surface regions of the lattice, differ, in agreement with eqns (48) and (49). The ETA curve of sample 1 indicates a recrystallization which takes place during heating of the sample at 1103 K (830°C).

Diffusion properties of solids are believed to depend on the structure of the crystal lattice, its density and perfectness. For example, the CsCl-lattice is considered more dense than the NaCl-lattice; the rutile lattice more dense than the anatas-lattice, etc.[14].

The importance of the value of the ΔH of the activation enthalpy of inert gas diffusion on the shape of the *E–T* curve is shown in Fig. 21. Curves 1 and 4 in Fig. 21 show the release behavior of emanation at assumed ΔH values of 62.8 and 125.6 kJ mol^{-1} (15 and 30 kcal mol^{-1}), respectively, for the same grain size (1 μm) of the sample.

3.8.6. Structural and chemical changes

At the beginning of this chapter, it was stated that any changes in structure such as phase transition and/or chemical changes strongly influence the inert gas release from solids. Changes of structure, the appearance of a new condensed phase including a liquid one, are usually accompanied by the change of conditions for the diffusion of inert gas in the lattice of the solid. Chemical reactions in the solid state, such as decompositions, gas–solid reactions, solid–solid reactions, etc., are usually also accompanied by the changing conditions of diffusion for inert gas atoms.

The gas–solid reaction between NiO and H_2 was chosen to demonstrate the shape of the ETA curve (see Fig. 23) measured during the heating of NiO in a stream of hydrogen[137]. The rate of water formation simultaneously measured during the reaction is also shown in the Fig. 23.

Changing diffusion conditions of solids during structural and chemical transformations can exhibit sudden changes in the emanating power. In cases of rapidly increasing emanating power the above-described model of emanation release, derived under assumption of radioactive equilibrium, cannot be used. The destruction of radioactive equilibrium by a sudden increase in the emanating power of a solid will result in an even larger increase in the apparent emanating power. For example, if the emanating power of a sample suddenly increases from 0.5 to 0.8, the apparent

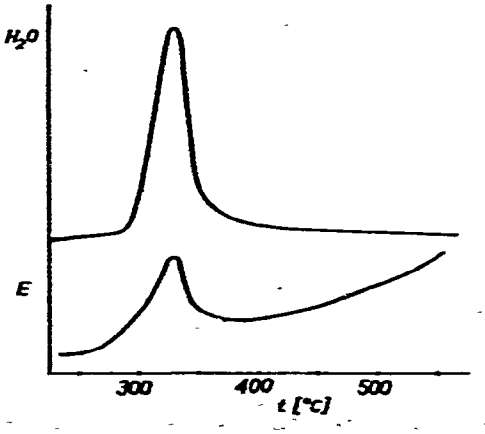

Fig. 23. ETA curve and water release curve during heating of NiO in H_2. Heating rate 5°C min^{-1}.

emanating power, measured immediately during the change, may be as high as 2.0. This phenomenon, called the "peak effect", is the result of the finite lifetime of radioactive inert gas atoms. Some of the inert gas atoms formed before the sudden change, and would have decayed in the solid if no change had occurred, now escape from the solid and contribute to the apparent emanating power.

From eqn (46) it follows that, the radioactive equilibrium after the structural and/or chemical changes of solids is re-established in the time comparable to the inert gas half-life. Using ^{220}Rn, this period corresponds to about 60 seconds. Therefore, about 60 seconds after the end of structural or chemical change the above described model and derived expressions are again applicable.

3.8.7. Mechanical treatment

The effect of milling on the emanation release from zinc oxide is shown by the example in Fig. 24. The ZnO sample was prepared[138] by thermal decomposition of

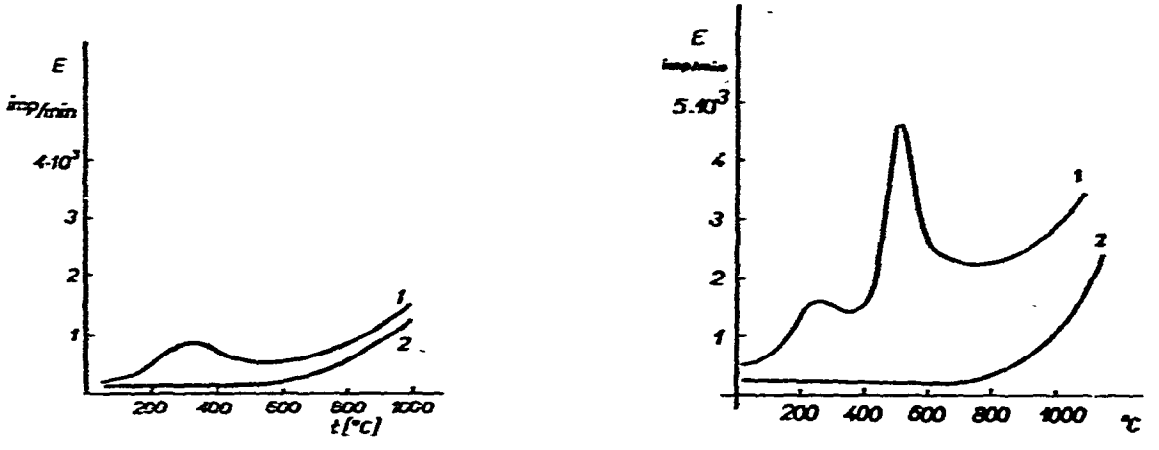

Fig. 24. Effect of milling on the emanation release from ZnO during heating in air (cf. ref. 138). Curve 1, sample milled; curve 2, second heating run.

Fig. 25. Influence of radiation effects induced by ion bombardment on emanating power of iron(III) oxide during heating (cf. ref. 143). Curve 1 and 2 correspond to the first and second heating runs, respectively.

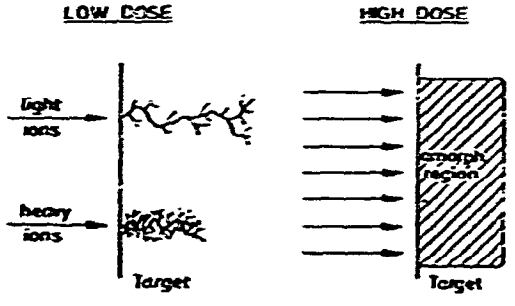

Fig. 26. Schematic drawing of the lattice disorder produced by ion bombardment of high and low doses.

zinc hydroxide homogeneously labeled with ^{228}Th and milled before the ETA measurement. The emanation heating curve is represented by curve 1 in Fig. 24. The effect on curve 1 in the temperature range 333–703 K (60–430 °C) corresponds to the annealing of a lattice damage induced by the mechanical treatment. The effect does not appear in the second heating run (curve 2 in Fig. 24).

3.8.8. Radiation damage

A sample of ferric oxide[22] homogeneously labeled with ^{228}Th was submitted before ETA-measurement to ion bombardment with Kr-ions (energy of 2 keV reached in TESLA transformer). The radiation effects of the ion bombardment on the emanation release are demonstrated in Fig. 25, curve 1; curve 2 corresponds to the repeated heating run. The collisions of the heavy krypton ions cause displacements in the surface layers of the sample which could lead to a gross damage of the lattice, such as amorphization. Fig. 26 shows the schematic drawing of lattice disorder produced by ion bombardment at high and low doses. By heating the bombarded sample the radiation effects are accompanied by the release of emanation. As is seen in Fig. 25, curve 1, two effects on the emanating curve of Fe_2O_3 are observed. First, in the temperature range 393–553 K (120–280 °C), believed as corresponding to the release of emanation atoms located at positions, where the diffusion path was shortened by

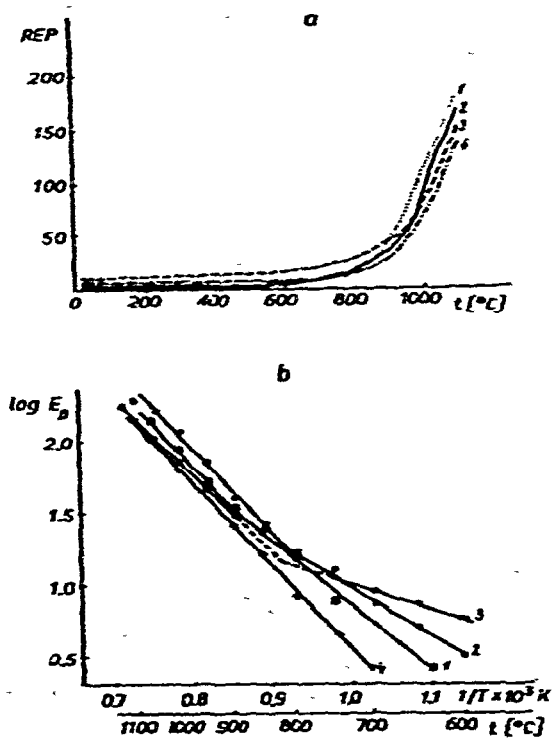

Fig. 27. ETA curves of iron(III) oxide prepared by heating various iron salts to 1100 °C: iron(II,III) carbonate (curve 1); iron(II) sulphate (curve 2); Mohr's salt (curve 3); and ferrous(II) oxalate (curve 4). (a) As dependence of E versus T; (b) as dependence of log E_D versus $1/T$.

the bombardment. Second, in the temperature range 673–873 K (400–600°C), believed to be caused by annealing, of a gross disorder in the lattice of α-Fe_2O_3. Jech and Kelly[139] ascribed this effect to the annealing of bombardment-induced amorphousness.

3.8.9. Non-equilibrium defects

In addition to the above-mentioned factors, there exists a number of factors influencing the mobility of inert gas atoms in solids, e.g., non-equilibrium defects, presence of impurities and non-stoichiometry. The concentration of non-equilibrium defects is usually reflected on the emanation release curve in the temperature range of "frozen-in" defect equilibrium, i.e., below the so-called Tammann temperature.

Figure 27a, b, shows ETA curves of iron(III) oxide samples prepared by the heating of various iron salts (Mohr's salt, iron(II) sulphate, iron(II) oxalate and iron(II, III) carbonate) to 1373 K (1100°C). Values of activation enthalpies for the diffusion of emanation[136] ΔH = 46.06; 79.6; 117.2; 125.6 kJ mol^{-1}, respectively, were determined in the temperature range between 873 and 1123 K (600 and 750°C). These values express quantitatively the influence of the non-equilibrium "frozen-in" defects on the inert gas mobility in the α-Fe_2O_3 lattice[136].

The different behavior of the iron(III) oxide sample of various history (expressed in their reactivity, solubility in acids, catalytic activity) was named by Hedvall[140] structural memory. According to Hedvall[140], "the structure of the salt remained in the structure of the ferric oxide sample until the mobility of the crystal lattice increased to such a degree that the equilibrium state in the lattice was reached".

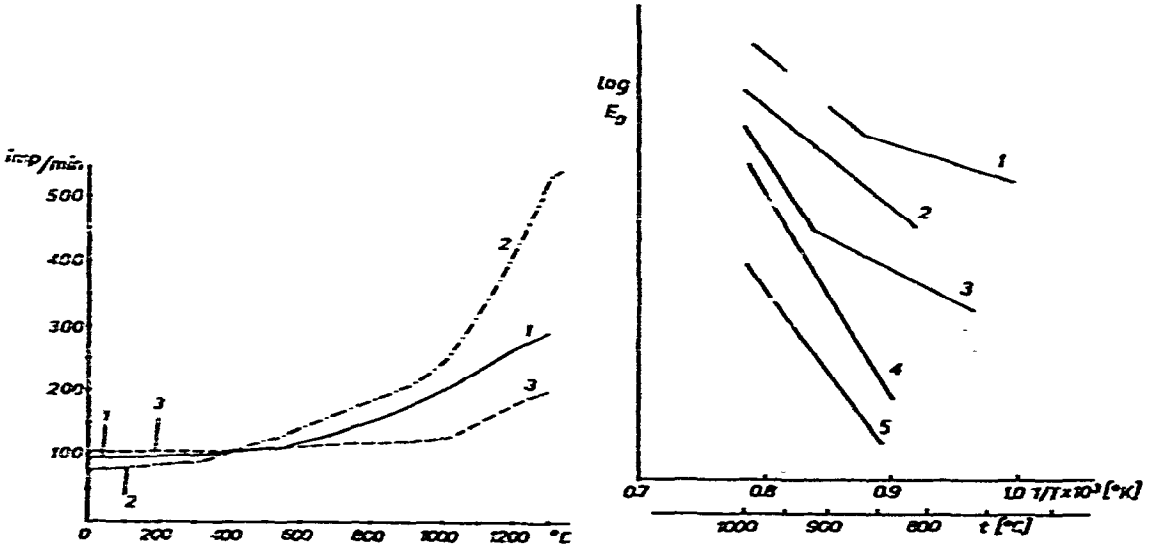

Fig. 28. Effect of Li^+ and Ga^{3+} on ETA heating curve of ZnO. Curve 1: pure ZnO; curve 2: ZnO containing Li^+; curve 3: ZnO containing Ga^{3+}.

Fig. 29. The log E_D–$1/T$ relationship obtained during cooling of TiO_2 (rutile) samples containing various additives: 0.1% SO_3 (curve 1), 0.28% K_2O (curve 2), 0.5% ZnO (curve 3), 0.24% Al_2O_3 (curve 4), and sample especially purified by NH_3 (curve 5).

3.8.10. Impurities

The presence of impurities may strongly influence the diffusion release of emanation from solids. The ETA curves[4] of pure ZnO and ZnO containing 0.5 at. % Li_2O and ZnO containing Ga_2O_3 are shown in Fig. 28. The increase of emanating power, evidently caused by the temperature increase of radon mobility in the crystal lattice, for pure ZnO began at about 1073 K (800°C) (curve 2), whereas for ZnO with Li^+ additives this state is reached at a considerably lower temperature and the emanating power increases more sharply with temperature (curve 1). It is known[141] that the presence of Li^+-ions in the ZnO-lattice leads to the creation of a defect structure in the oxide characterized by the appearance of an excess of interstitial zinc atoms. The presence of Ga^{3+}-ions in the ZnO lattice causes an inverse effect (curve 3).

Another example is demonstrated in Fig. 29 by the ETA cooling curves of TiO_2 (rutile) plotting log E_D against $1/T$. The behavior of TiO_2 samples containing various additives (0.1% SO_3, 0.28% K_2O, 0.5% ZnO, 0.24% Al_2O_3 and sample especially purified by NH_3) annealed to 1273 K (1000°C) is represented by curves 1 to 5. The presence of impurities influences the defect equilibrium and the formation of a perfect rutile lattice producing a change in the inert gas mobility[142].

3.8.11. Non-stoichiometry

Appreciable alterations of equilibrium vacancy concentration may occur as a result of deviations from stoichiometry. The diffusion emanating power, E_D, of a number of solids proved to be dependent on non-stoichiometry. Even if chemical analysis is not sensitive to detecting the degree of non-stoichiometry, emanation release measurements still point towards it. For example, titania(TiO_2) when heated in a reducing atmosphere may lose oxygen and form a solid of formula, Ti^{4+}_{1-2x} Ti^{3+}_{2x} O^{2-}_{2-x} $[A.V.]_x$, where [A.V.] is an anion vacancy. The difference due to the non-

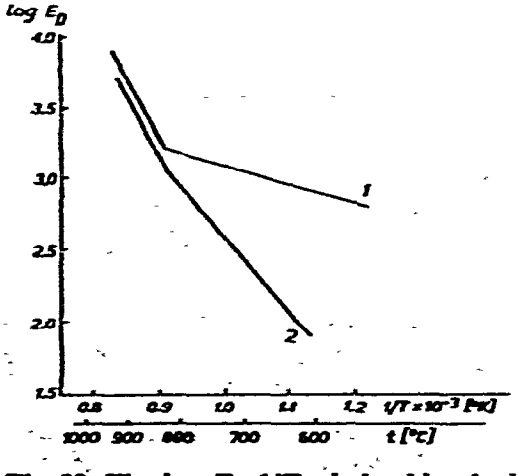

Fig. 30. The log E_D–$1/T$ relationship obtained during cooling of TiO_2 (curve 2), and of TiO_{2-x} (curve 1).

stoichiometry of TiO_2 (annealed to 1373 K (1100°C) in air) and TiO_{2-x} (annealed to 1373 K (1100°C) in nitrogen) is illustrated in Fig. 30. The log E_D–$1/T$ relationship is shown here by curves 2 and 1, corresponding to samples cooled in air and nitrogen, respectively. The values of the activation enthalpy, ΔH, within the temperature range of 873–1123 K (600–850°C) are 213.5 and 50.2 kJ mol^{-1} (51 and 12 kcal mol^{-1}). The decrease of the ΔH value for TiO_{2-x} is ascribed[143] to the increased concentration of anion vacancies [A.V.].

3.9. Information from emanating power measurement

From the emanating power measurement two types of information can be obtained. First, indirect information about processes taking place in the solid. Any process proceeding within a solid and leading to a change either in the surface to volume ratio or in the diffusivity of the emanation atoms becomes indirectly observable from the measurement of the emanating power. This is the basis of the numerous qualitative applications of ETA to the study of solid-state processes, as aging, recrystallization, modification changes, dissociation, solid-state reactions, etc.

Due to the complexity of the release processes, supplementary information about the studied solid are usually necessary for the correct evaluation of ETA curves. Methods such as DTA, TG, dilatometry, X-ray analysis, etc. are frequently employed. To provide this indirect, qualitative information the choice of the incorporation technique for the radioactive label and distribution of the label is directed only by the proper aim of the ETA measurement. Should information about changes in the surface layers of the solid be obtained, a surface distribution of the inert gas is sufficient.

Secondly, from emanating power measurements, it is possible to obtain direct information about specific surface or diffusion parameters of the inert gas in the solid. The experimental conditions must be maintained so that the state of radioactive equilibrium is not destroyed during the measurement of the emanating power. For this quantitative information the question of labeling of samples becomes extremely important, since any theoretical approach starts with the assumption of some well-defined distribution of the immediate parent of emanation throughout the solid. To provide direct information about the specific surface and the diffusion coefficient, a separation of the total emanating power E into E_R and E_D is usually necessary. The simplest but approximative way, applicable for solids with small D, consists in the subtraction of the E_R (obtained as the room temperature value of E) from the total emanating power at the relevant temperature, $E_D = E - E_R$. Other methods of analysis of E_R and E_D will be described later. In some cases, when one of the terms composing the total emanating power E is negligible compared with the other, the precise analysis of E-values into E_R and E_D is not necessary. For example, for the room temperature measurement of emanating power, E_D can be negligible compared with E_R when $E_D < 1/E_R$. This is accomplished[5] for ^{220}Rn atoms when $D < 10^{-16}$ cm^2sec^{-1}.

The evaluation of the diffusion coefficient D and the activation enthalpy ΔH of diffusion of emanation makes possible the quantitative estimation of factors influencing the diffusion parameters of the solid such as non-equilibrium defects, non-stoichiometry, presence of impurities, etc. It has already been shown in paragraph 3.8. that the inert gas diffusion characteristics, D and ΔH of the solid, provide valuable information on the properties of the solid and its state. In the low temperature range, where $T < \tau$, the diffusion characteristics usually reflect a non-equilibrium state of the lattice; in the high-temperature range, where $T > \tau$, an equilibrium state of the lattice is described.

From the plot of log E_D versus $1/T$ obtained during the heating or cooling of the sample, the Tammann temperature can be estimated. The temperature, τ, estimated from the ETA cooling curve of the sample, indicates the temperature at which the defect equilibrium achieved by previous heating, is being frozen. In addition, other phenomena connected with changes of the mobility of the inert gas atoms in the solid can be indicated by means of the ETA curves.

Chapter 4

RELEASE OF INERT GAS INCORPORATED WITHOUT PARENT IN SOLIDS

According to the method employed and the conditions of introducing the gas traces, it is possible to obtain samples in which the inert gas is distributed uniformly throughout the volume or located beneath the surface. The most common distribution profiles are:

(a) Homogeneous distribution which is usually obtained either by neutron irradiation generating inert gas atoms in the bulk of the solid, or in natural minerals containing inert gases of radiogenic origin.

(b) Distribution with a definite concentration profile beneath the surface (plane source, exponential, or peaked with an exponential tail) obtained by ion bombardment, diffusion or recoil techniques of labeling.

In this chapter the inert gas release with regard to the most common cases of gas distribution in the sample will be analyzed.

Release of the inert gas incorporated without parent in a solid can be caused by a number of processes, such as diffusion, instability of the surface, annealing of lattice damage during heating, evaporation of surface layers, recrystallization or phase changes, and chemical reactions of labeled sample, etc. For the sake of simplicity we shall first deal with a sample where neither chemical nor physical transformations occur during heating over the temperature range considered. Fractional release, F, or release rate, dF/dt, are most commonly measured in experiments where the inert gas release is studied. The heating at various temperatures for a definite time, so-called isothermal step-heating or isochronal heating, or the heating in conditions of increasing temperature are usually employed.

4.1. Kinetics of inert gas release

As inert gases are practically insoluble in solids, one expects a gas concentration gradient between the bulk and the surface of the sample as long as the sample is not completely exhausted. The time dependence of the inert gas concentration is given by Fick's 2nd law, and as the concentration of the gas may change by decay of the inert gas atoms, the following differential equation can be written:

$$\partial c/\partial t = D\nabla^2 c - c\lambda t \tag{54}$$

where c is the gas concentration, ∇^2 Laplace operator, λ is the inert gas decay constant, and t is the time. Inthoff and Zimen[144] solved this equation for the appropriate boundary conditions and the homogeneous distribution of the gas within the sample.

4.1.1. Homogeneous gas distribution

For the case of homogeneous gas distribution in an assembly of small grains

(diameter about 0.1 μm) a formula was derived[145] permitting the calculation of the release fraction, F, at any time, t,

$$F = A_t/A_\infty = 2(S/V)(Dt/\pi)^{1/2} \exp(-\lambda t) \qquad \text{for } F < 0.3 \tag{55}$$

where F is the amount of inert gas released after time t representing a fraction of the total amount of inert gas introduced into the substance, A_t is the activity of the gas measured at time t and A_∞ is the total activity taking into account the decay, λ is the radioactive decay constant, D is the diffusion coefficient, S is the surface of the sample grains, V is their volume, and $\exp(-\lambda t)$ is a decay correction term. The decay correction term can be omitted if the half-life of the inert gas is much greater than the duration of the experiment, $t_{1/2} \gg t$.

Equation (55) is valid for $F < 0.3$. Higher values, $F > 0.3$, require more involved expressions for F depending on the grain shape. For the case of a spherical grain, Inthoff and Zimen[144] derived the following expression, valid for all values of F:

$$F = 1 - (6/\pi^2) \sum_{n=1}^{\infty} (1/n^2) \exp(n^2\pi^2\alpha^2) \text{ for } 0 < F < 1 \tag{56}$$

where $\alpha^2 = (Dt/r_0^2)$, and r_0 is the radius of the spherical grain. Assuming values of $F < 0.3$ and using the parameter α, the following simplified expression is obtained:

$$F = 6\alpha/\pi^{1/2} \qquad \text{for } F < 0.3 \tag{57}$$

For higher values of F, the following useful approximation is obtained:

$$F = 1 - (6/\pi^2) \exp(-\pi^2\alpha^2) \tag{58}$$

Figure 31 shows the release fraction, F, related to parameter α, α being $(Dt/r_0^2)^{1/2}$. For $F < 0.3$, a linear dependence is expected as follows from eqn (57). Solutions for

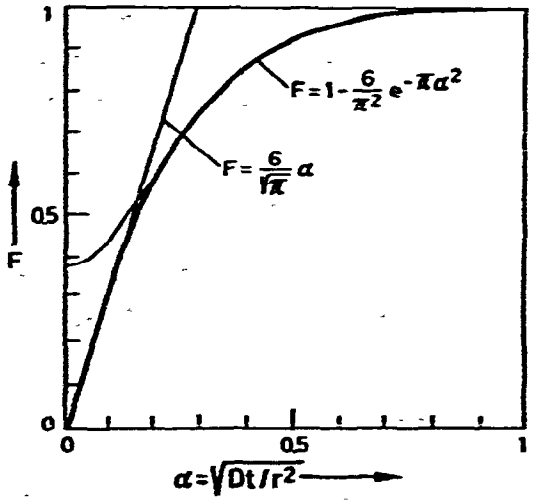

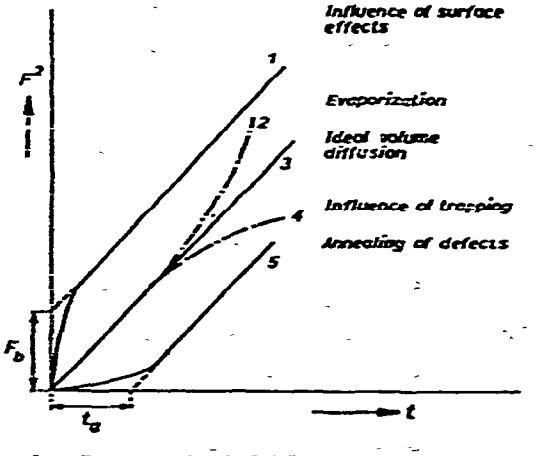

Fig. 31. Inert gas release as dependence of release fraction F versus $(Dt/r_0^2)^{1/2}$.

Fig. 32. Kinetics of inert gas release affected by various factors.

rectangular and cylindrical grain shapes were also derived by Inthoff and Zimen[144]. Lagerwall and Zimen[145] tabulated the function, $F = f(\alpha^2)$, for most of the common grain shapes. By plotting α^2 against t, the diffusion coefficient, D, can be evaluated from the slope.

The theoretical considerations and the above-reviewed expressions suppose an ideal volume diffusion mechanism of the inert gas release. A large number of gas release experiments did in fact follow this ideal diffusion pattern. However, most of the experimental work showed deviations. In the isothermal release curves, as a rule, more rapid release of the inert gas was observed in the first 5–10 min than would follow from the theoretical model given above. The authors explained this by the fact that the part of the solid close to the surface exhibits defects and structural anomalies. The imperfect structure of solid near the surface may further be disordered by the radiation damage caused by the inert gas incorporation. Felix[14] analyzed the factors effecting the ideal inert gas volume diffusion and distinguished four types of deviations of ideal gas release kinetics. Figure 32 shows the deviations on the $F^2 = f(t)$ diagram, assuming $F^2 < 0.06$. Curve 3 corresponds to the ideal non-disturbed kinetics of the inert gas release, where $F^2 \propto t$. Curves 1 and 2 correspond to diffusion influenced by surface effects, namely, the accelerated release at the beginning of the experiment. These so-called "burst effects" are characterized by a release fraction, F_b, at time $t = 0$ (curve 1) and the enhanced release caused by evaporation (curve 2). Curves 4 and 5 correspond to the diffusion hindered by gas trapping in the solid. Curve 4 demonstrates the changes of the ideal release kinetics caused by the presence of traps. Curve 5 shows the fraction of the gas released as a consequence of annealing the traps where the inert gas atoms have been collected. The hindering effect is characterized by a time, t_a.

Mathematically, these effects have been introduced in Fick's law by adding adsorption and desorption terms. A model of a quasichemical reaction between mobile gas atoms and a stable distribution of traps has been considered. Solutions of this problem were published by Hurst[146] in numerical and by Gaus[147] in analytical form. The authors proposed the following reaction between inert gas (G) and traps (T):

$$\text{gas mobile (G)} + \text{traps (T)} \underset{b}{\overset{\mu}{\rightleftarrows}} \text{gas trapped (GT)}.$$

We denote the concentration of the mobile gas atoms (G), equal to c, the concentration of trapped atoms (GT), equal to m, μ is the probability of trapping, b the probability of gas emission if the distribution of traps is uniform. By including the reaction rates, μ and b, and the fractions of mobile and trapped gas, c and m, respectively, into the differential diffusion eqn (54), we obtain:

$$\partial c/\partial t = D\Delta c - \mu c + bm \tag{59}$$

The initial fractions of mobile and trapped gas atoms at $t = 0$ are p_0 and q_0, respec-

tively, with $p_0 + q_0 = 1$. For such non-ideal release kinetics, eqn. (55) giving the fraction F of the released inert gas should be replaced by

$$F^2 = (4/\pi)(S/V)^2 [D/(1 + \mu/b)] (t - t_a) \quad (60)$$

This means that for the case of the "burst" release at the beginning of the experiment, the value of $t_a > 0$, and for the case of a hindered release, $t_a < 0$. The value, t_a, depends on the probability μ of trapping and the probability b of emission as well as on the initial concentrations of mobile and trapped gas atoms p_0 and q_0.

After a certain time ($t \gg t_a$) of inert gas release at a definite temperature, when a thermal equilibrium is reached, the differential equation is reduced to the simple Fick type (cf. eqn (55)) but with D_{app}, which is smaller than D for undisturbed diffusion

$$D_{app} = [D/(1 + \mu/b)] \quad (61)$$

Thus, regardless of the initial conditions of the experiment, reliable diffusion coefficients can be evaluated when thermal equilibrium is reached. This theory was found suitable for inert gas release evaluation in most solids labeled homogeneously by inert gas without the parent making possible the calculation of the diffusion coefficient, D, from experimentally obtained F values at constant temperature. For evaluation, it is convenient to use the graphical representation of $F = f(T)$ or $F = f(\sqrt{t})$. Table 10 shows some ways recommended by Felix[14] for the evaluation of F.

Figure 33 shows F plotted against $\sqrt{(t - t_i)}$ for a step-wise heating experiment according to Lagerwall and Schmeling[148] in which t_i is the time at which the temper-

TABLE 10

SOME WAYS FOR THE EVALUATION OF D

Type of release kinetics	*Experiment diagram used*	*Procedure for D evaluation*
Ideal volume diffusion and stepwise heating (curve 3, Fig. 32)	$F^2(t)$	Slope of any part of the diagram is proportional to D
Volume diffusion hindered by presence of traps at the beginning of the experiment (curve 5, Fig. 32)	$F^2(t)$	Slope of the linear part of the diagram proportional to D
Overlapping of volume diffusion and "burst effect" at the beginning of the experiment (curve 1, Fig. 32)	$F(\sqrt{t})$	Slope in the linear part is proportional to D
Step-wise heating overlapping processes in the first temperature step (T_1) (Fig. 32)	$F(\sqrt{(t - t_i)})$	for T_1: Slope in the linear part proportional to D for T_2 and higher: Slope of the asymptote to the curve is proportional to D

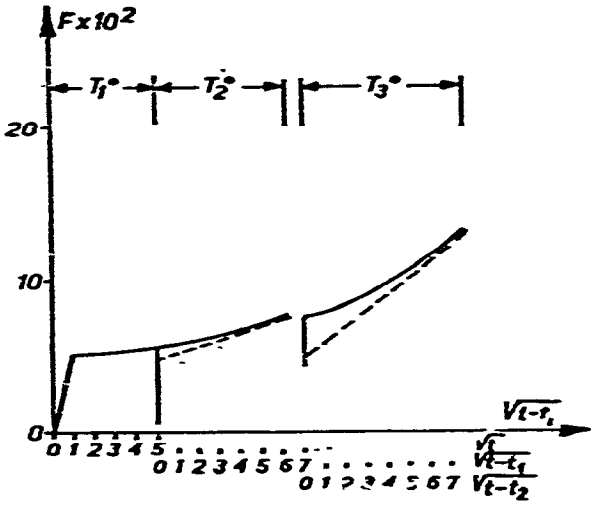

Fig. 33. Ideal inert gas release plotted as F against $\sqrt{(t - t_1)}$ superimposed by one single "burst", at the beginning of the anneal.

ature is changed. It represents the case of an initial burst at temperature T_1 but no burst release at T_2 and T_3.

4.1.2. Non-homogeneous gas distribution

In cases of a plane source, an exponentially decreasing profile, a linearly decreasing gas distribution, and a peak distribution with an exponential tail, which are important with ion bombardment labeling, were thoroughly analyzed by Kelly et al. and Matzke[149–152]. The cases of linearly decreasing and rectangular profiles, which occur in recoil doping technique of labelling, were theoretically treated by DiCola and Matzke[153] and the linearly decreasing distribution by Mears and Elleman[154]. Kelly and Matzke[152] used the diffusion equations modified by Hurst[146] and Gaus[147] but treated the problem using the discrete diffusion theory developed by Kelly[150, 155]. This theory involves making time continuous but space discrete. According to the authors, it is in principle better suited for discrete media such as the crystal lattice than conventional diffusion theory (both time and space continuous) or random walk (both time and space discrete).

Kelly and Matzke[152] denoted the concentration of gas in the presence of the trapping effect by c, the concentration of permanent traps by m (both in fractional units), and the diffusion length for permanent trapping L (in atomic layer spacing units a). The concentration of gas c and of traps m related to the distance from the surface can be either differential or integral, the relationship between the two forms being $C^{\text{diff}} = -(\partial/\partial x)\, C^{\text{int}}$. They[152] defined the diffusion coefficient D as

$$D = 1/2\, k\, a^2\, (1 - f) \approx 1/2\, k\, a^2 \tag{62a}$$

and the diffusion path L as

$$L^2 = (1 - f)/(6f) \approx 1/(6f) \quad (62b)$$

where $k = k_0 \exp(-\Delta H/RT)$ is the diffusion rate constant defined as the rate of jumping along a given line, f is the atomic fraction of atom-size traps, and a is the atom layer spacing. It is of interest to note that the conventional diffusion theory by Hurst[146] gives a value of L^2 twice as high. Diffusion coefficient D and diffusion trapping length L are defined by Kelly and Matzke[152] in a more fundamental atomic parameter, namely in the atom layer spacing a (denoted by the authors as λ). The mean atomic spacing a is equal to $(M/\rho N_0)^{1/3} \approx 0.25$ nm, where M is the molecular weight, ρ the density and N_0 Avogadro's number.

The following equation describing diffusion with both permanent and weak trapping for unidimensional gradient was proposed[152]

$$\partial c/\partial t = (D/a^2)(\partial^2 c/\partial t^2) - (D/L^2a^2)c + bm \quad (63a)$$

$$\partial m/\partial t = (D/L^2a^2)c - bm \quad (63b)$$

where c is the concentration of mobile gas atoms, m is the concentration of gas in traps, b is the rate of detrapping and L is the diffusion trapping length or the spacing of the trapping centers.

Solution of eqn (63a) gives appropriate expressions[152] for the fractional release in the absence of trapping (F_1), and the fractional release in the presence of permanent trapping (F_2). By solution of eqn (63b), the fraction of permanent traps F_m was evaluated[152].

Expressions for F_1 considering different gas concentrations profiles and the ideal volume diffusion kinetics are listed in Table 11. For expressions of F_2 and F_m assuming the trapping behavior we recommend the original paper of Kelly and Matzke[152]. In Table 11, z^2 stands for $(Dt/\bar{R}^2)$ where $\bar{R}$ denotes the range of the gas which is the limit in penetrations in the cases of a plane source, a rectangular and a

TABLE 11

EXPRESSIONS FOR FRACTIONAL RELEASE (F_1) CONSIDERING VARIOUS GAS CONCENTRATION PROFILES

Geometry	$F_1 = f(z)$; $z^2 = Dt/R^2$	*Ref.*
plane source	$\operatorname{erfc}(1/2z)$	150
peak distribution with exponential tail	$1 - 2z/\pi^{1/2} - (1 - 2z^2)\exp(z^2) \cdot \operatorname{erfc}(z)$	151, 152
exponential	$1 - \exp(0.480z^2)\operatorname{erfc}(0.480z^2)^{1/2}$	149, 152
linearly decreasing	$1 - \{(2z^2 + 1)\operatorname{erfc}(1/2z) + 2z/\pi^{1/2} \cdot [\exp(-1/4z^2) - 2]\}$	153, 154
rectangular	$2z/\pi^3 \cdot \{1 - \exp(1/4z^2)\} + \operatorname{erfc}(1/2z)$	153, 154

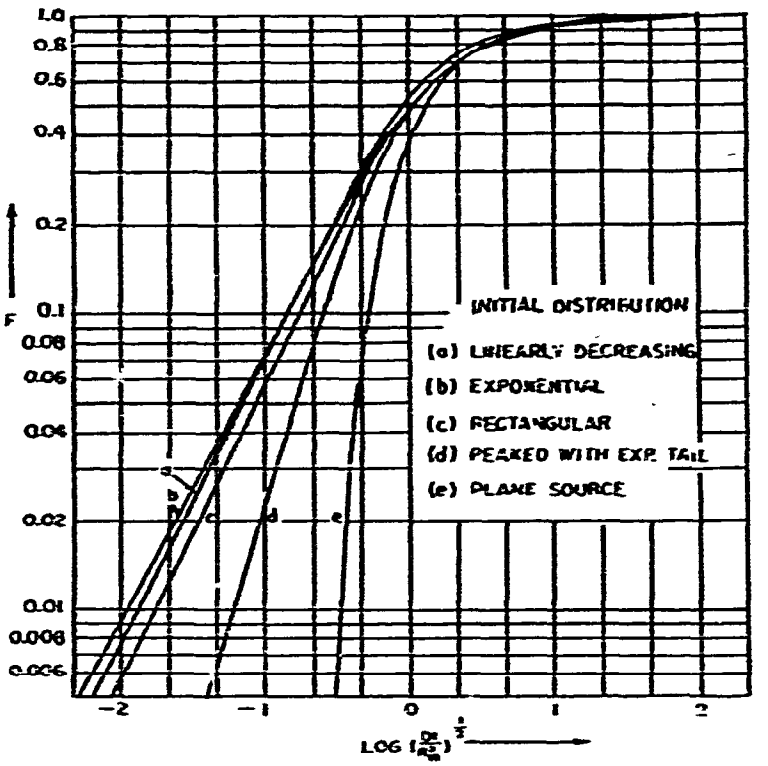

Fig. 34. Theoretical fractional release curves for different initial gases distributions as listed in Table 11.

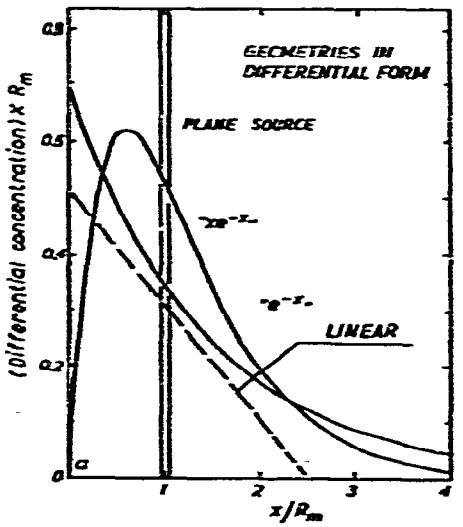

Fig. 35. Idealized concentration profiles suited for ion bombardment, recoil and diffusion techniques of labeling.

linearly decreasing concentrations profile. In the case of a peak distribution with an exponential tail, the most probable or peak range R_p is to be used; with exponential distribution, the median range R_m is to be used. Figure 34 shows the results plotted in bilogarithmic scale as $F = f(z)$, z^2 being (Dt/R^2).

Theoretically, the inert gas distribution in ion bombarded solids will be determined by the energy of bombarding ions, and by properties of the solid such as atomic mass, type of lattice, crystallinity, lattice defects, etc. The gas distribution also depends on whether the solid is amorphous, polycrystalline or monocrystalline, as well as on the dose of gas ions applied.

Figure 35 shows differential forms of four idealized concentration profiles, suited for most cases of ion bombardment, recoil labeling and diffusion labeling:

(a) Plane source assuming inert gas concentration in the vicinity of R_p, the most probable or peak range. It is suitable for example (i) for low and high mass solids with very low bombardment energies (1 keV) so that R_m equals only 1 or 2 atomic layers. It is also a possible representation of (ii) low-mass solids at very high bombardment energies (300 keV)[91, 102] and (iii) for amorphous solids where the distribution is generally compact due to the absence of chanelling[102].

(b) Peaked with an exponential tail distribution (or "$x \cdot e^{-x}$"), where the theoretical most probable 50% range is given by $R_m = 1.68\ R_p$. This geometry is suitable, for example, for polycrystalline material labeled by gas ions at energies where R_m equals roughly 2 to 10 atomic layers as can be seen from the differential distribution curves of 2–100 keV Rn in aluminium[102] (cf. Fig. 11).

(c) Exponential (or "e^{-x}") distribution is suitable (i) for polycrystalline solids and bombardment energies such as $R_m \geq 10$ atomic layers[102, 156, 157] and (ii) for some solids labeled with diffusion technique[105] and many cases of diffusion which can be attributed to "bubble diffusion"[158].

(d) Linearly decreasing distribution is suitable for solids labeled by recoil technique[151] and in some cases for diffusion technique[105].

(e) When high energy bombardments are used for labeling fine powders or with alpha Rn recoil or fission Xe recoil, the concept of a homogeneously labeled sphere[152] can be used. Equation (56) is applicable in this case.

In most cases actual distribution lies between these idealized cases. With exponential or linearly decreasing distribution, most of the gas is close to the surface. It can be seen from Fig. 34 that with D and R_m constant, most of the releases occur within a short time. With peaked distributions and especially with a plane source, the gas is deeper in the solid. Hence, the release corresponding to the undisturbed volume diffusion starts at higher values of t. On the other hand, the exponential distribution contains some gas very deep in the solid, thus the values of F are not reached before high values of t are attained.

4.2. Inert gas release during non-isothermal heating

In this section the fractional release F obtained in step-wise isochronal experi-

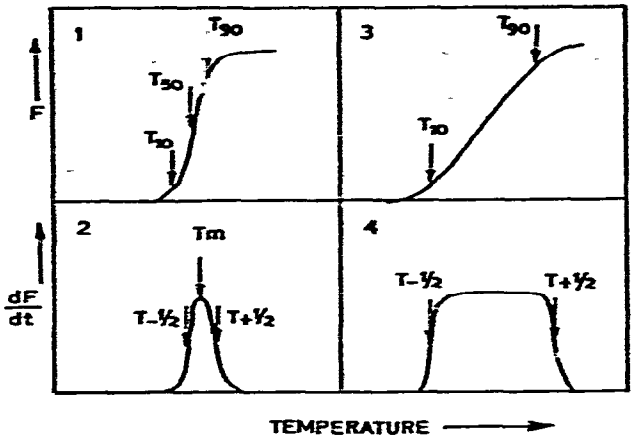

Fig. 36. Temperature-dependence of fraction release F (curves 1 and 2) and of release rate dF/dt (curves 3 and 4).

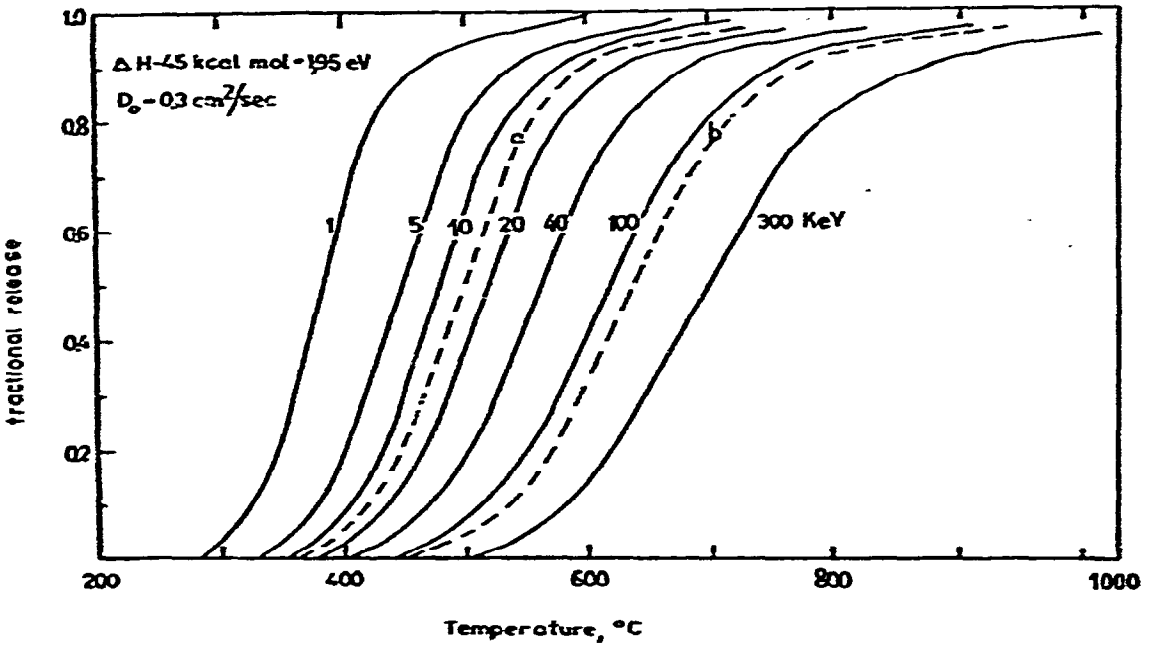

Fig. 37. Theoretically expected release curves for volume diffusion process with $\Delta H = 1.95$ eV = 226 kJ mol^{-1}. The full curves are for $D_0 = 0.3$ cm^2 s^{-1} and bombardment energies of 1, 5, 10, 20, 40, 100 and 300 keV, assuming a linear relation between energy and median range of the ions. The dotted (curves (a) and (b)) are for 40 keV and $D_0 = 0.03$ and 3 cm^2 s^{-1}.

ments and the release rate dF/dt obtained under conditions of linearly increasing temperature will be analyzed. Fig. 36 shows the temperature dependence of the fractional release, F, (curves 1, 2) and of release rate, dF/dt, (curves 3, 4). Curves 1 and 3 describe a process with one discrete value of the activation enthalpy of diffusion. Curves 2 and 4 describe a process with a uniform spectrum of activation enthalpies. The exponential distribution of inert gas in the solid and absence of trapping effects

are supposed in all cases. The $F = f(T)$ curves show the expected basically sigmoid shapes. The curves can be regarded as being characterized by the temperatures for 10, 50 and 90% release. The dF/dt curves show the expected basically peaked shapes for discrete values of activation enthalpy. The curves can be characterized by the temperatures, $T_{-1/2}$, $T_{+1/2}$ and T_m, which denote the half-heights and the maximum temperature of the peak, respectively.

As was shown in the paragraph 4.1., the release curves strongly depend on the median range, R_m, of bombarded ions in the solid. Figure 37 shows some theoretically expected release curves predicted by Matzke et al.[159] for a volume diffusion with a discrete value of ΔH (45 kcal mol^{-1}) assuming an exponential distribution profile and $D_0 \approx 0.3$ cm^{2}sec^{-1}. Increasing the bombardment energy (1, 5, 10, 20, 40, 100 and 300 keV) shifts the release curves towards higher temperatures (for these calculations a linear relationship between R_m and energy was assumed). Simultaneously, the release curves cover a wider temperature interval. The two dotted curves a and b show the effect of change in D_0 (both curves are for 40 keV but for $D_0 = 0.03$ and 3 cm^{2}sec^{-1}, respectively). Varying the annealing time is expected to yield a similar shift in temperature. Similar shifts occur in the peaks of the dF/dt curves. For comparison of the F–T and (dF/dt)–T plots, we can suppose that a linear temperature increase of 10 K per 60 sec corresponds to a stepwise heating with a 60 sec annealing time. More complex F–T diagrams are obtained when the inert gas release is governed

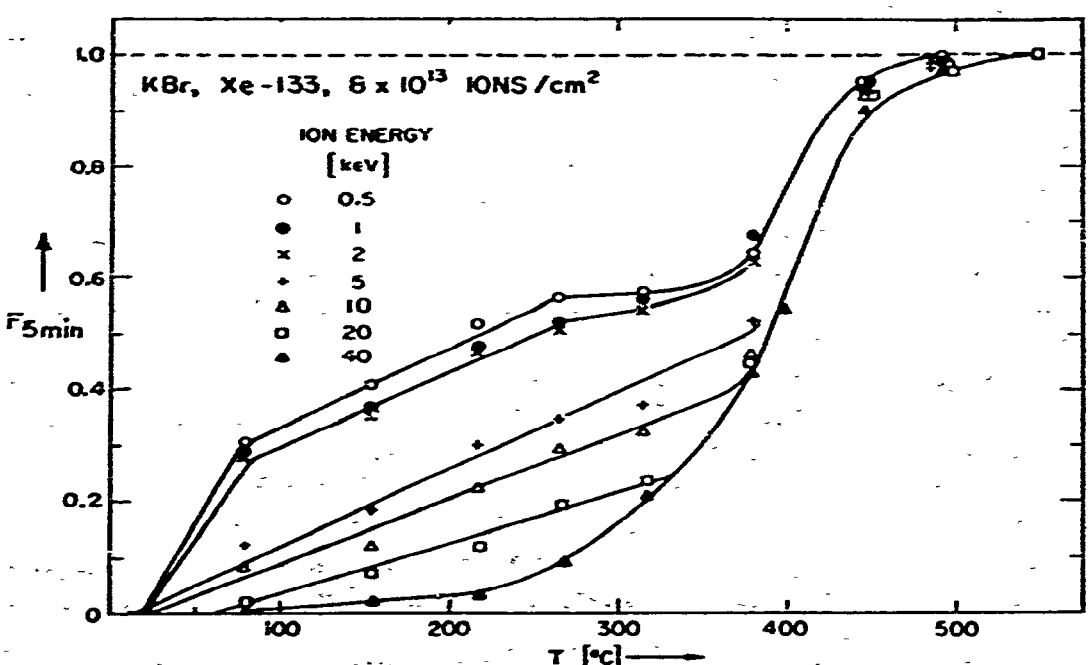

Fig. 38. Isochronal release of ^{133}Xe from KBr single crystals following ion bombardment to a dose of 4×10^{13} ions per cm^2. By varying the energy of the incident ion beam between 0.5 and 40 keV the effect of surface proximity on gas release at low temperature is shown.

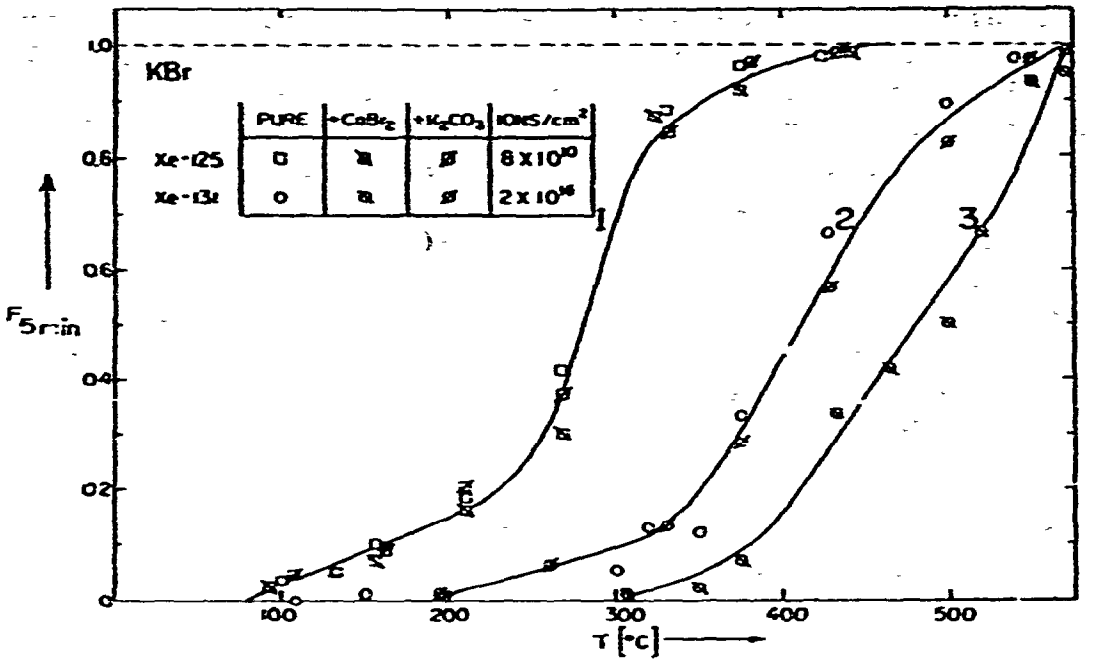

Fig. 39. Isochronal release of ^{125}Xe (low dose of 8×10^{10} ions per cm^2) and ^{131}Xe (high dose of 2×10^{16} ions per cm^2) from pure and doped KBr single crystals.

by trapping and mechanisms other than normal volume diffusion. Selected examples of such release behaviors are shown in Figs. 38 and 39.

Figure 38 shows the *F–T* curve of ^{133}Xe release from KBr single crystals following ion bombardment with a dose of 4×10^{13} ions per cm^2. By varying the energy of the incident beam between 0.5 and 40 keV, Matzke[160] proved the effect of surface proximity on the gas release at low temperature. It can be seen that with decreasing energy a decreasing percentage of the gas is released at temperatures below 230°C (503 K) which corresponds to 0.5 melting point on the absolute temperature scale. At an energy of 40 keV, this release at low temperatures is negligible and the curve represents the normal volume gas diffusion which occurs for most materials at temperatures compatible with self-diffusion. When the inert gas release occurs at temperatures well below that for normal diffusion, it is supposed that the inert gas release is subject to the effect of diffusion along boundaries or diffusion pipes and release due to excess point defects, etc. This type of release process has been called "damage diffusion". The low temperature xenon release from KBr seems to be due to the proximity of gas to the surface rather than to damage and annealing only. In some experiments a shift of the sigmoidal release curve to higher temperatures can be observed. This retarded release indicates a trapping of the inert gas on defects in the solid.

Figure 39 shows *F–T* curves of pure and doped KBr single crystals. The ion energy in these experiments was kept constant at 40 keV to avoid influences of surface proximity. Using a very low dose (8×10^{10} Xe ions per cm^2) Matzke[160] stated that

TABLE 12

VALUES A IN eqn (64)

Distribution	$F = 0.1$	$F = 0.5$	$F = 0.9$
plane source	78.8	75.2	68.5
xe^{-x} (peaked with exponential tail)	80.9	75.2	67.9
e^{-x} (exponential)	83.3	75.5	67.2
linearly decreasing	91.2	83.7	75.9
rectangular	86.8	76.5	70.7
sphere with radius r_0	89.3	82.2	78.8

the gas release corresponds to normal volume gas diffusion for all three materials: pure KBr, doped with 200 ppm K_2CO_3 and doped with 500 ppm $CaBr_2$ (curve 1). At higher ion doses (2×10^{16} Xe ions per cm^2) the release is retarded, i.e., is shifted to higher temperatures (curve 2). The effect is more pronounced in the specimen doped with $CaBr_2$ (curve 3).

4.2.1. Approaches to evaluate release curves of the F–T type

(a) For analyzing experimental release data of ion bombarded solids, it is often convenient that F be made explicit in $\Delta H/T$. A correlation between the activation enthalpy ΔH and some recognized temperature T can then be found. Kelly and Matzke[152] gave relations for cumulative gas release at $F = 0.1$, 0.5 and 0.9, assuming various gas distributions and geometries. The general form of these relations is

$$\Delta H/T = (A \pm 5) + 4.6 \log_{10} t/R_m^2 \qquad (64)$$

where ΔH is in cal mol^{-1} (4.187 J mol^{-1}), R_m the median range is in units of atomic spacings a, t the annealing time a given temperature in minutes, and A a constant which depends on the geometry and F values. The uncertainty of ± 5 arises from the assumptions of D_0 values ($3 \times 10^{-1 \pm 1}$ cm^2 s^{-1}); this range of values agrees well for metals and quite well for halides and oxides with diffusion literature[151]. The different values of A are given in Table 12. The values obtained for ΔH differ only slightly for various geometries and shapes of the distribution curves. The relations are valid under the assumption that the values of F correspond to a normal diffusion mechanism only and are not perturbed by damage diffusion or trapping.

For experiments conducted with step-heating, the width of a gas release peak was defined by Kelly et al.[151] as the difference between the temperatures for 90 and 10% release, i.e., T_{90}–T_{10}, and can be estimated by rearranging the $\Delta H/T$ formulas of eqn (64) and Table 12.

(b) Another approach to evaluating the release data was proposed by Matzke[160]. Is is based on the relation between F and (Dt/R_m^2) and is shown in Fig. 34. Using the respective curve according to the distribution geometry, it is possible to read the D values corresponding to each F value. By plotting these data with the Arrhenius

equation, $D = D_0 \exp(-\Delta H/RT)$, both ΔH and D_0 can be found. This approach does not assume a value for D_0. The experimental errors of this method can easily be obtained by a least square fit.

(c) Pronko and Kelly[162] used a relation for retained gas to evaluate D, ΔH and D_0 from the experimental release data.

In the case of an exponential initial distribution, the following expression was proposed for the fraction of gas retained after annealing:

$$(1 - F) = \exp(Dt/R_m^2)\,\mathrm{erfc}\,(Dt/R_m^2)^{1/2} \tag{65}$$

where F is the fractional gas release, D is the diffusion coefficient, t is the annealing time and R_m is the mean range. A plot of $(1 - F)$ plotted against Dt/R_m^2 was used to determine the actual value of D. The error in D as a result of this approach was less than 10%. The values of the activation enthalpy, ΔH, and diffusion constant, D_0, can be obtained from the Arrhenius equation.

4.2.2. Approaches to evaluate release curves of the (dF/dt)–T *type*

Various approaches to evaluate the temperature dependence of the release rate, dF/dt, for a linear rise of temperature are given in papers by Redhead[163], Carter[164], and Kelly and Matzke[152].

Redhead assumed that the release of gas lying close to the surface occurs in one jump, i.e., by the mechanisms of diffusion with a definite activation enthalpy, ΔH. Assuming that the desorption is a reaction of the first order, the rate of gas release can be expressed in differential form as

$$-(dN/dt) = \nu \cdot N \cdot \exp(-\Delta H/RT) \tag{66}$$

where N is the number of atoms trapped in a unit surface, ν is a constant (the frequency of oscillation of atoms in the lattice is assumed to equal $10^{-13}\ s^{-1}$) ΔH the activation enthalpy of the inert gas, and R is the molar gas constant equal to 8.3143 $JK^{-1}\,mol^{-1}$. A linear rise of temperature ($T = T_0 + \beta t$, where β is the heating rate) and ΔH independent on N was also assumed.

By differentiating expression (66) and equating it to zero, the following expression for T_{max} was obtained:

$$\Delta H/RT_m = (\nu/\beta)\exp(\Delta H/KT_m) \tag{67}$$

and

$$\Delta H/T_m = \ln(\nu T_m/\beta) - 3.64 \tag{68}$$

The value of the activation enthalpy, ΔH, can be determined directly from the experimentally found temperature of the maximum, T_m, (see Fig. 40). The relationship between ΔH and T_m over the given temperature range is close to linear[163, 164].

Kelly et al.[152] derived on the basis of their theory for constant temperature[149], a similar formula taking into account different gas distribution profiles in the sample and different types of diffusion.

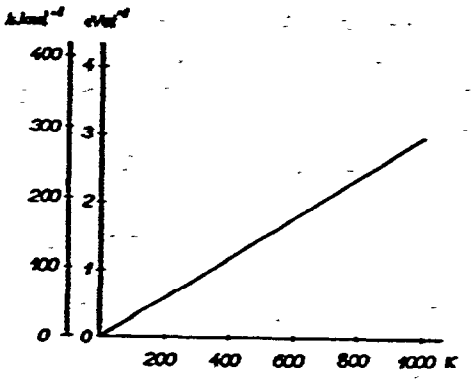

Fig. 40. The relationship between activation enthalpy, ΔH, and maximum temperature T_m on the release curve $dF/dt = f(T)$ (see eqn (68)).

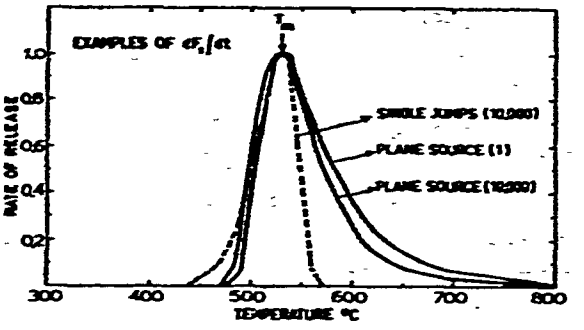

Fig. 41. Examples of inert gas release peaks, $dF/dt = f(T)$, for linearly increasing temperature. Curves are given for true diffusion of a plane source and for single jump diffusion with discrete ΔH. all cases with $T_m = 530$°C and with the values of $T_m/B^2\beta$ (in sec) as indicated in brackets.

TABLE 13

VALUES OF A IN eqn (69) AND B AND C OF eqn (70)

Distribution profile or type of diffusion	*A for* $d^2F/dt^2 = 0$	*B*	*C*
plane source	69.5	0.0935	0.0063
$x \cdot e^{-x}$	68.3	0.138	0.0092
e^{-x}	67.5	0.175	0.0117
single jump diffusion with discrete ΔH	69.5	0.0673	0.0044
sphere with radius r_0	73.2	—	—

The (dF/dt) curves generally exhibit peaks, the maxima (T_m) of which are governed mainly by the value of ΔH (one exception is a single jump diffusion with a uniform spectrum of ΔH's where, according to Grant and Carter[165] there is no maximum). Figure 41 gives examples of these peaks and shows that the shapes depend markedly on the type of diffusion and on the heating rate β and the median or 50% range, R_m. The (dF/dt) curves for linearly increasing temperature are given for ideal volume diffusion (without trapping) of a plane source and for single jump diffusion with discrete ΔH, in all cases with $T_m = 530$°C and with the value ($T_m/R_m^2 \cdot \beta$ (in s)) as indicated in parentheses. The values of $T_m/R_m^2 \cdot \beta$ from 1 to 10.000 are typical for the usual experimental conditions with ion bombardment labeling where it is assumed that $R_m = 1$ to 100 mean atomic spacings and $\beta = 5$ to 20 K min^{-1}. The expression given by Kelly and Matzke[152] for $\Delta H/T_m$ is

$$\Delta H/T_m \simeq (A \pm 5) + 4.6 \log_{10} T_m/R_m^2 \cdot \beta \qquad (69)$$

where the activation enthalpy, ΔH, is given in cal mol^{-1} (where 1 cal mol^{-1} =

4.187 J mol^{-1}) and the heating rate β in K min^{-1}. Constant A depends on the distribution profile and the diffusion type. Values of A are listed for different distribution profiles and diffusion types in Table 13. R_m is the median range in units of atomic spacings a, which for a single jump mechanism equals 1 and for a sphere is taken as the radius r_0. The uncertainity of ± 5 arises from the assumption of D_0 values ($D_0 = 3 \times 10^{-1 \pm 1}$ $cm^2 s^{-1}$).

Peak width. As can be seen from Fig. 41, the widths of the peaks depend mainly on the character of the gas distribution. The narrowest (within a temperature range 60–100°C) corresponds to a single jump mechanism and, while a wider peak was obtained with a plane source, the width of the peaks being increased with the median range R_m. Kelly et al.[161] defined the width of a gas release peak under conditions of linearly increasing temperature as the width at half-height, $\Delta T_{1/2}$. The expressions for $\Delta T_{1/2}$ can be written in general form as follows:

$$\Delta T_{1/2}/T_m = B - C \cdot \log_{10} T_m \cdot D_0/R_m^2 \cdot \beta \, 0.3 \qquad (70)$$

where T_m is the maximum temperature, R_m the median range in units of atomic spacings a, β the heating rate in K min^{-1}, and D_0 is assumed to equal $3 \times 10^{-1 \pm 1}$ $cm^2 s^{-1}$. B and C are constants which depend on the geometry. Different values of B and C are given in Table 13 for various shapes of the distribution curves.

Estimation of errors. The evaluation of ΔH based on Kelly's theory is subject to a number of errors. The first error, of a minor nature (of the order of 8 to 12 kJ mol^{-1}), is caused by the uncertainty in the penetration depth and as to whether the distribution profile is exponential or peaked. Secondly, estimated by the authors as the greatest error, is the use of an idealized range of values for D_0. The range taken, $D_0 = 3 \times 10^{-1 \pm 1}$ $cm^2 s^{-1}$, is obeyed closely in metal diffusion[151] and also applies moderately well to self-diffusion in the ionic crystals as alkali halides.

The formulas for $\Delta H/T$ reviewed above concern unperturbed volume diffusion. Other processes, namely trapping of the gas on the lattice defects or interaction between inert gas atoms, may occur in the solid as it is heated, and give rise to slight shifts in release temperature. This can be a third source of errors (of the order of 29 to 40 kJ mol^{-1}). A precaution should therefore be taken when ΔH values obtained from the experimental release data are compared with other inert gas release data, in comparison with self-diffusion and with the discussion of diffusion mechanism.

4.2.3. Temperature-dependence of diffusion

Norgett and Lidiard[166] gave a complete description of the temperature-dependence of gas diffusion with interaction of point defects in the extrinsic and intrinsic region of defects induced by radiation. They assumed the inert gas atoms to be interstitially incorporated in the crystal lattice and to diffuse via random walk interrupted by the trapping of these gas atoms in various imperfections existing in the crystal lattice. The same authors have calculated the energies of migration and trapping of the inert gas on the basis of the extended classical Born model of an ionic

crystal[167]. Like Hurst[146] and Gaus[147], the authors interpreted the interaction of the atoms and lattice defects as a quasi-chemical reaction

$$G + T \rightleftarrows GT \tag{71}$$

where G signifies the mobile gas, T the traps of various types, and GT the immobile gas.

The equilibrium partition of the gas atoms between mobile and immobile sites is considered here. The simple case of undisturbed (untrapped) diffusion can be written as

$$D = D_0 \exp(-Q_m/RT) \tag{72}$$

where Q_m is the activation energy for the fundamental diffusion process, D_0 is the diffusion constant, and R is the gas constant.

If the gas can be trapped, and the average probability p of gas atoms remain untrapped, the apparent diffusion coefficient observed experimentally can be written as

$$D_{app} = p\,D \tag{73}$$

The probability p is given as the fraction of the untrapped gas atoms and was calculated by Norgett and Lidiard[167] with the help of the mass action law as

$$p = G/(G + GT) \tag{74}$$

Two limit cases can be distinguished:

(i) constant trap concentration (extrinsic region);

(ii) thermal equilibrium of traps (intrinsic region).

In the first case a crystal containing a small fixed concentration of traps is assumed, which in principle can involve a number of j types.

The probability p can than be written as

$$p = 1/\left[1 + \sum_{j=1}^{n} (c_j/k_j^0) \exp(-Q_{Bj}/RT)\right] \tag{75}$$

where c_j is the molar fraction of traps of the j-th type, k_j^0 is the pre-exponential factor of the trapping equilibrium constant which for the j-th type of trap is equal to $k_j = k_j^0 \exp(-Q_{Bj}/RT)$, and Q_{Bj} is the binding energy between gas atoms and the lattice traps of the j-th type. Under the simplifying assumption of the traps of the i-th type being predominant in the crystal in the concentration c_i, D_{app} can be expressed by

$$D_{app} \approx (D_0 k_i^0/c_i) \exp[-(Q_{M,i} + Q_{B,i})/RT] \tag{76}$$

where k_j^0 is the pre-exponential factor of the trapping equilibrium constant. In this case the apparent diffusion coeffiient D_{app} has a temperature dependence involving an activation enthalpy which is the sum of the activation energy for simple interstitial diffusion and a contribution for the binding energy into the trap. In the second case the traps are supposed to be present in a thermal equilibrium and their concentration c_i is given by

$$c_i = c_i^0 \exp(-Q_{F,i}/RT) \tag{77}$$

where Q_F is the formation energy of traps of the i-th type. In this case the concentration of the traps increases with temperature:
If $Q_{F,i} > Q_{B,i}$ the diffusion coefficient is given by eqn (72),
if $Q_{B,i} > Q_{F,i}$ the diffusion coefficient is

$$D_{app} \approx (D_0 k_i^0/c_i^0) \exp[-(Q_M + Q_{B,i} - Q_{F,i})/RT] \tag{78}$$

The observed activation enthalpy for diffusion thus involves the formation energy of the traps.

In the intrinsic region (traps in thermal equilibrium) a simple Arrhenius type equation is valid, however, with an activation enthalpy slightly larger than the value for pure undisturbed diffusion, corrected by the difference between the binding energy of the gas in the trap and the formation energy of the trap itself. The expressions for the apparent diffusion coefficient, D_{app}, are correct if this equilibrium is established rapidly compared with the rate of inert gas diffusion. This condition was fulfilled in many experiments. Figure 42 shows the possible diffusion curves with inert gas trapping. Curve 1 corresponds to the undisturbed (untrapped) diffusion mechanism with an activation energy, Q_m. The trapping occurs either when the binding energy, Q_B, exceeds the energy of formation, Q_F, of defects (curve 3), or, at low temperatures ($T < T_0$) when there is a fixed concentration of trapping centres associated with radiation damage of heterovalent ions (curve 2). At higher temperatures ($T > T_0$) the term $\exp(Q_B/RT)$ decreases and this corresponds to the release of gas atoms from the traps. At low temperatures, the activation energy is $(Q_M + Q_F)$, which at high temperatures decreases to Q_m. Similar diffusion curves were obtained by Mears and Elleman[168] who assumed a mobile cluster diffusion mechanism for inert gas. In this case, the inert gas atom is assumed to move with a defect cluster through the lattice

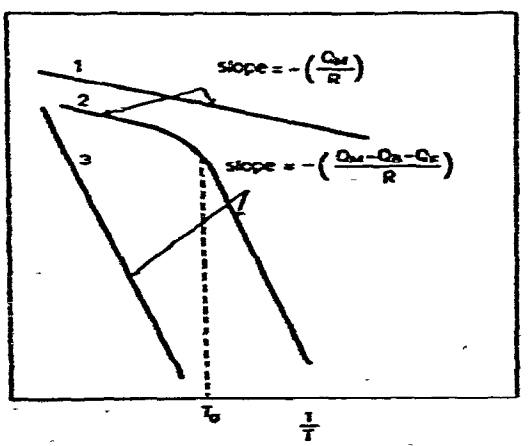

Fig. 42. Possible inert gas diffusion curves with gas trapping. Curve 1 corresponds to the untrapped diffusion mechanism with an activation energy Q_m, curves 2 and 3 correspond to the diffusion mechanism with trapping.

and becomes immobilized when the cluster dissociated. The various mechanisms for inert gas diffusion in solids are discussed in paragraph 4.4.3.

4.3. Factors influencing the mobility of inert gas in solids

Numerous experimental results showed that the mobility of inert gas in solids is influenced by various types of radiation damage and their annealing, proximity of the gas to the surface, impurities, gas concentration and other factors. The importance of such individual factors depends on the labeling technique (reactor irradiation, recoil doping, ion bombardment, diffusion technique, etc.) applied. The factors influencing the mobility of inert gas will be critically discussed in this section in the attempt to help investigators in evaluating and analyzing the inert gas release measurements. Inconsistencies in inert gas diffusion data reported in the literature by various authors can mostly be explained by these factors.

4.3.1. Natural crystal defects

Eileman et al.[169] showed that the natural defects of the crystal lattice influence the mobility of Xe in CsI homogeneously labeled with ^{133}I. The "natural defects" were introduced into single crystals of CsI by using a high growing speed or by oscillating the melt temperature during the production of the crystals. These natural defects consist most likely of small voids or dislocation loops.

Radioactive inert gas collected in open pores and microcracks of the specimen will, of course, be easily released by heating and this release has accelerated kinetics. Similarly, grain boundaries permit a higher diffusion rate than does the lattice[148]. The gas atoms located in grain boundaries are likely to leave the specimen upon heating before temperatures corresponding to a volume diffusion. Contrary to the homogeneous labeling, in most ion bombardment or recoil labelings, the "short circuiting" of inert gas by natural defects is considered to be unimportant. The reason is, that for ion bombardment labeled solid, the diffusion distance is much shorter (order of magnitude 10 nm) than the spacing of various pre-existing defects, grain boundaries, dislocations, lines, pores, etc. (order of magnitude μm)[151]. In diffusion technique labeling the release of inert gas atoms is supposed to be influenced by the presence of natural defects[105]. With a single crystal specimen, the grain boundary effects are supposed to be absent.

4.3.2. Impurities

Numerous investigators have shown that impurities present in the lattice which change the concentration of cation or anion vacancies may influence the mobility of inert gases. The influence on gas mobility depends on the gas diffusion mechanism. For instance, it was observed that impurities influenced inert gas mobility in solids labeled by ion bombardment or reactor irradiation when higher ion or neutron doses were applied.

Matzke[170] studied the release of xenon from pure ThO_2, ThO_2 + 0.1 mol %

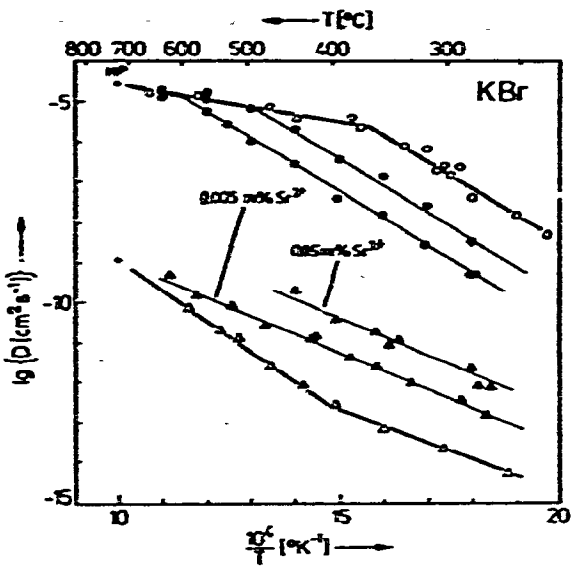

Fig. 43. Influence of Sr^{2+} doping in KBr on Ar-release from KBr (cf. ref. 171).

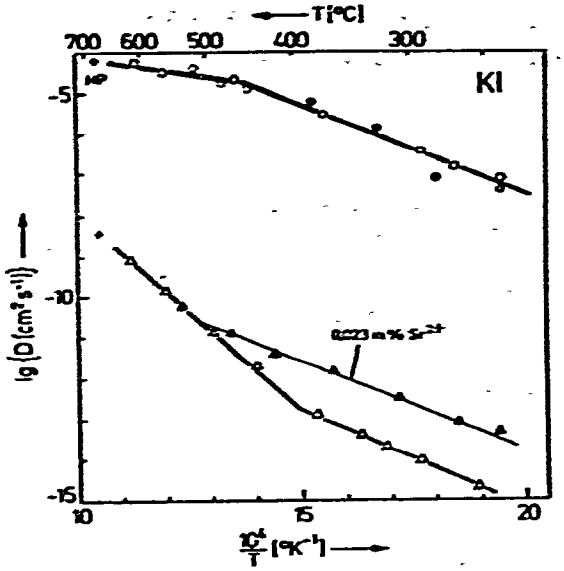

Fig. 44. Influence of Sr^{2+} doping on Ar-release from KI (cf. ref. 171).

Nb_2O_5 (to increase the cation vacancy concentration) and ThO_2 + 0.1 and 0.5 mol % Y_2O_3 (to lower the cation vacancy concentration). The samples were labeled by 40 keV xenon bombardment to three doses of 8×10^{10}, 4×10^{13} and 2×10^{16} ions per cm^2.

Felix and Müller[171] proved that the release of argon from neutron irradiated KBr is influenced by the presence of Sr^{2+} ions in concentrations of 0.005 and 0.05 mol %. Figure 43 (thick line) shows the Arrhenius diagram or argon release in pure KBr crystals. A neutron dose of 10^{15} cm^{-2} was used for inert gas production. The comparatively high values of the diffusion coefficient and the low activation enthalpies in the high temperature region (indicating an interstitial diffusion mechanism) varied at about 400°C but are explained by gas trapping. In KBr crystals doped with Sr^{2+} ions, a decrease of argon mobility was observed. This behavior is in agreement with the trapping mechanism mentioned in paragraph 4.2.3. By the addition of impurities, the concentration of extrinsic defects serving as traps for the inert gas atoms can be increased and the trapping equilibrium shifted in favor of the trapped gas atoms. The resulting increase in the concentration of cation vacancies was determined by measuring the ionic conductivity. In Fig. 43 these values are transformed by the Nernst-Einstein relation into D values to enable direct comparison with gas diffusion. Figure 43 clearly shows the double nature of cation vacancies in KBr, which act as diffusion carriers for self-diffusion and as traps to decrease gas mobility.

The effect of impurities observed in the mobility of inert gas agrees fairly well with the theory of Norgett and Lidiard[166]. This theory allowed to state a direct correlation of the gas diffusion coefficient to the concentration of well-defined lattice defects

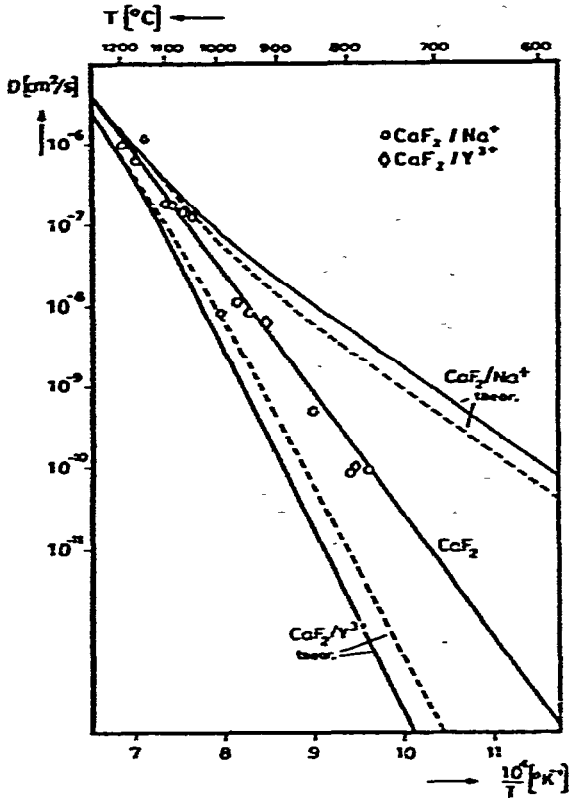

Fig. 45. Theoretical temperature dependence of diffusion coefficient, $D = f(1/T)$, for Ar in CaF_2 single crystals (pure and doped with 0.5 mol % Na or 2 mol % Y).

$$D_{gas} \approx 1/c_{\text{cation vacancies}} \tag{79}$$

Figure 44 gives the interesting case of KI where the mobility of argon is obviously unaffected by an increase of cation vacancies, caused by Sr^{2+} in the concentration of 0.023 mol %. Similarly, Largewall et al.[172, 173] found that the mobility of argon in CaF_2 crystals was not influenced by the presence of 0.5 mol % Na^+ or 2.0 mol % Y^{3+} (see Fig. 45). The effect of impurities on the gas mobility in a solid obviously depends on the mechanism of the gas diffusion. Diffusion in small vacancy clusters was assumed.

4.3.3. Radiation damage and its annealing

It is known that inert gas atoms are trapped when they meet specific defects while diffusing through a solid. Such defects may be large vacancy clusters, dislocation loops, pre-existing natural voids, gas filled bubbles, etc. Introducing the inert gas into the solid by bombardment with a beam of energetic inert gas ions, trapping of the gas is observed at high gas concentrations that coincide with high damage concentrations. Kornelsen[67] studied the influence of the number and energy of bombarding ions on inert gas release curves. Figure 46 shows the release curves of polycrystalline

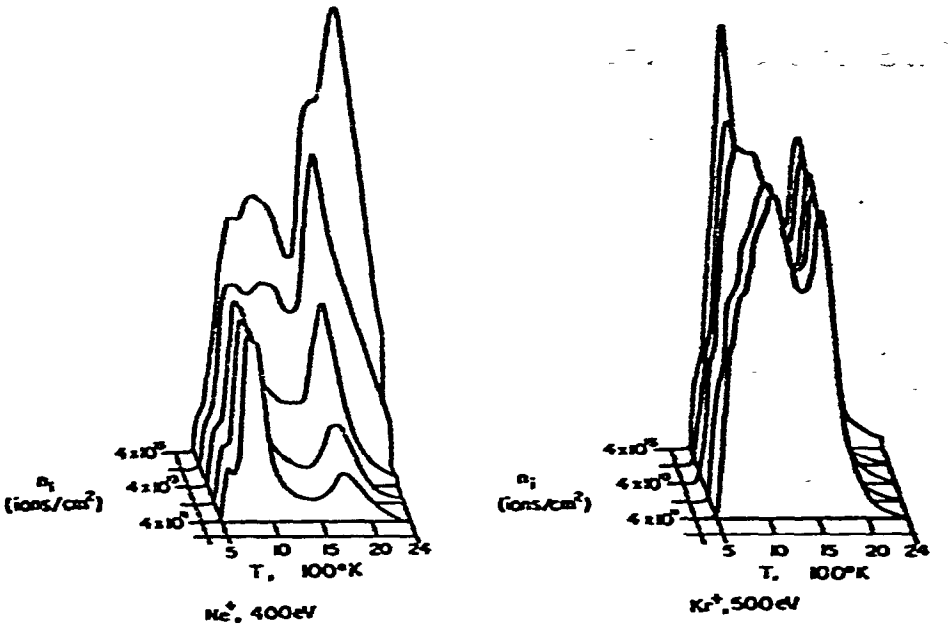

Fig. 46. The influence of the number of bombarding ions on the inert gas release curves from polycrystalline tungsten.

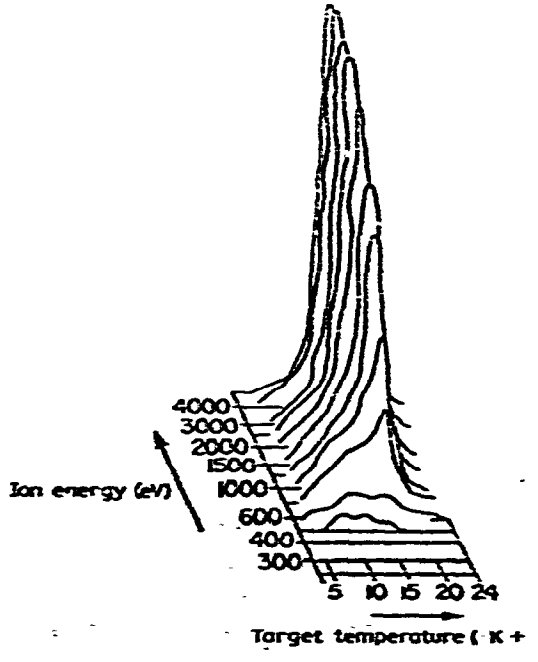

Fig. 47. Xenon release curves from polycrystalline tungsten labeled by ion bombardment with various energies.

tungsten after bombardment with Ne and Kr ions of various doses: 4×10^{11}, 4×10^{13} and 4×10^{15} ions per cm^2. The dependence of release curves on the ion energy is shown for the case of Xe release from polycrystalline tungsten in Fig. 47. As follows from Fig. 46, the "lower temperature peaks" observed were almost independent of the ion energy but the temperature for the "higher temperature peaks" increased slightly with increasing ion energy. It was shown by Matzke[170] that both high concentrations of the gas and the defects are needed for trapping to occur.

In addition to the gas trapping, radiation induced structural changes, excess of point defects in the lattice, proximity of the gas to a surface, etc., can influence the mobility of inert gas. Their importance markedly depends on the condition of gas incorporation, as has been discussed in Section 4.3.

The effect of the radiation induced trapping has been described by various authors. The effect of pre-bombardment with various ions on the mobility of xenon in KCl crystals was studied by Matzke[174]. The high dose of 2×10^{16} ions per cm^2 with beams of mass 2 (hydrogen), beams of 28 (nitrogen and CO) and beams of chlorine and indium were used for pre-bombardment. Figure 48 shows the *F–T* release curve for crystals bombarded to the low dose (8×10^{10} xenon ions per cm^2) which reflects undisturbed volume diffusion of xenon atoms as well as the *F–T* release curve for the high dose (2.5×10^{16} xenon ions per cm^2). The latter is shifted towards higher temperatures by more than 200 K as compared to the release curve for low dose bombardment. This indicated a strong interaction of gas atoms with radiation damage, or interaction with other gas atoms, or gas filled bubbles.

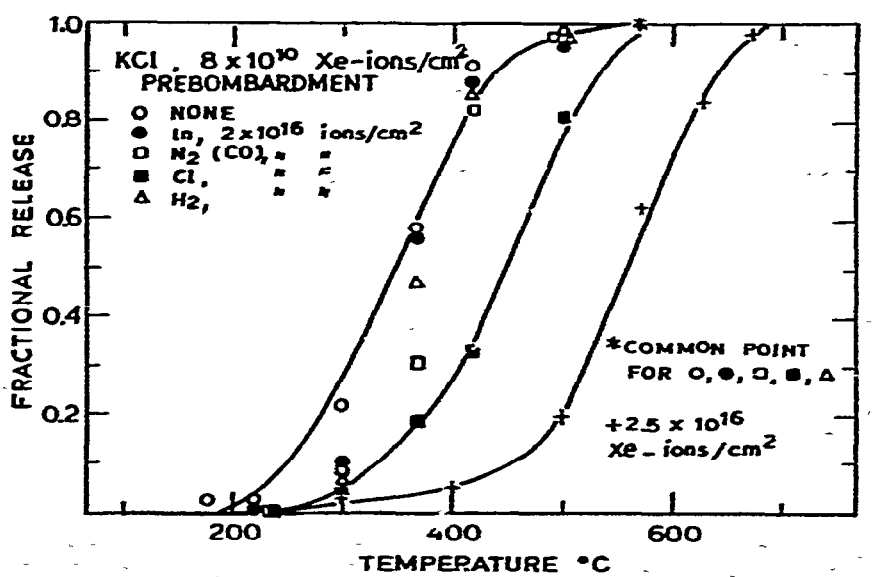

Fig. 48. Isochronal release of Xe from KCl single crystals following various ion bombardment conditions that lead either to high damage concentration alone, or to a combination of high damage and high gas concentrations.

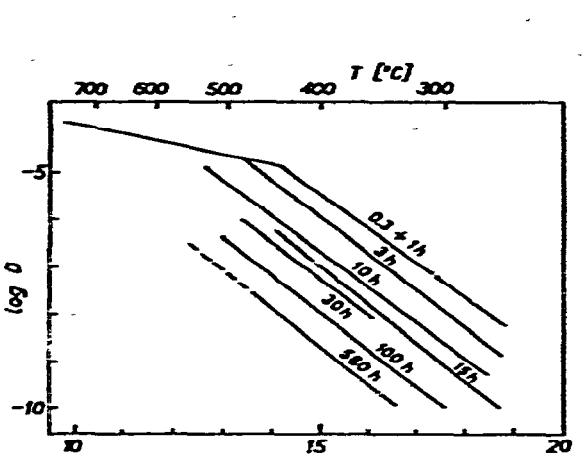

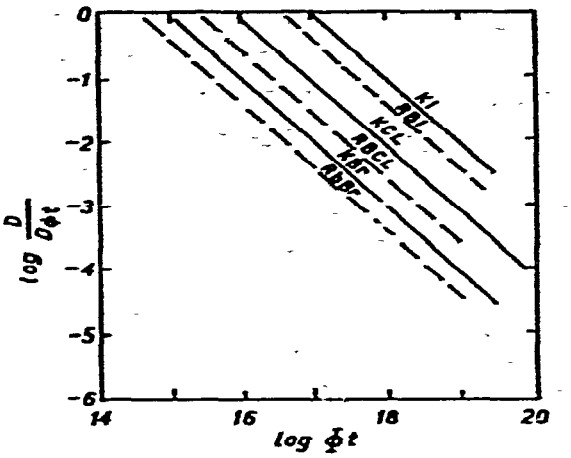

Fig. 49. Temperature-dependence of the diffusion coefficient, D, of Ar in KBr under various neutron doses (cf., ref. 14).

Fig. 50. Dependence of inert gas diffusion in alkali halides on neutron doses.

Other examples can be given with neutron irradiated solids. The decrease in argon mobility of neutron irradiated KBr by increasing the neutron dose is shown in Fig. 49. Within the limits of experimental errors a parallel shift of the low temperature branch towards higher temperatures was observed[175]. A similar dose dependence of the inert gas diffusion coefficient was also found by Felix and Müller[175] for other alkali halides (see Fig. 50). These authors stated that: (a) below a certain dose D_{app} becomes independent of neutron dose; and (b) with increasing neutron doses, D_{app} decreases in inverse proportion to the neutron dose. From this, Felix drew the conclusion that irradiation, in fact, induces a new type of gas trap. From the experimentally obtained relationship

$$D_{app} \approx (1/\phi_S)\, t \tag{80}$$

an expression was proposed similar to that valid for chemically produced cation vacancies[175], or

$$D_{app} \approx 1/c_{trap}^{irrad} \tag{18}$$

TABLE 14

DIFFUSION CHARACTERISTICS OF CaF_2

Fission fragment conc. (ff cm^{-2})	*D_0 (cm^{2}s^{-1})*	*H (kJ mol^{-1})*
3×10^{11}	9.5×10^{6}	427 ± 12
3×10^{12}	2.3×10^{3}	355.8
2.4×10^{13}	7.9×10^{-2}	297

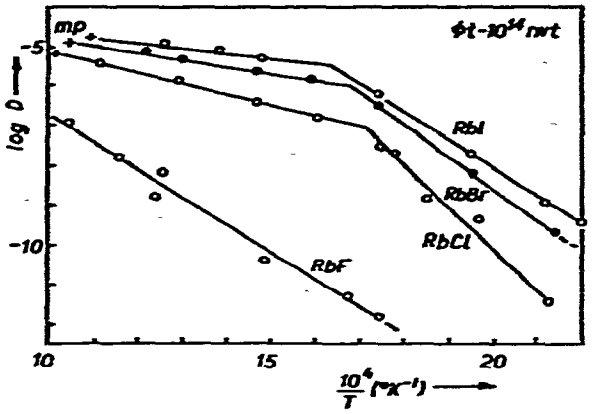

Fig. 51. Temperature-dependence of Kr diffusion in Rb-halides (cf., ref. 14).

TABLE 15

LATTICE PARAMETERS AND Kr-DIFFUSION CHARACTERISTICS OF Rb-HALIDES

Sample	*d* (nm)	*High-temperature region*			*Low-temperature region*	
		$D_{m.p.}$ (cm^2s^{-1})	D_0 (cm^2s^{-1})	ΔH ($kJ\,mol^{-1}$)	D_0 (cm^2s^{-1})	ΔH ($kJ\,mol^{-1}$)
RbF	0.282	4.5×10^{-6}	2.5	133.15	—	—
RbCl	0.327	6.3×10^{-6}	7.5×10^{3}	53.59	1.4×10^{-10}	196.8
RbBr	0.343	1.0×10^{5}	5.0×10^{-6}	29 02	4.0×10^{7}	162.46
RbI	0.366	2.0×10^{-5}	1.6×10^{-3}	29.18	1.3×10^{6}	136.5

where the defect concentration c_{trap}^{irrad} increases proportionally with the neutron dose.

Sy Ong and Elleman[62] measured the release of ^{133}Xe from CaF_2 crystals labelled through fission recoil and found that the gas mobility was also strongly influenced by trapping. The diffusion characteristics of Xe in CaF_2 influenced by the fission fragment concentration are summarized in Table 14. Normal volume diffusion results were supposed to be obtained at low gas fission fragments concentrations. At higher fission fragment concentrations, lower values of diffusion activation enthalpy resulted.

Other types of radiation damage affecting the inert gas mobility will be discussed in section 4.4.

4.3.4. Crystal lattice parameters and orientation

Figure 51 gives the Arrhenius diagrams of krypton release for Rb-halides labeled by neutron irradiation[56] (all Rb-halides have the NaCl lattice type). A low neutron exposure (1×10^{12} $cm^{-2}s^{-1}$) was used for Kr-production. The parameters of the lattice and of krypton release measurements are summarized in Table 15. It can be seen from Table 15 that the activation enthalpy, ΔH, and diffusion coefficient, D, of the inert gas are related to the lattice parameters d. The diffusion coefficient

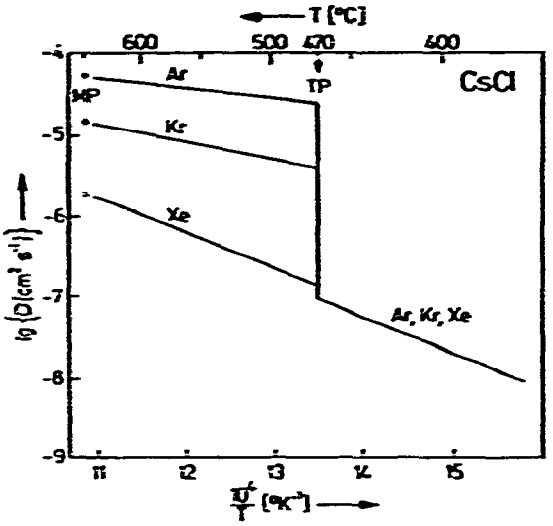

Fig. 52. Inert gas release from CsCl (cf., ref. 176).

decreases and the activation enthalpy, in both high and low temperature regions, increases as the lattice parameters are reduced. The difference in gas diffusion with respect to the NaCl and CsCl lattices was very instructively shown by Felix and Meier[176] for CsCl with its $\alpha \rightarrow \beta$ phase transformation at 469 °C. Figure 52 shows an Arrhenius diagram for the mobility of Ar, Kr and Xe in the CsCl single crystal. In the low temperature CsCl phase all gases have practically the same mobility, but in the NaCl phase (above 469 °C), a large separation of Ar, Kr and Xe takes place; Ar-diffusion has a 200-fold higher D than Xe-diffusion. The much higher diffusivities and the low activation energies of inert gas migration in β-CsCl (NaCl phase) indicate an interstitial diffusion mechanism, which is comparable to the inert gas diffusion results in the other NaCl type alkali halides. As the interstitial space is extremely small in the α-CsCl phase (CsCl lattice), the gas has to move by another mechanism. The calculations of Müller and Norgett[177] showed that the mobile gas/divacancy quantitatively fits the exponential results.

Crystal orientation effect. Several authors found that different crystal faces gave different gas release rates and apparent diffusion coefficients. Sy Ong and Elleman[62], for example, investigated CaF_2 crystals labeled with ^{133}Xe through the fission recoil technique and found that at all temperatures crystals with surfaces parallel to ⟨111⟩ planes have higher gas release rates than crystals cut parallel to ⟨001⟩ planes. An Arrhenius diagram of the diffusion coefficients gave different activation enthalpies: 337 kJ mol^{-1} for ⟨111⟩ and 289 kJ mol^{-1} for ⟨001⟩ faces.

The crystal orientation effect is emphasized for the ion bombardment and fission recoil techniques of labeling, i.e., where chanelling of the inert gas atoms is possible. Kornelsen and Sinha[178] observed an effect of crystallographic direction of ion bombardment on the inert gas release from tungsten single crystals. Figure 53 shows variations of Xe-release spectra of tungsten crystals for identical 400 eV — Xe-bombardment of three different faces ⟨110⟩, ⟨100⟩ and ⟨211⟩. Similarly,

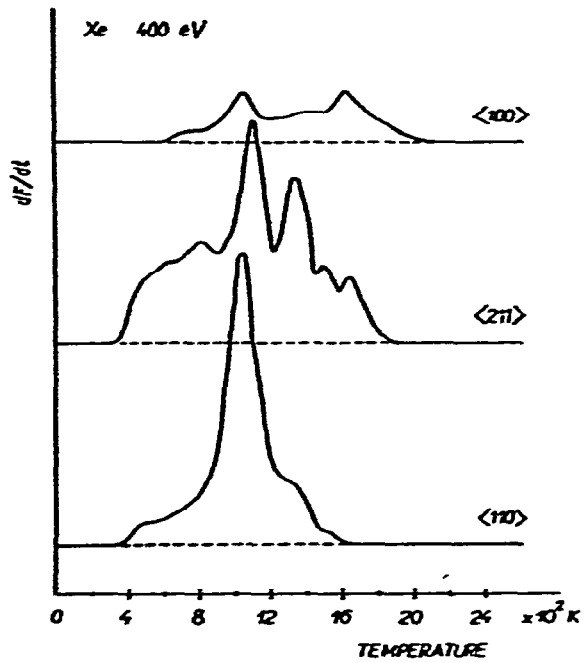

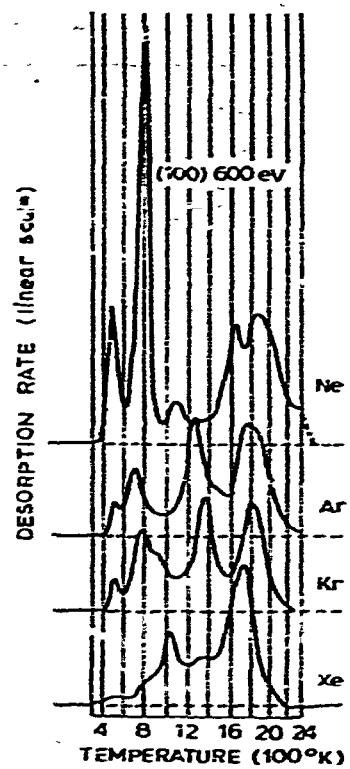

Fig. 53. Xenon release from three different faces of tungsten single crystals after 400 eV Xe bombardment.

Fig. 54. Release curves of Ne, Ar, Kr and Xe from tungsten labeled by ion bombardment; a dose of 5×10^{12} ions per cm^2.

Matzke[12] obtained different values of diffusion activation enthalpy from release curves of SiO_2 crystals bombarded with 40 keV xenon. At a low dose (8×10^{10} ions per cm^2), diffusion release along and perpendicular to the c-axis dominated with activation enthalpies of 243 and 255.4 kJ mol^{-1}, respectively. The value of ΔH = 301 kJ mol^{-1} was found for Xe-bombarded fused silica. Diffusion in the amorphous phase was markedly slower than diffusion in the crystalline phase.

4.3.5. Type of inert gas and its concentration

Kornelsen and Sinha[180] observed that various gas atoms implanted at the same energy, 600 eV, into the ⟨100⟩ face of tungsten crystals released differently. Figure 54 shows the release curves for Ne, Ar, Kr and Xe from tungsten bombarded by a dose of 5×10^{12} ions per cm^2. The results of Fig. 54 are interpreted under the assumption that atoms of different inert gases are released from positions in the lattice with different trapping energy. The gas release may pertain to a quite different trapping configuration than that in what the ion came to rest at the bombardment temperature, since annealing and re-trapping may occur as the solid is heated. It has been reported by Matzke[181], Felix et al.[56, 176] and others that the inert gas diffusion data (D, D_0 and ΔH) of a solid could differ according to the inert gas used.

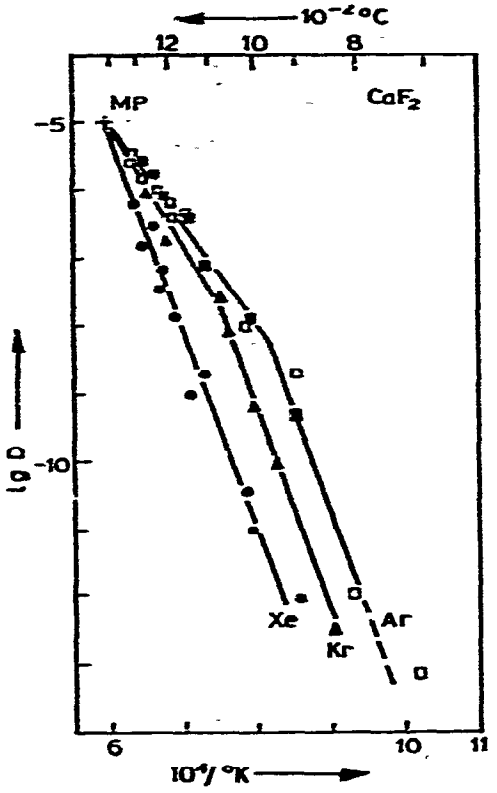

Fig. 55. Temperature-dependence of Ar, Kr and Xe diffusion in CaF_2.

TABLE 16

PHYSICO-CHEMICAL CHARACTERISTICS OF INERT GASES

Gas	*Ne*	*Ar*	*Kr*	*Xe*	*Rn*
Atomic radius (nm)	0.112	0.154	0.169	0.190	0.214
Boiling point (°C)	−246	−186	−153	−107	−65
Melting point (°C)	−249	−189	−157	−112	−71

A very instructive example of different mobility of argon, krypton and xenon atoms in β-CsCl (NaCl-lattice) has already been shown in Fig. 52. The mobility of the inert gas atoms decreases in the order Ar–Kr–Xe, i.e., in the same order as the atomic radii of diffusing gases increase[176]. Felix and Lagerwall[173] showed differences in the mobilities of argon, krypton and xenon on the alkaline earth fluorides, CaF_2, SrF_2 and BaF_2 (CaF_2 lattice). Figure 55 shows an Arrhenius diagram for the Ar, Kr and Xe diffusion in CaF_2. As in the NaCl lattice type, the gas mobility depends on the type of inert gas used for diffusion measurement and decreases in the order of increasing atomic radii: Ar–Kr–Xe. At the melting point, high D values were found again, however, with higher activation enthalpies with respect to the NaCl lattice due

to the much denser structure of the CaF_2 lattice. The lower mobility for argon and krypton in the low temperature region was interpreted by a trapping[166, 167] of the gas atoms in the lattice. For xenon atoms with the relatively largest atomic radius, the trapping takes place in the whole temperature region considered. The atomic radii, binding energies of the gas atoms in the lattice and other factors mainly determine the mobilities of inert gas in solids. Table 16 summarizes the main physicochemical characteristics of inert gases[14, 182] usually used in diffusion measurements.

The effect of gas concentration on the mobility of the inert gas, as observed by a number of investigators, has already been mentioned. Mears and Elleman[168] studied diffusion coefficient of xenon in KI using high concentrations of fission xenon (5×10^{14} Xe atoms per cm^3) and of xenon produced from ^{133}I parent (4×10^{13} Xe atoms per cm^3). Lower values of the xenon diffusion coefficient in KI were observed in both cases compared to its theoretical values. The labeling using a ^{133}I parent produced negligible radiation damage so that the lowering of the diffusion coefficient must reflect gas trapping from gas–gas interactions. For gas release fractions, $F = 0.1$, the released gas was estimated as undergoing an average of 3000 gas–gas interactions (prior to release) when gas atoms occupy adjacent lattice sites. This is apparently a sufficient number of interactions to produce a measurable reduction in gas diffusion rates.

4.3.6. Evaporation of the sample

Using ion bombardment, fission recoil or reactor irradiation technique for labeling, a possibility arises that the release of inert gases may be caused by the evaporation of the sample. Since the ranges (penetration depths) of the inert gas atoms in ion bombardment, fission recoil doping, etc. usually vary between a few tenths of nm up to about 1000 nm, evaporation losses of the order of one or a few μg per cm^2 of surface can cause a release of the inert gas atoms located in this surface region. If the activation enthalpy, ΔH, for inert gas diffusion is lower than the ΔH for vaporization, evaporation will dominate the release at high temperatures. Therefore, due to the short diffusion distances of inert gas atoms in solids labeled by ion bombardment, high temperature processes at or near the melting point can usually not be studied when ion bombardment is used for labeling. An unambiguous interpretation of diffusion data is possible only if one knows whether or not inert gas is being released by vaporization of the sample. For this purpose, Kelly and Matzke[151] defined a "minimum vaporization temperature" or "MVT" for the beginning of vaporization of a sample. This is the temperature at which the amount of vaporization in the time scale of the experiment is comparable to the median range, R_m. The simplest method of derivation proposed by Kelly and Matzke[151] is to use weight-loss data, the MVT then follows directly. In Table 17 the MVTs are listed[151] for some most common oxides and halides. Kelly et al.[161] proposed formulas for evaluating the MVTs from experimental data obtained at both step heating and linear heating rate.

TABLE 17

MINIMUM VAPORIZATION TEMPERATURE "MVT" FOR SOME HALIDES AND OXIDES

Material	*MVT (°C)* *5 atom layers in 5 min*
BaF_2	775– 800
CaF_2	875– 900
KCl	365– 385
α-Al_2O_3	1690–1750
ThO_2	1775–1800
UO_2	1450–1475

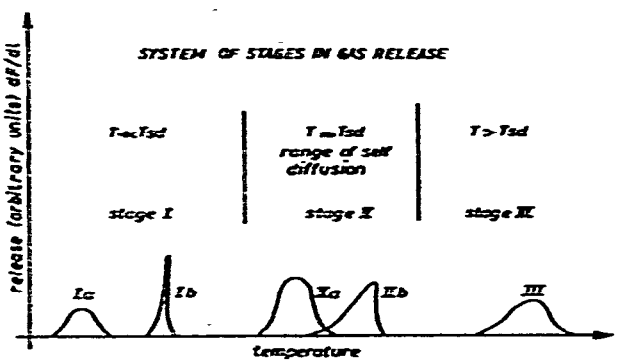

Fig. 56. System of stages in gas release studies for the case of a linear temperature increase in the representation dF/dt against temperature T. T_{sd} refers to the temperatures of self-diffusion for the conditions of ion bombardment.

4.4. Classification and models of inert gas mobility

4.4.1. System of stages for inert gas mobility

The application of the ion bombardment labeling technique with well-defined ion beams makes it possible to separate the surface from the bulk release processes. By varying the ion energy, the position of the gas with respect to the sample surface can be chosen and by varying the ion dose, the inert gas concentration in the solid can easily be provided. In this way a clear separation of various processes that contribute to the overall release[12, 183, 184] is possible. These processes were grouped into a system of stages in analogy to the recovery stages observed in electrical resistivity studies in quenched or irradiated materials.

Figure 56 shows a schematic presentation of the stages. Similar to the recovery of metals, the stages are grouped according to their temperatures with respect to those of self-diffusion and are attributed to specific transport processes[12].

Stage I involves gas mobility at unusually low temperatures:
Stage IA is due to gas fortuitously located in high mobility sites.

Stage IB is due to annealing of structural radiation damage, the most common form of which is radiation induced amorphousness.

Stage II involves gas mobility at "normal" temperatures, i.e., temperatures similar to those of self-diffusion of the matrix atoms.

Stage IIA is due to the unperturbed mobility of single gas atoms.

Stage IIB is due to temporary trapping of gas, i.e., to weak interactions of gas atoms with radiation damage or pre-existing defects, or with other gas atoms.

Stage III involves gas mobility at unusually high temperatures and is due to strong trapping of gas at pre-existing defects or in gas-filled bubbles.

As a consequence, stages IB, IIB and III are dominant at high irradiation exposures leading to high concentrations of damage and gas. In contrast, stages IA and IIA dominate in the absence of damage and hence at low irradiation exposure. In general, stage IA will predominantly occur in surface near layers and stage IIA further in the bulk. Examples for all these stages will be given in this section and the possible mechanism of mobility will be discussed.

Aluminum oxide (α-Al_2O_3) labeled by the ion bombardment technique was selected to demonstrate the stages. Results published by Jech and Kelly[185] on α-

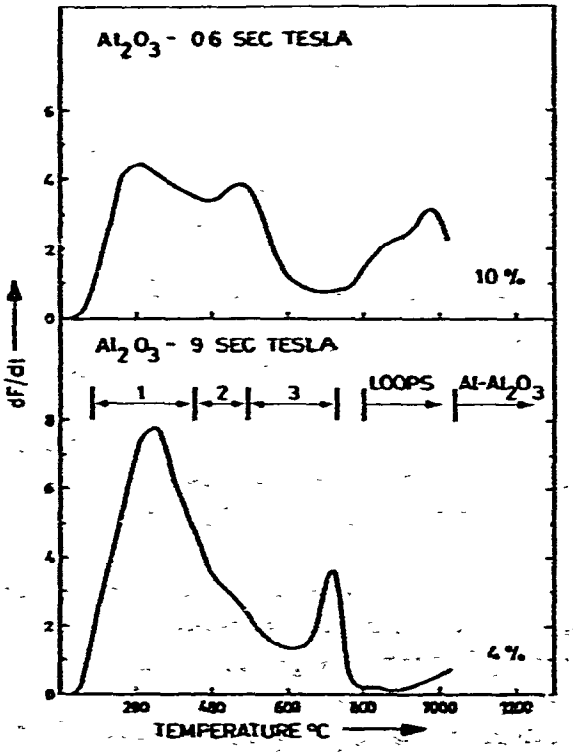

Fig. 57. dF/dt release curve for ^{85}Kr from α-Al_2O_3, labeled by ion bombardment, during heating in nitrogen at 20 °C min^{-1} (cf., ref. 185). The duration of the Tesla-discharge used for labeling and the percentage of activity remaining at 1000 °C are given for each curve. Also indicated are the stages of color-center annealing[191] (1, 2, 3) the temperature for the beginning of loop annealing[205] and the temperature for the beginning of atomic scale Al–Al_2O_3 diffusion.

Al_2O_3 single crystal bombarded with Kr-ions which reveal the most typical features are demonstrated in Fig. 57. Labeling in a Tesla-discharge under 20 Pa of Kr was carried out using discharge durations of 0.6 and 9 sec to obtain the various gas concentrations, 3×10^{13} Kr per cm^2 and 13×10^{14} Kr per cm^2, respectively. Depth distribution of Kr-ions in the sample was estimated to be about 1–2 nm. The respective amounts of the gas remaining after heating to 1100°C were 10 and 4%, as indicated in Fig. 57.

4.4.1.1. Gas release from high mobility sites (Stage IA). This stage is most prominent at low bombardment energies and low doses. It can be explained in terms of gas which is fortuitously located in high mobility sites.

In Fig. 57 (upper curve), stage IA is represented by two peaks in the temperature region of 100–550°C. The peak at 100–375°C was ascribed to the release of gas from the surface proximity. The peak at 375–550°C possibly indicates the role of excess point defects. According to the authors[185], such release is also present at higher bombardment energies and doses but its contribution falls off rapidly with increasing energy. The second sub-stage, with a maximum 375–550°C corresponds to ΔH = 228.2 kJ mol^{-1} (ΔH being evaluated by eqn (69) under the assumption of single jump kinetics with a discrete ΔH). As the ΔH value is similar to that for point defect motion in α-Al_2O_3, a connection with excess point defects, presumably created in the bombardment process was suggested. For example, it was shown in various annealing experiments[186–188] on fast neutron irradiated α-Al_2O_3 that the recovery of the lattice damage began at temperatures corresponding to ΔH values of roughly 205–243 kJ mol^{-1}, while a value of 243 kJ mol^{-1} has been proposed for extrinsic O-Al_2O_3 diffusion[189]. Further comparisons were made with the density recovery data of Desport and Smith[190] and the color-center work of Levy[191]. The three stages distinguished in his work are indicated in Fig. 57.

Other evidence for stage IA has been observed with KBr, KCl, Fe_2O_3, SiO_2, TiO_2, Nb_2O_5, Si and W (cf. refs. 150, 160, 185, 192–195).

The stage IA inert gas release would be expected to be described by the equations for diffusion with irreversible trapping (eqn (63)). These equations are valid not only for stage IA release (some gas coming to react in high mobility sites and to rest ending up in either normal sites or deep traps), but also for the case of stages IIA and IIB, where one part of the gas moves via normal sites and the other part becomes trapped in deep traps (e.g., radiation damage).

4.4.1.2. Annealing of structural radiation damage (stage IB). The next stage encountered with increasing temperature is that where inert gas motion coincides with the annealing of a bombardment-induced structural change. Such behavior has been reviewed for a number of anisotropic or covalent materials such as Al_2O_3, Fe_2O_3, SiO_2, TiO_2, U_3O_8 and the semiconductors Ge, Si and GaAs (cf. refs. 17, 151, 196, 139, 180). Since the temperatures in all of the cases studied to date were well below those for self-diffusion or normal gas diffusion, gas motion involving a structural change is basically part of "damage diffusion", or stage IB. Probably the best understood example is α-Al_2O_3. As shown in Fig. 57 (lower curve), α-Al_2O_3

bombarded with krypton to high doses shows a narrow release peak at 600–800°C. This peak is present[185] whenever the gas concentration exceeds about 10^{14} atom cm^{-2}. Direct evidence of an amorphous crystalline transition was obtained by Matzke and Whitton[196] on the basis of electron diffraction patterns. A further indication of the structural transitions is the character of the peak at 600–800°C. The width at half maximum of the peak, $\Delta T_{1/2}$, has an observed value of 60 ±10°C. It is to be compared with a predicted value of about 60°C for release governed by single jump kinetics with a discrete ΔH[139]. Release governed by diffusion kinetics would have given half-widths perhaps of double value[139]. A value of 322 ±8 kJ mol^{-1} was obtained for the activation enthalpy by substituting the following data into the appropriate $\Delta H/T$ formula for single jump motion with a discrete ΔH (eqn (69)), the temperature of the maximum release rate at 700–760°C using a heating rate of 20°C/min and the usually assumed value for the diffusion pre-exponential term, $D_0 = 0.3\ cm^2 s^{-1}$.

The gas release linked with the amorphous-crystalline transitions of α-Al_2O_3 (ΔH = 322 ±8 kJ mol^{-1}) has close analogies in the work[191] on the annealing of color centers in reactor irradiated α-Al_2O_3 and in the work[186] on the annealing of density changes. The solubility changes described by Kelly and Jech[198] and the DTA exothermal effect accompanied the annealing of the neutron irradiated sample[199].

Stage IB is most readily observed with ion bombardment labeling. It is a common

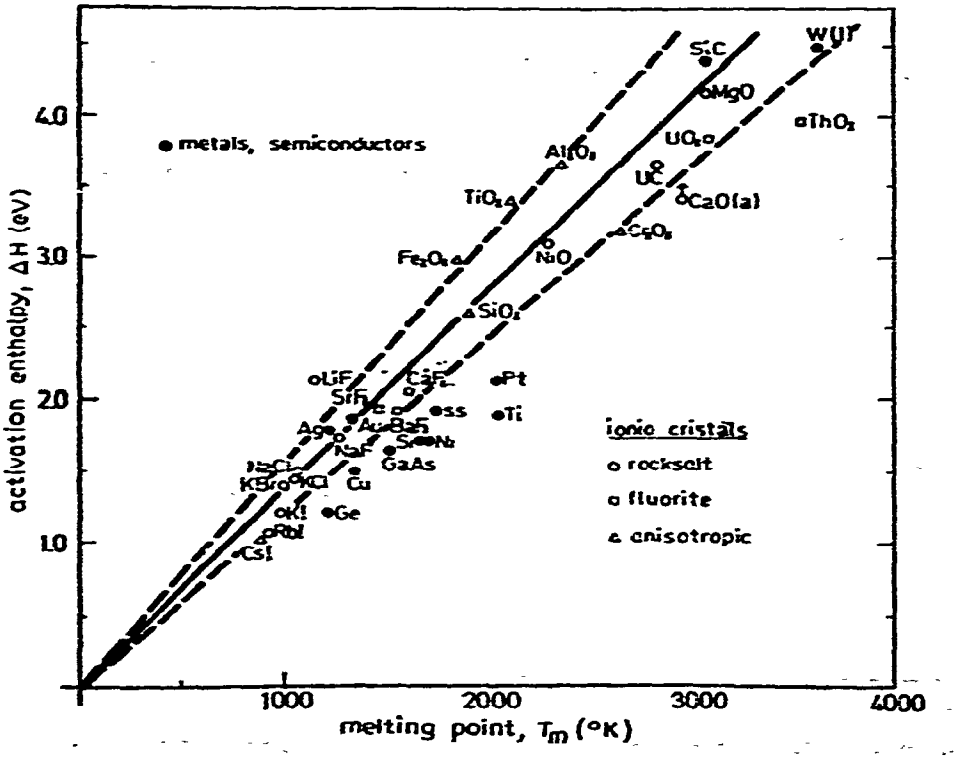

Fig. 58. Dependence of activation enthalpy, ΔH, of normal volume diffusion (stage IIA release) on the melting point, T_m.

though not universal phenomenon and is due to the annealing of gross structural damage.

4.4.1.3. Normal volume diffusion (unperturbed gas mobility) (stage IIA). Stage IIA is due to the unperturbed mobility of single gas atoms and will therefore be prominent at low doses. The self-diffusion of Kr-bombarded α-Al_2O_3 or normal gas diffusion begins at 800–900 °C, as can be seen in Fig. 57 (upper curve). Matzke[11] has shown that this stage of gas release starts between 0.4 and 0.5 $T_{melting}$ for a surprisingly large variety of ionic crystals of different lattice structure. The temperatures of peaks and temperature widths of stage IIA release could be interpreted in terms of activation enthalpies by means of eqns (64) and (69), using experiments with stepwise or linear heating, respectively. The values of ΔH deduced from the gas release curves in relation to the melting point $T_{melting}$ are shown in Fig. 58 for ionic crystals and metals of different lattice structure. Evidently, ΔH values increase linearly with the melting point. This relation can be expressed by

$$\Delta H_{IIA} = (1.4 \pm 0.2) \cdot 10^{-3}\, T_{melting} \tag{82}$$

where ΔH is in eV at^{-1} (1 eV at^{-1} = 96.427 kJ mol^{-1}) and the two limits of error are indicated by dashed lines.

4.4.1.4. Retarded gas release due to a weak trapping (stage IIB). Higher gas concentrations, and hence higher damage concentrations, lead to a decreased mobility which is expressed by stage IIB. This stage occurs within the temperature range of self-diffusion of the matrix atom, similar to stage IIA. Since there are many types of defects, vacancy clusters of different size, dislocation loops, stacking faults, etc., one cannot necessarily expect the same trapping energies for different irradiation conditions.

Examples for stage IIB include nearly every material labeled by ion bombard-

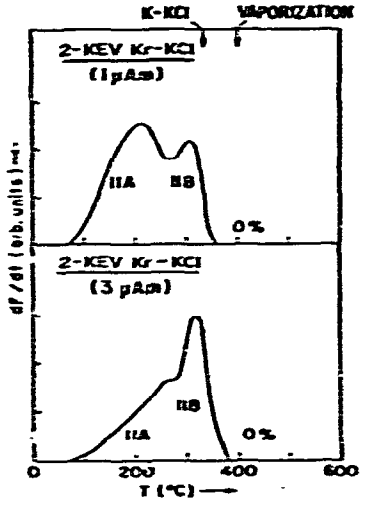

Fig. 59. dF/dt release curves for ^{85}Kr from KCl after labeling by 2 keV ion bombardment. Heating rate of 10 °C min^{-1}. The arrows show the temperatures at which K–KCl self-diffusion and vaporization should occur for a 2 keV (3.8 nm) distance scale.

ment or nuclear reactions by neutron irradiation, though the clearest are ion bombarded CaF_2, LiF, KCl, Pt, ThO_2, UO_2, W, together with neutron irradiated KBr, KCl and RbCl (cf. refs. 52, 105, 201, 159–161, 182, 56). In Fig. 59 a typical example of stage IIB is shown, krypton-bombarded KCl illustrating a dose-dependent fine structure within the self-diffusion temperature range[183]. Peak IIB is more pronounced when higher doses are used.

4.4.1.5. Gas-filled bubbles (stage III). Stage III might be described as any gas release well above the temperature of volume self-diffusion. This stage is due to strong trapping of gas in pre-existing defects (such as porosity) or in gas-filled bubbles. A pre-requisite for bubble formation is a sufficiently high gas concentration. Stage III was therefore found to be most prominent at very high doses and, moreover, with materials not subject to bombardment-induced disorder. Usually, bubbles are quite immobile before very high temperatures are reached. Inert gas atoms precipitated into bubbles can be released by three mechanisms:

(i) volume diffusion of the matrix atom;
(ii) surface diffusion of the matrix atoms;
(iii) vaporization-condensation mechanism.

Insofar as bubble motion is involved, one would expect the same diffusion theory as for stage IIA to hold, including the same F and $\Delta H/T$ expressions, except D should be replaced by D_{bubble}. Thus, we should use one of the following three expressions, depending on whether the rate-controlling process involves surface self-diffusion, volume self-diffusion or vaporization-condensation[203]

$$\begin{aligned} D_{\text{bubble}} &= 3/(2\pi r^4)\, D_{\text{surface}} \\ D_{\text{bubble}} &= 3/(2\pi r^3 \varphi)\, D_{\text{volume}} \\ D_{\text{bubble}} &= 3/(4\pi r^3)\, D_{\text{gas}} C_{\text{gas}} a^3 \end{aligned} \qquad (83)$$

Here r is the bubble radius in units of a, φ the correlation factor, and C_{gas} the equilibrium vapour concentration in atoms cm^{-2}. In addition R_m should be replaced by $(L \cdot \ln 2)$, where L is the diffusion trapping length appropriate to bubble formation.

Examples for stage III behavior include the Xe-bombarded gold[203] and platinum[158]. Bubbles are most common in metals but have also been found in UO_2, UC, MgO, Al_2O_3, etc.[204, 205]. Transmission electron microscopy is frequently used to study bubble nucleation, growth, and mobility.

4.4.2. Possible diffusion mechanisms

Four diffusion mechanisms have been proposed at various times to explain inert gas migration in solids:

Vacancy diffusion. The inert gas atoms are assumed to occupy vacancy sites in the lattice and diffuse through either the cation or anion sublattice by jumping into appropriate adjacent vacancies.

Interstitial diffusion. Inert gas atoms occupy interstitial sites in the lattice and diffuse by jumping into adjacent interstitial sites.

Interstitial diffusion plus trapping. Inert gas atoms diffuse interstitially but may

be trapped at defects in the lattice such as vacancies. If the binding energy to the defect is sufficiently large, the rate-controlling step in diffusion will be the release rate from the defect, and the measured diffusion activation energy will involve both the defect binding energy and the energy of migration of the gas atom.

Mobile cluster diffusion. Inert gas atoms associate with mobile vacancy clusters and move through the lattice with the cluster. Dissociation of the gas atom from the cluster may occur which immobilizes the gas atom until another vacancy cluster diffuses to the lattice position adjacent to the gas atom.

4.4.2.1. Vacancy diffusion. Self-diffusion usually occurs through a vacancy mechanism. The validity of this mechanism can be proved experimentally if divalent impurities which substitute for lattice atoms in monovalent solids produce an increase in the diffusion coefficient. The presence of divalent impurities in a monovalent solid will create cation or anion vacancies to maintain the total charge balance in the solid. The impurity-generated vacancies may exceed the concentration of thermally generated vacancies and an increase in the diffusion coefficient is observed.

However, Mears and Elleman[168], Sy Ong and Elleman[62] and Matzke[170,159,160] failed to detect an impurity increased inert gas diffusion with ThO_2, NaCl, KBr, CsI and other alkali iodides. Schmeling[201] and Felix[171] have observed an impurity effect in $SrCl_2$ doped crystals of KCl and KBr, respectively, with Ar as the diffusion gas. However, the impurity reduced the inert gas diffusion rate (due to a trapping), which is the opposite of the trend expected for vacancy diffusion. Another reason against the vacancy diffusion of inert gases is the large difference frequently observed between the inert gas and self-diffusion coefficient in a solid. For example, for Xe-diffusion in CsI the diffusion coefficient was reported by Mears and Elleman[168] to be at least two orders of magnitude higher than the self-diffusion coefficient measured by Lynch[206], while the activation enthalpies are similar. Since the vacancy migration rates are controlled by self-diffusion, diffusing gas atoms present in trace concentrations should exhibit values of D within an order of magnitude of the self-diffusion coefficients, even if the gas atoms always competed successfully for available vacancies with the host ions.

The diffusion activation enthalpy, ΔH, in this model is $\Delta H = Q_m + Q_F$; the sum of the gas migration energy, Q_m, and the formation energy, Q_F, of cation vacancy.

Matzke[207] and Matzke and Davies[208] studied the channeling of alpha particles from ^{222}Rn decay as a means for ascertaining the position of the ^{222}Rn-atoms in the lattice. They concluded that the gas atom in KCl, CaF_2 or UO_2 does not occupy a lattice site, and therefore, apparently does not diffuse by a simple vacancy process.

4.4.2.2. Interstitial diffusion. Diffusion by a simple interstitial process also appears incompatible with many of the experimental results. Norgett and Lidiard[167] have calculated values for the diffusion activation enthalpies for inert gas diffusion in alkali halides by interstitial mechanism and have obtained values in the range between 0.10 and 0.34 eV at^{-1}, which corresponds to 9.64 and 32.73 kJ mol^{-1} (the transformation factor is: 1 eV = 96.427 kJ mol^{-1}). The diffusion activation enthalpy for the interstitial mechanism $\Delta H = Q_m$, corresponds to the gas atom migration

energy only. Atoms in interstitial positions are supposed to produce lattice strain which lowers the migration energy for movement from one interstitial position to an adjacent position. However, measured values for Ar, Kr and Xe-diffusion in alkali halides lie in the range 0.30 to 2.0 eV with most values above 0.8 eV. This disagreement with the calculated values is too great to explain inert gas diffusion in terms of an interstitial model.

4.4.2.3. Interstitial diffusion plus trapping. Norgett and Lidiard[166, 167] have suggested a model in which inert gas atoms diffuse interstitially but are also trapped by lattice vacancies. The diffusion activation enthalpy, ΔH, will contain a term which reflects the binding of the gas atom to the vacancy trap, so it is possible to obtain large values of ΔH even though the gas migration energy Q_m is low. The authors have used this model in calculating expected values of ΔH which satisfactorily agreed with experimental values in certain cases. This model has considerable flexibility in fitting experimental results and presents a number of obvious advantages. It is possible to explain Arrhenius diagrams with two activation enthalpies, such as those observed by Felix[56] in terms of different rate-controlling processes in the two temperature ranges. The high activation enthalpy region at low temperatures can be assumed to involve appreciable trapping, so that the diffusion activation enthalpy contains for the trap binding energy Q_B, the trap formation energy Q_F, and the gas migration energy Q_M or $\Delta H = Q_M + Q_B + Q_F$. The high temperature diffusion component is assumed to result from interstitial diffusion only with no trapping.

Different crystals with different lattice parameters, host ion sizes, and structures are expected to yield different interstitial activation enthalpies. The calculations of Norgett and Lidiard[167] do predict different activation enthalpies for different crystal/gas systems. The model also readily explains why the gas diffusion coefficient can greatly exceed the self-diffusion coefficient since the mechanisms are different. Also, diffusion results with a single activation enthalpy, such as KF/Ar and RbF/Kr which may be explained by assuming that trapping dominates over the entire temperature range of measurement.

The lowering of diffusion coefficients through the introduction of impurities, as observed by Schmeling[201] and Felix[171], is also consistent with the model, but the results in which no impurity effects were observed would appear inconsistent if single vacancies act as traps. The lowering of the diffusion coefficient through the radiation induced traps can also be consistent with the model since the radiation induced traps are believed to be defect clusters. One would expect a larger binding energy for a gas atom in a defect cluster than for a gas atom in a single vacancy.

4.4.2.4. Mobile cluster diffusion. Matzke[160] was the first to suggest that inert gas atoms could possibly associate with mobile defect clusters and move with clusters through the lattice. The size of the mobile vacancy cluster is unknown and presumably lies between a divacancy and the seven or eight vacancies postulated for stable void formation. One of the simplest possible cluster models, a Schottky defect consisting of one cation and two anion vacancies, was described by Sy Ong and Elleman[62]. An inert gas atom is assumed to associate with the defect and move through the lattice

with the clusters. The gas atoms may periodically dissociate from the clusters to become trapped in the lattice, so observed gas diffusion coefficients may be lower than the cluster diffusion coefficients. An equilibrium between diffusion gas atoms in the clusters and immobile gas atoms is assumed. The equilibrium can be represented in terms of quasi-chemical equilibrium with the equilibrium constant K_s. The diffusion activation enthalpy for this diffusion model is given by: $\Delta H = Q_m + Q_m(c) + Q_F(c) - Q_d(c)$, where Q_m is the migration energy for the mobile cluster; $Q_m(c)$ is the migration energy for the mobile cluster containing an inert gas atom; $Q_F(c)$ the cluster formation energy; and $Q_d(c)$ the cluster dissociation energy with a contained gas atom. Like the trapped interstitial model, the mobile cluster diffusion qualitatively explains most of the features in inert gas diffusion experiments.

An Arrhenius diagram with the break of the type observed by Felix[56] is explicable by this mechanism also. The low temperature component results from appreciable gas dissociation of all of the gas that remains in the cluster. The straight line of the Arrhenius diagram is also possible. The model is compatible with gas diffusion coefficients, which are considerably higher than the self-diffusion coefficients since the mechanisms are different. There may or may not be impurity effects for gas diffusion since some cluster concentrations are altered by impurities while others are not. For example, in divalent salts, the divacancy concentration is impurity-independent (the product of cation and anion vacancy concentrations is unaltered by impurities) but the trivacancy concentration is impurity-dependent. The model predicts a decreasing fraction of mobile gas atoms with increasing gas concentration which is compatible with the generally observed decrease in diffusion coefficients with increasing gas concentrations. The model is also compatible with the channeling of Matzke[207] and Matzke and Davies[208] which showed that gas atoms are not on single lattice sites.

The problem with the model is, that currently, it does not appear possible to specify values of D_0, Q_m, $Q_F(c)$ in advance and it is therefore possible to fit almost any shaped curve by a suitable choice of parameters. The mobile cluster model has been found[62] to be the best explanation for diffusion of inert gas atoms in CaF_2.

Chapter 5

MEASUREMENT OF INERT GAS RELEASE AND INSTRUMENTATION

5.1. Methods of inert gas release determination

The inert gas release can be measured as:

(i) The amount $N(t)$ of gas released from the sample in time t. From the measured $N(t)$ value the released fraction F of the gas is usually evaluated: $F = N(t)/N_0$, N_0 being the total gas amount initially present in the sample,

(ii) The release rate $\dot{N}(t)$ of the gas. The measured $\dot{N}(t)$ value is usually expressed as the release rate dF/dt of the inert gas* but it can be used for evaluating the emanating power E ($E = \dot{N}(t)_{rel}/\dot{N}_{form}$) when a sample labeled by the parent of emanation was measured.

Apart from the direct measurement of the inert gas release, the residual gas remaining in the sample can be measured and the release calculated. The latter case has been employed with samples labeled by the gas without its radioactive parent. The time or temperature dependence of the inert gas release can therefore be expressed by an integral release curve (i), and by an differential release curve (ii).

5.1.1. Released fraction F of inert gas

The determination of the fraction F of the inert gas released ($F = N(t)/N_0$) can be made by collecting the gas in an activated charcoal trap at low temperature[60, 211] or by using a closed circuit apparatus[211]. The amount $N(t)$ of the collected gas may be measured continuously or periodically (every 5 minutes). The carrier gas flow or a circulation pump are used to transport the inert gas into the measuring chamber. The amount $N(t)$ of the gas released can also be determined[212] by counting the remaining radioactivity of the labeled sample after step-wise heating and cooling to room temperature, using a flow-type proportional counter.

To express the fraction F of the inert gas released, the total activity (N_0) of the inert gas present in the sample must be determined. Many investigators determine the value N_0 by dissolving the sample in acid or another solvent. In order not to destroy the sample, a second sample labeled together with the specimen may be separately dissolved. Matzke[212] proposed to heat the sample to the temperature at which all the gas present is supposed to be released.

For experiments lasting a relatively long time when compared with the half-life of the inert gas used, the decay of the measured inert gas should be taken into account. The fractional release $F(t)$ is then expressed[60] as

$$F(t) = \left[N(t) + \lambda \int_0^t N(\tau)\, d\tau \right] / N_0 \qquad (84)$$

* dF/dt should be rigorously understood as $\dot{N}(t)/N_0$.

where $N(t)$ is the number of inert gas atoms presented in the charcoal trap and measured. N_0 is the number of inert gas atoms present in the sample in time $\tau = 0$, the term, $\lambda \int_0^t N(\tau)d\tau$, represents the number of decayed atoms of the radioactive gas released in time t, and λ being the decay constant of radioactive gas.

5.1.2. Release rate dF/dt *of inert gas*

When the release rate of the inert gas is to be determined, the amount of inert gas escaping from the sample in unit time is measured ($\dot{N}_{rel} = dF/dt$) and expressed in terms of emanation release rate or emanating power. The emanating power E (used with samples containing an inert gas parent nuclide as the source of emanation) is defined as the ratio of the emanation release rate, $\dot{N}_{rel}$, and the emanation formation rate, $\dot{N}_{form}$, or $E = \dot{N}_{rel}/\dot{N}_{form}$.

(1) *Determination of gas formation rate,* $\dot{N}_{form}$, *and release rate,* $\dot{N}_{rel}$. Several methods can be used for this purpose. Dissolution of the sample in acid or another solvent and measurement of the inert gas release from the solution[1] is usually applied. The radon formed during the definite time interval is removed from the solution by elution with a gas and measured (^{222}Rn escapes quantitatively from hot acid solutions). A static or a flow method can generally be used for the measurement of the radon released. The static method (which can be applied for ^{222}Rn measurement) consists of measuring the radioactivity of the sample after radioactive equilibrium between radon and its active deposit (daughter products) has been established (~ 4 hours). When the radioactivity of short-lived nuclides, ^{220}Rn and ^{219}Rn, is to be measured, the flow method is usually employed. In this method the escaping inert gas is swept through the measuring chamber at a constant rate. Alpha particles emitted by ^{220}Rn or ^{219}Rn decaying in the measuring chamber and by their immediate daughters, ^{216}Po ($t_{1/2} = 0.158$ s) or ^{215}Po ($t_{1/2} = 0.00183$ s), are measured. The radioactivity measured is proportional to the rate of escape of inert gas from the sample measured.

(2) *Comparing to standard specimen*[1] *method.* The rates of inert gas release from the sample and standard, denoted $(\dot{N}_\alpha)_s$ and $(\dot{N}_\alpha)_{st}$, respectively, are measured. The rates of the inert gas formation in the sample and standard, $(\dot{N}_\beta)_s$ and $(\dot{N}_\beta)_{st}$, are determined by measurement of their α and β activities in sealed containers after radioactive equilibrium has been attained. The emanating power is equal to:

$$E_s = E_{st} \frac{[(\dot{N}_\alpha)/(\dot{N}_\beta)]_s}{[(\dot{N}_\alpha)/(\dot{N}_\beta)]_{st}} \tag{85}$$

The method of comparison to a standard specimen is usually employed for the determination of the emanation formation rates when the inert gases, ^{220}Rn and ^{219}Rn, are used since they do not escape quantitatively from aqueous solutions. The emanating power of the standard E_{st} is determined in another way, e.g., by the active deposit method. The emanating power of barium palmitate or stearate, which are usually employed as the standards, are $E = 98$–99%.

(3) *Active deposit method*[1]. This method (suitable for samples of fairly high

emanating power) consists in the measurement of beta or gamma activity of the active deposit in equilibrium with the radioactive inert gas. A sample labeled with the inert gas parent (where the inert gas is in radioactive equilibrium with the parent) is thoroughly washed in a dry stream of nitrogen, until radioactive equilibrium between short-lived active deposit and inert gas remaining in the sample has been attained. The sample is then placed in a container and its beta and/or gamma activity is measured immediately after sealing the container. The measured radioactivity, $\dot{N}_1$, is proportional to the rate of decay of the radioactive inert gas in the sample. The inert gas escaping from the solid into the sealed container is then allowed to grow until radioactive equilibrium is reached between incorporated parent, escaping inert gas and active deposit on the walls of the sealed container. When ^{222}Rn and ^{220}Rn nuclides are employed, approximately 1 month and 10 minutes, respectively, are needed. The activity of the sealed sample, $\dot{N}_2$, is then measured again. This activity is proportional to the rate of formation of radon in the solid. The emanating power in absolute values can be calculated as

$$E = (\dot{N}_2 - \dot{N}_1)/\dot{N}_2 \tag{86}$$

If conditions of steady radioactive equilibrium are not fulfilled, the measured ratio E is called "apparent emanating power".

5.2. The equipment for inert gas release measurement

The ETA apparatus consists in general of several components, ensuring

(i) inert gas detection, monitoring and recording;
(ii) sample heating and temperature control and measurement;
(iii) carrier gas supply with flow stabilization and measurement;
(iv) measurement of complementary parameters.

5.2.1. Inert gas detection

Various inert gas detectors have been proposed in the past to measure the amount of the inert gas released from the sample. If the inert gas used is a radioactive emitter, one of the methods for the detection of radioactivity can be used. If the inert gas is non-radioactive, a mass spectrometer (e.g., Omegatron type) can be employed for its detection and measurement. The experimenter faced for the first time with the problem of radioactivity detection must be referred to standard texts on the subject, e.g. ref. 213.

Techniques which can be used for the detection and measurement of the inert gas radioactivity can be divided into several categories. All of them are commercially available:

Geiger-Müller counters	(for α, β and γ emitters),
Ionization chambers	(for α, β emitters),
Scintillation detectors	(for α, β and γ emitters),
Semiconductor detectors	(for α, β, γ emitters).

The choice of detector depends on the type and energy of the radiation, half-life of inert gas nuclide and the information desired. Coupled detectors[24] are sometimes used for simultaneous detection of several gaseous nuclides. Early investigators used the ionization chambers of 200–600 cm^3 volume as detectors for measuring alpha activity. The conditions for measuring ^{220}Rn and ^{219}Rn by means of an ionization chamber have been examined in detail by Voltz and Adloff[215]. The use of ionization chambers for alpha activity measurements ensures a high efficiency of measurement, however, the efficiency of counting depends on the nature of the gas used as the carrier gas and other gaseous components (moisture and organic impurities). The same drawback has to be taken into account when using flow-type G.M. counters. The efficiency of activity measurement by means of the end-face G.M. counters, scintillation and semiconductor detectors is almost unaffected by impurities in carrier gas. These detectors are therefore advantageously used when solids are studied which undergo decomposition accompanied by evolution of gases or water vapor.

5.2.1.1. Measuring chambers. The detector itself is usually placed in a measuring chamber, the shape and volume of which are designed according to conditions of the radioactivity measurement and the information desired. Figures 60–64 show the principal types of measuring chambers. Figure 60 shows the classical ionization chamber[2] connected to an electroscope and used to measure the release rate of the radon isotopes, ^{220}Rn (1) and ^{222}Rn (2). Figure 61 shows the measuring chamber for ^{220}Rn release rate using an alpha-scintillation detector (ZnS) connected to a photomultiplier[216–218]. Various shapes of measuring chambers[23, 108] for krypton ^{85}Kr are illustrated in Fig. 62: (a) small volume chamber with one or two end-face G.M. tubes, (b) small volume chamber bored in the beta-scintillation crystal directly,

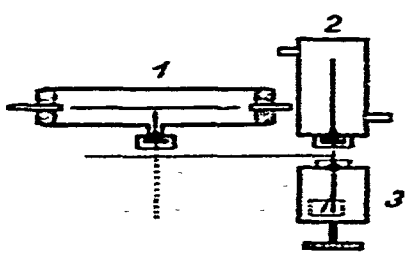

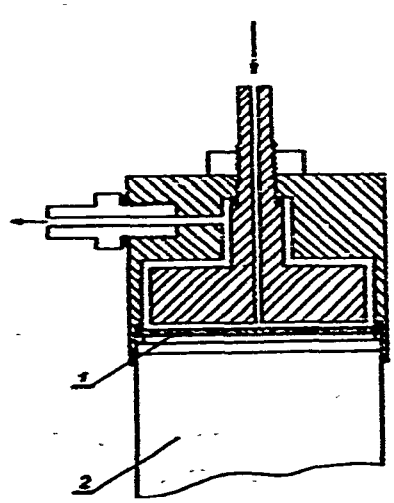

Fig. 60. Schematic drawing of a classical ionization chamber connected to an electroscope and used for measuring the release rate of radon isotopes, ^{220}Rn and ^{222}Rn (after Hahn[2]): 1 = condenser for ^{220}Rn measurement; 2 = condenser for ^{222}Rn measurement; 3 = electroscope.

Fig. 61. Measuring chamber for ^{220}Rn release rate using an alpha scintillation detector (1) connected to a photomultiplier tube (2) (after Quet et al.[216] and Balek[213]).

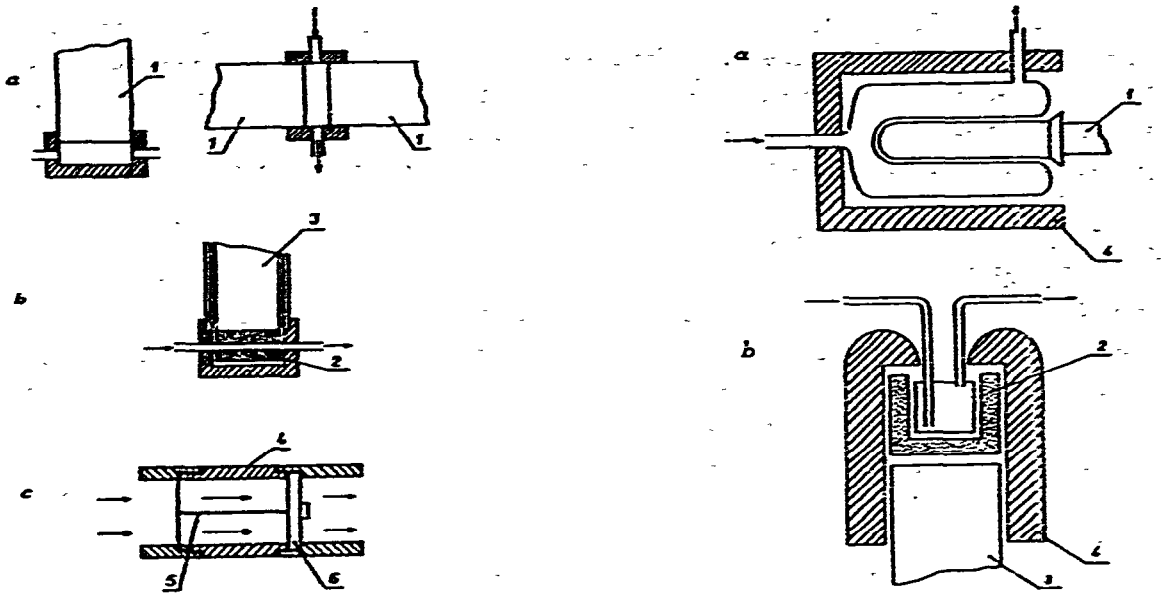

Fig. 62. Various shapes of chambers used for the measurement of beta-active inert gases (^{85}Kr): a = small volume chamber connected to one or two end-face G.M. tubes; b = small volume chamber drilled in a beta-scintillation crystal connected to a photomultiplier tube; c = flow-type G.M. tube (after Tölgyessy et al.[23, 108]). 1 = end-face G.M. tube; 2 = scintillator; 3 = photomultiplier; 4, 5 = negative and positive electrodes, respectively, of the flow-type G.M. tube; 6 = electrode holder

Fig. 63. Chambers used for measuring release rate of gamma-active inert gases (^{133}Xe), equipped (a) with a G.M. tube (after Lindner and Matzke[211]) or (b) with a gamma-scintillation crystal connected to the photomultiplier tube (after Ichiba[219]). 1 = G.M.-tube; 2 = scintillator; 3 = photomultiplier tube; 4 = Pb-shielding.

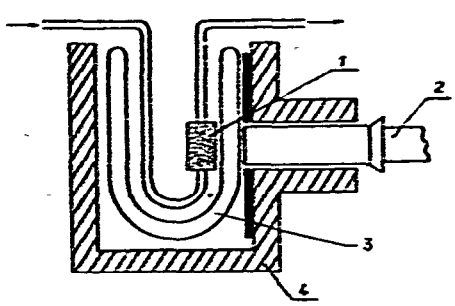

Fig. 64. Measuring chamber for measuring released fraction F of inert gases beta or gamma active (after Koss[60]) 1 = charcoal trap cooled; 2 = end-face G.M. tube or scintillation detector; 3 = Dewar flask; 4 = Pb-shielding.

and (c) flow-type G.M. tube. Fig. 63 shows two measuring chambers for gamma-activity, e.g., ^{135}Xe. The chambers are equipped with G.M. tube[211] (part a) or with a gamma-scintillation crystal connected to a photomultiplier[58, 219] (part b). Figure 64 shows the chamber with a charcoal trap[60] for measurements of released fraction, F. An end-face G.M. tube or a scintillation detector can be used for the measurement of beta or gamma activity. The same types of detectors can be used for counting the residual radioactive inert gas in the sample.

5.2.1.2. Monitoring and recording of inert gas release. The output of the radioactivity detectors (G.M. tube, scintillation and semiconductor detectors) is connected to a count-meter, a count-rate meter, or a spectrometer. The recording of the experimental results is provided by a printer, a recorder or recently by a punch tape printer which enables the immediate use of a computer for data evaluation.

5.2.2. Systems of carrier gas flow and stabilization

The ETA of the sample is performed in a gas stream which serves as a gaseous medium for the solid sample and as a carrier gas for the inert gas and volatile products released from the sample. The carrier gas is usually supplied from a pressure vessel; in some cases it can be also drawn through the apparatus by a vacuum pump. When the emanation release rate is measured, the continuous flow system is usually employed to transport the inert gas released from the sample to the measuring chamber with a detector. The good stabilization of the flow-rate is essential, otherwise false effects on the ETA curve can appear. In the cases of short-lived inert gas nuclides (as ^{220}Rn) the gas flow-rate must be sufficiently high to prevent too much loss by decay before the measuring chamber is reached. On the other hand, a high flow-rate means that the inert gas atoms spend less time in the chamber and the probability of detection by their disintegration is less.

The maximum flow-rate depends on the volume proportions of the flow system, the volume of the measuring chamber and the decay constant of the radioactive inert gas nuclide. Assuming a linear flow-rate in the system (which is a simplification of the reality), V_1 the volume between the sample and the measuring chamber, V_2 the volume of the measuring chamber, u the rate of the gas flow, λ the decay constant of the radioactive inert gas measured, and a_0 the number of the inert gas atoms released from the sample in unit time, the number of inert gas atoms a decaying in the measuring chamber in unit time can be expressed[220] as:

$$a = a_0 \exp(-\lambda V_1/u)\,[1 - \exp(-\lambda V_2/u)] \tag{87}$$

The gas flow-rate corresponding to the maximum efficiency of the measurement can be found as:

$$u_{max} = [\lambda V_2/2][1 + (1 + 4V_1/V_2)^{1/2}] \tag{88}$$

Figure 65 shows the experimentally found dependence[218] of the efficiency of the carrier flow system on the gas flow-rate when the radioactivity of ^{220}Rn is measured. The curve can differ for different carrier gases. The working flow-rate, u_{exp}, is usually chosen on the descending part of the curve where the measured activity does not change as much with the possible accidental changes of the flow-rate. For the case given in Fig. 65, the working flow-rate is $u_{exp} = 20$ cm^3 min^{-1}.

To ensure the gas tightness of the carrier gas flow system two gas flow meters are usually built into the gas line; one at the beginning and the other at the end of the system, as shown in Fig. 66. The traps for purification and drying of the carrier gas can also be built into the gas line. After passing through the purifying traps, the

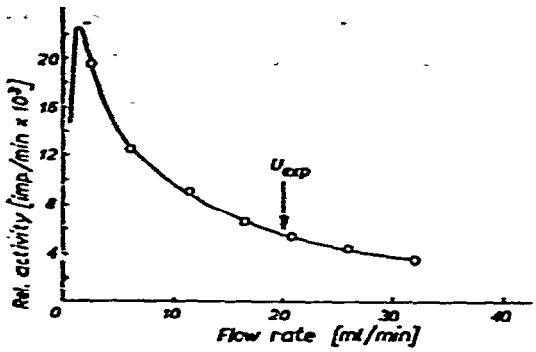

Fig. 65. Experimentally determined count-rate as a function of carrier gas (air) flow for small volume measuring chamber (V_2 = 8.4 cm³) and ^{220}Rn counting. Working flow rate chosen u_{exp} = 20 cm³ min⁻¹.

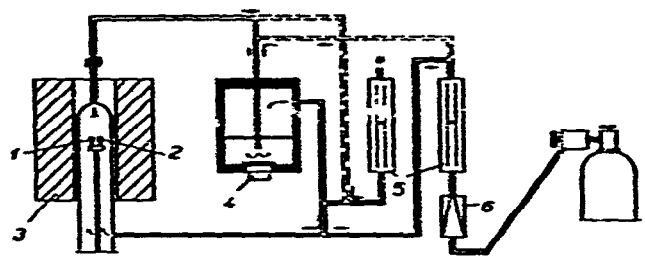

Fig. 66. Diagram of ETA-DTA simultaneous apparatus. 1 = sample; 2 = DTA reference sample; 3 = detector; 4 = detector; 5 = flow-rate meters; 6 = flow-rate stabilizer. The carrier gas piping during sample and background measurement are demonstrated by a full or dashed line, respectively.

carrier gas enters the reaction vessel and passes in close proximity to the sample. The inert gas released from the solid is carried by the carrier gas into the measuring chamber and then to the exhaust. For the radioactivity background determination, the apparatus should permit the measurement of the carrier gas flow directly to the measuring chamber. (see Fig. 66).

5.2.3. Sample heating and temperature control and measurement

The sample is placed into the reaction vessel which is heated by an electrical furnace, the temperature program of which is controlled by a temperature control unit. The temperature programmers of DTA or TG devices[221] can be used for this purpose. The temperature is measured by thermocouples placed directly in the sample or the sample holder.

5.2.4. Complementary measuring systems

The investigation of solids needs the application of not only one but several experimental methods. To ensure identical experimental conditions, some authors proposed devices enabling the simultaneous performance of ETA and other thermoanalytical methods as DTA, dilatometry, TG, EGA, etc. A conventional heating system is used in the simultaneous equipment and various parameters are measured

together with the inert gas release. A multichannel recorder or digital output measuring unit can be used for the recording of experimental data. Figures 66 to 69 show diagrams of instruments permitting the simultaneous measurements using the

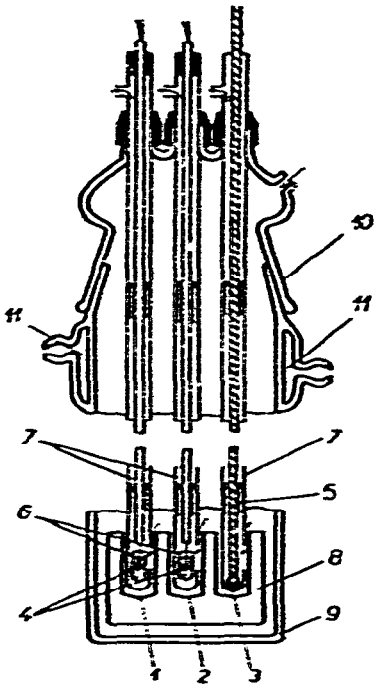

Fig. 67. Reaction vessel of ETA-DTA-dilatometry simultaneous apparatus (after Balek[77]). 1 = labeled sample; 2 = DTA-reference sample; 3 = dilatometer sample; 4 = composite thermocouples; 5 = quartz dilatometer rod; 6 = quartz vessels; 7 = supporting pipes; 8 = metal block; 9 = quartz outer vessel; 10 = ground glass joint; 11 = coolant tube.

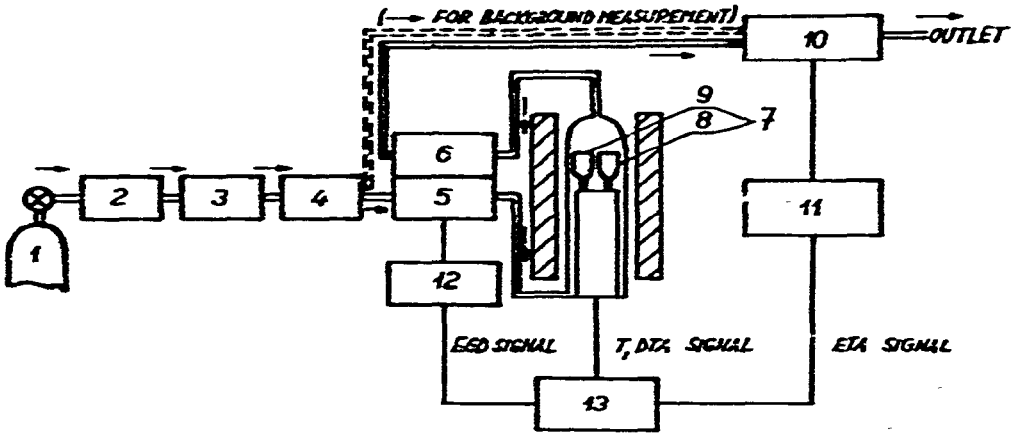

Fig. 68. Diagram of ETA–DTA–EGA simultaneous apparatus (after Balek and Habersberger[29]). 1 = carrier gas supply; 2 = flow stabilizer; 3 = flow meter; 4 = freezing trap; 5, 6 = cells of reference and sample thermoconductivity detectors, respectively: 7 = sample holder; 8 = labeled sample; 9 = DTA reference sample; 10 = measuring chamber of inert gas; 11 = counts-rate meter; 12 = bridge circuit; 13 = multichannel recorder.

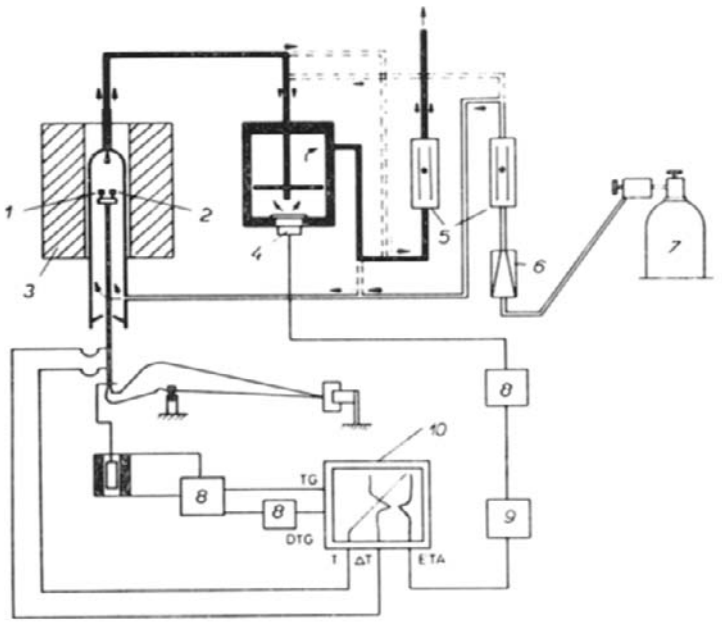

Fig. 69. Diagram of ETA–DTA–TG/DTG simultaneous apparatus (after Emmerich and Balek[138]). 1 = labeled sample; 2 = DTA reference sample; 3 = furnace; 4 = silicon surface barrier detector; 5 = flow-rate meter; 6 = flow-rate stabilizer; 7 = carrier gas supply; 8 = amplifier; 9 = count-rate meter; 10 = multichannel recorder.

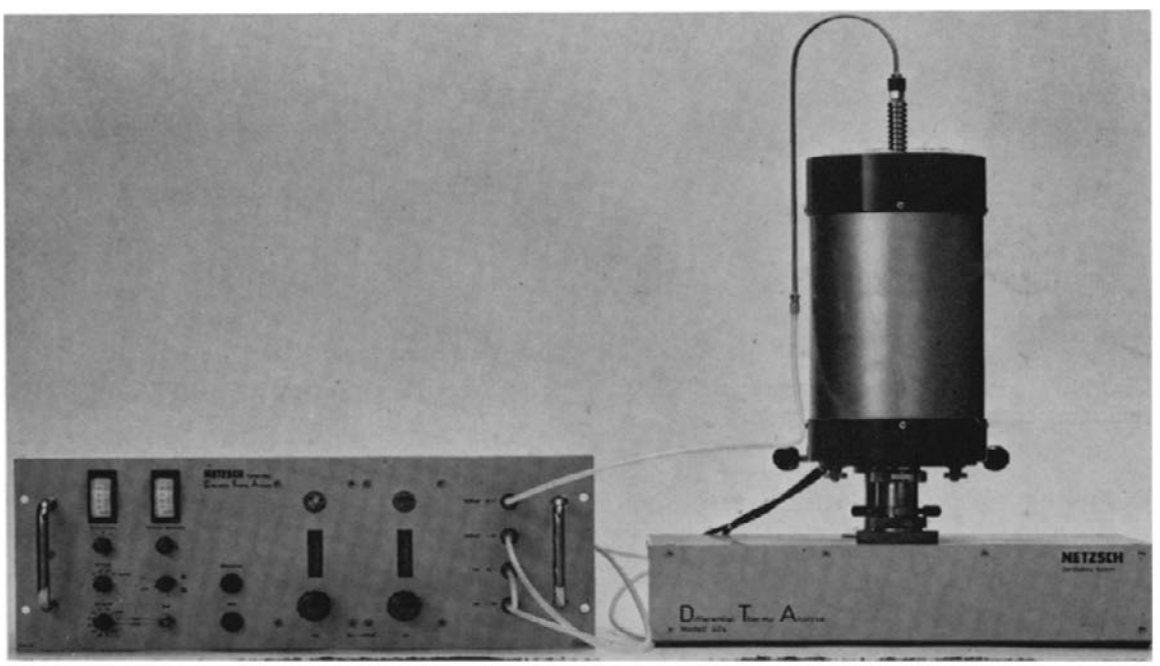

Fig. 70. General view of commercial Netzsch device for simultaneous ETA–DTA.

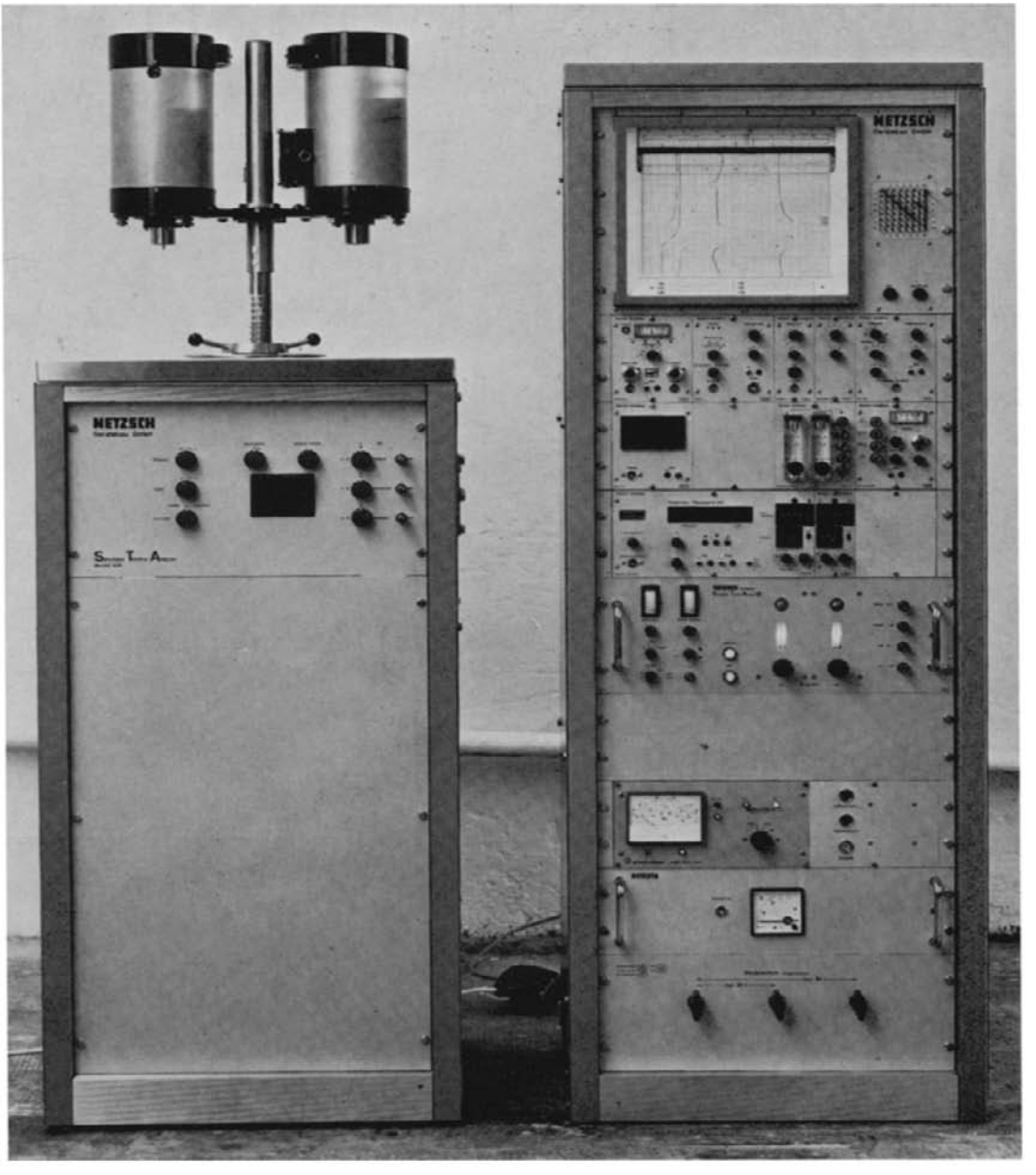

Fig. 71. General view of commercial Netzsch device for simultaneous ETA–DTA–TG/DTG, including temperature control unit.

following thermoanalytical methods: ETA–DTA, ETA–DTA–dilatometry, ETA–DTA–EGA, and ETA–DTA–TG/DTG. The ETA–DTA apparatus[222] (see Fig. 66) commercially built by Messrs. Netzsch, Selb, (West Germany), is equipped with a semiconductor detector. A labeled sample is used for ETA as well as DTA measurement. The reaction vessel of the simultaneous ETA–DTA–dilatometry apparatus is schematically shown in Fig. 67. Figure 68 schematically shows the ETA–DTA–EGA

instrument, constructed by adapting the commercial Netzsch high-temperature apparatus with a gas flow sample holder[29]. The EGA is performed by thermal conductivity detectors. Before entering the measuring chamber for the inert gas, the carrier gas passes through the reference and sample cells equipped with a thermal conductivity detector. The gas line for the background measurement is shown by the dotted line. A diagram of the Netzsch apparatus[136] for the simultaneous measurement of ETA–DTA–TG/DTG is shown in Fig. 69. General views on the commercial Netzsch devices for ETA coupled with DTA and DTA–TG/DTG are shown in Figs. 70 and 71, respectively.

5.2.5. Radiation safety of ETA measurements

In the course of all the years when ETA has been applied, the question has been posed about the biological hazards of radioactive inert gases used for labeling solids. According to the actual knowledge of protection of a human body against radioactive radiation, the following remarks seem to be appropriate.

The labeling of samples by radioactive inert gas or their parent has to be performed in a specially equipped laboratory certified for work with radioactive isotopes. Any handling of the radioactive labeled substances (as weighing, inserting into a furnace, taking out from the furnace, etc.) requires safety precautions normal for work with radioactive emitters. Rubber gloves are used to protect the hands and the crucibles are handled by a tweezers. The labeled samples have to be stored in a box under a small vacuum to minimize the hazard of the escape of the radioactive emanation into the laboratory atmosphere (active deposits nuclides formed by the decay of radon isotopes could enter the lungs as aerosols).

The ETA apparatus itself can be installed in any chemical or physical laboratory equipped with a digestory exhaust. ETA is the micromethod (the sample amount needed for a measurement is about 10–100 mg), the carrier gas system has to be gas tight, the gas led to a suitable exhaust. The labeling of substances is made by traces of inert radioactive gases which, after dilution by the carrier gas, do not represent a biological hazard. The inert gases themselves do not enter into the metabolic system of the organism. Especially when ^{85}Kr is used as the inert gas label, the work with labeled substances requires a minimum of safety precautions. The isotope, ^{85}Kr, does not form any radioactive deposit and decays to a stable nuclide. It is used in medicine as a radioactive tracer for the examination of heart function.

5.3. The apparatus response to inert gas release

The apparatus response with ETA is always somewhat delayed and distorted to the actual inert gas release from the sample studied. For evaluation of ETA measurements involving the change of inert gas release with time or temperature, it is essential to know quantitatively the relation between the apparatus response and the actual inert gas input. This knowledge enables the changes on the ETA curve to be properly identified with a particular time or temperature. The detailed analysis of the

degree of distortion of the apparatus response curve to the actual inert gas changes is also essential to ascertain the magnitude and rate of changes of the inert gas release.

The most frequently used ETA apparatus is based on the continuous flow system of inert gas release rate measurement. This type of apparatus enables the measurement of the inert gas release rate in dynamic conditions of the sample treatment, that is, using the same conditions as other thermoanalytical methods.

In this Paragraph attention will therefore be paid to the response curves of the ETA apparatus representing the emanation release rate as a function of time or temperature. The degree of distortion of the response curve will be analyzed by comparing the ETA release signal to the inert gas input. When a change of inert gas release rate of the sample occurs during an experiment, the full response in the measuring chamber to this change will be slightly delayed, and as shown in practice, it will be somewhat distorted. The delay of the signal caused by the transport of the inert gas from the sample to the measuring chamber and the distortion of the signal caused by a dilution of the inert gas in the carrier gas are analyzed in the following. Under steady-state conditions, with uniform gas flow and constant emanation release rate, the signal of the inert gas detector is proportional to the rate of inert gas release from the sample. If a change in emanating release rate occurs in the sample, the ETA signal to this change will not be immediate. The change in inert gas release will firstly alter the concentration of the inert gas in the carrier gas flowing at the rate u. This new concentration must then be carried through volume V_1 of the system between sample and measuring chamber before any change in activity is detected. The time between the change and the first sign of response to a change is approximately (V_1/u)sec. The steady-state activity of the new inert gas concentration will not be fully attained until a sufficient quantity of the carrier gas has been swept through the system to fill the measuring chamber completely at the attained inert gas concentration. The rate of activity change in the measuring chamber due to the new inert gas concentration will also be a function of volume V_2 of the measuring chamber and the carrier gas flow-rate u. The time needed for attainment of the steady-state activity is approximately (V_2/u) (in sec). This means that the carrier gas flow system has a definite time constant which can be denoted as T_f. The detection system itself, consisting of the inert gas detector (ionization chamber, G.M. tube, scintillation or semiconductor detector) and connected with the count-rate meter or γ-spectrometer, has the time constant, T_d.

5.3.1. Mathematical analysis of practical cases

If $x(t)$ is the total radioactivity of gas in the measuring chamber at time t and $y(t)$ is the response of the ETA apparatus, we can write

$$dy/dt + (1/T_d)y = A \cdot x(t) \tag{89}$$

where T_d is the detection system time constant and A is the instrumental constant which includes amplification factors and has the dimension $[s^{-1}]$.

The actual change of gas radioactivity in the measuring chamber is then evaluated by

$$dx/dt = \alpha(t) - \lambda x - (u/V_2)x = \alpha(t) - (1/T_m)x \tag{90}$$

where $\alpha(t)$ is the rate of adding the radioactive gas in the chamber which is related to the input of the radioactive gas $\alpha_1(t)$ as $\alpha(t) = \alpha_1(t) - \lambda(u/V_1)$, λx is the gas radioactivity decrease due to decay, $(u/V_2)x$ is the activity decrease due to the gas flow from the chamber, $\lambda(u/V_1)$ is the decrease of gas radioactivity due to the decay during the transport from the sample to the measuring chamber, T_m is the time constant of the measuring chamber, $1/T_m = \lambda + (u/V_2)$.

It follows from eqns (89) and (90) that the radioactivity signal $y(t)$ measured by the ETA apparatus is related to the unknown activity, $\alpha(t)$, entering the chamber by

$$d^2y/dt^2 + [(1/T_m) + (1/T_d)]\, dy/dt + (1/T_m T_d)\, y = A\alpha(t) \tag{91}$$

The solution of eqn (91) given by Gregory and Howlett[220] is

$$y = \frac{A}{(1/T_d) - (1/T_m)} \left[e^{-t/T_m} \int_0^t e^{t/T_m}\, \alpha(t)dt - e^{-t/T_d} \int_0^t e^{t/T_d}\, \alpha(t)dt \right] \tag{92}$$

This entirely general expression makes it possible to derive the apparatus effect of any variation of initial activity. The appropriate function, $\alpha(t)$, has to be substituted in eqn (92). Particular cases will next be analyzed.

(A) Constant value of activity. If $\alpha_1(t)$ has a constant value (so that $\alpha(t)$ is constant), then $y(t)$ will tend to have a constant value. The steady state value of y can be written

$$y = A\, T_d T_m \alpha \tag{93}$$

This means that if $A\, T_d T_m = 1$, then y can be measured directly without change of scale.

(B) Linearly varying activity. If the activity input is a linear function of time, $\alpha(t) = K\, t$, then the response is

$$y = \frac{K\, A}{(1/T_r) - (1/T_m)} [T_m\{t - T_m(1 - e^{-t/T_m})\} - T_d\{t - T_d(1 - e^{-t/T_d})\}] \tag{94}$$

The function inside the square brackets in eqn (94) is plotted in Fig. 72. It follows from eqn (94) and Fig. 72 that the actual response is linear since the non-linear terms, e^{-t/T_m} and e^{-t/T_d}, converge to zero after a long time compared with either T_m or T_d. For this case, eqn (94) can be written as

$$y = K[t - (T_d + T_m)] \tag{95}$$

if $AT_dT_m = 1$. This means that ultimately the response rises (or falls) at the same rate as the input but lags behind by a time $(T_d + T_m)$. This lag is independent of the rate change of the input but depends on the volume of measuring chamber V_2 and the

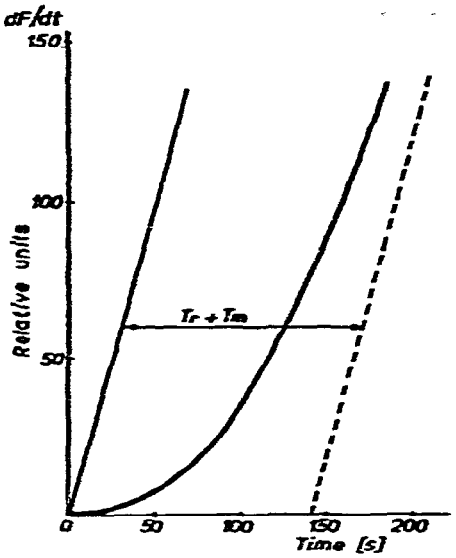

Fig. 72. Apparatus response to linear rise in inert gas release.

rate of the carrier gas flow u. The response of the activity drop is proportional to its input for slower release rate measured during the drop than that of the "decay curve" (the "decay curve" is familiar to experimenter since it occurs whenever the carrier gas flow is switched to background measurement). There is no limit to the inert gas release rate in which the observed activity can rise, as this is also dependent on the rate of the inert gas mixing to the carrier gas stream.

(C) Particular pulses of activity input. Response curves were calculated[220] for selected types of activity pulses which are approximations to the actual inert gas release input:

(i) Square pulse (vertical rise of inert gas release to a constant value h and after a certain period vertical drop to the original value). This example can be very easily produced artificially and afford opportunity to test the theory against practical results. It can also serve as an approximation to the input in the case of certain phase transitions when the rise of inert gas release is almost instantaneous.

(ii) Triangular pulse (the inert gas release rises linearly with time from zero to a certain time and then falls at a rate equal to the rate of rise).

(iii) Sharp peaked "parabola sided pulse" (the inert gas rises proportionally to the square of the time for a fixed interval and then falls along a curve which is a mirror image of the rise curve).

Examples (ii) and (iii) approximate the inert gas release during certain solid-state reactions. The response functions of these three pulses have been calculated[220]. Figure 73 shows the shapes of pulses in the origin and in the distorted form resulting from the ETA apparatus equipped with an ionization chamber and the count-rate meter (the respective time constants being $T_m = 59.4$ s and $T_d = 82.3$ s). It has been shown that the areas of the input and response curves are equal. For simplicity of

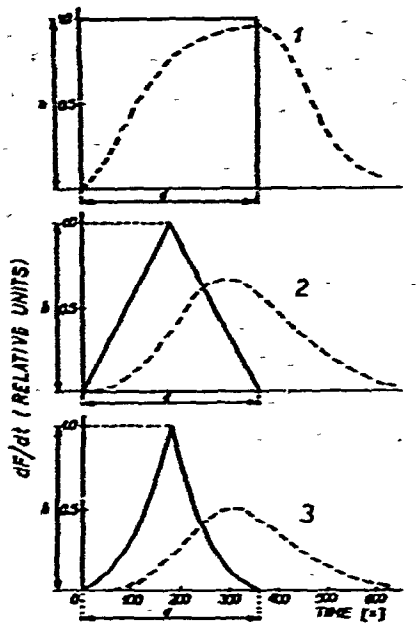

Fig. 73. Apparatus response to square (1), triangular (2) and parabolic (3) pulses of inert gas release. The input pulses are represented by full lines; the apparatus response by dotted lines.

calculations, the zero basic line of activity was taken in all three pulses but the same type of response occurs when the pulses are superimposed on a steady activity.

In all cases, the output curve is related to the original curve of activity change in that the amplitude is reduced and the duration extended. The time interval between the actual and observed maxima of activity can be exactly determined. Gregory and Howlett[220] derived expressions for evaluating positions of the maxima, $t_{max.}$, on the time axis and stated that the lag, $[t_{max.} - (d/2)]$, representing the distortion of the pulse for a given type of input effect is only a function of d (the pulse basis) and is entirely independent of the pulse magnitude h. When d approaches zero, the lag, $[t_{max.} - (d/2)]$, approaches the same limiting value for all of the pulse types and can be expressed as

$$t_{max.} - (d/2) = [T_d T_m/(T_d - T_m)] \log_e(T_d/T_m) \qquad (\text{for } d \to 0) \qquad (96)$$

For the ETA apparatus utilizing the small volume measuring chamber (V_2 = 8.4 cm^3) with a scintillation detector connected to a count-rate meter (integration time being 10–30 s) and the gas flow-rate used, 0.33 cm^3 s^{-1}, for T_m = 20 s and T_d = 10–30 s, the limit value of the lag $[t_{max.} - (d/2)]$ is 24.3 s. This time can be regarded as the displacement of the maxima of input and response for any peak and is very important for the practical evaluation of inert gas release measurements and the interpretation of the ETA curves.

Let us estimate the average uncertainty of ETA curves during linear rise of temperature when the lag between the input and response signal is not taken into account. When a change of emanation release rate is observed on the ETA curve, the

response will lag ($T_m + T_d$) sec behind the input. For the small volume chamber with a scintillation detector and using an integration time on the count-rate meter of 10–30 s, the constants T_d = 10–30 s, and T_m = 10–20 s. When a heating rate of 5°C min^{-1} is used, the observed temperature of the effect is by 2–3°C too high. Another conclusion arising from the above analysis is that a possibility exists not to detect a short sharp peak even of considerable amplitude when the time constants of the apparatus are excessive. It is therefore advisable to design the rate-determining constants of the ETA apparatus to give it rapid response characteristics, i.e., to make T_m and T_d sufficiently small. The value T_d for the ionization chamber itself can be reduced to a few seconds and for a scintillation and semiconductor detector connected to a count-rate meter, T_d is of the order of counting integration time, usually between 10 and 30 s.

The value T_m can be reduced by increasing u, the gas velocity and decreasing V_2, the volume of the measuring chamber, since

$$1/T_m = \lambda + (u/V_2); \tag{97}$$

The volume between the sample holder and the measuring chamber should be as small as possible. However, a reduction in the total time constant makes the ETA apparatus respond more readily to statistical fluctuations in the activity. No further advantage can be therefore attained by reducing T_m and T_d beyond the stage where statistical fluctuations begin to compare in magnitude with the variations of the inert gas release measurement. The optimum velocity of the carrier gas flow can be evaluated by means of eqn (87). In view of the analysis of the response curve of ETA equipment it is possible, in principle, to calculate the exact shape of an input pulse producing a given response by using the differential eqn (91). In eqn (89) the function, $\alpha(t)$, is the input function to be determined, $y(t)$ is known, dy/dt and d^2y/dt^2 are to be found by numerical differentiation. The digital form of the monitoring experimental results is most suited for the immediate evaluation of the input curve from the response curve. It should be mentioned, however, that this is not a quite satisfactory way, since the differentiation accentuates all the irregularities in the observed response and no very precise information is to be expected from it.

5.4. Some recommendations for practice

The reproducibility as well as the accuracy of the experimental measurements depend mainly on the determination of optimal experimental conditions of the measurement. Some recommendations for the practice of ETA measurements are summarized here.

What should be done before the proper measurement of the ETA curve?

1. Choice of the carrier gas flow velocity.
2. Determination of apparatus time constants T_f, T_m, T_d.
3. Choice of working voltage for G.M. tube or scintillation detector, measurement of the detector characteristics.
4. Measurement of the radioactivity background.

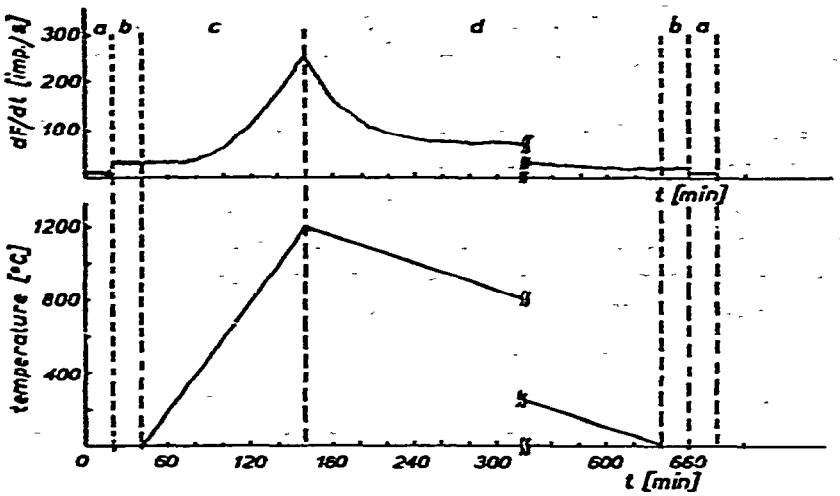

Fig. 74. An example of the ETA curve when no chemical nor physical transition takes place in the sample measured. The curve is recorded as the time-dependence of emanation release rate dF/dt during (a) background measurement; (b) sample measurement at room temperature; (c) sample measurement during linear heating rate; (d) sample measurement during linear cooling rate.

5. Measurement of ETA standard, determination of the "decay curve" after having switched to background measurement.

6. Choice of the appropriate heating (cooling) rate with respect to the solid-state process studied.

What should be done during the ETA measurement?

1. The stability of the working parameters of the apparatus (voltage, flow-rate, etc.) to be checked.

2. The radicactivity background determination is sometimes carried out during the experiment. Using radon isotopes, the background increases slightly in the course of the ETA measurement, which is caused by the presence of an active deposit in the measuring chamber. A $\pm$ 1.5% deviation of the background was found after a 9-hour measurement of the steady state emanation release rate of ^{220}Rn at 18,700 $\pm$ 160 counts s^{-1}. After a few minutes, in case of ^{220}Rn, the background diminishes as the active deposite itself decays.

3. It is recommended to make the ETA measurement of one sample at least twice to be sure of the reproducibility of results and to exclude the accidential irregularities of the curve. Figure 74 shows the general view of the registered ETA curve of a sample labeled by ^{228}Th and when radon diffusion takes place only at sample heating and cooling.

What should one know before evaluating the ETA release curve? In view of the possible distortion and the time shift of the ETA apparatus, the following items should be borne in mind:

1. The steady state activity value on the ETA response curve is proportional to the input activity.

2. When the activity changes linearly, the slope of the response curve is not

distorted and the time shift caused by the lag between the inert gas change and the observation of this event must be taken into account. The time shift is determined by apparatus constants ($T_m + T_d$).

3. For peak-like effects on the ETA curve (when inert gas release rate dF/dt is measured), a limited quantitative relationship between the actual inert gas release rate and its response can be obtained. The areas under the response curves and the corrected curves (evaluated input) are equal. The exact shape of the input pulse as well as the time lag for the maxima of input and response for any peak can be evaluated. Therefore, only the time shift of the ETA curve should be taken into account with integral emanation release curves (when released fraction F is measured).

4. Prior to making any conclusions about the solid-state process, one has to establish the relation between the evaluated input release data and the proper change in the solid. If the inert gas release measured reflects the process studied through the parent or intermediate nuclide, their roles should be determined.

Chapter 6

APPLICATIONS OF ETA

6.1. Possibilities and limitations of the method

6.1.1. Potentialities of ETA investigations

As mentioned earlier changes in emanation release rate serve as the indication of processes occurring in solids such as loss of water, decomposition, behavior of gel structure, recrystallization of the solid, solid-state interaction, etc., permitting the investigation of metastable pseudo-amorphous phases issuing from the thermal decomposition. At higher temperatures, the general breakdown in structure immediately preceding the solid transitions is demonstrated by a sudden increase of the emanation release rate of the substance followed by a sharp drop when the new phase recrystallizes. A large number of investigations describing such phenomena was published during the last fifty years.

Recently, ETA was applied to well-defined systems in an attempt to gain some further insight into the migration processes which occur in solids. There is no a priori reason why the diffusion of the inert gas atoms in the solid lattice should in any way be related to self-diffusion processes but some studies[11, 12] strongly suggest some kind of empirical relationship, the nature of which depends on the mechanism of inert gas diffusion in the respective solid. Nevertheless, it was proved that the inert gas diffusion reflects very sensitively transport phenomena in solids. For example, the degree of disorder, biographical or radiation defects in definite temperature ranges can be estimated. Of these two types of investigation, the former is essentially qualitative and the latter quantitative. In the first case, it is not possible to do more than associate trends in emanation release measured with changes in the solids and to use this method as a rather convenient and objective means of arriving at the sort of results in principle also obtainable by other physical measurements such as DTA, TG, microscopy, surface area measurement, etc. Where actual phase transitions are being sought for, ETA serves as a useful complement to classical thermoanalytical techniques, with the advantage that sensitivity is not dependent on the heat of transition or changes of mass.

The mode of solid labeling in ETA is chosen with regard to the type of measurement. In the first type of investigation, where no special attention is paid to the mechanism of inert gas diffusion in the solid, the inert gas distribution within a solid should be estimated. On the other hand, if any attempt is to be made to derive quantitatively diffusion characteristics from the ETA measurements, the questions of inert gas distribution within the solid and diffusion mechanism become extremely important since any theoretical approach must start with the assumption of some well-defined constant distribution of the inert gas or its immediate parent within the solid.

There exists one drawback when using a parent of emanation for labeling solids.

This is the fact that the inert gas, ^{220}Rn, is obtained only from ^{228}Th through the intermediate daughter, ^{224}Ra. Starting from an initially uniform distribution of ^{224}Ra in the solid, some redistribution can occur as a result of diffusion at high temperatures. This can give rise to a concentration of ^{224}Ra near the surface in excess of the normal radioactive equilibrium concentration and the resulting values of inert gas release rate are higher than would correspond to the equilibrium. This "^{224}Ra rejection" has been observed in solids of the cubic form CaF_2, after having been heated to fairly high temperature (about 2/3 of the absolute melting point). With substances of the hexagonal corundum type, the "^{224}Ra rejection" was not observed. The probability of this process depends on the nature of solids and on the type of lattice and the density of lattice defects. When the density of trapping sites for ^{224}Ra and ^{220}Rn in the structure of the labeled solid is high enough, the uniform distribution of the parent should remain during the heat treatment. It was recommended[223] to use the carrier gas medium for this type of ETA investigations which would diminish the eventual "^{224}Ra rejection" in the lattice, such as for UO_2, a hydrogen-containing gas medium. To avoid this complication in principle, the direct incorporation of the inert gas atoms without parent is usually employed for sample labeling when the inert gas diffusion characteristics in a solid have to be determined.

6.1.2. Limitations of the method

Using the parent nuclide ^{228}Th for sample labeling, a high-temperature limitation exists for the ETA application with substances where so-called "^{224}Ra rejection" described in the previous paragraph 6.1.1. takes place. Otherwise no high temperature limitation exists with regard to the inert gas used for the ETA investigations. However, a low-temperature limitation of the ETA applications exists, being caused by the condensation of the inert gas used for sample labeling. The respective temperatures as given in Table 16, are: — 65°C for radon, — 107°C for xenon, — 153°C for krypton and — 186°C for argon. The processes taking place in solids at lower temperatures than those indicated cannot be investigated by ETA.

There exists a limitation of the sensitivity of the ETA apparatus. The sensitivity of the apparatus using a continuous flow system is very dependent on the apparatus constants, T_f, T_d and T_m (see Paragraph 5.2.2.). It is therefore no surprise that the ETA equipment used by early investigators may not have been able to detect small changes in emanation release and the possibility of a quick response did not exist. The results of the ETA measurements, published in the years before electronic counting and recording equipment became widely available, may have a relatively high degree of uncertainty. In spite of this, some results of this period have been quoted and demonstrated in this work.

6.2. Surface area investigations

6.2.1. Direct surface area measurements

As follows from the theoretical considerations given in Paragraphs 3.2.3.3 and

3.4, the emanation power of the solid labeled by an inert gas parent is proportional to the surface area:

$$E = E_R + E_D = K(T)\,S \tag{98}$$

This expression has been verified experimentally by Heckter[120] who measured the emanation power of labeled glass rods at 25°C and determined the surface area under a microscope. The proportionality has been found between E_R (ranging from 0.2–1.0 $\times$ 10^{-6}) and the surface area (ranging from 8–10 cm^2g^{-1}). The expressions derived are mathematically justified for single grains of solid larger than the path of recoil atoms R in the solid (about 1 μm in diameter) in which the diffusion coefficient is small and where spacing of grains is larger than the path of recoil atoms in air or respective medium. If the surface area should be directly determined on the base of the emanation release rate measured, the experimentally found E value has to be separated into E_R and E_D. The separation usually causes no problems for ionic solids where inert gas diffusion can be neglected at room temperature and $E_{25°C}$ measured can be taken for the E_R. For other cases, another method has been proposed for the resolution of E_R and E_D, consisting of the application of two inert gases. By incorporation of the parents of two isotopic inert gases in the same solid and measurement of the emanating power of the sample for each inert gas, the surface area and the inert gas diffusion coefficients in the solid can be determined.

Where a homogeneous distribution of inert gas parent within the solid was assumed, a direct proportionality between E_R and S was found by experiment. For a non-homogeneous distribution, a linear dependence instead of the direct proportionality has been verified[116] or:

$$E_R = C' + K\,S \tag{99}$$

In solids where the size of grains are comparable or smaller than the recoil path R, or where the grains agglomerate, there is no mathematical justification to use the simple expressions for direct surface determination from the emanating power measured. In spite of this, in some cases of finely dispersed solids a simple linear relationship between E_R and S has been found experimentally for such examples as γ-Al_2O_3[224], ThO_2, MgO, ZrO_2[225], NiO, γ-MnO_2[226] and MgO[227]. Figure 75 shows the experimentally found dependence between E_R and S for ThO_2, MgO and ZrO_2 (Fig. 75a) as well as for NiO prepared by thermal decomposition of Ni-hydroxide and Ni-carbonate (Fig. 75b). The proportionality constants K for the two NiO specimens differ which indicates that constant K depends on the texture of the dispersed solids. For samples where the simple relationship existed between E_R and S, the values of surface area ranged between 1.0 and 300.0 m^2g^{-1}. However, there exist a number of dispersed solids where the simple relationship between E_R and S has not been found, such as Fe_2O_3[23], ThO_2[228, 229], Ag_2O[230]. The surface area values of these samples ranged between 0.1 to 10 m^2g^{-1}.

As no a-priori reason exists for the existence of the simple relation between E_R and S of the dispersed solids, it is necessary to verify the existence of this simple

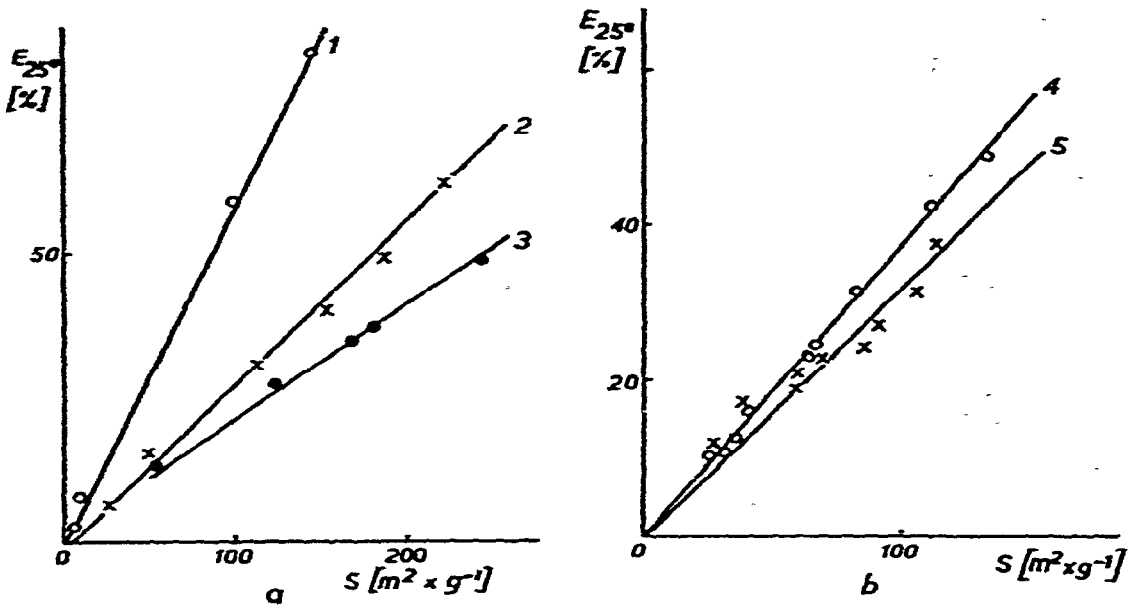

Fig. 75. Dependence between emanation release $E_{25°C}$ measured at room temperature and specific surface area. (a) For ThO_2 (1), MgO (2), and ZrO_2 (3). (b) For NiO prepared by thermal decomposition of Ni-hydroxide (4), and Ni-carbonate (5).

relationship in each case of solid and the range where surface area is to be determined. There is no necessity to use ETA for measuring the surface area of isolated grains or dispersed solids, as the BET and other methods are available. However, ETA seems to be the most suitable method to investigate the surface area (and texture) evolution immediately at the experimental conditions of treatment of solids. ETA has been advantageously employed for the investigation of aging of precipitates, sintering solids under dynamic experimental conditions, etc.

6.2.2. Development and changes of surface in gelous materials

In the early period, ETA has been employed for studying the effects of aging of iron(III) and thorium hydroxides. The ^{228}Th parent was coprecipitated with hydroxides by addition of ammonia. Emanating power values were determined by the active deposite method by measuring the beta radiation. When precipitated cold, freshly prepared iron(III) and thorium hydroxides have high emanating powers (about 80%). When the hydroxides are stored in moist air (80% relative humidity) their emanating power values are practically constant, decreasing by 1–5% in one year. The digestion of gels under water at 100°C greatly accelerates the aging process. The acceleration of the aging has been studied by ETA and the results are shown in Fig. 76. Under the given experimental conditions the aging process proceeds much more intensively with iron(III) hydroxide than with thorium hydroxide. Hahn and Graue[231] associated the decreasing emanating power with surface shrinkage and recrystallization. The relationship between the aging of gel and the storage time of thorium colloid solution was established[231].

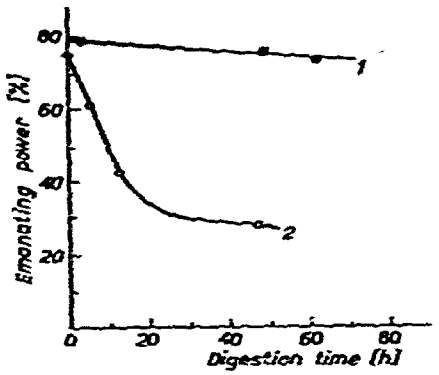

Fig. 76. Aging of Th-hydroxide (curve 1) and Fe(III) hydroxide (curve 2) during digestion in water at 100°C.

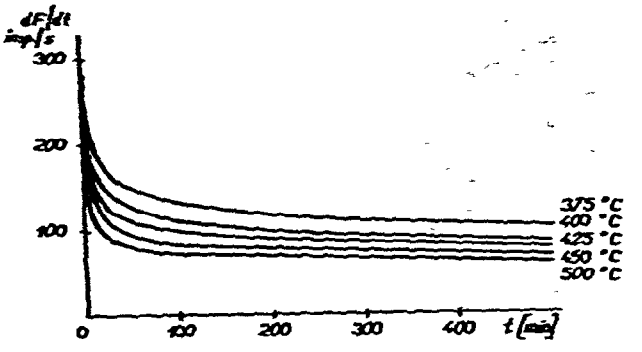

Fig. 77. ETA curves of NiO (ex-carbonate) during isothermal treatment in nitrogen at temperatures: 375, 400, 425, 450 and 500°C.

Other gels have also been studied by ETA. The difference in behavior between freshly precipitated and aged (recrystallized) gelous ammonium diuranates was shown by Balek and Urbánek[232].

6.2.3. Sintering and related phenomena

Qualitative studies on the kinetics of sintering first stages of powdered solids have been published for Cu powder by Schreiner and Glawitsch[233] and for Fe_2O_3 by Balek[136]. Quantitative evaluation of the kinetic studies of surface area changes has been made by Gourdier et al.[226] for NiO, Quet and Bussière[227] for MgO and Balek and Bussière[228] for ThO_2. Recoil emanation release rate as well as diffusion emanation release rate have been used for evaluating the kinetics of the first stages of sintering. How the recoil emanation release rate E_R has been employed[226] will be described below.

First of all, the simple relationship between E_R and S has been verified for NiO powders. As E_R has been found to be proportional to S in the respective surface area range (see Fig. 75b), the ETA curves measured during isothermal treatment at temperatures where E does not substantially differ from E_R, can be used for the evaluation sintering kinetics. Figure 77 shows the emanation release rate of NiO measured during isothermal treatment in nitrogen at temperatures between 375 and 500°C. These curves are claimed[226] as providing continuous measurement of surface area changes with a relative accuracy of about 2% for the sample treated. For the first hour of the isothermal treatment, the following kinetic law has been proposed:

$$dS/dt = -KS^n \qquad (100)$$

where S is the surface area, t time, and n the apparent reaction order, equal to 7.

A second stage of sintering beginning after one hour of initial heating and lasting several hours, is described by the equation:

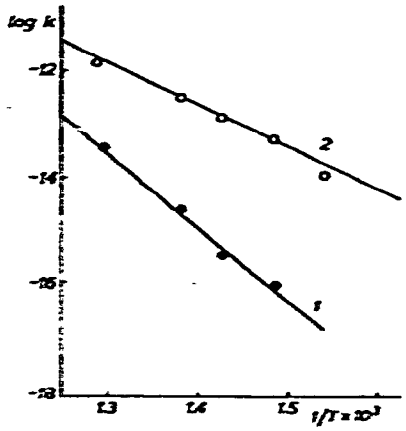

Fig. 78. Temperature-dependence of kinetic constant K of NiO sintering during isothermal treatment in oxygen (curve 1) and nitrogen (curve 2).

$$\log (S - S_{eq}) = k\,t \tag{101}$$

where S and S_{eq} are the surface area values at time t, and after equilibrium has been reached, t is the time.

The temperature dependence of the kinetic constants differ when NiO samples were heated in nitrogen or oxygen. The apparent activation energy evaluated from the Arrhenius plots in Fig. 78 equal 276 and 155 kJ mol^{-1} (i.e., 66 and 37 kcal mol^{-1}) for nitrogen and oxygen treatment, respectively. An analogous evaluation of the kinetics of sintering first stages was made[227] for MgO.

In cases where no simple relation between E_R and S has been found, the described method cannot be applied. For these cases, values of E_D have been proposed[228] to be used for evaluating the kinetics of the sintering process. The evaluation of the sintering initial stage using E_D-values has been made for ThO_2 powder in the temperature range between 700 and 825°C. This temperature range corresponds to 0.30–0.34 of the absolute melting temperature. No simple relationship has been found between E_R and S ranging between 0.1 to 15 m^{2}g^{-1}.

Figure 79a shows the time dependence of total emanation release rate E measured during isothermal treatment at 705, 735, 780 and 825°C. Fig. 79b shows the dependence between the respective values of E_D and time (E_D being determined as $E_D = E - E_R$) plotted on a bilogarithmic scale.

As $E_D = K_2\,S$, where $K_2 = (D/\lambda)^{1/2} \cdot \rho$ and S the effective surface area, the following kinetic law has been proposed for the thoria sintering first stage:

$$\log S = n \log t + \text{const.} \tag{102}$$

The results obtained permitted the authors[228] to make the conclusion that the sintering of the sample studied in the respective temperature range is controlled by a single mechanism. The effective surface area used in eqn (102) can differ from the surface area determined by adsorption methods. This value, resulting from the slowing down emanation release rate at the given temperature, involves information about the state

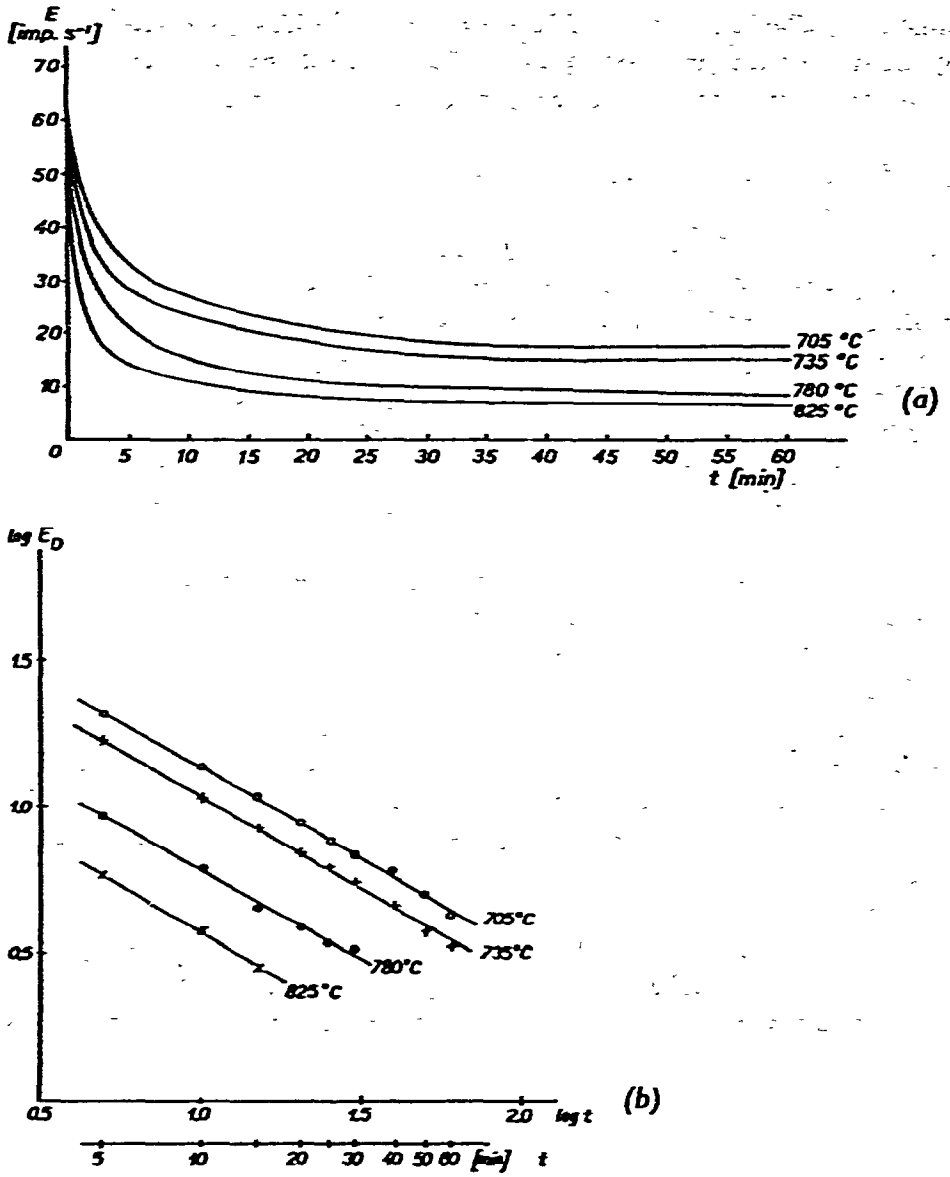

Fig. 79. ETA curves of ThO_2 (ex-oxalate) during isothermal treatment in air at temperatures: 705, 735, 780, 825°C. (a) Values of emanation release rate, E_{total}, related to time. (b) Dependence of log E_D = f (log time) where E_D is evaluated as $E_{total} - E_{25°C}$.

of active surface controlling the sintering initial stages. The effective surface area reflected by the measurement of diffusion emanation release rate is therefore more convenient to describe the powder behavior during the first stages of sintering, than the surface measured by an adsorption method. ETA makes it possible to follow immediately the changes in active surface, including its annealing, and to evaluate quantitatively the kinetics of these changes. By studying the temperature dependence of the kinetic constant K_2, the activation energy of radon diffusion in thoria powder

has been determined[234]. The value, $\Delta H = 222 \pm 20$ kJ mol^{-1} (52.9 ± 4.6 kcal mol^{-1}), supports the supposition of the grain boundary diffusion mechanism which controls the first stage of sintering of thoria in the temperature range studied.

6.3. Investigation of single phase systems

6.3.1. Inert gas release as a probe of the state of solids

6.3.1.1. Mobility of the inert gas atoms in relation to other properties of solids. The mobility of inert gas atoms has proven to be a suitable parameter for describing the state of solids and studying its changes. Generally speaking, the inert gas mobility is determined by the diffusion mechanism which takes place in the respective solid. The possible mechanisms of inert gas diffusion in ionic crystals are discussed in Paragraph 4.4.2. The change in the mobility of inert gas in solids is usually connected with the change in other properties of the solids. Property changes normally occur when

(i) The solid undergoes a phase change or sinters (see Paragraph 6.2.3).
(ii) The solid reacts with the surrounding medium.
(iii) A change in lattice defects concentration takes place.
(iv) The mechanism of diffusion changes.

Examples covered under items (i), (ii) and (iii) have been given in Paragraph 3.8. and 6.2.8. (sintering), respectively. As this Paragraph is dealing with the investigation of single phase systems, the properties of solids will be discussed in relation to the inert gas mobility in solids, which do not undergo any structural or chemical change within the studied temperature range.

A. Diffusion properties of solids.

The diffusion properties of α-Al_2O_3 were demonstrated by Gregory and Moorbath[47] using radon ^{220}Rn diffusion after homogeneous labeling of the samples. Figure 80 shows two independent processes which characterize the diffusion properties

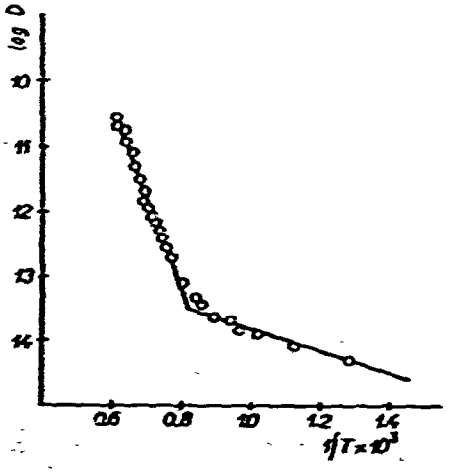

Fig. 80. Plot of log D versus $1/T$ for α-Al_2O_3 preheated to 1350°C.

of the solid. The transition from one process to another takes place at 1198 K which is 0.52 times the absolute melting temperature, T_{melt}. Schneider[235] reported that for metallic Cu, Fe and Mo homogeneously labeled by ^{224}Ra, the intersections of the lines corresponding to two radon diffusion processes have been found at temperatures between 0.3 and 0.4 T_{melt}. At the temperature ranges of 0.5–0.52 T_{melt} for ionic crystals and 0.3–0.4 T_{melt} for metals[12], originally described by Tammann[124], many physical effects dependent on diffusion begin to proceed at a rate which is readily measurable in a reasonable time. This temperature has a close connection with the speeding up of sintering, annealing, recrystallization, etc.

From the $\log D = f(1/T)$ curve of α-Al_2O_3 (Fig. 80), it was found that the activation energy of radon diffusion above the intersection point is $\Delta H_1 = 250 \pm 2$ kJ mol^{-1} (59.6 $\pm$0.5 kcal mol^{-1}), whereas the low energy low temperature process has an activation energy of $\Delta H_2 = 33.5 \pm 8$ kJ mol^{-1} (8.0 $\pm$0.2 kcal mol^{-1}). The low temperature low energy diffusion of radon below the intersection point is supposed to be controlled by non-equilibrium lattice defects. Such a structure-sensitive diffusion process is therefore dependent on the previous thermal history of the oxide. Similar radon diffusion behavior has been observed with other oxides[41, 133] such as TiO_2, α-Cr_2O_3 and α-Fe_2O_3.

If the high energy high temperature radon diffusion in the oxides quoted becomes the dominant factor at a temperature identical to that at which self-diffusion is known to become appreciable, a connection between the two processes has been suggested. For example, in α-Al_2O_3 there appeared to be a connection between inert gas diffusion and lattice defect equilibrium (see further Paragraph 6.3.3). This connection cannot, however, be generally assumed in all solids as the mechanism of impurity-diffusion of the inert gas in various lattice types can differ.

TABLE 18

EMANATION RELEASE RATE MEASURED AT 25°C, SURFACE AREA AND VALUES $E_{25}{}^{\circ}c/S$ FOR BARIUM PHTHALATE, ISOPHTHALATE AND TEREPHTHALATE

Barium salt	*Formula*	*Emanation release rate* $E_{25}{}^{\circ}c$	*Surface area* (m^2g^{-1})	$E_{25}{}^{\circ}c/S$
phthalate	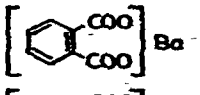	0.111	3.6	0.031
isophthalate	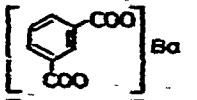	0.114	1.0	0.114
terephthalate	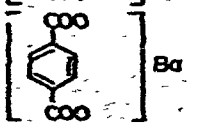	0.098	8.1	0.012

There exists the possibility to evaluate the radon diffusion characteristics of a solid directly from emanation release measurements. Correct relative values of diffusion coefficient D and quite accurate diffusion activation energies can be obtained. For determination of diffusion characteristics, see Paragraphs 3.3 and 4.2.

The diffusion properties of some organic solids and polymers have been studied on the basis of the inert gas release rate by Strassmann[135], Müller[236], Meares[237, 238], Zaborenko et al.[239–241], Gregory and Moorbath[242] and Balek et al.[243, 244]. Experimentally determined values of the ratio $E_{25\,°C}/S$ were used[244] for characterizing diffusion properties of barium salts of isomeric organic acids (phthalic, isophthalic and terephthalic). The positional isomerism of organic molecules was proved to markedly influence their diffusivity in the solid state. Table 18 shows the $E_{25\,°C}/S$ values determined for the organic positional isomers.

Progressively rising emanating power has been reported[242] for barium salts of long-chain monocarboxylic fatty acids. From barium acetate to laurate and palmitate the emanating power rose from 0.03 to 1.0. The increase in room temperature emanating power, which was explained to be due to high-diffusion release rate, may be better understood when looking at Fig. 81. Figure 81 shows the temperature dependence of emanating power for barium stearate, $(C_{17}H_{35}COO)_2$ Ba, and barium caprate, $(C_9H_{19}COO)_2$ Ba. This is typical for all barium salts of fatty acids where no decomposition or phase transformation occurs. In general, the salts of lower fatty acids were displaced more to the right than the higher fatty acids. At temperatures ranging from 0 °C with barium stearate to 50 °C for barium caprate, the emanating power reached a maximum and no further increase was observed with rise in temperature. The rapid decrease in emanating power with decreasing temperature immediately shows that the high values of emanating power at room temperature are due to the high diffusion rate of radon. At temperatures below 160 to 180 K, the diffusion contribution to the emanating power is very small and one would expect E values

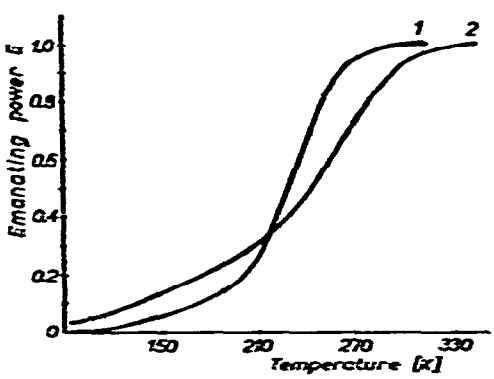

Fig. 81. Temperature-dependence of emanating power for barium stearate (curve 1) and barium caprate (curve 2) (after Gregory and Moorbath[242]).

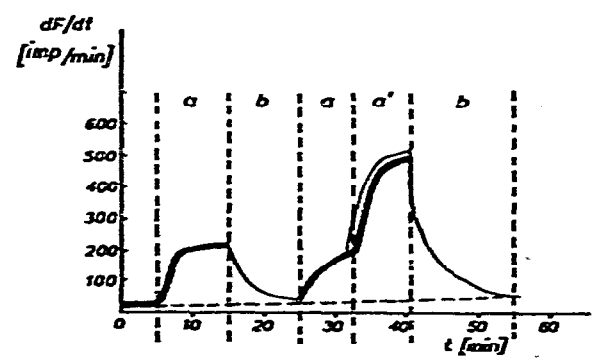

Fig. 82. Release of ^{222}Rn from nickel foil during vibration with corundum powder at room temperature (after Heinicke et al.[245]) a, a′ = at frequencies 4.2 and 7.2 Hz, respectively; b = in the time interval after vibration.

corresponding to the recoil fraction, dependent only upon the specific surface. However, at such temperatures and lower, an adsorption of radon on the surface of the solid took place and lower E values than expected were reported[242]. Relatively low values of activation energy for radon diffusion in all barium salts of fatty acids (ranging between 30 and 40.2 kJ mol^{-1} (7.0 and 9.6 kcal mol^{-1}) have been found in the temperature range of 200–300 K. The similar values of ΔH in all cases suggest that the mechanism of radon diffusion is the same for each barium salt.

The high proportion of structural defects has been suggested to explain the high diffusion rate of radon in the barium salts of fatty acids. The lower the molecular weight of the barium salt studied, the better defined is the crystal structure with less defects to provide low-energy diffusion paths. The disorder in Ba-salts of long-chain fatty acids was explained as resulting from the fact that the molecule is firmly bound in the lattice at the polar end only. The disorder therefore becomes greater the longer the chain and the lower the proportion of the polar groups to hydrocarbon groups. The high diffusion release rate in the barium salts of certain organic solids seem to be related to the presence of methyl group in the molecules[135]. The replacement of a terminal methyl group in barium caprate by a carboxylate group reduces the rate of diffusion one thousand-fold.

B. Mechanical properties of metals

The release of inert gas incorporated by ion bombardment into a metal surface can serve as the indicator of plastic deformation in the metal[245]. Figure 82 shows the release rate of radon from Ni-foil during its mechanical treatment. Ni-foil labeled by ^{222}Rn was vibrated with corundum powder at frequencies 4.2 and 7.2 Hz under dry nitrogen stream. The release rate of the inert gas has been found to be dependent

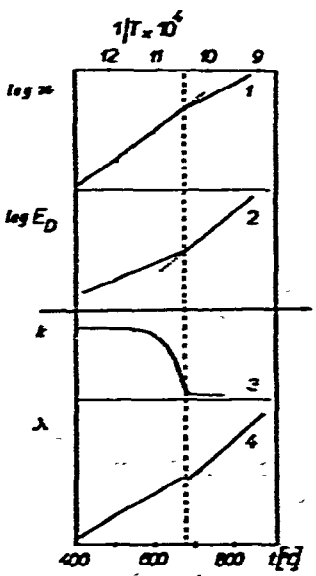

Fig. 83. Comparison of electrical conductivity (curve 1), magnetical susceptibility (curve 3), thermal conductivity (curve 4), and emanation release rate (curve 2) of ferric oxide measured in the temperature interval from 400 to 900°C.

on the intensity of the exposure of the metal surface to the mechanical treatment. As shown in Fig. 82, 3–5 minutes after the onset of the mechanical treatment a stationary stage of the radon release rate has been attained.

C. Electrical conductivity, thermal conductivity, magnetical properties

For comparison of electrical conductivity, thermal conductivity, magnetical susceptibility with the emanation release rate during a linear rise of temperature, a sample of α-ferric oxide was chosen[246]. The measurements were not carried out simultaneously[247, 248]. Figure 83 shows that changes of the above-mentioned properties take place in the same temperature range. When investigating the physical properties of solids and measuring the emanation release, it should be borne in mind that the state of diffusion equilibrium has to be maintained during sample heating or cooling. The rate of temperature rise or fall should be chosen after the evidence was obtained that the diffusion equilibrium is attained so rapidly that continuous heating or cooling at the chosen rate is justified. For the oxides investigated (α-Al_2O_3, α-Fe_2O_3 and α-Cr_2O_3), a heating rate of 5 K min^{-1} was justified and used.

6.3.1.2. Emanation characteristics of rocks and minerals. The natural rocks and minerals containing a known uranium concentration can be characterized by radon (^{222}Rn) escape. Studies on radon release rate from uranium-rich minerals have been reported by Homes[249], Gilette and Kulp[250], Lind and Whitemore[251] and others. For example, the emanating power of carnotites range from 0.16 to 0.50. The emanating power of bröggerite increases with decreasing grain size of the mineral.

Data on emanation release rate from common rocks and soils are very scarce in literature[36, 252, 253]. Baretto[253] published ^{222}Rn emanation characteristics of some common rocks and minerals using alpha scintillators combined with a photomultiplier tube as the measuring system. Under identical laboratory conditions, rocks have the emanating power values ranging from 0.01 to 0.20 and a specific radioactivity of 7×10^{-3} to 3×10^{-1} s^{-1} h^{-1} g^{-1} (i.e., 2 to 80×10^{-4} pCi h^{-1} g^{-1}). The highest *E*-values were found among granitic rocks, sandstone and conglomerates whereas basic and calcareous rocks showed the lowest values. Accessory minerals, although rich in uranium show very low radon emanating power (less than 0.01–0.02). The results clearly showed that the radon emanating power of a mineral is not related to the uranium concentration. Thus, xenotime and monazite with 6000 ppm and 400 ppm uranium, respectively, show smaller radon emanating power than biotite apatite or sphene with 11, 17 and 84 ppm of uranium, respectively. Figure 84 shows emanating power values of some minerals of constant grain size (60–115 mesh) measured at room temperature at constant humidity.

Emanation release measurements of the minerals heated up to 1200°C have demonstrated a progressive decrease in the emanation release rate with temperature. Two examples of ETA curves, for granite (origin Minnesota, U.S.A.) and for monazite (origin Beach deposite, Brazil) are shown in Fig. 85. The decrease in the emanation release rate was suggested to be a result of annealing surface defects, mechanical damage and natural radiation damage. The temperature effect on the ETA curve can characterize the stability of the crystal structure of the mineral once damaged.

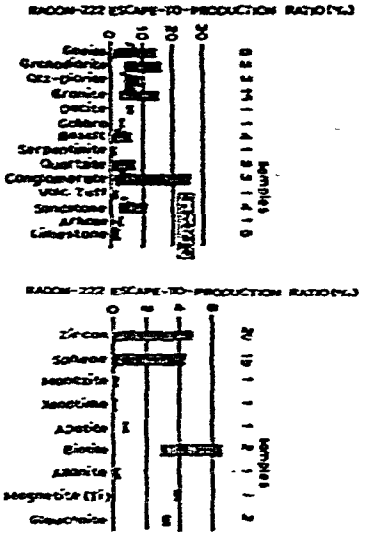

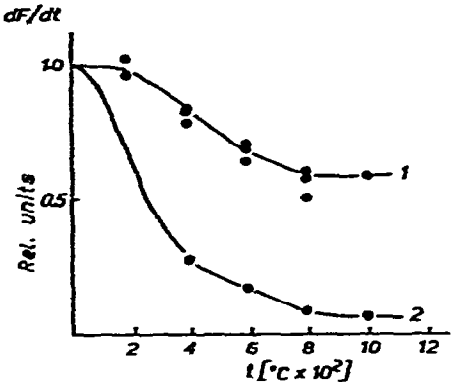

Fig. 84. Values of emanating power of some rocks and minerals (after Baretto[253]).

Fig. 85. Emanation release measurements of granite (curve 2) and monazite (curve 1) heated to 1200 °C (after Baretto[253]).

Minerals whose atomic structure will retain the radiation damage effects especially when reaching the metamictic state exhibit high emanating powers. Minerals of self-annealing properties, by contrast, will show a small emanation power value. In this case the diffusion is mainly through grain surface and mechanical defects, cracks, dislocations, etc. The emanation characteristics of minerals can serve as the indicator of the stability of their crystal structures. Because no chemical treatment is involved and soil samples can be analyzed as they are collected, ETA has been proposed[253] as an attractive tool for the detection of any mixture of uranium-bearing industrial products, such as tailings, in the regional soil background, road-base and the selection of construction material for schools and hospitals.

Evernden et al.[254] published data on diffusion of radiogenic argon in glauconite, microcline, sanidine, leucite and phlogopite. Measurements of argon release during sample heating have revealed dynamic lattice changes taking place in the mineral. Glauconite and phlogopite were characterized by identical diffusion parameters. The argon diffusion measurements at elevated temperatures enable the dating of events[49] which took place in the mineral a few million years ago.

6.3.2. Characterization of material properties

6.3.2.1. Texture of materials and annealing of lattice defects. As the recoil emanation release rate, E_R, strongly depends on the texture of the material (see Paragraphs 3.6 and 3.8), the E_R value can be used for characterizing the texture of powder as well as compact materials. Emanation release rates of Ba–Zn alloys (6–8 wt. % Ba) measured at room temperature after various degrees of plastic deformation can serve as an example[255]. The emanation release rate, E_R, was found to be dependent

on the degree of deformation of alloys homogeneously labeled by ^{224}Ra. The initial increase in E_R found with increasing deformation degree was in a good agreement with the decrease in density of the alloys.

It has been shown[255] for Zn–15Ba alloy (50% deformation degree) that the emanation release rate value, $E_{25°C}$, reflects changes in texture which have taken place

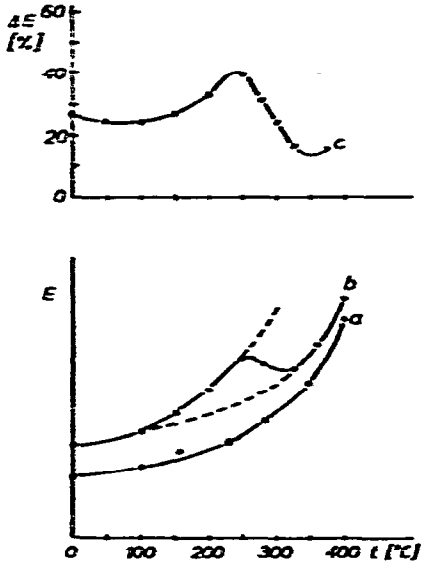

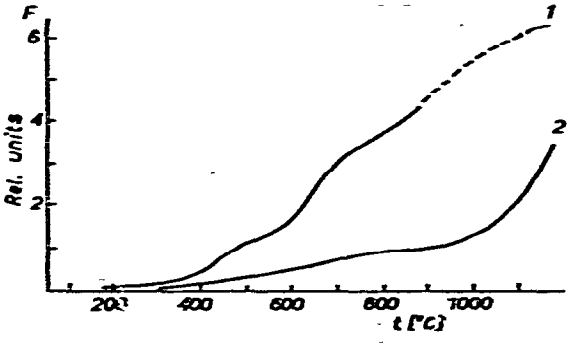

Fig. 86. Emanation release of Zn–1.5 Ba alloy (50% plastic deformation) heated to 410°C. a = Recrystallized sample after heating to 410°C; b = cold worked sample; c = differential curve obtained by subtraction of curve b from a.

Fig. 87. Released fraction F of ^{133}Xe from cold worked (curve 1) and soft silver (curve 2).

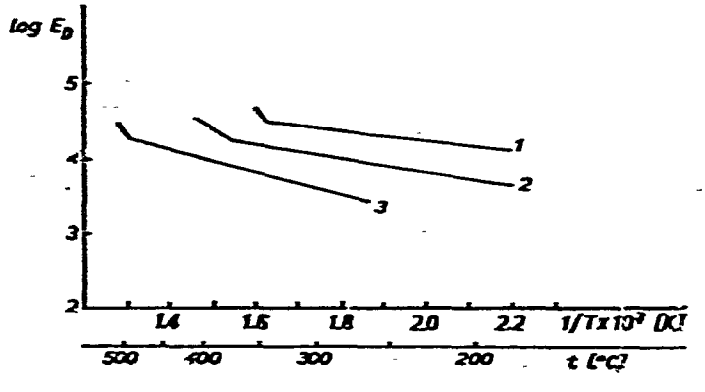

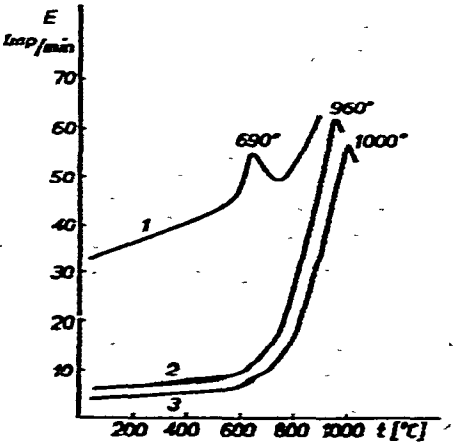

Fig. 88. Plot of log E_D versus $1/T$ for ferric oxide (ex-hydroxide) obtained during cooling samples pre-heated to 350 (curve 1), 410 (curve 2) and 530°C (curve 3).

Fig. 89. ETA heating curves of ferric oxide (ex-hydroxide) preheated to 500 (curve 1), 900 (curve 2) and 1000°C (curve 3).

during sample heating. The recovery of the deformation has taken place at about 250°C, which was indicated by the decrease of $E_{25°C}$ values, as shown in Fig. 86.

The evolution of the texture and its changes can be directly investigated when the emanation release is measured during sample heating. Results of more recent investigation[60] which characterize the textures of cold worked and soft silver on the basis of ^{133}Xe release during linear temperature rise are shown in Fig. 87. The annealing of the texture of cold worked metal (deformation degree was not indicated) is revealed when comparing curves 1 and 2. These curves correspond to the cold worked (deformed) and soft (non-deformed) silver samples, respectively.

The diffusion emanation release rate E_D measured at temperatures where surface and grain boundary diffusion are the controlling factors (see Paragraph 3.7) makes characterization of the texture possible.

Figure 88 shows the ETA curves of α-Fe_2O_3 measured during cooling at a linear rate of 2.5 K min^{-1}. Ferric oxide samples differing in texture were prepared by heating Fe(III) hydroxide to 350, 410 and 530°C. The ETA curve corresponding to the dispersed sample of more developed texture lies higher than that of the sample of a less developed texture, mainly because of smaller mean grain size causing increased E_D and E_R. The ETA cooling curve has been proposed to be used for the characterization of the material preheated to temperatures where annealing of the textural defects occurred. Since the inert gas diffusion in the "low-temperature range" is controlled by the texture defects (grain boundaries, dislocations and other non-equilibrium defects), the activation energy of inert gas diffusion in this temperature range can be used as a parameter characterizing the texture of dispersed solids. The ΔH values evaluated from the slopes of the log E_D = f(1/T) plots in Fig. 88 equal 25, 35 and 55 kJ mol^{-1} (i.e., 5.9, 8.34 and 13.1 kcal mol^{-1}) for ferric oxide samples preheated to 350, 410, and 530°C, respectively.

6.3.2.2. Sinterability of materials. As shown in previous paragraphs, the ETA heating curves reflect in a sensitive manner any surface area change and recrystallization. As sintering, namely its initial stage, is usually connected with these processes, ETA can be employed for estimating sinterability of materials. Figure 89 shows ETA heating curves of Fe_2O_3 samples. The samples were prepared by Fe(III) hydroxide decomposition and its pre-treatment to 500, 900 and 1000°C. Each curve characterizes, in the low temperature region, the texture of the powdered sample. The onset of the decrease in emanation release rate has been proposed[256] to be taken as a characteristic of the actual sinterability of the sample. The temperature of the change observed on the ETA curve can be taken as the parameter which characterizes the sinterability of the material. This method has been found suitable for characterizing sinterability of UO_2 droplets prepared by a sol–gel technique[257] as well as UO_2 pellets[258]. The form of the material does not play an important role in the application of this method.

Apart from ceramic materials, metal powders as Cu and (Cu + Fe) mixture have been examined[233] and their sinterability estimated. Thus, ETA has become a suitable tool in powder metallurgy.

6.3.2.3. Characterization of heat-treated products. The control of technological

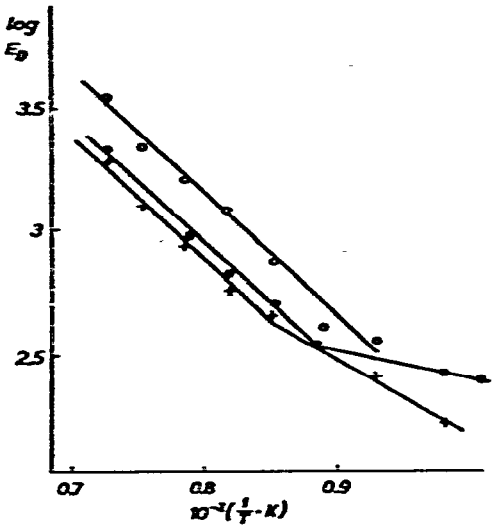

Fig. 90. Log E_D as a function of $(1/T)$ for ^{220}Rn release from zinc ferrite formed during heating of ZnO and Fe_2O_3 to 1100°C using Fe_2O_3 preheated to 700 (●), 900 (+) and 1100°C (○) (after Balek[25]).

processes frequently requires methods which enable to characterize the properties of the intermediate and final products of heat-treatment. ETA has been successfully used for characterizing the state of the solid material after heat-treatment. Several examples are quoted in the following.

Emmerich and Balek[135] have characterized by ETA the intermediate products of kaolin treatment in porcelain production. Structure properties of zinc ferrite prepared by heating the mixture of oxides have been characterized by Balek[25]. Figure 90 shows the temperature dependence of log E_D = f(1/T) obtained by the ETA of zinc ferrite samples. Samples were formed by heating the mixture (Fe_2O_3 + ZnO) to 1100°C; the ZnO was labeled by ^{228}Th and the Fe_2O_3 used was preheated to 700, 900 and 1100°C. As follows from Fig. 90 in the temperature range of 850–1000°C, the slope of the ETA curves is equal for all three samples studied, however, the diffusion coefficient values D differ. The relatively highest D value corresponds to $ZnFe_2O_4$ prepared from Fe_2O_3 heated to 1100°C. This statement was confirmed by X-ray diffraction patterns. The crystal lattice of ferrite formed was found to be more perfect when ferric oxide was preheated to 700 and 900°C, which is consistent with the supposition that ferric oxide preheated to 1100°C is more deactivated and has less ability to build a perfect spinel structure of $ZnFe_2O_4$ than ferric oxide preheated to 700 and 900°C. The activation energy of radon diffusion in zinc ferrite samples above 850°C (almost independent of the ferric oxide prehistory) is ΔH = 197 ±20 kJ mol^{-1} (47 ±5 kcal mol^{-1}). At lower temperatures where grain boundary diffusion and surface diffusion take place, a difference in activation energies is observed.

The ETA characterization of the intermediate products of nuclear ceramic fuel (U_3O_8) has been published by Balek et al.[259, 260]. Properties of the products prepared by the so-called "sol–gel" technique depend on the time of gel washing and on the

TABLE 19

CHARACTERISTICS OF INTERMEDIATE PRODUCTS OF CERAMIC NUCLEAR FUEL

Sample notation	*Relative porosity (%)*	*Activation energy, ΔH, of ^{220}Rn diffusion (kJ mol^{-1})*	*Emanation release rate, $E_{25°C}$*
3V	34.1	106.8	0.07
3D	72.8	54.4	0.17
3T	76.6	71.6	0.08
3S	75.9	82.2	0.08
O5S	66.6	69.6	0.10
9S	76.9	41.1	0.18

drying conditions. Table 19 summarizes the characteristics of the products obtained by heat treatment of dried initial gelatinous material to 800°C in air. The technological conditions of sample preparation are given in the original paper[260]. It is interesting to compare the values of activation energy of radon diffusion evaluated from ETA cooling curves, the values $E_{25°C}$ for the cooled samples, and the relative porosity of the materials. The relatively highest value, $\Delta H = 108.6$ kJ mol^{-1} (25.9 kcal mol^{-1}), was found for a material which exhibits the lowest porosity and lowest value of $E_{25°C}$. Contrarily, the relatively lowest value of $\Delta H = 71.6$ kJ mol^{-1} (i.e., 17.1 kcal mol^{-1}) corresponds to the material where the highest porosity and highest value of $E_{25°C}$ were found. The agreement is satisfactory, as in the considered temperature interval (between 25 and 800°C) radon diffusion is controlled by a grain boundary mechanism.

6.3.3. Defect equilibrium changes at elevated temperatures in non-stoichiometric solids

In this paragraph the applicability of the ETA will be shown to reveal the changes in defect equilibrium taking place at elevated temperatures in non-stoichiometric solids.

Figure 91a, b shows the ETA curves of α-Al_2O_3 subsequently measured during heatings in various atmospheres affecting the stoichiometry of the sample. Aluminum oxide homogeneously labeled by ^{228}Th and previously annealed has first been heated in nitrogen containing a small amount (few k Pa pressure) of oxygen[47]. Curves 1 and 2 in Fig. 91 correspond to this heating. As the two curves do not differ, it is possible to speak of the reversible defect equilibrium established during heating in oxygen-containing atmosphere. Curves 4 and 5 in Fig. 91 were measured during heating of the sample to about 1400°C in nitrogen containing 5% hydrogen; they represent the defect equilibrium established in aluminum oxide during heating in the reducing atmosphere. The differences in emanating power between curves 1, 2 and 4, 5 appear at temperatures higher than the Tammann temperature. Thus, a change in the lattice defect equilibrium can be assumed. Curve 3 in Fig. 91 was measured during heating

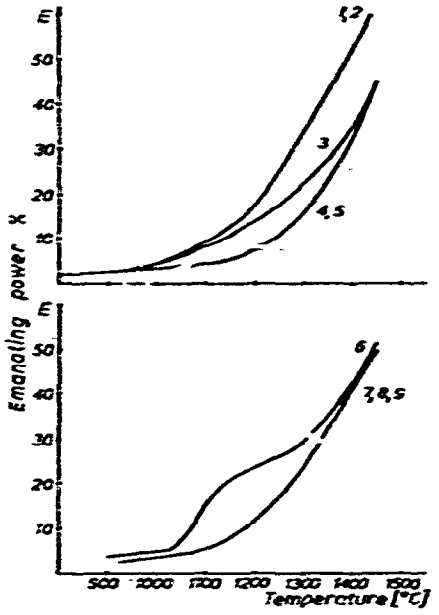

Fig. 91. Dependence of emanating power of α-Al_2O_3 on oxygen partial pressure (after Gregory and Moorbath[47]). Curves 1 and 2: successively measured ETA heating curves of a sample preheated to 1475°C. Curve 3: ETA heating curve of the same sample as in curves 1 and 2 measured in nitrogen + 5 H_2. Curves 4 and 5: successive repetitions of curve 3 in nitrogen + 5 H_2. Curve 6: ETA heating curve of the same sample as in curves 1–3 measured during repeated heating in commercial nitrogen. Curves 7, 8, 9: successive repetitions of curve 5 obtained during subsequent heating in commercial nitrogen. Heating rate 5 K min^{-1}.

in a reducing atmosphere, the sample previously annealed in an oxygen containing atmosphere. It reflects, therefore, the process of transition of one defect equilibrium into another. α-Al_2O_3 has been shown to be a metal excess semiconductor at high temperatures and the lattice becomes more defective on the reduction of the oxygen pressure. Excess metal ions are situated in interstitial positions. When the sample is reheated in nitrogen a peculiar transition curve 6 (Fig. 91) occurs, and subsequent heating in nitrogen gives the reproducible curves 7, 8 and 9. As these curves are not identical with the original curves 1 and 2, one can state that the effect of hydrogen of the aluminum oxide stoichiometry is only partly reversible. Since reduction of oxygen pressure enhances sintering and recrystallization[261], Gregory and Moorbath[47] ascribed the irreversible effect to grain growth. The reversible effect is no doubt due to changes in the equilibrium defect concentration with variation in the oxygen pressure.

The differences in the ETA curves corresponding to two various lattice defect equilibria can be explained using values of activation energy of radon diffusion evaluated from curves 1, 2 and 4, 5, and equalling 238 $\pm$0.4 and 320 $\pm$2 kJ mol^{-1} (56.9 $\pm$0.1 and 76.6 $\pm$0.6 kcal mol^{-1}), respectively. If the excess metal ions occupy interstitial positions (Frenkel defects) in the corundum lattice, an increase of their number may possibly hinder the interstitial movement of the inert gas atoms. Curves 3

and 5 reflecting the transitions from one state of lattice defect equilibrium to another may be used for the description of this process.

ETA curves of similar shapes were described by Jagitsch[246] for a number of non-stoichiometric oxides and sulfides, such as for Cu_xO, MnO_{2-x}, PbO_x, $Ag_{2-x}S$, $Zn_{1-x}S$, $Cd_{1-x}S$ and $Cu_{2-x}S$. Jagitsch[246] proposed a way for evaluating the degree of lattice disorder on the basis of ETA data. Another method is also under investigation[262].

6.4. Physical changes in multi-phase systems

6.4.1. Phase transitions in solids

Phase transitions caused by the heating of solids and investigated by ETA include the following:

(a) aragonite–calcite transformation in $CaCO_3$[263]

(b) rhombic–hexagonal lattice transformation in $BaCO_3$[264]

(c) orthorhombic–rhomboedric lattice transformation in KNO_3[265]

(d) transitions of γ-Fe_2O_3 to α-Fe_2O_3[58] and γ-Al_2O_3 to α-Al_2O_3[47]

(e) transitions in $NaNO_3$ corresponding to the rotation change of the NO_3^- anion about the trigonal crystal axis[265]

(f) polytypic transition[266] of 2H type PbI_2, etc.

Modification changes in minerals, metals, polymers and other materials have been revealed by means of ETA. In most cases, ETA confirmed the results obtained by other physical or physico-chemical methods, and sometimes yielded more detailed information about the onset of the solid-state process, its mechanism, etc.

Figure 92 shows the ETA curves of KNO_3 labeled by ^{228}Th measured during heating and cooling a sample at a linear rate. The heating curve shows the increase in emanation release rate up to 123°C where the structure dissociates. The point of maximum change in the emanation release rate has been reported by Balek and

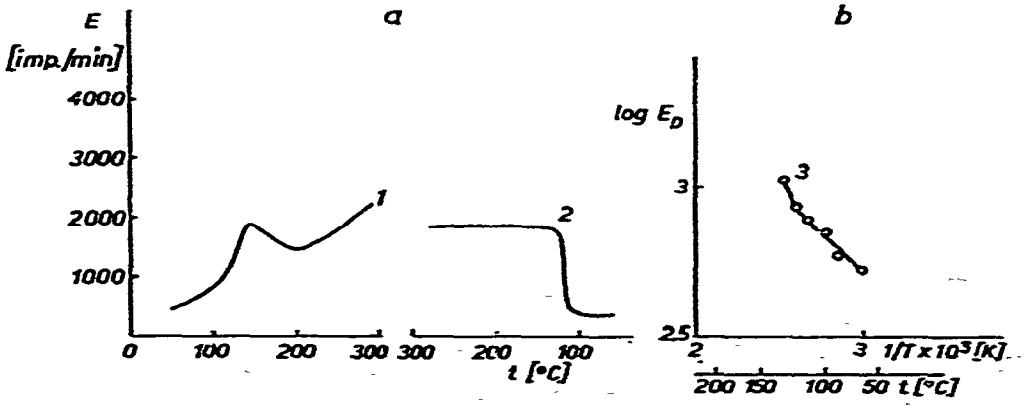

Fig. 92. ETA curves of KNO_3 in the region of polymorphic transformation. (a) When plotted E versus temperature t. (b) When plotted log E_D versus $1/T$. Curves 1 and 3 are measured during sample heating, curve 2 during sample cooling (after Balek and Zaborenko[245]).

Zaborenko[265] as corresponding to the maximum rate of the modification change. Moreover, the log $E = f(1/T)$ curve permits the determination of the temperature where the deviation of the basic exponential begins. This temperature (110°C) corresponds to the formation of the first nuclei of the new phase and is difficult to obtain so quickly by another method. According to the mechanism of the transformation proposed by Frenkel[267], a continuous creation of nuclei of the new phase and the disintegration of the old phase take place in the solid during the sample heating from this temperature to the breaking point of the curve.

Observation of the first stages of the modification change is made possible by ETA, especially when using the surface impregnation technique for sample labeling.

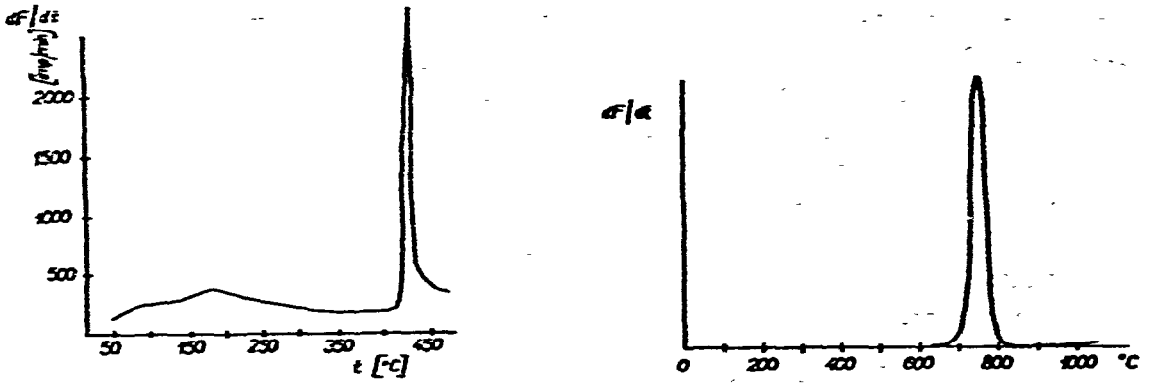

Fig. 93. Radon release rate of amorphous ZrO_2 (ex-hydroxide) during heating (after Jech et al.[269]).

Fig. 94. Temperature-dependence of ^{85}Kr release rate of α-Al_2O_3 after bombardment with 5×10^{15} Kr ions per cm^2 (after Jech and Kelly[185]).

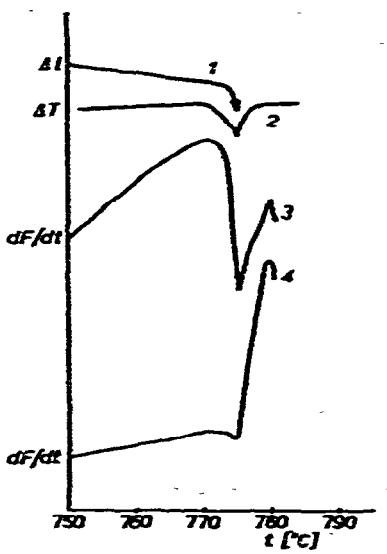

Fig. 95. Heating curves of KCl measured in the temperature range between 750 and 790°C. Dilatometry, DTA and ETA curves of a powdered sample are represented by curves 1, 2 and 3, respectively. ETA curve during reheating of previously molten sample is given by curve 4.

On cooling, a sharp step appears at the ETA curve at 120–115°C corresponding to the reversible modification change. The large drop in emanation release rate suggests that the low temperature structure is more compact[268].

6.4.2. Crystallization and recrystallization of solids

ETA as a structure sensitive method makes it possible to reveal even fine changes in structure of solids. Using the surface labeling method, the state of the surface layers of the solids can be investigated separately from the bulk of the solids. Two examples are given here.

Figure 93 shows the ETA curve of ZrO_2 labeled by ^{222}Rn ion bombardment during heating[269]. The crystallization of the initially amorphous phase at about 420°C is demonstrated by a sharp maximum.

Another example, presented by Jech and Kelly[185], is α-Al_2O_3 single crystal bombarded with 5×10^{14} Kr ions per cm^2. The ion bombardment caused an intensive radiation damage of surface layers and formation of a quasi-amorphous solid. The damaged layer of the solid is annealed during sample heating at 700–800°C, as shown by Matzke[11]. As the recovery of the original structure is accompanied by the instantaneous release of the incorporated krypton ^{85}Kr, this process can be observed immediately by means of ETA under dynamic conditions of the heat treatment (see Fig. 94).

Results important for silicate research, as well as for the investigation of polymers and inorganic pigments have been obtained by the ETA. The processes of crystallization of glasses[270], crystallization of terylene[239], and recrystallization of anatase[142] can serve as examples of the above-mentioned applications.

6.4.3. Melting

Melting is usually accompanied by a change in lattice type or the transformation of an amorphous structure with sudden release of the gas incorporated in the solid. An increase of the emanation release rate is usually observed some degrees before the melting point, arising from the increased mobility of the lattice components.

Figure 95 shows the melting of KCl powder[271] labeled by ^{228}Th impregnation, as investigated by dilatometry (curve 1), DTA (curve 2) and ETA (curve 3). The melting of the powdered KCl is characterized by an endothermic effect on the DTA curve and a volume shrinkage is observed on the dilatometric curve. The ETA curve exhibits a decrease of emanation release rate in the temperature range of 770–775°C, i.e., before the melting point. The decrease of the emanation release rate before melting point does not appear on the ETA curve of a repeatedly heated, previously molten sample (curve 4, Fig. 95). The decrease of E has been ascribed[271] to the surface annealing of powdered sample, annealing of irregularities and cracks and other molecular defects in the lattice. Actually, the steep fall of the ETA curve with powdered samples overlaps the rise of the curve in the beginning of the melting process. This effect has been observed by a number of authors investigating the melting of solids such as Na_2CO_3[272], Li_2CO_3[222], KNO_3[265, 273] and K_2SO_4[273].

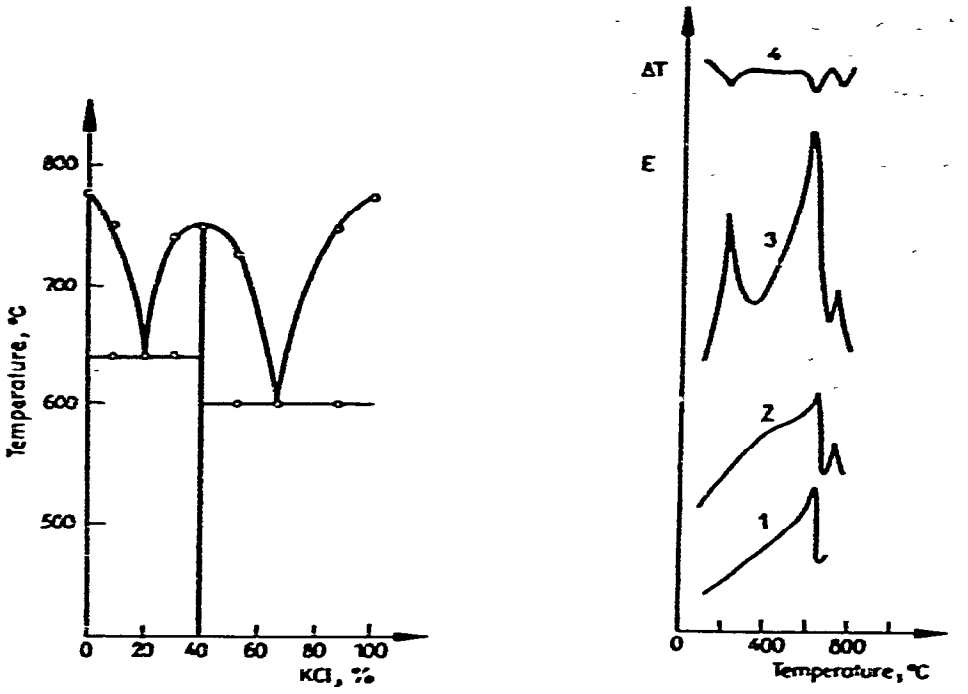

Fig. 96. (a) Phase diagram of the salt KCL–$CaCl_2$. O, points obtained by means of ETA curves demonstrated in Fig. 96b. (b) ETA curves of KCl–$CaCl_2$ mixtures in various molar ratios: curve (1) 75 : 25; curve (2) 60 : 40; curve (3) 40 : 60; curve (4) DTA curve of KCl–$CaCl_2$ mixture (40 : 60) (after Zaborenko et al.[275]).

6.4.4. Phase diagrams of multicomponent systems

As follows from Paragraph 6.4.3., the phase changes are reflected by ETA curves in a very sensitive manner. The ETA curves can, therefore, be used for the determination of phase diagrams in multicomponent systems.

The phase diagram[274] of the system KCl–$CaCl_2$ is given in Fig. 96a. The points indicated O were obtained by Zaborenko et al.[275] by means of ETA curves shown in Fig. 96b for various mixtures of the two components. The phase diagram of the CaO–Fe_2O_3 system was determined analogously[276].

The application of ETA is most advantageous for determining the phase diagrams of poorly crystalline or glass-like systems where conventional methods do not provide satisfactory results in the determination of phase change temperatures. The systems, $NaBeF_3$–$NaPO_3$ and $NaBeF_3$–KPO_3, investigated by Levina et al.[277] and the system of pyrophosphoric acid $H_4P_2O_7$–carbamid $CO(NH_2)_2$ investigated by Czekhovskich et al.[278] should be mentioned here.

6.5. Chemical reactions in solids

6.5.1. Dehydration and thermal decomposition

Numerous investigators measured the ETA curves during dehydration of crystal hydrates[e.g., 22, 26, 279–281], metal hydroxides[e.g., 41, 123, 133, 225, 226, 282–284]

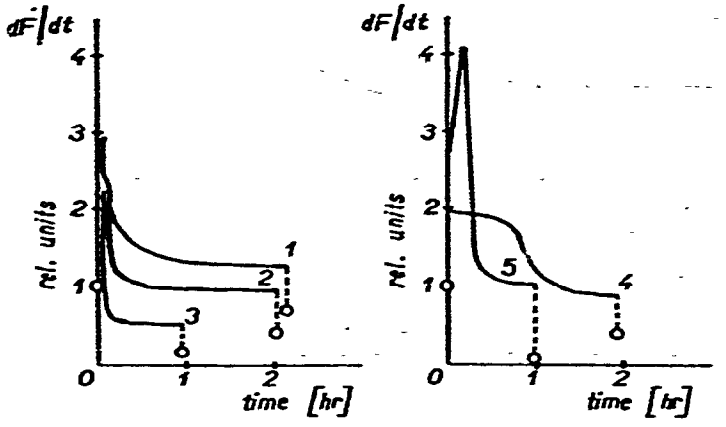

Fig. 97. Isothermal ETA curves of Ca-hydroxide at: 105 (curve 1), 205 (curve 2), 350 (curve 3), 500 (curve 4) and 600°C (curve 5) (after Zaborenko and Thätner[284]). Values of $E_{25°C}$ corresponding to initial hydroxide and final hydroxide–oxide product are given by O-points. Chemical compositions of the respective isothermally treated samples are: CaO · 1.1 H_2O (1), CaO · 1.1 H_2O (2), CaO · 1.03 H_2O (3), CaO · 0.15 H_2O (4), CaO · 0.05 H_2O (5).

and zeolites[23] and in the course of the thermal decomposition of carbonates[e.g., 29, 41, 230], oxalates[e.g., 77, 280, 285], nitrates[e.g., 22, 286, 287], sulfates[286, 287], iodates[288] and other substances[e.g., 241–243, 289–293]. ETA, with great similarity to DTA, TG and EGA, evaluated the temperature intervals where the decomposition processes take place and the loss of differently bound water molecules. Moreover, structural changes accompanying the dehydration and decomposition of solids have been sensitively reflected on the ETA curves even in cases where conventional methods were not sensitive enough.

Zaborenko and Thätner[284, 289] used ETA to investigate the thermal decomposition of metal hydroxides and salts of inorganic and organic acids. ^{228}Th has been used for labeling samples by both incorporation and impregnation techniques. Some of the ETA curves are reproduced in Figs. 97 and 98.

6.5.1.1. Revealing structure and texture changes and the active state of solids. Figure 97 shows ETA isothermal curves of calcium hydroxide measured[284] at 105, 205, 350, 500 and 600°C. The curves yield information on the state of texture and structure of the hydroxide–oxide product at any instant of the isothermal treatment. The emanation release rate is expressed in relative units of $E/E_{25°C}$, where $E_{25°C}$ is the E value measured at room temperature. The activity of the finely dispersed hydroxide–oxide product can be easily followed.

As dehydration of calcium hydroxide takes place in the temperature interval between 400 and 500°C, the ETA isotherms measured at lower temperatures must reflect the changes in the state of the solid due to the departure of physically bound (adsorbed) water. The isotherm at 500°C reflects the proper decomposition process of calcium hydroxide. After the loss of structural water from the solid, the emanation release rate decreases slowly indicating ordering of the structure. At 600°C, the dehydration proceeds so quickly that it is reflected on the ETA curve by a sharp maximum occurring after a few minutes of the isothermal treatment.

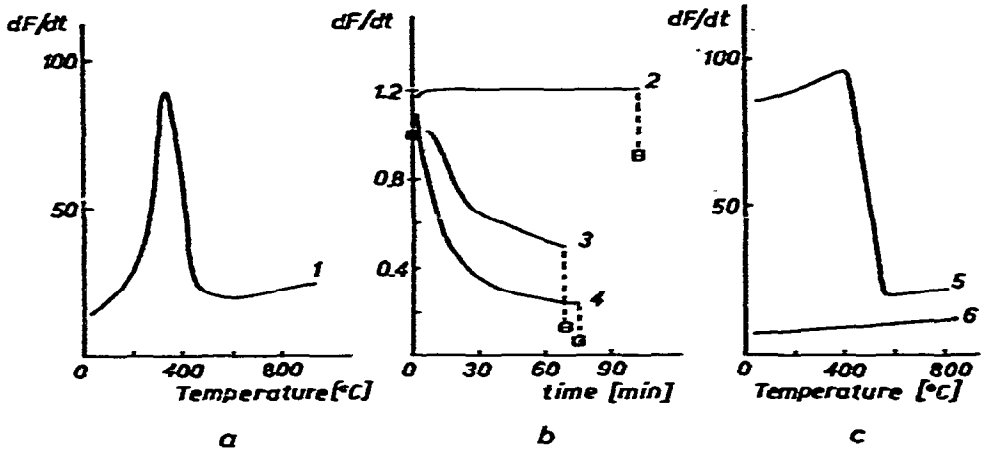

Fig. 98. ETA heating curves of Th-propionate measured: (a) during heating of the initial salt (curve 1) at a linear rate of 6 K min^{-1}. (b) during isothermal heatings of the initial salt at 300 (curve 2), 400 (curve 3) and 500°C (curve 4). The respective portions of the initial salt decomposed after the isothermal treatment are 86.93 and 95%, the respective $E_{25°C}$ values are indicated by ⊡-points. (c) during heating at a linear rate of 6 K min^{-1} of the samples preheated to 300 (curve 5) and 500°C (curve 6) (after Thätner and Zaborenko[289]).

Fig. 98 shows the decomposition of thorium propionate in air[289]. Figure 98a shows the ETA curve of the initial salt during heating at the linear rate of 6 K min^{-1}. The peak effect observed between 300 and 420°C corresponds to the decomposition of the salt. Figure 98b shows the ETA curves measured when thorium-propionate was isothermally heated at 300, 400 and 500°C. No change in emanation release rate was observed during the isothermal heating at 300°C, despite the decomposition of the salt (86% of the salts decomposed after 90 min isothermal heating at 300°C). As the $E_{25°C}$ value of the solid measured after the isothermal treatment does not change significantly compared to $E_{25°C}$ of the initial salt, it can be assumed that annealing of the active ThO_2 formed during decomposition does not occur. The annealing took place however, at 400 and 500°C, the rate of which could be determined from the ETA isotherms. The portions of the initial salt decomposed during the treatment at 400 and 500°C rose, as is indicated in Fig. 98b.

Figure 98c shows ETA curves of samples pre-treated at 300 and 500°C under isothermal conditions, according to Fig. 98b. The linear heating rate was employed in this case. During the heating of the sample, which was pre-heated to 300°C, the decomposition of the remaining thorium-propionate (14%) is completed and the annealing of the active thorium oxide takes place. Both processes are reflected by a sharp drop on the ETA (curve 5) at temperatures between 400 and 580°C. As shown in curve 6, no more decomposition and annealing have been observed during this heating in the sample pre-treated at 500°C.

Thus, when combining the ETA curves measured subsequently at: (i) linear temperature rise; (ii) suitably chosen constant temperatures; and (iii) linear temperature rise again; more complete information on the active state of solids formed by the thermal decomposition can be obtained.

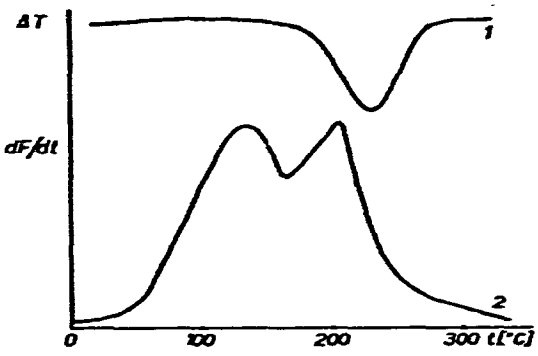

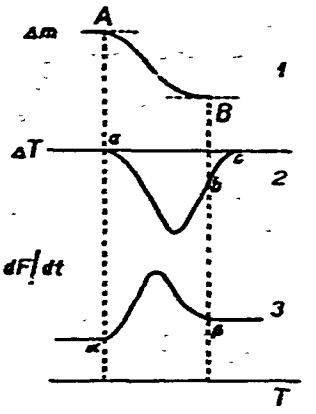

Fig. 99. ETA (curve 2) and DTA (curve 1) of $CuSO_4 \cdot H_2O$ (ex-$CuSO_4 \cdot 5H_2O$) during heating at a linear heating rate of 6 K min^{-1}. (after Balek and Zaborenko[281]).

Fig. 100. Idealized curves ETA (3), DTA (3) and TG (1) of a one-step endothermic decomposition.

Metastable pseudostructures of solids can be revealed when investigating the intermediate decomposition products by ETA. Figure 99 shows ETA and DTA curves of $CuSO_4 \cdot H_2O$ (radon ion bombardment used for sample labeling). The first peak on the ETA curve (curve 2), to which no effect on the DTA (curve 1) corresponds, has been attributed[281] to the conversion of metastable pseudostructure of trihydrate preserved after its dehydration at 120°C to the monohydrate. The second peak on the ETA (curve 2) corresponds to the dehydration of the monohydrate to the anhydrous salt. This process is reflected by an endothermic effect on the DTA (curve 1). Mutual positions of the effects on the ETA and DTA curves will be discussed next.

6.5.1.2. Relation of ETA, DTA and TG curves. The idealized curves[292] of ETA, DTA and TG, which result in the course of a one-step endothermal decomposition, are given in Fig. 100. The solid is supposed to be homogeneously labeled by a parent of emanation (^{228}Th). The beginning of the weight loss (point A of curve 1) corresponds to the onset of an endothermic effect on the DTA (point a of curve 2) and to that of the increase of emanation release rate (point α of curve 3). The end of the thermal decomposition process is denoted by point B on the TG (curve 1), which can have the same temperature as point β of the ETA (curve 3) provided that the gas transport retardation effect is eliminated. Due to thermal inertia, the DTA peak (curve 2) is usually prolonged to point c beyond point b, which corresponds to points B and β. The shape of the peak on the ETA curve is dependent on the kinetics of the decomposition as well as on the inert gas distribution within the solid. The ETA curve of a solid, where the inert gas is incorporated in the surface layers, differs from the curve obtained with homogeneously labeled solid. The difference is due to the topochemical nature of the decomposition process and gives the possibility to distinguish the initial stage of a topochemical process of the centripetal type from its next stages — the decomposition in bulk.

The influence of heating rate employed for the decomposition study by ETA

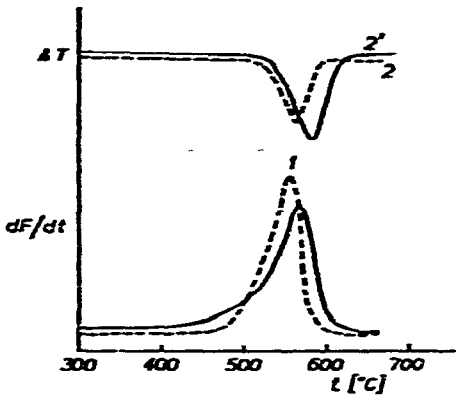

Fig. 101. ETA and DTA curves (1,1′ and 2,2′, respectively) obtained during heating of Pb_3O_4 in nitrogen (after Fouqué et al.[293]). Curves 1 and 2 represent ETA and DTA curves measured at a linear heating rate of 2.5 K min^{-1}. Curves 1′ and 2′ represent ETA and DTA curves measured at a heating rate of 5 K min^{-1}.

is demonstrated here. Figure 101 shows the ETA and DTA curves obtained in the thermal decomposition of Pb_3O_4 to PbO_2 in nitrogen[293]. The solid was labeled by ^{222}Rn without parent using ^{226}Rn alpha-decay. If two different heating rates (2.5 and 5 K min^{-1}) are employed, shifts to higher temperatures for greater heating rate are observed on the ETA and DTA curves. As it appears from Fig. 101, the shape and height of the ETA peaks depend on the heating rate also. When analyzing the shape and height of the peaks on the ETA curves of solids labeled by a parent of emanation, it should be considered that the equilibrium between the parent and emanation is

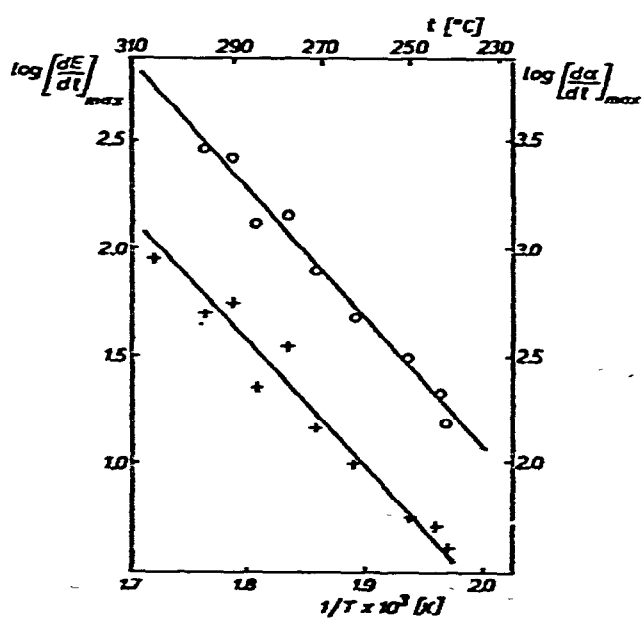

Fig. 102. Kinetic study of NiO reduction by hydrogen in the temperature range between 230 and 300°C (after Quet et al.[42]).

destroyed during the decomposition reaction. This leads to higher values of the emanating power and the "apparent emanating power" shall be used in this case (for details, see Paragraph 3.5).

6.5.2. Solid–gas reactions

6.5.2.1. Kinetic study of reduction and oxidation. The reaction,

$$NiO\,[^{222}Rn] + H_2 \rightarrow Ni + H_2O + {}^{222}Rn \qquad (103)$$

was investigated by Quet et al.[43]. The reaction kinetics can be followed by means of ^{222}Rn released from labeled NiO (^{226}Ra alpha-recoil was used for sample labeling). During heating NiO in hydrogen atmosphere, a peak appears on the ETA curve at temperatures between 230 to 300°C (see Fig. 23 in Paragraph 3.8.6). A similar peak of water release was simultaneously recorded by a catharometer. In the kinetic study, NiO was heated isothermally at various temperatures in this range and the heights of the water peaks were proportional to the maximum rate $(d\alpha/dt)_{max.}$ of the solid-gas reaction (where α is the degree of transformation in time t). Analogously, the heights of the maxima of the ETA isotherms were considered proportional to the maximum rate of radon release $(dF/dt)_{max.}$ at the given temperatures. Figure 102 shows the peak heights of the ETA isotherms as well as the peak heights of water release in isotherms (measured simultaneously at several temperatures between 230 and 300°C) plotted on a logarithmic scale against $1/T$. The similarity of the plots, $\log (dF/dt)_{max.} = f(1/T)$ and $\log(d\alpha/dt)_{max.} = f(1/T)$, showed that ETA can be successfully used for the kinetic study of this solid–gas reaction. The apparent activation energy of the reaction, evaluated from the slopes of both plots in Fig. 102, is 117.2 kJ mol^{-1} (28 kcal mol^{-1}).

The application of the ETA becomes especially advantageous for studying gas–solid reactions with industrial gases such as hydrocarbons where the gaseous products of reaction can hardly be detected. Various gas–solid reactions have been investigated by ETA from the viewpoint of chemical kinetics and reaction mechanism. One of the most important reactions, the oxidation of metals, shall be mentioned. The surface oxidation of metallic copper labeled by ^{85}Kr was studied by Chleck et al.[294] and the reaction rate, reaction order, concentration and temperature dependence were all determined. The loss of ^{85}Kr has been shown to be directly proportional to the rate of the oxidation process taking place on the metal surface. The measurement of inert gas released as well as residual ^{85}Kr activity in the sample can be used for this investigation. Figure 103 shows results of the experiments by Chleck et al.[294]. The percent loss of ^{85}Kr activity of copper labeled expressed as $d(N_t/N_0)/dt$ was found to be linearly dependent on the log of the oxygen concentration over the range 10^{-2} to 10^4 ppm O_2. From the Arrhenius dependence, $\log[d(N_t/N_0)/dt]$ versus $1/T$, the reaction order was determined. The temperature dependence of the metal oxidation was given[294] by the expression,

$$d(N_t/N_0)/dt = -K[O_2]^{1/2} \exp(-24.2/RT) \qquad (104)$$

where the value of K is 0.085% min^{-1} $ppm^{1/2}$. As the rate of oxidation and the surface

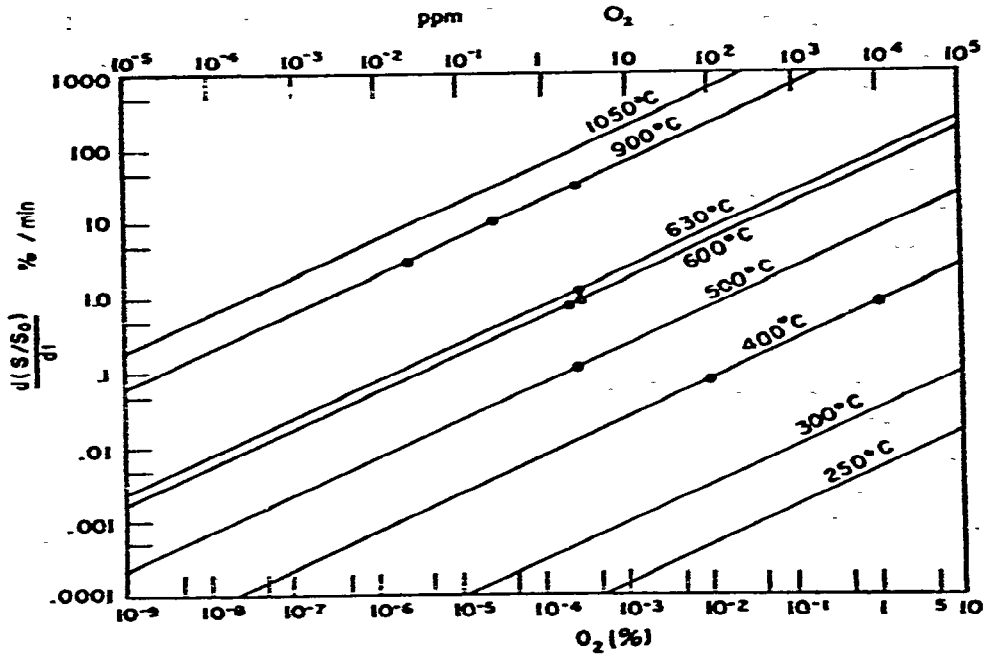

Fig. 103. Inert gas release kinetics of kryptonated Cu metal as response to oxygen at various temperatures (after Chleck[294]).

temperature have a combined effect on the release of ^{85}Kr, a "thermal stabilization" of the labeled sample is required before the oxidation itself can be investigated. The "thermal stabilization" is made by heating the sample in an inert atmosphere to a temperature about 50°C higher than the maximum surface temperature expected during the oxidation process. Oxidation during friction wear can be measured by comparing ^{85}Kr loss in air and then in an inert atmosphere. The difference in the activity loss obtained during experiments in air and in an inert atmosphere is due to the degree of oxidation.

Matzke[295] used ^{133}Xe-release measurements to establish the temperature dependence of the growth of the oxide layers on stainless steel, Ti, Ni, Cu and α-brass, 40 keV-Xe ion bombardment being used for labeling metals.

6.5.2.2. Analytical chemistry applications. The solid–gas reactions followed by the radioactive inert gas release have been widely used for the determination of gaseous components and traces of impurities in air and other gas media. Methods have been developed for the determination[7] of ozone (O_3), oxygen (O_2), sulphur dioxide (SO_2), fluorine (F_2), chlorine (Cl_2), nitric oxide (NO), amines (NH_2), hydrogen fluoride (HF), carbon monoxide (CO), hydrogen sulphide (H_2S), and hydrogen (H_2). Some of these methods[296, 297] are intended for the determination of the components mentioned in the atmosphere of other planets (Mars and/or Venus). They are of great importance in industry for the determination of explosive and/or toxic components in the atmosphere of hazardous workplaces.

As an example of gas analysis via ETA let us consider the measurement of

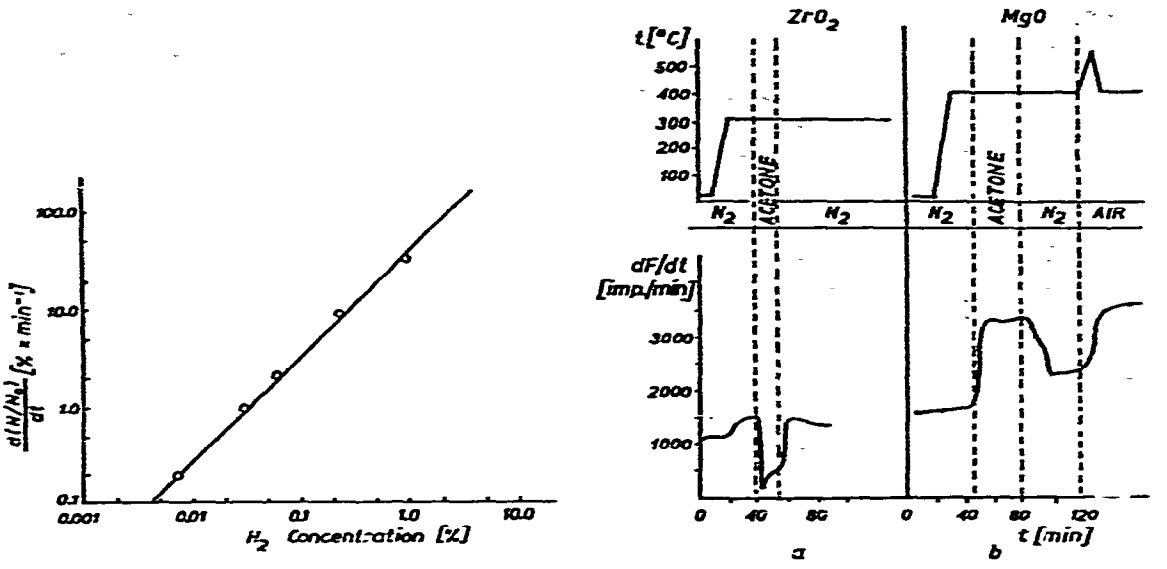

Fig. 104. Dependence of ^{85}Kr release rate of PtO_2 on various concentrations of hydrogen in nitrogen measured at room temperature (after Chleck[298]).

Fig. 105. Emanation release rate, dF/dt, and temperature measured during interaction of ZrO_2 (a) and MgO (b) with acetone vapor at 300 and 400°C, respectively (after Zhabrova et al.[299]).

hydrogen content in nitrogen by means of ^{85}Kr labeled PtO_2. The following gas–solid reaction[298] takes place on the surface of labeled PtO_2:

$$PtO_2\,[^{85}Kr] + 2\,H_2 \rightarrow Pt + 2\,H_2O + {}^{85}Kr \qquad (105)$$

Figure 104 demonstrates the dependence of the rate of ^{85}Kr activity loss of PtO_2 at room temperature and at various concentrations of hydrogen.

In the Trace Lab Research Institute (U.S.A.), two types of apparatus for the determination of oxidizing and reducing atmospheres in the atmosphere in concentrations of the ppm order were developed. Gases that can react directly or indirectly (by chemical, catalytic or thermal reaction) with the labeled solid are measurable by these instruments.

6.5.2.3. Application to heterogeneous catalysis. A special kind of solid–gas reactions are catalytic reactions taking place on solid surfaces. Figure 105 shows emanation release rates and temperatures of ZrO_2 and MgO catalysts[299] during their interaction with acetone vapors added to a nitrogen stream. As seen from Fig. 105 acetone vapors differently influence the emanation release rate of ZrO_2 and MgO heated to 300 and 400°C, respectively. With ZrO_2, the interaction leads to a decrease of emanation release rate and with MgO to its increase. The different character of the ETA response was explained by Zhabrova et al.[299] as the different character of the catalytic interaction. The increase of MgO emanation release rate during the reaction of acetone is thought to be accompanied by a partial decomposition of acetone. The subsequent flow of pure nitrogen leads to a decrease of emanation release rate of the MgO catalyst. The regeneration of the catalyst in the air is accompanied by the

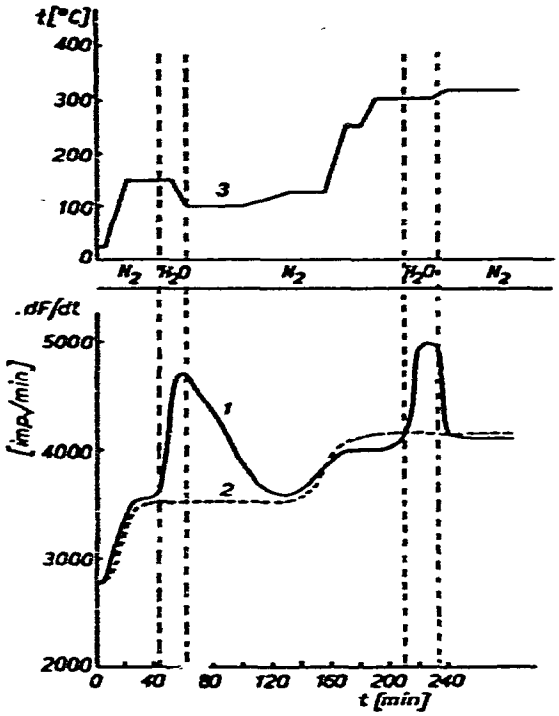

Fig. 106. Time-dependence of emanation release rate, dF/dt, for ThO_2 during its interaction with water vapor (curve 1) and in the absence of water vapor (curve 2). Time-dependence of the temperature of the sample measured during ETA (curve 1) is demonstrated in curve 3.

increase of both the emanation release rate and the temperature of the catalyst surface layer.

The release of inert gas was also observed by Jech[300] when a hydrogen–oxygen mixture was allowed to react on a Pt-foil labeled by ^{222}Rn. The increased rate of radon release during the first stage of the catalytic reaction on Pt-foil was supposed to be due to the reduction of the chemisorbed oxygen, which is the first step of the catalytic hydrogen oxidation. The ETA measurements carried out by Bekman et al.[301], in the course of various catalytic reactions, supported the theoretical considerations about the selectivity of the active centers on the catalyst surface.

6.5.3. Solid–liquid reactions

6.5.3.1. Hydration. Figure 106 (curve 1) shows the time-dependence of emanation release rate which takes place during the interaction[299] of ThO_2 labeled by ^{228}Th with water vapor, at 150 and 300°C. The dotted line (curve 2) shows the time-dependence of the same ThO_2 during analogous heating, but without interaction of water vapor. The increase of emanation release rate demonstrated in Fig. 106 is therefore caused by the surface hydration of ThO_2. After the pulse of the water vapor has been added to the nitrogen flow, the emanation release rate of the sample falls to the value corresponding to temperature.

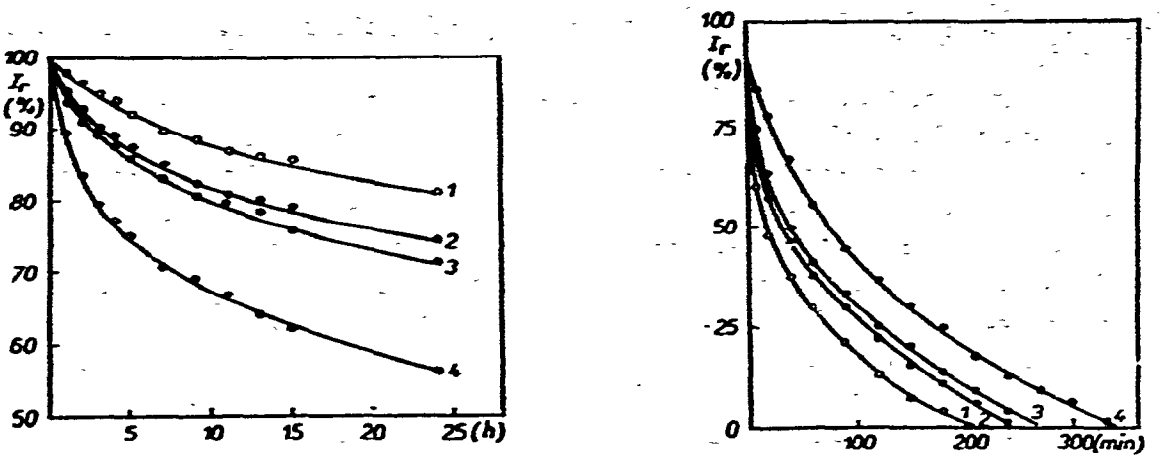

Fig. 107. Loss of ^{85}Kr activity due to corrosion of four glass samples. 1 = quartz glass; 2 = Jena-Schott; 3 = Sial; 4 = sheet glass. (a) Corrosion in 1M HCl; (b) corrosion in 1M NaOH (after Jesenák et al.[302]).

ETA has also been successfully used[26, 281] for studying the hydration of $CaSO_4 \cdot 1/2\ H_2O$.

6.5.3.2. Chemical endurance of glass. The sensitivity towards external influences is a very important property of glass. The effect of water, alkalies or acids on glass surface can be investigated by ETA after labeling the glass with an inert radioactive gas. The difference in behavior of Jena glass and barium glass in moist air has been studied by ETA by Heckter[120], who employed homogeneous glass labeling with radium. Recently, Jesenák et al.[302] proposed a method for the determination of the chemical resistivity of glasses based on measuring the loss of ^{85}Kr previously incorporated on the surface.

Fig. 107 shows the time-dependence of the ^{85}Kr activity loss in various glasses upon corrosion in 1M HCl (Fig. 107a) and in 1M NaOH (Fig. 107b). At the glass–acid interface, alkali metal ions from the glass are exchanged for hydrogen ions, according to the reaction:

$$(\text{glass-Me}[^{85}\text{Kr}])_{\text{solid}} + H^+ \rightarrow (\text{glass-H})_{\text{solution}} + Me^+ + {}^{85}\text{Kr} \qquad (106)$$

along with the formation of a film of silicic acid. This equation does not describe the effect of hydrofluoric or phosphoric acids which destroy the glass–silicate structure. After 1 hour of contact with the 1M HCl, the relative ^{85}Kr activity remaining in quartz glass decreased by 2%, in Jena-Schott by 5%, in Sial by 6% and in sheet glass by 10.3% (see Fig. 107a). The same order of reactivity was found at long contact times. Basic media destroy the silicon glass structure, causing other glass components also to go into solution. A plot of the time-dependence of the ^{85}Kr activity of labeled glass in contact with 1N NaOH is given in Fig. 107b. The endurance to alkalies can be determined by this method in one minute. After 10 minutes, the relative activity of quartz glass decreased by 16%, Sial glass by 26%, Jena-Schott glass by 32% and

sheet glass by 41%. The results obtained correspond to those obtained by classical methods.

Jesenák and Tölgyessy[303] proposed a method for the determination of the rate constant of corrosion, which is based on the measurement of ^{85}Kr loss of the labeled solid after its exposure to a corrosive medium. The method permits rapid determination of extremely slow corrosion rates. ETA can be used in the study of corrosion processes which cause changes in the surface or damage of the structure of the solid studied. Current methods used to evaluate anti-corrosion or protective agents are generally unreliable, as in many cases they take several months to complete. ETA, using ^{85}Kr labeled solids, permits such studies to be carried out relatively quickly and simply. For example, the labeled metal is put into various anti-corrosion solutions which will react with the uppermost layer of metal. The more effective anti-corrosion agents will react with the thinner layers and in a short time, thus preventing corrosion in the deeper layers. A plot of the residual ^{85}Kr activity of the labeled metal foil versus time will characterize the process. Corrosion imperceptible to the human eye can be demonstrated by this method within several hours. The method is suitable primarily for relative measurements, or for comparison of various substances using a qualitative scale. The work by Chleck et al.[304] dealing with the corrosion study of aluminium alloys in 10% NaCl and the relative oxidation rates of painted and unpainted iron samples can be mentioned.

6.5.3.3. Analytical chemistry applications. Many liquid–solid reactions, where the solid was previously labeled by ^{85}Kr, have been employed for determination of liquids. Analytical results are achieved by the use of calibration curves. Chleck et al.[304–306] proposed a method for the determination of traces of water in organic liquids based on the following reaction:

$$CaC_2[^{85}Kr] + 2\,H_2O \rightarrow Ca(OH)_2 + C_2H_2 + {}^{85}Kr \qquad (107)$$

The total activity of ^{85}Kr release is measured and is directly proportional to the

TABLE 20

KRYPTON-LABELED SOLIDS APPLICABLE AS END-POINT INDICATORS

Solid	*Substance determined*	*Titrant solution*
Mg	NaOH	HCl
Zn	NaOH, F^-	HCl
Ag	Ba^{2+}	$K_2Cr_2O_7$
AgI	Ni^{2+}	KCN
$AgIO_3$	Ca^{2+}, Mg^{2+}, Sr^{2+}	EDTA
$Y_2(C_2O_4)_3$	Fe^{3+}	EDTA
Glass	Ca^{2+}, Cd^{2+}	NaF
	Th^{4+}, H_2SO_4	NaOH
	HCl, HNO_3	

amount of water reacting with CaC_2 added to the solution investigated. The method is applicable for the determination of 0.25–2.0% H_2O in methanol[306]. The importance of the method can be seen when noting that the effectiveness of jet fuels is influenced by the amount of water present as an impurity.

A special application of solids labeled with ^{85}Kr is in radiometric titration methods[7, 108]. The application of krypton labeled solids (called also kryptonates) to the end-point indication requires that a kryptonated solid does not react with the solution, the concentration of which is sought by titration, but does react with the titrant. The onset of the release of ^{85}Kr by the kryptonate marks the appearance of excess titrant and, hence, the passing of the equivalence point. This concept provides a new completely objective type of end-point indicator. Solids commonly used after labeling by ^{85}Kr as end-point indicators in volumetric analysis are listed in Table 20.

6.5.4. Solid–solid reactions

After examples given in the preceding Paragraphs on the application of the ETA for the investigation of solid-state processes, it is natural to apply the method to the study of chemical reactions in which mixtures of two or more components react with one another at elevated temperatures. A number of publications deal with the application of ETA to the investigations of the mechanism of reactions in mixtures of solids.

6.5.4.1. Information on reaction mechanisms. Jagitsch et al.[307, 308] obtained qualitative information about the interaction at elevated temperatures between the mixtures of SiO_2–$CaCO_3$, Al_2O_3–$CaCO_3$ and CuO–Fe_2O_3. A quantitative approach to evaluate the kinetics of the reaction, $PbO + SiO_2 \rightarrow PbSiO_3$, was made[309] using isothermal ETA heating curves of the reaction mixture, where SiO_2 was labeled by

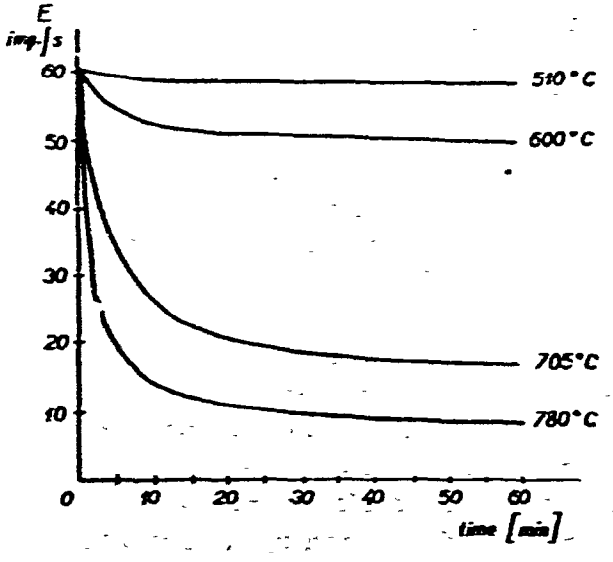

Fig. 107. Isothermal ETA curve of SiO_2 (labeled by ^{228}Th) mixed with PbO (1 : 1) (after Jagitsch[309]).

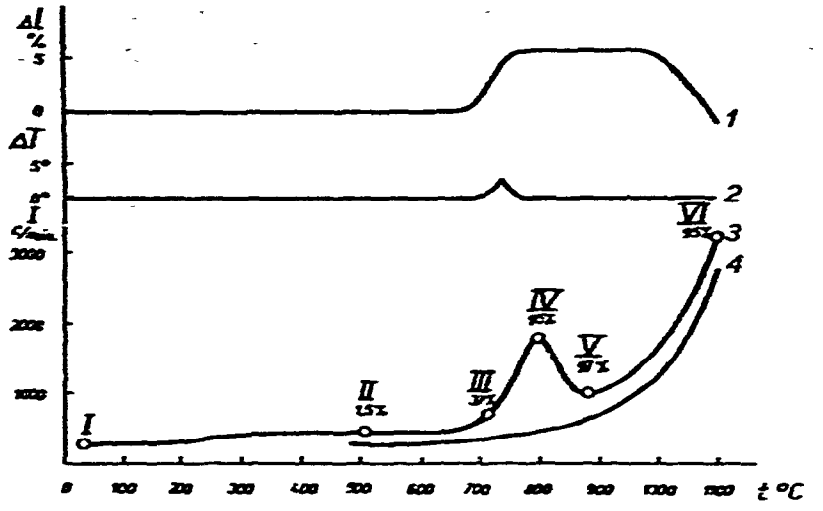

Fig. 109. ETA (curve 3), DTA (curve 2) and dilatometry (curve 1) of ZnO–Fe_2O_3 mixture when heated at 10 K min^{-1}. The ETA curve of the mixture during reheating after it was heated to 1100°C and cooled to 400°C is shown by curve 4. ZnO component was labeled by ^{228}Th. Percentage of ZnO taking part in the reaction is shown for samples I–VI (after Balek[25]).

^{288}Th. Figure 108 shows the decrease in apparent emanating power of the mixture of PbO–SiO_2 during isothermal heating at 500, 600, 640 and 700°C. Apparently, the lead silicate formed during the reaction exhibits lower E_R and E_D or both. The radon diffusion in the solid containing PbO, SiO_2 and $PbSiO_3$ is rather complex, and, therefore, the quantitative interpretation of the ETA data given by Jagitsch[309] seems unwarranted.

Schröder[41, 310] and Kittel[312] investigated the formation of spinel-type compounds ($CdFe_2O_4$, $ZnFe_2O_4$, $BeAl_2O_4$, $CuFe_2O_4$ and $MgFe_2O_4$) from reaction of metal(II) oxides and metal(III) oxides at elevated temperatures. At first, single components (hydroxide, carbonate or oxide) were checked as to their behavior during heating and after successive sudden cooling to room temperature, the E_R-values were measured. Later, the molecular mixtures were checked in the same way. Besides ETA, conventional methods were used to show that ETA gives results which cannot be obtained simply, if at all, by other methods. Other solid–solid reactions investigated by ETA are reactions of the mixtures: BeO_2–Fe_2O_3[313], ZnO–Al_2O_3[314], UO_2–ZrO_2–CaO[315], U_3O_8–TiO_2 and U_3O_8–ZrO_2[316], TiO_2–$BaCO_3$[317], and CaO–SiO_2[318].

In the following, ETA curves of a mixture of ZnO–Fe_2O_3 (ZnO being labeled by ^{228}Th) will be described and compared with results of other methods[25]. Figure 109 shows results of the ZnO–Fe_2O_3 mixture obtained by ETA, DTA, dilatometry and chemical analysis[25]. ETA curves of the starting components[23, 77] were exponential over the temperature range studied. Zinc and iron(III) oxides interact in a series of stages[319–321]. The initial layers of the product begin to form by surface diffusion at the most favorable sites at 250°C to 400°C[319, 321], their formation is reflected by

an increase in the rate of emanation release (Fig. 109, curve 3). The DTA and dilatometry curves (curves 1 and 2, Fig. 109) did not change at these temperatures. Changes in catalytic activity, adsorption properties, magnetic and other properties of the mixture have been reported[319] in this temperature range. At 500°C, 1.5% of the ZnO has reacted. A sharp change in all of the curves of Fig. 109 was observed at 670 to 700°C. X-ray patterns of the mixture heated to 730°C confirmed the sharply increased amount of ZnO (37%) which is reacting. The DTA curve (curve 2) shows a small exothermic peak. Interaction between the basic mass of the initial oxides occurs by volume diffusion above 750°C. On the ETA curve, a slowing down of the emanation release rate appears at 790°C, indicating that the reaction is completed. The dilation of the sample, which is probably caused by the formation of very fine reaction products, ceases at this point and at higher temperatures (up to the sintering temperature of the zinc ferrite) remains constant. At 850°C, the X-ray patterns indicate the presence of zinc ferrite only in the sample. Further increase in temperature is accompanied by the diffusion release of Rn from the sample. The exponential shape of the ETA curve of the $ZnO–Fe_2O_3$ mixture during the second heating (curve 4, Fig. 109) shows that the reaction was terminated in the course of the first heating. The reaction of $ZnO–Fe_2O_3$ has also been investigated by Ichiba[322] (ZnO labeling by xenon produced at uranium fission was used), and analogous results were obtained.

Valuable information regarding the mechanism of solid–solid reactions can be obtained by means of ETA. In many cases, where ETA has been used to investigate solid–solid reactions, the investigators stated higher sensitivity of the ETA method than with X-ray patterns or other methods.

6.5.4.2. Estimating the reactivity of components in reaction mixtures. A method has been proposed by Balek[323, 324] for estimating the reactivity of ferric oxide in the solid-state reaction between ZnO and Fe_2O_3. The method consists in measuring the emanation release rate during heating of the reaction mixture where one component at least has to be labeled with ^{228}Th.

The labeled component (ZnO in this case) is mixed in a stoichiometric ratio (1 : 1) with the component to be tested (Fe_2O_3 in this case) and the homogenized mixture heated to 1100°C at a constant rate of 10 K min^{-1}. The ETA curves of the mixtures, containing different types of ferric oxide, exhibited the differences between the initial surface stage and the volume stage of the solid-state reaction of $ZnO + Fe_2O_3$ described in Paragraph 6.5.4.1. The temperature of the most pronounced peak on the ETA curves, i.e., the start of the slowing down of emanation release rate after zinc ferrite formation, was chosen as a characteristic parameter for testing the ability of ferric oxide to react with ZnO. The higher the temperature of the peak, the lower the reactivity of the ferric oxide. In this way, ferric oxide powders prepared by the thermal decomposition of various iron salts at 700, 900 and 1100°C, as well as commercial ferric oxide specimens, have been tested[323]. Comparing the ETA results with those obtained by means of current methods based on surface area and catalytic activity measurements, it has been stated that the current methods do not always

TABLE 21

COMPARING REACTIVITY CHARACTERISTICS OF FERRIC OXIDE SAMPLES

Sample	*Fe_2O_3 (ex-carbonate) heated to °C*			*Commercial samples*		
	700	*900*	*1100*	*DF*	*PPG*	*ČDA*
Specific surface area (m^2g^{-1})	5.9	0.9	0.3	3.8	14.8	7.8
Effect on ETA curve (°C)	790	925	980	720	880	920

give a true picture of the reactivity of ferric oxide relevant to the solid-state reaction. The method based on ETA offers a more objective assessment of this property.

Table 21 lists the reactivity characteristics of ferric oxide samples prepared by thermal decomposition of iron(II, III) carbonate at 700, 900 and 1100°C and of three commercial (Made in U.S.S.R.) ferric oxide samples of unknown history, denoted "D.F.", P.P.G.", "Č.D.A.". By comparing the ETA results obtained and the specific surface areas we can see that ferric oxide (ex-carbonate) loses its reactivity with a decreasing surface area. For the commercial ferric oxide, sample "D.F." exhibits the highest reactivity even though its surface area is relatively low (3.8 $m^2\ g^{-1}$). The reactivities of the three commercial ferric oxide samples decrease in the sequence: "D.F.", "P.P.G.", Č.D.A.". No dependence between reactivities and specific surface areas of these commercial samples was found.

REFERENCES

1 K. E. Zimen, *Z. Phys. Chem.*, A 191 (1942) 1, 95; A 193 (1943) 1.
2 O. Hahn, *J. Chem. Soc. Suppl.*, S 259 (1949).
3 D. Chleck, R. Maehl and D. Cucchiara, *Int. J. Appl. Radiat. Isot.*, 14 (1963) 581, 593.
4 G. M. Zhabrova and M. D. Shibanova, *Usp. Khim.*, 36 (1967) 1406.
5 S. Ichiba, *Kagaku to Kogyo*, 19 (1966) 366.
6 V. Balek and K. B. Zaborenko, *Sov. Radiochem.*, 10 (1968) 436.
7 J. Tölgyessy and Š. Varga, *Talanta*, 17 (1970) 659.
8 V. Balek, *Chem. Listy*, 58 (1964) 1201, *Silikáty*, 13 (1969) 39.
9 V. Balek, *Anal. Chem.*, 42 (1970) 16A.
10 V. Balek, *High Temp. – High Pressures*, 5 (1973) 77.
11 Hj. Matzke, *Can. J. Phys.*, 46 (1968) 621.
12 Hj. Matzke, in B. Navinšek (Ed.). *Physics of Ionized Gases*, Institut Josef Stefan, Ljubljana, Yugoslavia, 1970, p. 326.
13 P. Bussière, in *Proc. 2nd Int. Conf., Fine Particles*, Boston, U.S.A., 1972, p. 69.
14 F. W. Felix, *Report HMI-B*, 93 (1970).
15 F. W. Felix, *J. Phys. (Paris)*, 34 (1973) C9-149.
16 O. Hahn, *Applied Radiochemistry*, Cornell University Press, Ithaca, NY, 1936, pp. 191–257.
17 A. C. Wahl and N. A. Bonner, *Radioactivity Applied to Chemistry*, Wiley, New York, 1951, pp. 284–320.
18 Y. Adda and J. Philibert, *La diffusion dans les solides*, Presses Universitaires de France, Paris, 1966.

19 K. E. Zimen and H. D. Freyer, *AED-C-21-01*, 1966; *AED-C-21-02*, 1968.
20 K. E. Zimen and W. Mickeley, *AED-C-21-03*, 1973.
21 A. Hée, *Compt. Rend.*, 223 (1946) 749.
22 P. Bussière, B. Claudel, J. P. Renouf, Y. Trambouze and M. Prettre, *J. Chem. Phys.*, 58 (1961) 668.
23 V. Balek, *Ph.D. Thesis*, Moscow State University, 1967.
24 V. Balek, *J. Radioanal. Chem.*, 2 (1969) 315.
25 V. Balek, *J. Am. Ceram. Soc.*, 53 (1970) 540.
26 Č. Jech, *Int. J. Appl. Radiat. Isot.*, 8 (1965) 179.
27 Č. Jech, *Radioisotopes in Scientific Research*, Vol. 2, Pergamon Press, London, 1958, p. 491.
28 M. Vaniš, Š. Varga and J. Tölgyessy, in W. G. Wiedemann (Ed.), *Thermal Analysis*, Vol. 2, Birkhäuser Verlag, 1972, p. 515.
29 V. Balek, K. Habersberger, *Thermochim. Acta*, 4 (1972) 457.
30 V. Balek, *Analusis*, 1 (1972) 445.
31 M. Curie, *Dissertation*, Paris, 1900.
32 E. Rutherford, *Phys. Z.*, 2 (1901) 429.
33 L. S. Kolowrat-Chervinskii, *Compt. Rend.*, 145 (1907) 425.
34 O. Hahn, *Ann. Chem.*, 440 (1924) 121.
35 K. E. Zimen, *Z. Phys. Chem.*, B 37 (1937) 231.
36 W. I. Baranow and E. G. Gracheva, *Tr. Gos. Radievogo Inst.*, 2 (1936) 61; 3 (1937) 117.
37 O. Hahn and F. Strassmann, *Naturwissenschaften*, 26 (1938) 755; 27 (1939) 11, 89.
38 S. Flügge and K. E. Zimen, *Z. Phys. Chem.* B 42 (1939) 179.
39 W. Seelmann-Eggebert, G. Pfennig and G. Münzel, *Chart of Nuclides*, Nucl. Res. Center Karlsruhe, 4th ed., 1974.
40 G. Friedlander and J. W. Kennedy, *Introduction to Radiochemistry*, Wiley, New York, Chapman & Hall, London, 1949, p. 107.
41 W. Schröder, *Z. Elektrochem.*, 52 (1948) 133, 140, 160 and 166.
42 V. Balek, S. D. Baikow and K. B. Zaborenko, *Sov. Radiokhem.*, 12 (1970) 137.
43 C. Quei, P. Bussière and R. Fretty, *C.R. Acad. Sci.*, 275C (1972) 1077.
44 A. Müller, *Z. Phys. Chem.*, A 149 (1930) 257.
45 O. Werner, *Z. Elektrochem.*, 39 (1933) 611.
46 L. D. Mears and T. S. Elleman, *Phys. Status. Solidi A*, 7 (1971) 509.
47 T. N. Gregory and S. Moorbath, *Trans. Faraday Soc.*, 47 (1951) 844.
48 Č. Jech, *Phys. Lett.*, 39A (1972) 417.
49 E. G. Gerling, *Contemporary State of the Argon Method of Age Determination* (in Russian). Izd. AN USSR, Moscow–Leningrad, 1961.
50 A. Wänke, *Fortschr. Chem. Forsch.*, 7 (1966) 322.
51 S. Kalbitzer, *Z. Naturforsch.*, 17a (1962) 1071.
52 T. Lagerwall, *Nucleonics*, 4 (1962) 158.
53 H. P. Mundt and A. K. H. Richter, *Z. Naturforsch.*, 20a (1965) 267.
54 A. K. H. Richter and K. E. Zimen, *Z. Naturforsch.*, 20a (1965) 666.
55 P. Schmeling, *J. Phys. Chem. Solids*, 28 (1967) 1185.
56 F. W. Felix, *Phys. Status Solidi*, 27 (1968) 529.
57 R. Lindner and Hj. Matzke, *Z. Naturforsch.*, 14a (1959) 582, 1074, 15a (1960) 1082.
58 S. Yajima, S. Ichiba, S. Kamemoto and K. Shiba, *Bull. Chem. Soc. Jpn.*, 33 (1960) 426; 34 (1961) 133.
59 S. Kawasaki, *J. Nucl. Sci. Technol.*, 4 (1967) 239; *J. Nucl. Mater.*, 22 (1967) 192.
60 P. Koss, *Acta Phys. Austriaca*, 26 (1967) 251.
61 D. L. Morrison, T. S. Elleman and D. N. Sunderman, *J. Appl. Phys.*, 35 (1964) 1616.
62 A. S. Ong and T. S. Elleman, *J. Nucl. Mater.*, 42 (1972) 191.
63 R. Kelly, *Can. J. Chem.*, 39 (1961) 2411.
64 G. Carter and J. S. Colligon, *Ion Bombardment of Solids*, Heinemann, London, 1968.
65 G. Dearnaley, J. H. Freemon, R. S. Nelson and J. Stephen, *Ion Implantation*, North Holland, Amsterdam, 1973.
66 E. A. Brown and J. H. Leck, *Br. J. Appl. Phys.*, 10 (1964) 364.
67 E. V. Kornelsen, *Can. J. Phys.*, 42 (1964) 364.
68 P. A. Redhead, E. V. Kornelsen and J. P. Hobson, *Can. J. Phys.*, 40 (1962) 184.

69 G. Brebec, V. Lévy and Y. Adda, *C.R. Acad. Sci.*, 252 (1961) 872.
70 Č. Jech, *Nature*, 178 (1956) 1343.
71 H. Maddix and M. A. Allen, *Trans. 10th Vacuum Symp. of the AUS*, MacMillan, London, 1963, p. 197.
72 H. T. Bayard and D. Alpert, *Rev. Sci. Instrum.*, 21 (1957) 71.
73 G. Carter, *Vacuum*, 9 (1959) 190.
74 C. Almen and G. Bruce, *J. Nucl. Instrum. Methods*, 11 (1961) 257, 279.
75 J. A. Davies, F. Brown and M. Mc. Cargo, *Can. J. Phys.*, 41 (1963) 829.
76 I. Bergström, F. Brown, J. A. Davies, J. S. Geiger, R. L. Graham and R. Kelly, *J. Nucl. Instrum. Methods*, 21 (1963) 249.
77 V. Balek, *J. Mater. Sci.*, 4 (1969) 919.
78 F. Brown and J. A. Davies, *Can. J. Phys.*, 41 (1963) 844.
79 B. Cobic, G. Carter and J. H. Leck, *Br. J. Appl. Phys.*, 12 (1961) 288.
80 W. Grant and G. Carter, *Vacuum*, 15 (1965) 477.
81 N. Bohr, *Phil. Mag.*, 25 (1913) 10.
82 H. A. Bethe, *Ann. Phys.*, 5 (1930) 325.
83 F. Bloch, *Ann. Phys.*, 16 (1933) 285.
84 N. Bohr, *Kgl. Danske Videnskab. Silskcb., Mat. Fys. Medd.*, 18 (1948) No. 8.
85 K. O. Nielsen, in M. L. Smiths (Ed.), *Elektromagnetically Enriched Isotopes and Mass Spectrometry*, Butterworths, London, 1956, p. 68.
86 J. Lindhard and M. Scharff, *Phys. Rev.*, 124 (1961) 128.
87 J. Lindhard, M. Scharff and H. E. Schiøtt, *Kgl. Danske Videnskab. Silskab., Mat. Fys. Medd.*, 33 (1963) No. 14, 1.
88 D. K. Holmes and G. Leibfried, *J. Appl. Phys.*, 31 (1960) 1046.
89 D. Powers and W. Whaling, *Phys. Rev.*, 126 (1962) 61.
90 M. T. Robinson and O. S. Oen, *Appl. Phys. Lett.*, 2 (1963) 30.
91 J. A. Davies, F. Brown and M. McCargo, *Can. J. Phys.*, 41 (1963) 829.
92 J. A. Davies, J. Friessen and J. D. McIntyre, *Can. J. Chem.*, 38 (1960) 1526.
93 M. M. Bredov and N. H. Okuneva, *Dokl. Akad. Nauk SSSR*, 113 (1957) 795.
94 J. L. Whitton, *J. Appl. Phys.*, 36 (1965) 3917.
95 H. Lutz and R. Sizzmann, *Phys. Lett.*, 5 (1963) 113.
96 R. L. Hines, *Phys. Rev.*, 120 (1960) 1626.
97 W. J. Kleinfelder, W. S. Johnson and J. F. Gibbson, *Can. J. Phys.*, 46 (1968) 597.
98 B. Domeij, I. Bergström, J. A. Davies and J. Uhler, *Ark. Fys.*, 24 (1963) 399.
99 I. Bergström, J. A. Davies, B. Domeij and J. Uhler, *Ark. Fys.*, 24 (1963) 389.
100 R. L. Graham, J. A. Davies and F. Brown, *Bull. Am. Phys. Soc. Ser.*, 11, 7 (1962) 491.
101 R. L. Graham, F. Brown, J. A Davies and J. P. S. Pringte, *Can. J. Phys.*, 41 (1963) 1686.
102 J. A. Davies, B. Domeij and J. Uhler, *Ark. Fys.*, 24 (1963) 377.
103 J. A. Davies, J. B. McIntyre, R. L. Cushing and M. Lounsbury, *Can. J. Chem.*, 38 (1960) 1535.
104 J. A. Davies, B. Domeij and J. Uhler, *Ark. Fys.*, 41 (1963) 1231.
105 G. R. Piercy, F. Brown, J. A. Davies and M. McCargo, *Phys. Rev. Lett.*, 10 (1963) 399.
106 J. S. Colligon and J. H. Leck, *Proc. 8th National Vacuum Symp. of the AVS*, Vol. 1, Pergamon Press, Oxford, 1962, p. 275.
107 E. V. Kornelsen, *Proc. 8th National Vacuum Symp. of the AVC*, Vol. 1, Pergamon Press, Oxford, 1962, p. 281.
108 J. Tölgyessy, Š. Varga and E. H. Klehr, *Radioisotopy*, 15 (1974) 623.
109 A. M. Trofimov and Ju. N. Kazankin, *Radiokhimia*, 7 (1965) 228.
110 V. Jesenák, Š. Varga and J. Tölgyessy, *Atompraxis*, 14 (1968) 204.
111 V. Jesenák, J. Tölgyessy and E. H. Klehr, *Radiochem. Radioanal. Lett.*, 19 (1974) 223.
112 D. L. Chleck, *IAEA Symposium on Radiochemical Methods of Analysis*, 1969, Paper No. SM-55/41.
113 J. Tölgyessy, M. Harangózó, P. Dillinger, Š. Varga and E. H. Klehr, *Radiochem. Radioanal. Lett.*, 19 (1974) 147.
114 R. Sizmann and W. Rupp, *Z. Naturforsch.*, 170 (1962) 179.
115 P. J. Hidalgo and R. Sizmann, *Ber. Dtsch. Keram. Ges.*, 43 (1966) 532.
116 C. Quet, J. Rousseau-Violet and P. Bussière, *Radiochem. Radioanal. Lett.*, 9 (1972) 9.
117 K. B. Zaborenko and O. A. Kapustin, *Radiokhimia*, 16 (1974) 611.

118 C. Quet, J. Rousseau-Violet and P. Bussière, *Radiochem. Radioanal. Lett.*, 23 (1975) 359.
119 I. D. Kurbatov, *J. Phys. Chem.*, 45 (1941) 851.
120 K. Heckter, *Glastech. Ber.*, 12 (1934) 156.
121 D. I. Roulch and I. E. Duncan, *Aust. J. Chem.*, 10 (1957) 112.
122 O. A. Kapustin and K. B. Zaborenko, *Radiokhimia*, 16 (1974) 618.
123 H. Götte *Z. Phys. Chem.*, B 40 (1938) 216.
124 G. Tammann, *Z. Angew. Chem.*, 39 (1926) 869.
125 R. Fricke and O. Glemser, *Z. Phys. Chem.*, 236 (1937) 27.
126 B. Burt and J. Kurbatov, *J. Am. Chem. Soc.*, 70 (1948) 2278.
127 M. Francis, *Kolloid Z.*, 59 (1932) 292.
128 B. Nikitin and E. Ioffe, *Bull. Acad. Sci. URSS, Ser. Sci. Chem.*, (1944) 210.
129 P. Wolf and N. Riehl, *Strahlentherapie*, 40 (1931) 1.
130 G Graue and H. Koch, *Ber.*, 73 (1940) 984.
131 G. Graue and N. Riehl, *Angew. Chem.*, 52 (1939) 112.
132 O. Hahn and M. Biltz, *Z. Phys. Chem.*, A 126 (1927) 323.
133 L. Z. Cook, *Z. Phys. Chem.*, B 42 (1939) 221.
134 G. Graue and N. Riehl, *Z. Anorg. Allg. Chem.*, 233 (1937) 365.
135 F. Strassmann, *Z. Phys. Chem.*, B 26 (1934) 362.
136 V. Balek, *Z. Anorg. Allg. Chem.*, 380 (1971) 82.
137 V. Balek, C. Quet and P. Bussière, unpublished results.
138 W. D. Emmerich and V. Balek, *High Temp. – High Pressures*, 5 (1973) 67.
139 Č. Jech and R. Kelly, *J. Phys. Chem. Sol.*, 30 (1969) 465.
140 J. A. Hedvall, *Solid State Chemistry*, Elsevier, Amsterdam, 1969.
141 G. M. Schwab and J. Block, *Z. Phys. Chem.*, 1 (1955) 92.
142 V. Balek in I. Buzás (Ed.), *Thermal Analysis*, Vol. 2, Akadémia Kiadó, Budapest, 1975, p. 551.
143 V. Balek, *J. Radioanal. Chem.*, 30 (1976) 599.
144 W. Inthoff and K. E. Zimen, *Trans. Chalmers Univ. Technol., (Göteborg)*, 176 (1956) 16.
145 T. Lagerwall and K. E. Zimen, *Report EUR-1372 e*, 1964.
146 D. G. Hurst, *Report AECL-1550*, 1962.
147 H. Gaus, *Z. Naturforsch.*, 20a (1965) 1298.
148 T. Lagerwall and P. Schmeling, *HMI-Report, B-27*, 1963.
149 R. Kelly and F. Brown, *Acta Metall.*, 13 (1961) 169.
150 R. Kelly, *Can. J. Chem.*, 39 (1961) 664.
151 R. Kelly and Hj. Matzke, *J. Nucl. Mater.*, 17 (1965) 179.
152 R. Kelly and Hj. Matzke, *J. Nucl. Mater.*, 20 (1966) 171.
153 G. Di Cola and Hj. Matzke, *Nucl. Instrum. Methods*, 51 (1967) 341; EURATOM, *Report EUR 2157e*, 1964.
154 L. D. Mears and T. S. Ellemann, *Oak Ridge operations 3508-2*, 1967.
155 R. Kelly, *Acta Metall.*, 12 (1964) 123.
156 M. McCargo, J. A. Davies and F. Brown, *Can. J. Phys.*, 41 (1963) 1231.
157 F. Brown and J. A. Davies, *Can. J. Phys.*, 41 (1963) 844.
158 R. Kelly and E. Ruedl, *Phys. Status Solidi*, 13 (1966) 55.
159 Hj. Matzke, G. Rickers and G. Sørensen, *Z. Naturforsch.*, 24a (1969) 820.
160 Hj. Matzke, *Z. Naturforsch.*, 22a (1967) 507.
161 R. Kelly, Č. Jech and Hj. Matzke, *Phys. Status Solidi*, 25 (1968) 641.
162 P. Pronko and R. Kelly, *Radiat. Eff.*, 3 (1970) 161.
163 P. A. Redhead, *Vacuum*, 12 (1962) 203.
164 G. Carter, *Vacuum*, 12 (1962) 245.
165 W. A. Grant and G. Carter, *Vacuum*, 15 (1965) 13.
166 M. D. Norgett and A. B. Lidiard, *IAEA Symposium on Radiation Damage in Reactor Materials*, Vol. 1, IAEA, Vienna, 1969, p. 61.
167 M. D. Norgett and A. B. Lidiard, *Phil. Mag.*, 18 (1968) 1193.
168 L. D. Mears and T. S. Ellemann, *Phys. Status Solidi*, 7 (1971) 509.
169 T. S. Ellemann, C. H. Fox, Jr. and L. D. Mears, *J. Nucl. Mater.*, 30 (1969) 89.
170 Hj. Matzke, *J. Nucl. Mater.*, 21 (1967) 190.
171 F. W. Felix and M. Müller, *Phys. Status Solidi*, 46 (1971) 265.
172 S. Y. T. Lagerwall, *Trans. Chalmers Univ. Technol. Gothenburg*, 307 (1965).

173 F. W. Felix and S. Y. T. Lagerwall, *Phys. Status Solidi*, 4 (1971) 73.
174 Hj. Matzke, *J. Nucl. Mater.*, 30 (1969) 107.
175 F. W. Felix and M. Müller, *Ind. J. Pure Appl. Phys.*, 14 (1976) 249.
176 F. W. Felix and K. Meier, *Phys. Status Solidi*, 32 (1969) K 139.
177 M. Müller and M. J. Norgett, *Z. Naturforsch.*, 289 (1973) 311.
178 M. Müller and M. J. Norgett, *J. Phys.*, 34 (1973) C-9-159.
179 E. V. Kornelsen and M. K. Sinha, *Appl. Phys. Lett.*, 9 (1966) 112.
180 E. V. Kornelsen and M. K. Sinha, *J. Appl. Phys.*, 39 (1968) 4546.
181 Hj. Matzke, *Phys. Status. Solidi*, 18 (1966) 285.
182 F. F. Momyer, *The radiochemistry of the Rare Gases*, USAEC, NAS-NS-3025, 1960, p. 9.
183 R. Kelly and Č. Jech, *Proc. Br. Ceram. Soc.*, 9 (1967) 243.
184 R. Kelly and Č. Jech, *J. Nucl. Mater.*, 30 (1969) 122.
185 Č. Jech and R. Kelly, *Proc. Br. Geram. Soc.*, 9 (1967) 259.
186 D. G. Martin, *J. Phys. Chem. Solids*, 10 (1959) 64.
187 B. S. Hickman and D. Walker, *J. Nucl. Mater.*, 18 (1966) 197.
188 J. J. Antal and A. N. Goland, *Phys. Rev.*, 112 (1958) 103.
189 Y. Oishi and W. D. Kingery, *J. Chem. Phys.*, 33 (1960) 480.
190 J. A. Desport and J. A. G. Smith, *J. Nucl. Mater.*, 14 (1964) 135.
191 P. W. Levy, *Disc. Faraday Soc.*, 31 (1961) 118.
192 R. Kelly and L. Q. Nghi, *Proc. Conf. Ion Implantation, Thousands Oaks, Calif., U.S.A., 1970.*
193 E. V. Kornelsen and M. K. Sinha, *Can. J. Phys.*, 46 (1968) 613.
194 R. Kelly, *Can. J. Phys.*, 42 (1964) 364.
195 J. A. Davies and P. Jaspersgard, *Can. J. Phys.*, 44 (1966) 1631.
196 Hj. Matzke and J. L. Whitton, *Can. J. Phys.*, 44 (1966) 995.
197 Hj. Matzke, *Radiat. Eff.*, 3 (1970) 93.
198 Č. Jech and R. Kelly, *J. Nucl. Mater.*, 20 (1966) 269.
199 R. M. Berman, *Bettis (USA), Report WAPD-TM-350*, 1962.
200 T. Lagerwall, *Nukleonik*, 6 (1967) 179.
201 P. Schmeling, *J. Phys. Chem. Solids*, 28 (1967) 1185.
202 Hj. Matzke, *Nucl. Appl.*, 2 (1966) 131.
203 R. Kelly, *Phys. Status. Solidi*, 21 (1967) 451.
204 C. W. Tucker and F. J. Norton, *J. Nucl. Mater.*, 2 (1960) 329.
205 C. M. Drum, *Phys. Status Solidi*, 9 (1965) 635.
206 J. Lynch, *Phys. Rev.*, 118 (1960) 468.
207 Hj. Matzke, *J. Nucl. Mater.*, 30 (1969) 110.
208 Hj. Matzke and J. A. Davies, *J. Appl. Phys.*, 38 (1967) 1805.
209 F. W. Felix and T. Lagerwall, *Phys. Status Solidi*, (a) 46 (1971) 265.
210 H. S. Rosenberg, *Report, Battelle Memorial Inst., BMI-1444*, 1960.
211 R. Lindner and Hj. Matzke, *Z. Naturforsch.*, 149 (1959) 582.
212 Hj. Matzke, *J. Mater. Sci.*, 2 (1967) 444.
213 B. B. Rosi and H. H. Staub, *Ionization Chambers and Counters*, National Nucl. Energy Ser., Div. V., Vol. 2, McGraw Hill, New York, 1949.
214 S. Flügge (Ed.), *Handbuch der Physik*, Vol. 45, *Nuclear Instrumentation II*, Springer Verlag, 1958.
215 R. Voltz and J. P. Adloff, *J. Chim. Phys.*, 57 (1960) 90.
216 C. Quet and P. Bussière, *J. Radioanal. Chem.*, 27 (1975) 5.
217 K. B. Zaborenko, L. L. Melichov and V. A. Portyanoy, *Radiokhimia*, 7 (1965) 319.
218 V. Balek, *Radiochem. Radioanal. Lett.*, (1978) in press.
219 S. Ichiba, *J. Jpn. Soc. Pow. Metal.*, 8 (1961) 137.
220 J. N. Gregory and J. Howlett, *Report AERE Harwell, C/R 490*, 1950.
221 W. W. Wendlandt, *Methods of Thermal analysis*, J. Wiley, New York, 2nd ed., 1974, p. 212.
222 W. D. Emmerich and V. Balek, in H. G. Wiedemann (Ed.), *Thermal Analysis*, Vol. 1., Birkhäuser Verlag, Basel, 1972, p. 475.
223 J. C. Clayton and S. Aronson, *Report WAPD-276*, 1963.
224 K. Jockers, *Z. Anorg. Allg. Chem.*, 265 (1951) 49.
225 G. M. Zhabrova and M. D. Shibanova, *Kinet. Katal.*, 2 (1961) 668.
226 F. Gourdier, P. Bussière and B. Imelik, *C.R. Acad. Sci.*, 264 C (1967) 1625.

227 C. Quet and P. Bussière, *C.R. Acad. Sci.*, 280 C (1975) 859.
228 V. Balek and P. Bussière, *Sci. Ceram.*; (1978) to be published.
229 S. B. Skladzien, *Report Argonne Nat. Lab., ANL-6335*, 1961.
230 J. C. Lagier, P. Bussière and M. Prottre, *C.R. Acad. Sci.*, 267 (1967) 277.
231 O. Hahn and G. Graue, *Z. Physik. Chem.*, Bodenstein-Festband, (1931) 608.
232 V. Balek and V. Urbánek, *Radiochem. Radioanal. Lett.*, (1978) in press.
233 H. Schreiner and G. Glawitsch, *Z. Metall.*, 45 (1954) 102.
234 V. Balek and P. Bussière, *Proc. Int. Conference, Lattice Defects in Ionic Crystals*, Berlin (West), 1976, p. 85.
235 H. Schreiner, *Oesterr. Chem. Ztg.*, 53 (1952) 233.
236 F. H. Müller, *Kolloid. Z.*, 109 (1942) 355.
237 P. Meares, *J. Am. Chem. Soc.*, 75 (1954) 3415.
238 P. Meares, *Trans. Faraday Soc.*, 53 (1957) 101.
239 K. B. Zaborenko, D. Nietzold and N. F. Bakeew, *Vysokomol. Soedin., Ser. A* 9 (1967) 240.
240 K. B. Zaborenko and I. N. Bekman, *Radiokhimia*, 10 (1968) 268.
241 I. N. Bekman and K. B. Zaborenko, *Radiokhimia*, 10 (1968) 382.
242 J. N. Gregory and S. Moorbath, *Trans. Faraday Soc.*, 47 (1951) 1064.
243 F. Charbonier, V. Balek and P. Bussière, *J. Therm. Anal.*, 7 (1975) 373.
244 V. Balek and J. Kroupa, *Thermochim. Acta*, 22 (1978) 157.
245 G. Heinicke, Č. Jech and K. Winkler, *Z. Phys. Chem.*, 225 (1954) 161.
246 R. Jagitsch, *Trans. Chalmers Tech. Univ., Gothenburg*, 11 (1942).
247 C. C. Bidwell, *Phys. Rev.*, 10 (1917) 756.
248 A. Forestier and G. Chaudron, *C.R. Acad. Sci.*, 179 (1924) 763.
249 A. Holmes, Edinburgh, *Geol. Soc. Bull.*, 14 Pt2 (1948) 176.
250 B. J. Giletti and J. L. Kulp, *Am. Mineral.*, 40 (1955) 481.
251 S. C. Lind and C. F. Whitemore, *J. Am. Chem. Soc.*, 36 (1914) 2066.
252 B. P. Pritchin, *At. Energ.*, 25 (1968) 324.
253 P. M. C. Barretto, in *Radon in Uranium Mining, Proc. of a IAEA Panel*, IAEA Vienna, 1975, p. 129, paper IAEA-PL-565/1.
254 J. F. Evernden, G. H. Curtis, R. W. Kister and J. Obradovich, *Am. J. Sci.*, 258 (1960) 583.
255 O. Werner, *Z. Metall.*, 26 (1934) 265.
256 V. Balek, *Čs. pat.*, 136737.
257 V. Balek and M. Vobořil, in I. Buzás (Ed.), *Thermal Analysis*, Vol. 3, Akademiai Kiadó, Budapest, 1975, p. 555.
258 V. Balek, J. Vachuška and M. Vobořil, *Report Nucl. Res. Inst. Řež*, 1975, ÚJV 3631-M.
259 V. Balek, H. Landsperský and M. Vobořil, *Radiochem. Radioanal. Lett.*, 28 (1977) 289.
260 V. Balek, H. Landsperský, V. Urbánek, J. Vachuška and M. Vobořil, *Report Nucl. Res. Inst. Řež*, ÚJV, 1977.
261 H. C. Castell, S. Dilnot and M. Warrington, *Nature*, 153 (1944) 653.
262 V. Balek and P. Holba, to be published.
263 K. E. Zimen, *Z. Phys. Chem.*, B37 (1937) 231.
264 K. E. Zimen, *Z. Phys. Chem.*, B37 (1937) 241.
265 V. Balek and K. B. Zaborenko, Russian. *J. Inorg. Chem.*, 14 (1969) 464.
266 I. N. Odin, V. Balek, B. A. Popovkin and A. V. Novoselova, *Vestn. Mosk. Univ., Sov. Chim.*, (1970) 115.
267 Ya. P. Frenkel, *Zh. Eksp. Teor. Fiz.*, 9 (1939) 952.
268 F. C. Kracek, *J. Phys. Chem.*, 34 (1930) 225.
269 Č. Jech, G. M. Zhabrova, S. Z. Roginskij and M. D. Shibanova, *Radiokhimia*, 4 (1962) 355.
270 V. Balek and J. Götz, in J. Götz (Ed.), *Proc. 11th Int. Glass Congress, Prague, 1977*, Vol. 3, p. 351.
271 K. B. Zaborenko and Yu. Z. Mochalova, *Radiokhimia*, 10 (1968) 123.
272 V. Balek and K. Habersberger, in H. G. Wiedemann (Ed.), *Thermal Analysis*, Vol. 2., Birkhäuser Verlag, Basel, 1972, p. 501.
273 R. Thätner and K. B. Zaborenko, *Radiokhimia*, 8 (1966) 482.
274 O. Menge, *Z. Anorg. Chem.*, 72 (1911) 162.
275 K. B. Zaborenko, V. P. Polyakov and J. G. Shoroshev, *Radiokhimia*, 7 (1965) 324.
276 K. B. Zaborenko, V. P. Polyakov and J. G. Shoroshev, *Radiokhimia*, 7 (1965) 329.

277 M. E. Levina, B. S. Shershev and K. B. Zaborenko, *Radiokhimia*, 7 (1965) 480.
278 A. I. Czekhovskikh, D. Nitzold, K. B. Zaborenko and S. I. Volfkovich, *Zh. Neorg. Khim.*, 11 (1966) 1948.
279 C. Lieber, *Z. Phys. Chem.*, B 42 (1939) 240; A 182 (1938) 153.
280 B. Sagortschev, *Z. Phys. Chem.*, A 177 (1936) 235.
281 K. B. Zaborenko and V. Balek, *Russ. J. Inorg. Chem.*, 14 (1969) 768.
282 O. Hahn and V. Senftner, *Z. Phys. Chem.*, A 170 (1934) 191.
283 R. Jagitsch, *Z. Phys. Chem.*, A 174 (1935) 49.
284 K. B. Zaborenko and R. Thätner, *Russ. J. Inorg. Chem.*, 11 (1966) 1177.
285 Č. Jech, G. M. Zhabrova, S. Z. Roginskij and M. D. Shibanova, *Dokl. Akad. Nauk. SSSR*, 164 (1965) 1343.
286 R. Thätner and K. B. Zaborenko, *Radiokhimia*, 8 (1966) 485.
287 V. Balek, *J. Mater. Sci.*, 5 (1970) 166.
288 V. Balek and J. Julák, *J. Therm. Anal.*, 4 (1972) 293.
289 R. Thätner and K. B. Zaborenko, *Vestn. Moskov. Univ., Ser. Khim.*, (1966) 54.
290 K. B. Zaborenko, T. I. Sheherbak, Z. M. Babeskhina and L. I. Martynenko, *Zh. Neorg. Khim.*, 11 (1966) 1744.
291 P. Fouilloux, P. Bussière and B. Imelik, *C.R. Acad. Sci.*, 256 (1963) 3682.
292 B. Claudel, *Ph. D. Thèses*, Lyon, 1962.
293 D. Fouqué, P. Fouilloux, P. Bussière, D. Weigel and M. Prettre, *J. Chim. Phys.*, 62 (1965) 1088.
294 D. J. Chleck and O. Cucchiara, *Int. J. Appl. Radiat. Isot.*, 14 (1963) 599.
295 Hj. Matzke, *Int. J. Appl. Radiat. Isot.*, 27 (1976) 27.
296 D. J. Chleck, *Trans. Am. Nucl. Soc.*, 5 (1962) 278.
297 P. E. Wilkins, *Atompraxis*, 12 (1966) 391.
298 D. J. Chleck, *IAEA Symposium on Radioisotope Tracers in Industry and Geophysik, Solzburg, 1964*, Paper SM-55/41.
299 G. M. Zhabrova, S. Z. Roginskij and M. D. Shibanova, *Kinet. Katal.*, 6 (1965) 1018.
300 Č. Jech, *Proc. 2nd Int. Congres on Catalysis*, Editions Technik, Paris 1961, p. 2285.
301 I. N. Bekman, personal communication.
302 V. Jesenák, J. Tölgyessy, Š. Varga and B. Sileš, *Silikáty*, 15 (1971) 65.
303 V. Jesenák and J. Tölgyessy, *Radiochem. Radioanal. Lett.*, 19 (1974) 267.
304 D. J. Chleck, R. Maehl and O. Cucchiara, *USAEC Report*, Parametrics Inc., NYO-2757-3, 1963.
305 D. J. Chleck, *Radiochemical Methods of Analysis*, IAEA, Vienna, 1965, p. 273.
306 D. J. Chleck, R. Maehl and O. Cucchiara, *Chemist-Analyst*, 54 (1965) 84.
307 R. Jagitsch, *Monatsh. Chem.*, 68 (1936) 1.
308 R. Jagitsch and A. Maschin, *Monatsh. Chem.*, 68 (1936) 101.
309 R. Jagitsch, *Z. Phys. Chem.*, B 33 (1936) 196.
310 W. Schröder, *Z. Elektrochem.*, 46 (1940) 680.
311 W. Schröder and H. Schmäh, *Z. Elektrochem.*, 48 (1942) 241 and 300.
312 H. Kittel, *Z. Phys. Chem. (Leipzig)*, A 178 (1936) 81.
313 G. F. Hüttig, H. Jöbstl and G. Glawitsch, *Monatsh. Chem.*, 85 (1954) 976.
314 G. F. Hüttig, H. Wörl and H. H. Weitzer, *Z. Anorg. Chem.*, 283 (1956) 207.
315 S. Ichiba, *J. Nucl. Sci. Technol.*, 2 (1965) 163.
316 G. Wolf, L. Ochs and F. Strassmann, in *Radioisotopes in Scientific Research, UNESCO Conf., Paris, 1957*, Vol. 1, Pergamon Press, London 1958, p. 516.
317 K. B. Zaborenko, A. M. Babeskhin and L. L. Melikhov, *Izv. Vyssh. Uchebn. Zaved., Khim. Khim. Tekhnol.*, 3 (1960) 288.
318 K. B. Zaborenko, R. Thätner and L. L. Melikhov, *Radiokhimia*, 5 (1963) 360.
319 G. F. Hüttig, *Z. Elektrochem.*, 41 (1935) 527.
320 R. Fricke and W. Dürr, *Z. Elektrochem.*, 45 (1939) 254.
321 J. Beretka and M. J. Ridge, *Nature (London)*, 216 (1967) 473.
322 S. Ichiba, *Oyobi Funmatsuyakin*, 9 (1962) 169.
323 V. Balek, *J. Appl. Chem.*, 20 (1970) 73.
324 V. Balek, *J. Therm. Anal.*, 12 (1977) in press.